Site-scale groundwater flow modelling of Aberg

Douglas Walker
Duke Engineering & Services

Björn Gylling
Kemakta Konsult AB

December 1998

SKB

Site-scale groundwater flow modelling of Aberg

Douglas Walker

Duke Engineering & Services

Björn Gylling

Kemakta Konsult AB

December 1998

Abstract

The Swedish Nuclear Fuel and Waste Management Company (SKB) SR 97 study is a comprehensive performance assessment illustrating the results for three hypothetical repositories in Sweden. In support of SR 97, this study examines the hydrogeologic modelling of the hypothetical site called Aberg, which adopts input parameters from the Äspö Hard Rock Laboratory in southern Sweden. This study uses a nested modelling approach, with a deterministic regional model providing boundary conditions to a site-scale stochastic continuum model. The model is run in Monte Carlo fashion to propagate the variability of the hydraulic conductivity to the advective travel paths from representative canister locations. A series of variant cases addresses uncertainties in the inference of parameters and the boundary conditions. The study uses HYDRASTAR, the SKB stochastic continuum groundwater modelling program, to compute the heads, Darcy velocities at each representative canister position and the advective travel times and paths through the geosphere.

The nested modelling approach and the scale dependency of hydraulic conductivity raise a number of questions regarding the regional to site-scale mass balance and the method's self-consistency. The transfer of regional heads via constant head boundaries preserves the regional pattern recharge and discharge in the site-scale model, and the regional to site-scale mass balance is thought to be adequate. The upscaling method appears to be approximately self-consistent with respect to the median performance measures at various grid scales. A series of variant cases indicates that the study results are insensitive to alternative methods on transferring boundary conditions from the regional model to the site-scale model. The flow paths, travel times and simulated heads appear to be consistent with on-site observations and simple scoping calculations.

The variabilities of the performance measures are quite high for the Base Case, but the variability between the studied variants is comparatively low. Variant 4.2, using conditional simulation, yields the shortest median travel time and greatest median canister flux. The anisotropic variogram case, Variant 3.1, yields the longest median travel time and lowest median canister flux. The Base Case results suggest that the expected performance measures of the Aberg hypothetical repository areas are as follows:

- The median travel time is 10 years, with an interquartile range from 3.4 years to 37 years.

- The median canister flux is 1.8×10^{-3} m/year, with an interquartile range from 3.7×10^{-4} m/year to 7.8×10^{-3} m/year.

- The median F-ratio is 1.0×10^{5} year/m, with an interquartile range from 3.4×10^{4} year/m to 3.7×10^{5} year/m.

Sammanfattning

SR 97 är en säkerhetsanalys av tre hypotetiska djupförvar i Sverige. Denna rapport, utförd som en del av SR 97, beskriver den hydrogeologiska modelleringen av Aberg. Aberg är en hypotetisk plats där indata och parametrar baseras på förhållanden vid Äspölaboratoriet (Äspö Hard Rock Laboratory) som är beläget i södra Sverige. I studien har en nästlad modellering använts där en deterministisk regional modell ger randvillkor till en stokastisk kontinuum modell i platsskala. Monte Carlo simulering har använts för att propagera variabiliteten i hydraulisk konduktivitet till advektiva partikelbanor som utgår från representativa kapselpositioner. I en serie varianter har osäkerheter vid tolkandet av parametrar och överförandet av randvillkor analyserats. För att beräkna tryck, Darcy-hastigheter (specifika flöden) vid kapselpositioner, advektiva gångtider samt partikelbanor genom geosfären har SKB:s stokastiska kontinuumprogram för grundvattenmodellering, HYDRASTAR, använts.

Den hydrauliska konduktivitetens skalberoende samt användandet av en nästlad modelleringsteknik väcker ett antal frågor rörande modellkonsistens samt massbalans mellan regional- och platsskalemodell. Vid överföringen av tidsoberoende tryckrandvillkor från den regionala modellen till platsskalemodellen bevaras mönstren i in- och utsrömningsområden samtidigt som massbalansen mellan modellerna är adekvat. Uppskalningsmetoden för konduktiviteter indikerar konsistenta resultat (i termer av medianvärden på beräknade mätetal) när olika storlekar på modellcellerna har använts. Serien av variationsfall indikerar att resultaten är relativt okänsliga för de alternativa metoder som använts för överföring av randvillkor från regional- till platsskalemodell. Partikelbanor, gångtider och simulerade tryck är i överensstämmelse med observationer gjorda på platsen och med förenklade överslagsberäkningar.

Variabiliteten i de beräknade mätetalen är förhållandevis hög inom basfallet medan skillnaderna mellan variationsfallen är förhållandevis små. Den lägsta medianen för gångtider och den högsta medianen för specifika flöden vid kapselpositioner erhölls för variationsfall 4.2 där konditionering på borrhålsdata använts i simuleringarna. Den högsta medianen för gångtider och den lägsta medianen för specifika flöden vid kapselpositioner erhölls i variationsfall 3.1 som är baserat på ett anisotropiskt variogram. Resultaten för basfallet ger mätetal för förvarsfunktionen i Aberg enligt följande:

- Medianen för gångtiderna är 10 år, med ett spann mellan kvartilerna från 3.4 år till 37 år.

- Medianen för specifikt flöde vid kapselpostioner är 1.8×10^{-3} m/år, med ett spann mellan kvartilerna från 3.7×10^{-4} m/år till 7.8×10^{-3} m/år.

- Medianen för F-faktorn är 1.0×10^{5} år/m, med ett spann mellan kvartilerna från 3.4×10^{4} år/m till 37×10^{5} år/m.

Contents

List of Figures

List of Tables

1 Introduction

1.1 SR 97

Swedish Nuclear Fuel and Waste Management Company (SKB) is responsible for the safe handling and disposal of nuclear wastes in Sweden. This responsibility includes conducting studies into the siting of a deep repository for high-level nuclear waste. The Safety Report 1997 (SR 97) will present a comprehensive performance assessment (PA) of the long-term safety of three hypothetical repositories in Sweden. The PA of each repository will include geosphere modelling to examine the possible transport of radionuclides from the emplaced waste packages through the host rock to the accessible environment. The hypothetical repositories, arbitrarily named Aberg, Beberg and Ceberg, take their data from sites previously investigated by SKB.

1.2 Study Overview

This report presents the site-scale hydrogeologic modelling study of the Aberg hypothetical repository. The Aberg site adopts input parameters from the Äspö Hard Rock Laboratory in southern Sweden, a site previously investigated by SKB. Walker et al. (1997b) summarises the site characterisation studies at Äspö and presents several possible representations for the site hydrogeology. This study applies a nested modelling approach to Aberg, with a deterministic regional model providing boundary conditions to a site-scale stochastic continuum model. The model is run in Monte Carlo fashion to propagate the variability of the hydraulic conductivity to the advective travel paths from representative canister locations. A series of variant cases address uncertainties in the inference of parameters and the boundary conditions.

The study uses HYDRASTAR, the SKB stochastic continuum (SC) groundwater modelling program, to compute the heads, Darcy velocities at each representative canister position, and the advective travel paths through the geosphere. The tasks involved in applying HYDRASTAR to Aberg include the interpretation of the hydrogeologic model into HYDRASTAR format, upscaling of parameters, simulation and sensitivity analysis, interpretation and illustration of results, and summary reporting. The report is organised into the following sections:

Sections 1 and 2 introduce SR 97 and the methods used in this study.

Section 3 describes the hydrogeologic interpretation of the Aberg data, and any adjustments to this data relative to previous reports.

Section 4 presents the Base Case simulation and examines several individual realisations and starting positions in detail.

Section 5 presents the variant case simulations.

Section 6 summarises and discusses the study results.

Appendix A defines the summary statistics.

Appendix B summarises additional regional model calculations specific to this study.

Appendix C presents supplemental calculations for rescaling, geostatistical inference and scoping calculations for travel times.

Appendix D summarises all input parameters used in this report.

Appendix E documents the data sources and data deliveries (e.g., SICADA log files for downloading the borehole data).

Appendix F summarises the additional software used in this study for statistical analysis, error checking and graphical display.

Appendix G presents the HYDRASTAR main input file used for the Base Case simulations in this study.

Appendix H documents the coordinate transforms used in this study and in Munier et al., 1997.

2   Modelling Approach

This study uses a stochastic continuum model of the fractured crystalline host rocks to analyse the groundwater flow and advective flow paths. Geostatistical analysis of hydraulic test data is used to infer a model of spatial correlation for the hydraulic conductivity of the site. Geostatistical simulation is used to create hydraulic conductivity fields for a numerical groundwater flow model, which provides groundwater velocities and flow paths from the hypothetical waste canisters (Neuman, 1988). The model is run in Monte Carlo fashion for a large number of simulated hydraulic conductivity fields to create an ensemble of possible flow paths and Darcy groundwater velocity at the representative canister positions (canister fluxes). Separate reports address the subsequent use of these flow paths and fluxes in transport and biosphere modelling.

The site-scale HYDRASTAR model requires a model domain of adequate grid density to represent the known fractures and adequate extent so that the model reflects the regional flow conditions. These conflicting requirements force this study to adopt a nested modelling approach, with the site-scale model taking its boundary conditions from a regional scale model. This permits the site-scale model to use a relatively dense grid while incorporating the regional flow patterns through constant head (Dirichlet) boundaries on the site-scale domain (Ward et al., 1987). The Base Case and several variants examine this nested approach and the resulting flux balances across the site-scale boundaries.

This study uses SKB's Convex 220 computer to run the HYDRASTAR version 1.7.2 code under a strict source code control system. Several additional SKB programs are used for pre- and post-processing of HYDRASTAR input and output. These include INFERENS, a geostatistical analysis and inference program that is used to regularise the variogram of the data to the model scale; TRAZON, which verifies the stream tube starting positions versus the fracture zones; and HYDRAVIS, a graphical post-processor developed from the commercial software package AVS. The commercial software package STATISTICA post-processes and summarises the statistics of HYDRASTAR output. These pre- and post-processing programs are summarised in Appendix F.

2.1   The PA Model Chain

The software tool for the geosphere portion of the safety analysis consists of a chain of PA models, HYDRASTAR – COMP23 – FARF31—BIO42, developed by SKB for use as a computational tool in the 1995 SKB safety analysis project (SR 95). The end product of the PA model chain is the calculation of the probable dose to the biosphere (Figure 2.1-1). This modular approach allows each component of the repository system to be studied separately, with the results combined at the finish to evaluate the performance. The hydrogeologic model, HYDRASTAR, determines the Darcy groundwater velocities at each stream tube starting position (canister flux) and the

advective travel paths through the geosphere. COMP23 is the near-field model, which uses the canister fluxes to determine the release rate for radionuclides from the representative canisters and into the groundwater flow system. FARF31 uses the release rates from the representative canisters and the travel paths through the groundwater flow system to determine the radionuclide flux through the geosphere. BIO42 is the biosphere module, which takes the radionuclide fluxes from the geosphere and determines the dose to potential receptors (SKB, 1996a). Monte Carlo simulations of the PA chain address uncertainty in the input parameters (e.g., hydraulic conductivity, porosity, etc.).

Note that this report presents only the hydrogeologic modelling study, and consequently discusses only the HYDRASTAR portion of the PA model chain.
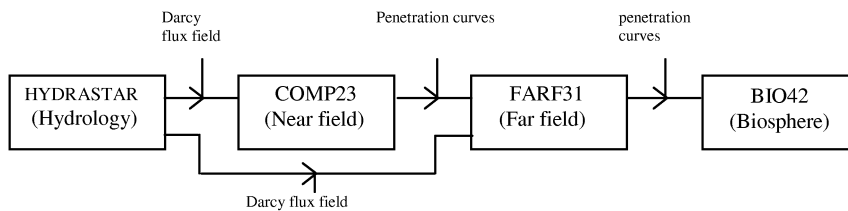
Figure 2.1-1. SKB PA model chain.

2.2 HYDRASTAR

HYDRASTAR is a stochastic groundwater flow and transport modelling program developed as a quantitative tool for support of the SKB 91 safety analysis project (SKB, 1992). A flow chart summarising the HYDRASTAR algorithm is presented in Figure 2.2-1. The current version, 1.7.2, uses the Turning Bands algorithm (Journel and Huijbregts, 1978) to generate realisations of the hydraulic conductivity field conditioned on the observed hydraulic conductivities. Trends in the data may be included implicitly through the use of ordinary kriging neighbourhoods or prescribed explicitly for specific regions. Hydraulic conductivity measurements at the borehole scale are upscaled to the model calculation scale using a regularisation scheme based on Moye's formula (a corrected arithmetic mean of the packer test hydraulic conductivities within a block; see Norman, 1992a, for details). HYDRASTAR uses the governing equation for either time-dependent or steady state groundwater flow in three dimensions, assuming constant density. The solution to this governing equation is approximated by a node centred finite-difference method to create a linear system of equations. A pre-conditioned conjugate-gradient algorithm solves the system of equations to arrive at a solution for the hydraulic head at each node. The pilot point inverse method (de Marsily et al., 1984) can be used to calibrate the input hydraulic conductivity field to minimise the error between the simulated and observed hydraulic heads. Transport in the resulting velocity field is modelled as pure advection using a particle tracking scheme.

The process of conditional geostatistical simulation of hydraulic conductivity, calibration via inverse modelling, and particle tracking can be repeated in Monte Carlo fashion to develop empirical probability distributions for the hydraulic conductivity field, and the travel paths and arrival times for advected contaminants (SKB, 1996b).

Starprog AB developed and tested the code under contract to SKB, beginning in 1989 (Norman 1991 and 1992a). Various authors have contributed to the development and testing of the code, most notably Norman (1991 and 1992a), Morris and Cliffe (1994), Lovius and Eriksson (1993, 1994), Walker et al. (1997a) and Walker and Bergman (1998). The test problems include comparisons to well-known analytical and numerical solutions, or are taken from the HYDROCOIN series of test problems (OECD, 1983; Hodgkinson and Barker, 1985). The code also has been applied successfully to the Finnsjön site, as part of the SKB 91 Project (Norman, 1992a and SKB 1992).

This study does not make use of all the available features in the current version of HYDRASTAR. Conditional geostatistical simulation using borehole data is not used, with the exception of Variant 4.2. The Moye's formula upscaling of borehole data is only used as part of INFERENS analysis of the data to infer a variogram model. Trends in the hydraulic conductivity are included as stepwise changes in the geometric mean to represent fracture zones, rock units and decrease with depth (i.e., no continuous decrease with depth is used). The calibration algorithm is not used, nor is the transient simulation of pumping tests.
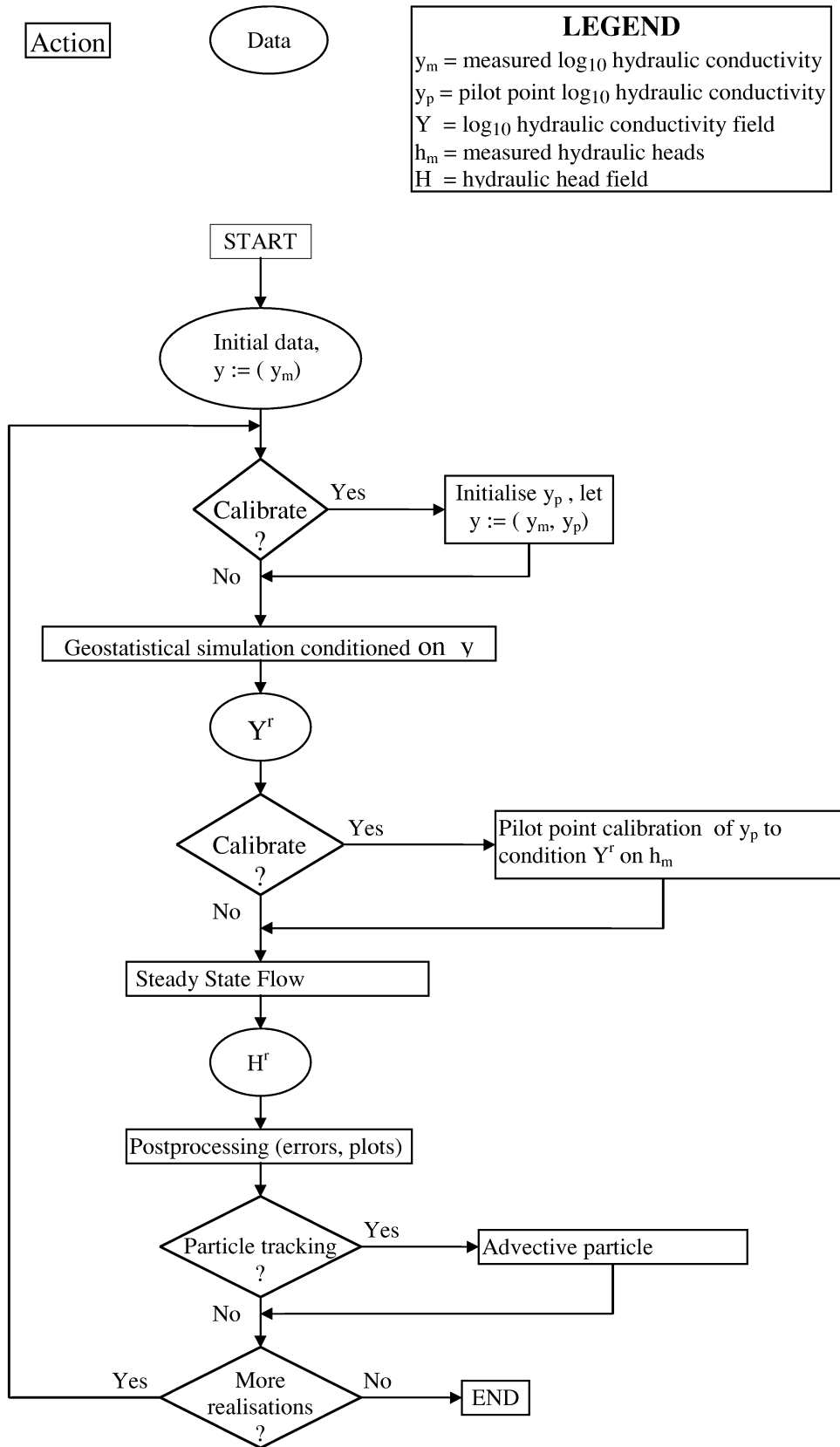
Figure 2.2-1. HYDRASTAR version 1.7 flow chart. Superscript "r" denotes realisation number.

2.3 Development of Modelled Cases

In addition to data analysis, computer simulation, and post-processing of results, the modelling process also requires that a set of relevant cases be analysed. In practice, expert judgement determines which assumptions to test and which uncertainties to evaluate. The result is a base case that represents the expected site conditions, and several variation cases that assess the uncertainty of inferences and assumptions. For this study, a separate group of scientists was convened by SKB, consisting of:

- Johan Andersson, Golder Grundteknik KB,
- Sven Follin, Golder Golder Grundteknik KB,
- Jan-Olof Selroos, SKB,
- Anders Ström, SKB, and
- Douglas D. Walker, Duke Engineering & Services, Inc.

This group met several times between November 1997 and March 1998, to discuss the reasoning behind the modelling assumptions, the derivation of model parameters and the modelling uncertainties. These discussions resulted in the parameters and assumptions that constitute the Base Case and variant cases addressed in this report.

3 Model Application

Walker et al. (1997b) summarises the hydrogeology of the site and proposes a series of parameter sets for use in hydrogeologic modelling. In addition to these preliminary parameter sets, HYDRASTAR also requires a geostatistical description of the hydraulic conductivity that is appropriate for the grid scale of interest. Appendix C presents additional computations for rescaling hydraulic conductivities and the inference of additional geostatistical parameters.

A nested modelling approach is used, with the site-scale model taking its boundary conditions from the much larger regional scale model of Svensson (1997a, and this report, Appendix B). Appendix B summarises the specific regional model simulations used to generate the boundary conditions for the local scale model. The extent of the model domain was evaluated as part of the Alternative Models Project (AMP) of SR 97 (Widén and Walker, 1998) and in preliminary modelling studies (Gylling et al., 1998; Follin, 1998).

The following sections describe the application of HYDRASTAR to the Aberg site, including the hydrogeologic conditions and modelling assumptions.

3.1 Site Description

Aberg takes its data from the Äspö site, which is located in southern Sweden, in the northern part of Småland (Figure 3.1-1). It is just off the Swedish coast in the Baltic Sea, near the Oskarshamn nuclear power plant. The Äspö site is also the location of the Äspö Hard Rock Laboratory (HRL), an underground research facility owned and operated by SKB. From a hydrogeologic perspective, the region is notable for the low topographic relief and the intrusion of saltwater from the Baltic Sea.
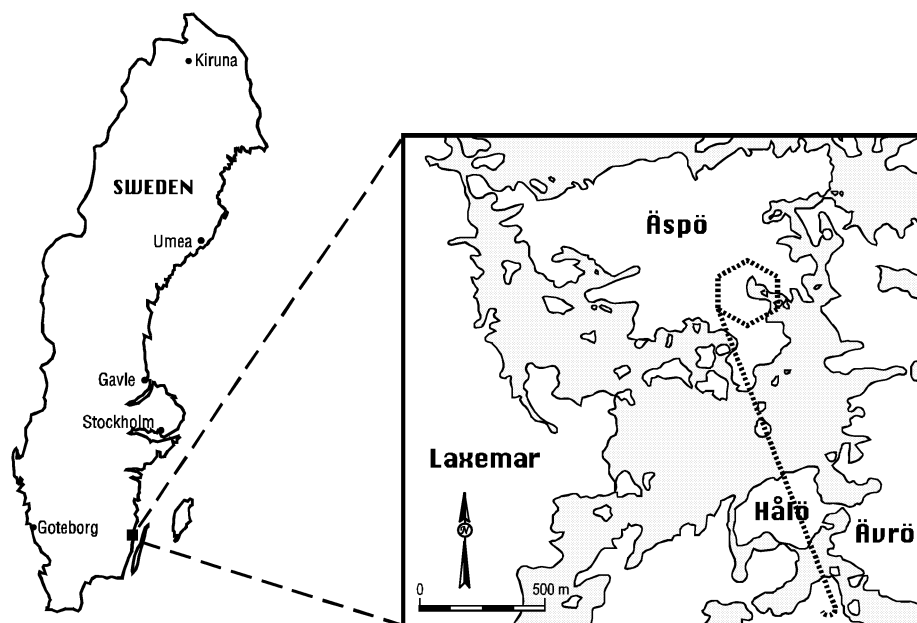
Figure 3.1-1. Location of the Äspö site and Hard Rock Laboratory.

3.2 Hydrogeology

The geology and hydrogeology of the Äspö site have been studied in great detail and are summarised in a series of reports (Wikberg et al., 1991; Rhén et al., 1997). Walker et al. (1997b), presents a summary of site conditions emphasising continuum modelling.

Äspö regional geology is dominated by fractured crystalline bedrock consisting of the heterogeneous Småland granite suite. The Äspö shear zone running SW-NE through Äspö Island divides the bedrock into two parts. The region continues to experience isostatic rebound as a consequence of the last period of continental glaciation. This glaciation also deposited bouldery till throughout the region. Peatlands are found in some depressions, as are fluvial sand and gravel. The soil cover is thin with numerous bedrock outcrops. Regional lineaments have been mapped and examined by various airphoto, aerogeophysical, outcrop, seismic and borehole studies, revealing a number of major discontinuities that have been interpreted as steeply dipping fracture zones. The salinity profile of the groundwater system is typical of islands and coastal areas: fresh groundwater near the surface rests on saline water that has intruded from the sea.

Hydrogeologic data of the area around and on Äspö were compiled during 1986-1987. Precipitation generally exceeds evapotranspiration, resulting in a small net recharge on the land surface. The classical model of topographic drive suggests that recharge will occur in higher elevations and flow to discharge areas in lower elevations. This should be combined conceptually with the classical model of seawater intrusion under freshwater in coastal areas and islands. Although simplistic, this general model is

consistent with the locations of streams, mires, observed hydraulic heads, salinity distributions and geochemical data available in the region. Svensson (1997a, 1997b) used a groundwater flow model to demonstrate that the overall pattern of groundwater flow at depth can be explained by this combination of conceptual models.

3.3   Regional Model and Boundary Conditions

This application of HYDRASTAR uses a nested modelling approach, taking the boundary conditions of the site-scale model from a much larger regional scale model. Svensson (1997a) used a finite difference continuum model, PHOENICS, to study regional flow patterns under various assumptions. Several complementary simulations of the Svensson regional model determined heads and fluxes along the boundaries of the site-scale domain used in this HYDRASTAR application. These complementary simulations were not reported in Svensson (1997a), but are documented in Appendix B. Figure 3.3-1 shows the extent and location of both the regional and site-scale modelling domains.

The model of Svensson (1997a) included the effects of saline Baltic seawater intruding under freshwater. HYDRASTAR cannot simulate density dependent effects, and the discrepancy might result in inappropriate heads being specified along the site model domain. To create boundary conditions more compatible with HYDRASTAR, the Svensson regional model was rerun using freshwater to create boundaries for use in this study. The specifications and the results of that run are summarised in Appendix B of this report. Figure 3.3-2 shows the resulting steady-state head values, which are used as Dirichlet (constant head) boundary conditions by the site model.

Note that the effects of the assumed boundary conditions are evaluated in the boundary condition variant case described in Section 5.1 of this report.

*Figure 3.3-1. Äspö site map, showing the Svensson (1997a) regional model (green) and
Aberg site-scale model (yellow) (Äspö local coordinate system).*

Bottom

North

West

Top

N

East

South

Approx. Scale

0   1000 m
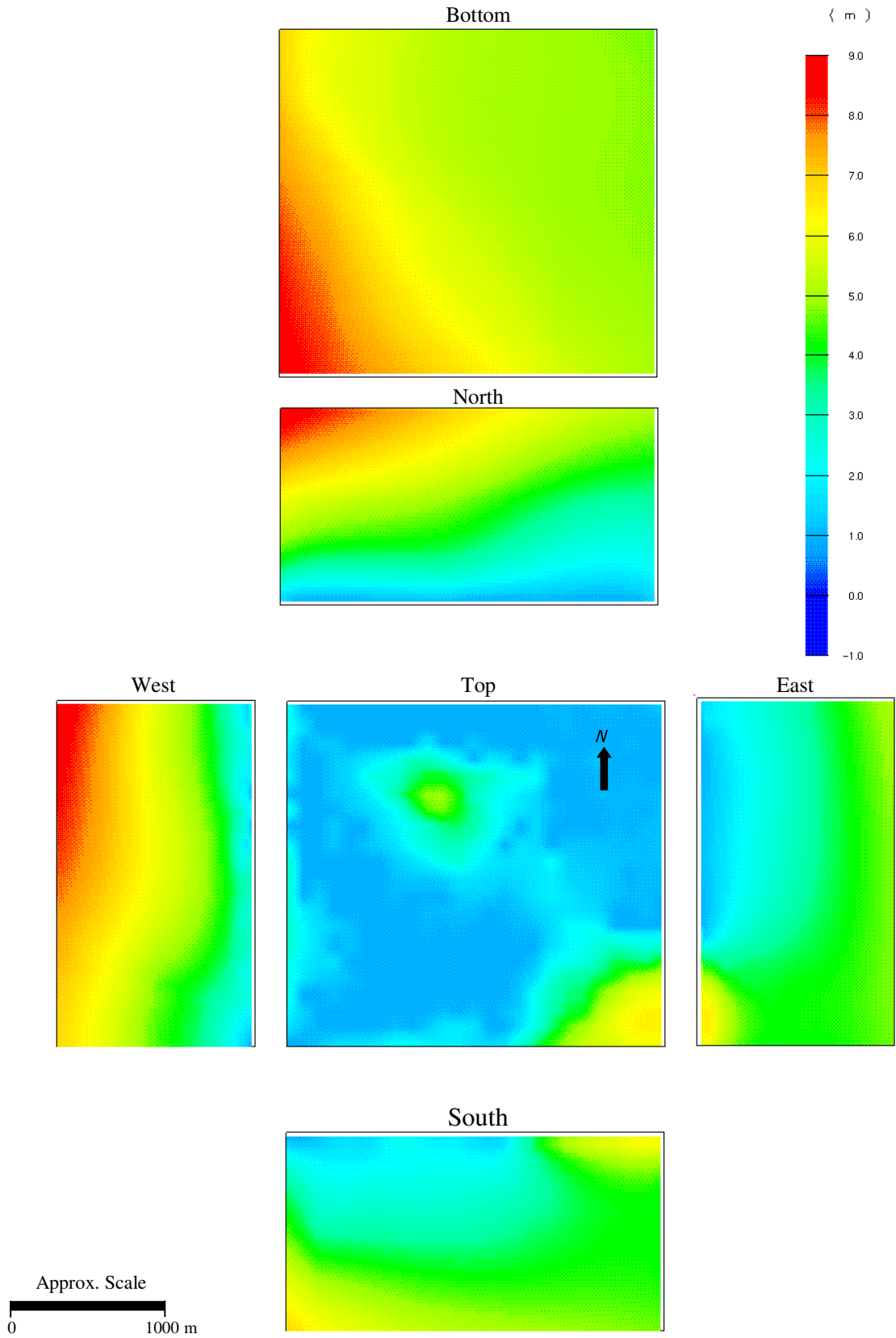
Figure 3.3-2. Constant head boundary conditions for the Aberg Base Case, on each face of the model domain (freshwater hydraulic head, in metres).

The head values pictured in Figure 3.3-2 require some adaptation for use in the smaller scale HYDRASTAR model. The head values generated by the regional model are generated on a 100 m grid spacing, and must be interpolated to the 25 m HYDRASTAR grid spacing. This was accomplished using a MATLAB program for two-dimensional linear interpolation to create a set of head values on each model surface. The output of this MATLAB program was written to a file in the required format for HYDRASTAR as a Dirichlet boundary condition. This process, several alternative methods, and the associated programs are described in Appendices B and F.

This interpolation of heads attempts to match the site-scale boundary heads to the regional scale heads for the same domain (i.e., conservation of energy). Although this approach is the same as used in other nested groundwater models (e.g., Ward et al., 1987), it is also important to verify that the fluxes across the boundary are the same (i.e., conservation of mass). The consistency of the boundary fluxes is discussed further in Section 4.0.

3.4 Model Grid and Repository Layout

The HYDRASTAR model for this application consists of a 3-dimensional finite difference grid with a uniform grid spacing of 25 m. Preliminary modelling studies by Widén and Walker (1998) and Gylling et al. (1998) determined a domain location and extent such that particle paths would not be intercepted by lateral boundaries. Figure 3.4-1 shows the location of the modelled domain, which covers an area of 2400 m by 2200 m and extends to a depth of 1250 m (i.e., approximately 6.3 km^3). The modelling domain extends slightly farther eastward than that used in Widén and Walker (1998). The resulting grid of 97 x 89 x 49 nodes (width, length and depth, respectively) gives a typical size for HYDRASTAR models that can be run on the SKB CONVEX in the time allotted for this study.

The performance assessment measures are based on travel paths and travel times to exit locations in the accessible environment (i.e., ground surface). Ideally, the model grid upper surface would correspond to the ground surface. This is not possible in this study because HYDRASTAR uses a flat plane for the upper model surface. Consequently the observed ground surface is represented as a horisontal plane with the modelled domain lying below sea level (0 masl). The HYDRASTAR particle tracking algorithm requires a minimum distance of one grid spacing from any model boundary to calculate the velocity vectors, and thus the exit location for these simulations is –25 masl. Depending on the step size for particle tracking, this distance actually varies between –50 to –25 masl with a median of –37 masl in the Base Case. That is, the performance assessment measures are based on exit locations on a horisontal plane at –37 masl.

Figure 3.4-1 also shows the hypothetical repository tunnel layout, a two-level design specified by Munier et al. (1997, tunnel design H). The layout avoids mapped fracture zones, allowing an exclusion zone whose width depends on the fracture zones' classification. The tunnels are placed no closer than 100 m to zones that are classified as certain, and no closer than 50 m to those classified as probable. Note that the tunnel design does not avoid fracture zones classified as possible, such as NNW-2 (see Section

4.5). This study represents the hypothetical waste canisters with 120 locations uniformly scattered over the repository tunnels (Figure 3.4-2). HYDRASTAR uses these 120 representative locations as starting positions for the stream tubes (advective flow paths) and the subsequent travel time, canister flux and F-ratio calculations.
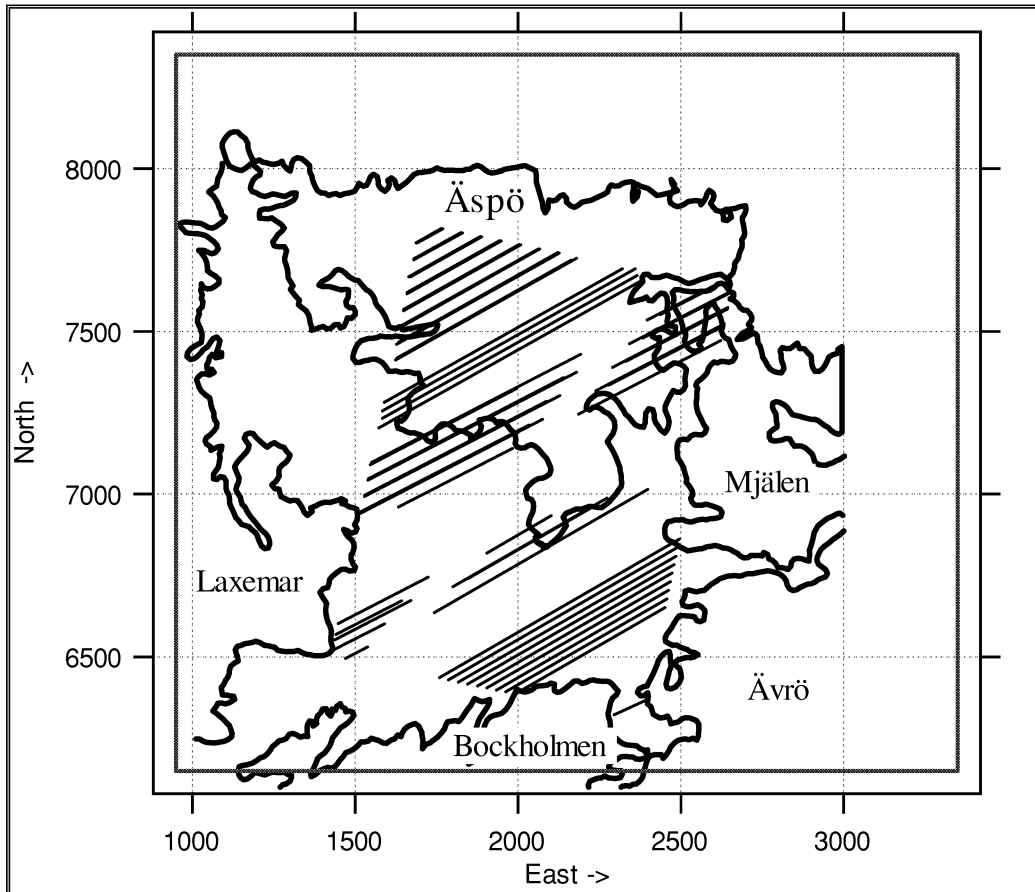
Figure 3.4-1. *Äspö island and the Aberg site-scale model domain (blue line). Both repository tunnel levels (-500 and -600 masl) are shown projected to ground surface. (Plan view, Äspö local coordinate system, in metres).*

Aberg, -500 m
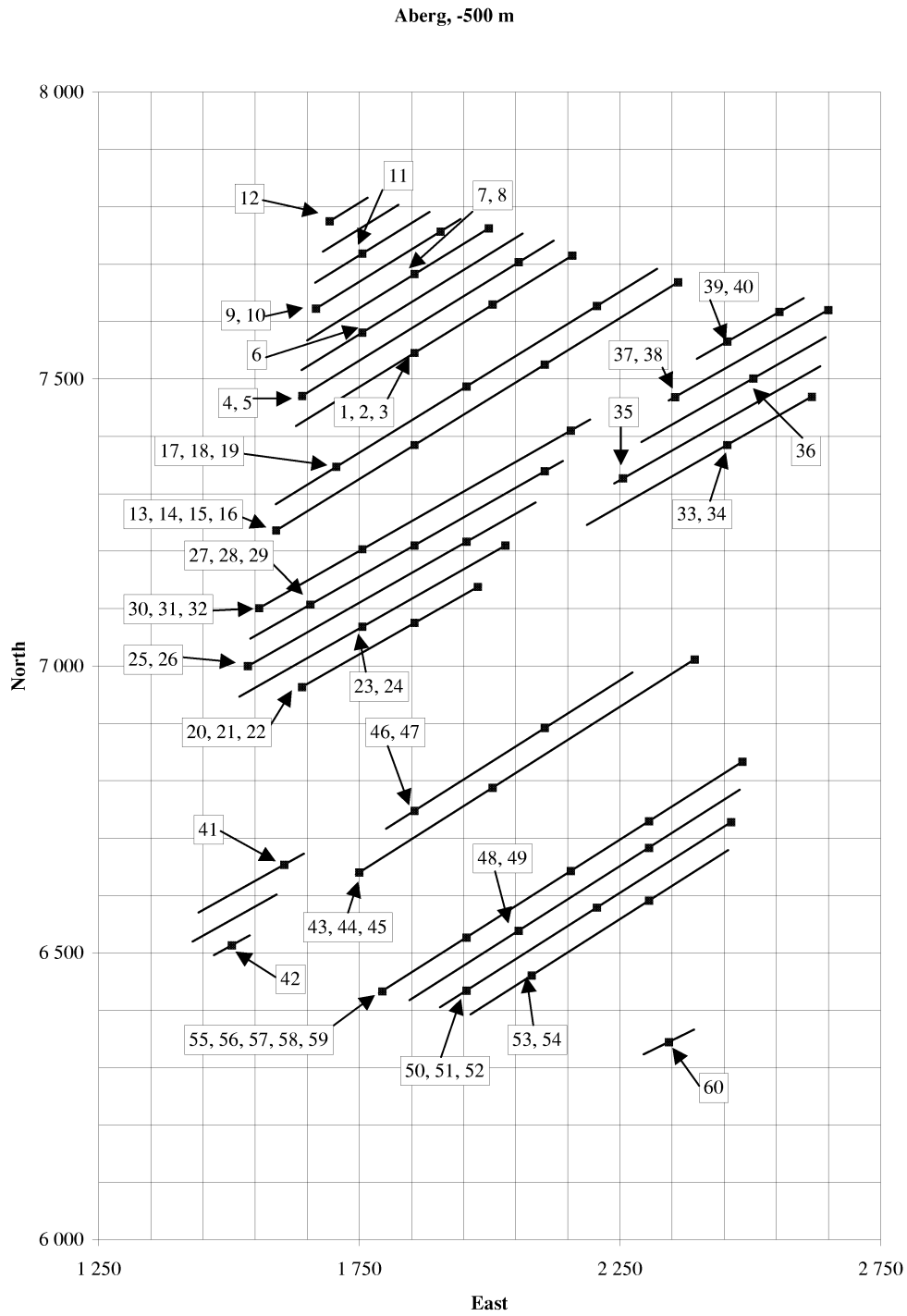
Figure 3.4-2a. Aberg hypothetical tunnel layout, upper level (–500 masl). Numbered locations are stream tube starting locations as representative canister positions.
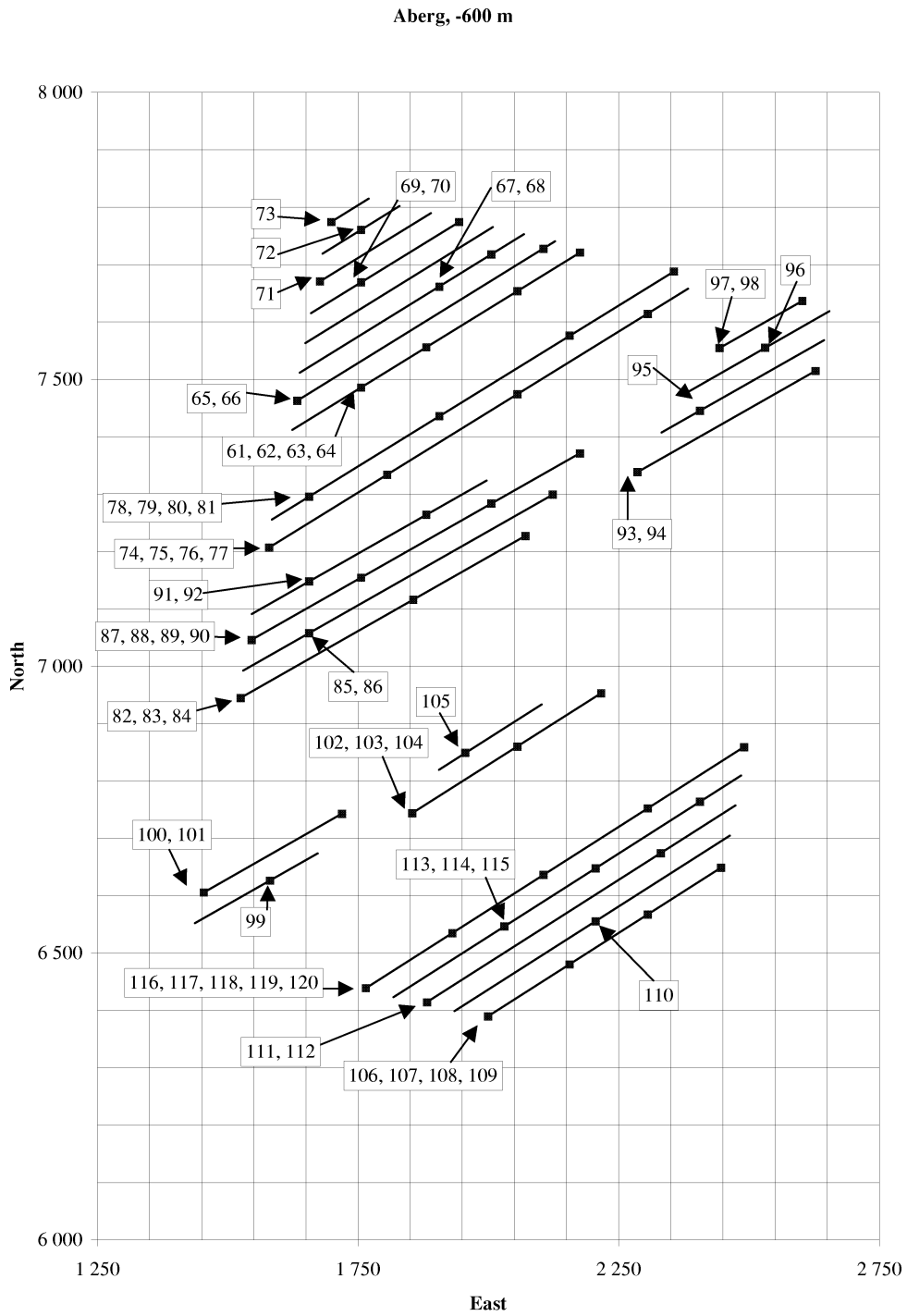
Figure 3.4-2b. Aberg hypothetical tunnel layout, lower level (–600 masl). Numbered locations are stream tube starting locations as representative canister positions.

3.5   Input Parameters

HYDRASTAR's input parameters require a structural, hydraulic, and geostatistical description of the site, all at appropriates scales. This study uses the site-scale description based on measurements taken from the pre-investigation and construction phases summarised in Rhén et al. (1997) and Walker et al. (1997b). Pre-construction investigations and tunnel construction identified a number of fracture zones between 5 to 50 m in width. Fractures elsewhere in the site (i.e., those not included in the deterministic zones) are collectively included in the hydraulic conductivity estimates for the rock mass. Consequently, the modelled domain and the hydraulic conductivity data are divided according to the site structural model (Rhén et al., 1997):

- Rock Domain (RD) – relatively unfractured rocks outside the deterministic conductors, whose hydraulic conductivity is inferred from 3 m packer tests in single boreholes. On the site-scale, there are six domains denoted SRD1 through 6.

- Conductor Domain (CD) – rocks within the deterministic conductors, whose hydraulic conductivities are inferred from interference tests. On the site-scale, the set of conductors are collectively referred to as SCD.

The principal source of hydraulic conductivity data is the injection and pumping tests performed in the cored boreholes and tunnel probeholes (Figure 3.5-1). The rock domain hydraulic conductivity is inferred from the interpreted hydraulic conductivities of the 3 m packer tests, found in the SKB SICADA database. The SKB geostatistical inference code, INFERENS, is applied to the 3 m tests to infer a variogram for the upscaled hydraulic conductivity of both the rock and conductor domains. The interference tests provide the hydraulic conductivity of the conductor domain (Walker et al., 1997b).

The scale of these measurements (as inferred from the packer length) is much different from the finite difference block scale of the model grid. As discussed in Walker et al. (1997b), hydraulic conductivity is a scale-dependent parameter, requiring that the interpreted hydraulic conductivities be appropriately rescaled for use in the model. That is, we need to determine a block-scale hydraulic conductivity, K_b, which preserves the expected flux through the domain represented by the block. This study uses the scale dependence of $\log_{10} K$ observed at Äspö to rescale the mean $\log_{10} K$ of block conductivities in a stochastic continuum model. Rhén et al. (1997) and Walker et al. (1997b) provide general analyses of the hydraulic conductivity data and a regression equation describing the Äspö scale dependence. Appendix C.2 of this report summarises the upscaling and inference of parameters for block scales of 25 m, 50 m and the effective conductivity (K_e) for the deterministic variant.
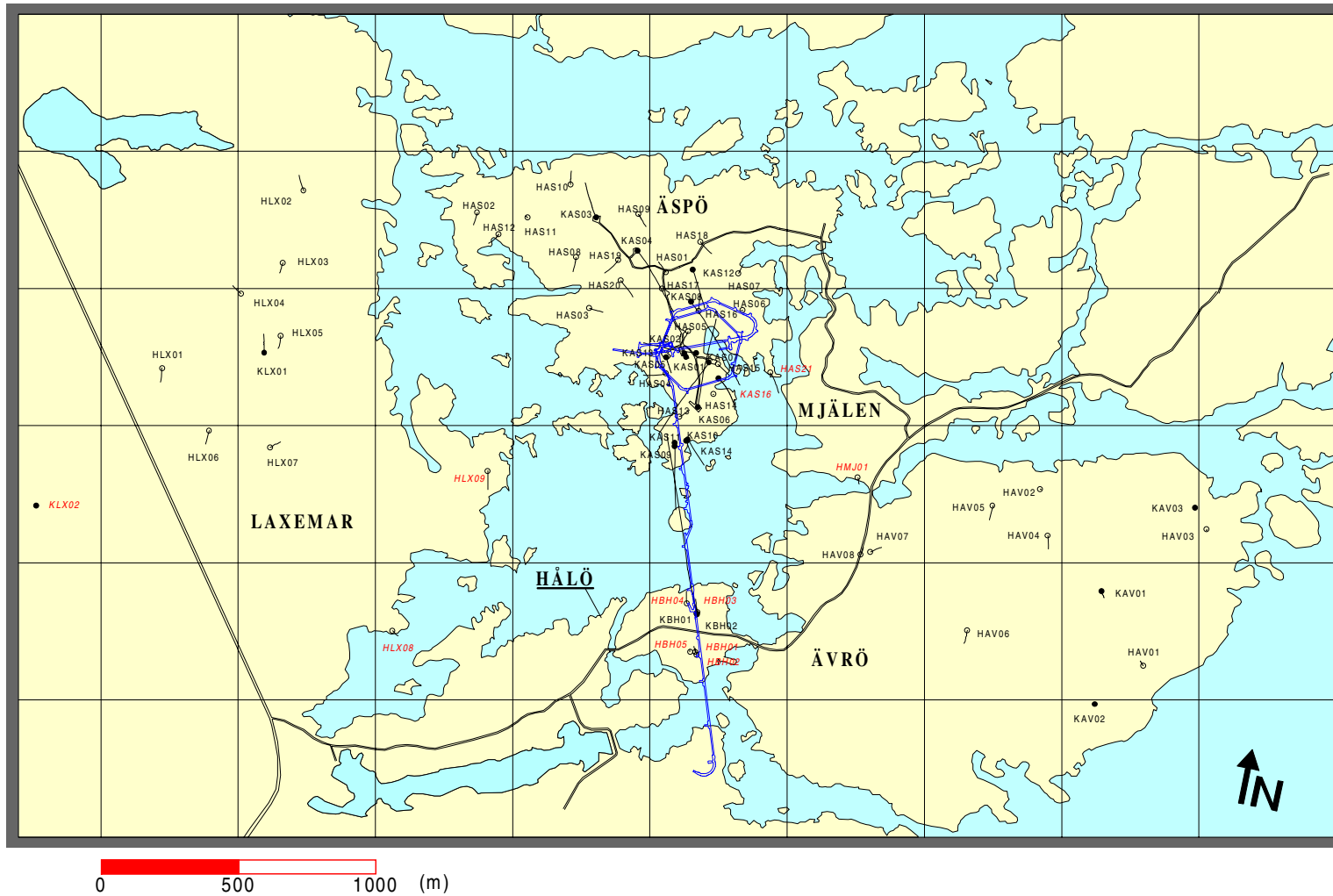
Figure 3.5-1. Äspö HRL tunnel and boreholes, from Rhén et al. (1997) (Äspö local coordinate grid).

3.5.1 Conductor Domain (SCD)

The geometries of the hydraulic conductor domains are defined by the major discontinuities described in Rhén et al. (1997) and represented as planar features of constant width (Figure 3.5-1). This study reduced the effective transmissivities of Rhén et al. (1997) to hydraulic conductivities using the specified widths. The specified width of several of the deterministic structures is less than the model grid spacing of 25 m. This presents a minor problem for HYDRASTAR, whose geostatistical simulation algorithm only includes deterministic features that directly intersect the centres of the block interfaces. Depending on the structure orientation, this might result in anomalous discontinuities in the structure that are solely the result of the grid spacing. To avoid these anomalies, the SCD widths are increased to a minimum width of 25 m and the hydraulic conductivities decreased proportionaly to maintain the transmissivity of the SCD. Note that one deterministic hydraulic conductor, NNW-8, is not shown in Figure 3.5-2 because it is not thought to reach the surface.

Several types of hydraulic tests were performed in the individual conductive structures, including a series of multi-hole interference tests (Rhén et al., 1997). These tests were on varying measurement scales, thought to be between 50 and 100 m (Rhén, personal communication, 1997). This study assumes that these interference tests have a measurement scale of 100 m and rescales the reported hydraulic conductivities using the observed scale dependence at Äspö (Appendix C.2; Table 3-1). As is suggested in Rhén et al. (1997), the median $\log_{10}$ hydraulic conductivities change by a factor of 1/10 below –600 masl.

Table 3-1. **Aberg site-scale conductors (SCD1). 100 m measurements from Rhén et al. (1997), scaled to 25 m. Below –600 masl, all hydraulic conductivities change by a factor of 1/10.**

Zone	Median Log_{10} K (m/s)		Width (m)	Sample size
	100 m	25 m		
EW-1N	-7.3	-7.8	30	4
EW-1S	-6.1	-6.6	30	4
EW-3	-5.8	-6.3	15	4
EW-7	-5.2	-5.7	10	3
NE-1	-5.0	-5.5	30	16
NE-2	-7.1	-7.6	5	12
NE-3	-5.2	-5.7	50	9
NE-4	-6.1	-6.6	40	8
NNW-1	-6.3	-6.7	20	7
NNW-2	-5.6	-6.0	20	4
NNW-3	-6.3	-6.8	20	(ave. of all NNW)
NNW-4	-4.8	-5.3	10	8
NNW-5	-7.0	-7.5	20	3
NNW-6	-6.3	-6.8	20	(ave. of all NNW)
NNW-7	-6.6	-7.1	20	5
NNW-8	-6.3	-6.8	20	3
NW-1	-7.8	-8.3	10	3
SFZ, w	-6.9	-7.4	20	(site data upper quartile)
SFZ, ww	-5.4	-5.9	20	(site data lower quartile)
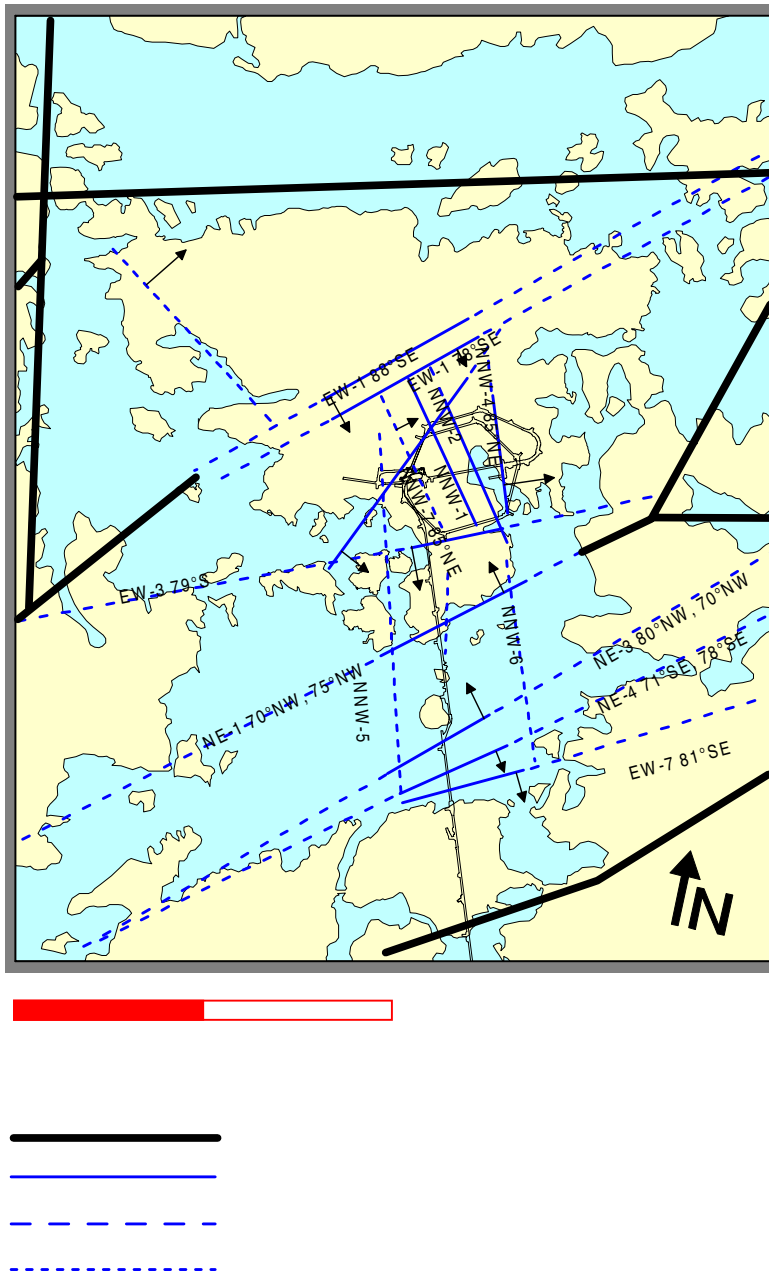
Figure 3.5-2. Aberg site-scale conductor domains (SCD), from Rhén et al. (1997).

3.5.2   Site-scale Rock Domain (SRD)

Based on observations during the pre-investigation and construction of the Äspö HRL, the Aberg site is divided into five rock mass domains (SRD) as given by Walker et al. (1997b; see also Figure 3.5-3 in this report). The arithmetic mean of $\log_{10}$ hydraulic conductivities for domains SRD1-3 is based on the interpreted hydraulic conductivities of the 3 m packer tests. The areas outside the SRDs but inside the model domain are assigned the geometric mean of all the 3 m interpreted hydraulic conductivity. As discussed above, these values must be upscaled from 3 m and 15 m measurement scale to 25 m finite difference grid scale. Table 3-2 presents the upscaled values used in this
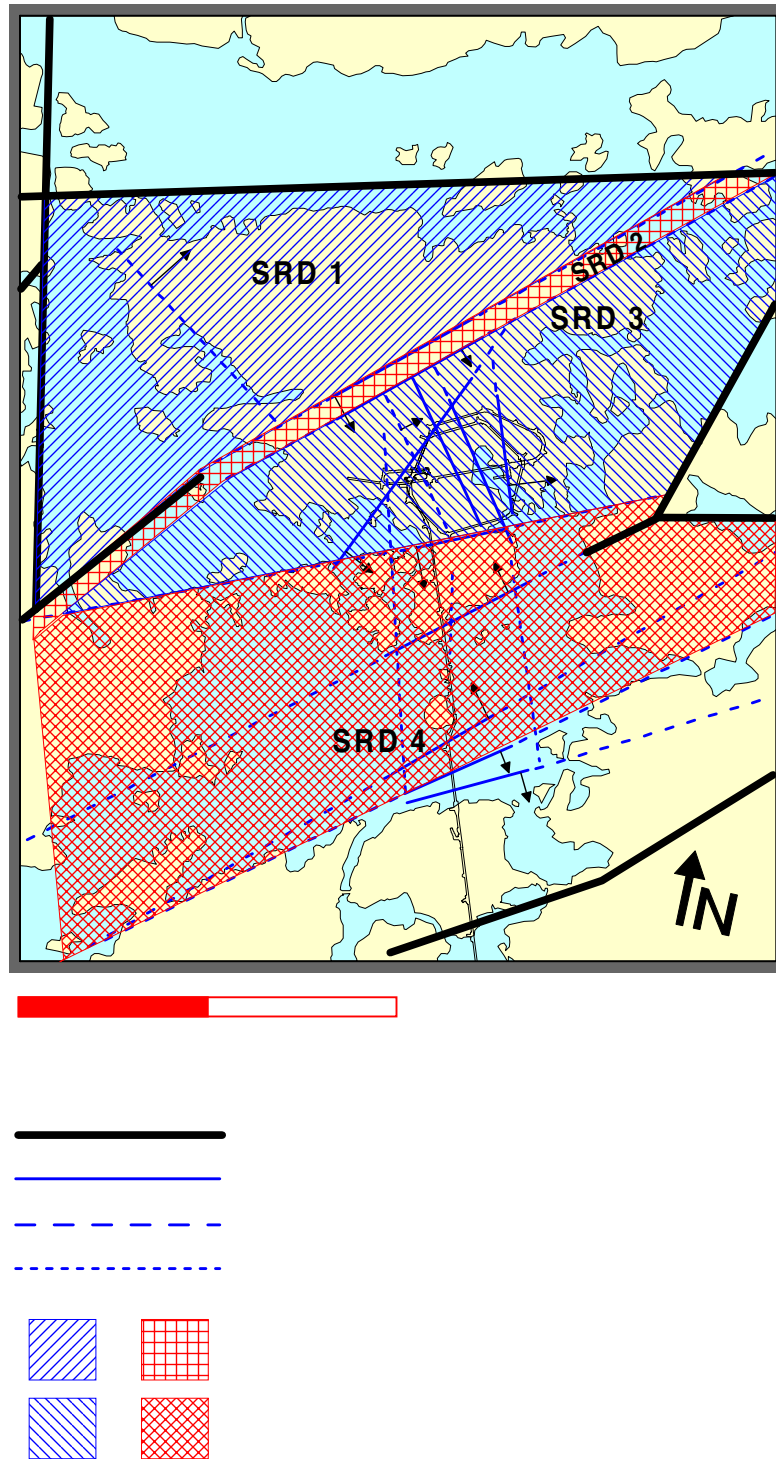
Figure 3.5-3. Aberg site-scale rock domains (SRD), from Rhén et al. (1997).

study. The SRDs extend through the entire model depth, with a uniform change in hydraulic conductivity by a factor of 1/10 at -600 masl. This study differs from that of Widén and Walker (1998) in this respect, since the Widén and Walker (1998) model of Aberg had no change below -600 masl.

Table 3-2. **Hydraulic conductivity for Aberg site-scale rock mass (SRD). 3 m measurements from Rhén et al. (1997), scaled to 25 m. Hydraulic conductivity of all SRD units changes by a factor of 1/10 below –600 masl.**

SRD	$Log_{10}K$ (m/s)	
	3 m	25 m
SRD1	-8.7	-8.0
SRD2	-7.8	-7.1
SRD3	-9.5	-8.8
SRD4 *	-7.6*	-7.5
SRD5	-8.3	-7.6
Other (average of SRD1 - 3)	-9.3	-8.5

Hydraulic properties for SRD4 are somewhat difficult to infer from the data. There are no 3 m tests within SRD4 (southern Äspö, south of NE-1); consequently, the interpreted hydraulic tests in the tunnel probeholes are used to infer hydraulic properties for SRD4. These probehole tests were conducted and interpreted in a different manner from the 3 m tests in the cored boreholes, leaving a suspected bias (Rhén, personal communication, 1997). Svensson (1997a) evaluated the conductivity of SRD4 via inverse modelling of the drawdowns of hydraulic heads induced by the excavation of the HRL. Svensson found that reducing the hydraulic conductivity of SRD4 by approximately one order of magnitude improved the agreement between model-predicted and observed drawdowns. This study uses Svensson's calibrated value of mean log_{10} hydraulic conductivity for SRD4, with adjustments for scale (Table 3-2).

3.5.3   Geostatistical Model

The Aberg site-scale geostatistical model of hydraulic conductivity consists of the rock blocks described for SRD1 through 5, the SCD and a single variogram model. As is discussed in Walker et al. (1997b), the variogram must be adjusted (regularised) to account for the difference between measurement and grid scales. Note that only one variogram model can be specified in HYDRASTAR for both domains. Because the experimental variogram of the 3 m data in the conductors is erratic, this study infers a regularised variogram model based on the upscaled 3 m packer test data in the rock domain for both the SRD and SCD (Walker et al., 1997b). Unlike previous geostatistical studies of the Äspö data (La Pointe, 1994; Winberg, 1994; Niemi, 1995), this study uses the interpreted hydraulic conductivities of Rhén et al. (1997) for the 3 m packer tests. This is important because the Rhén interpretation has no lower measurement limit, a characteristic that can effect the statistics of the data. The interpreted conductivities are taken from cored boreholes KLX01, KAS02, KAS03, KAS04, KAS05, KAS06, KAS07 and KAS08, as found in SICADA. The SKB code INFERENS was used to upscale the 3 m data to 25 m and fit a model variogram and trends to the upscaled data (Walker et al., 1997b).

Results of this analysis indicated the following variogram model for the 25 m grid scale (Figure 3.5-4):

- Exponential model, isotropic,

- Practical range of 97 m, and

- Zero nugget, $\log_{10}$ K variance 2.72.

The SRD and SCD are treated as step changes in the logarithm of block conductivities (i.e., 0 order trends in arithmetic mean of $\log_{10}$ K_b), with values provided in Tables 3-1 and 3-2. Figure 3.5-5 shows the HYDRASTAR representation of the SCD, and Figures 3.5-6 and 3.5-7 show the combination of the SCD and SRD via a plot of the deterministic $\log_{10}$ K_e field. The combined effects of this geostatistical model of Aberg are illustrated in Figure 3.5-8, which presents a single realisation of the Base Case hydraulic conductivity field.
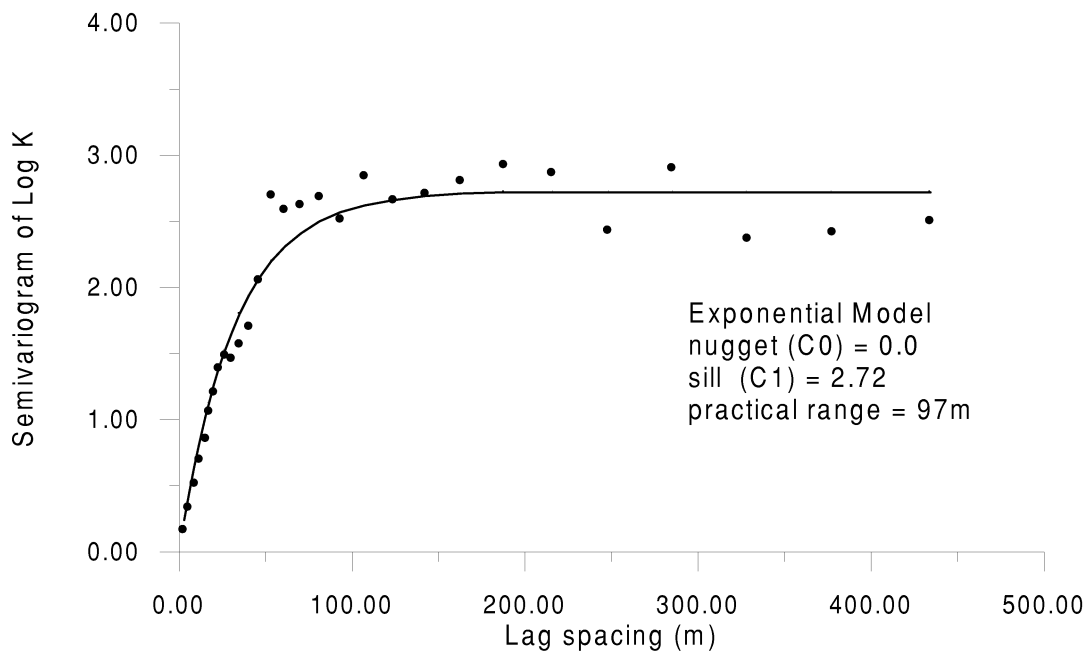
Figure 3.5-4. Semivariogram of log_{10} of hydraulic conductivity for Aberg rock domain. 3 m data in rock domain, upscaled to 25 m and fitted via INFERENS.
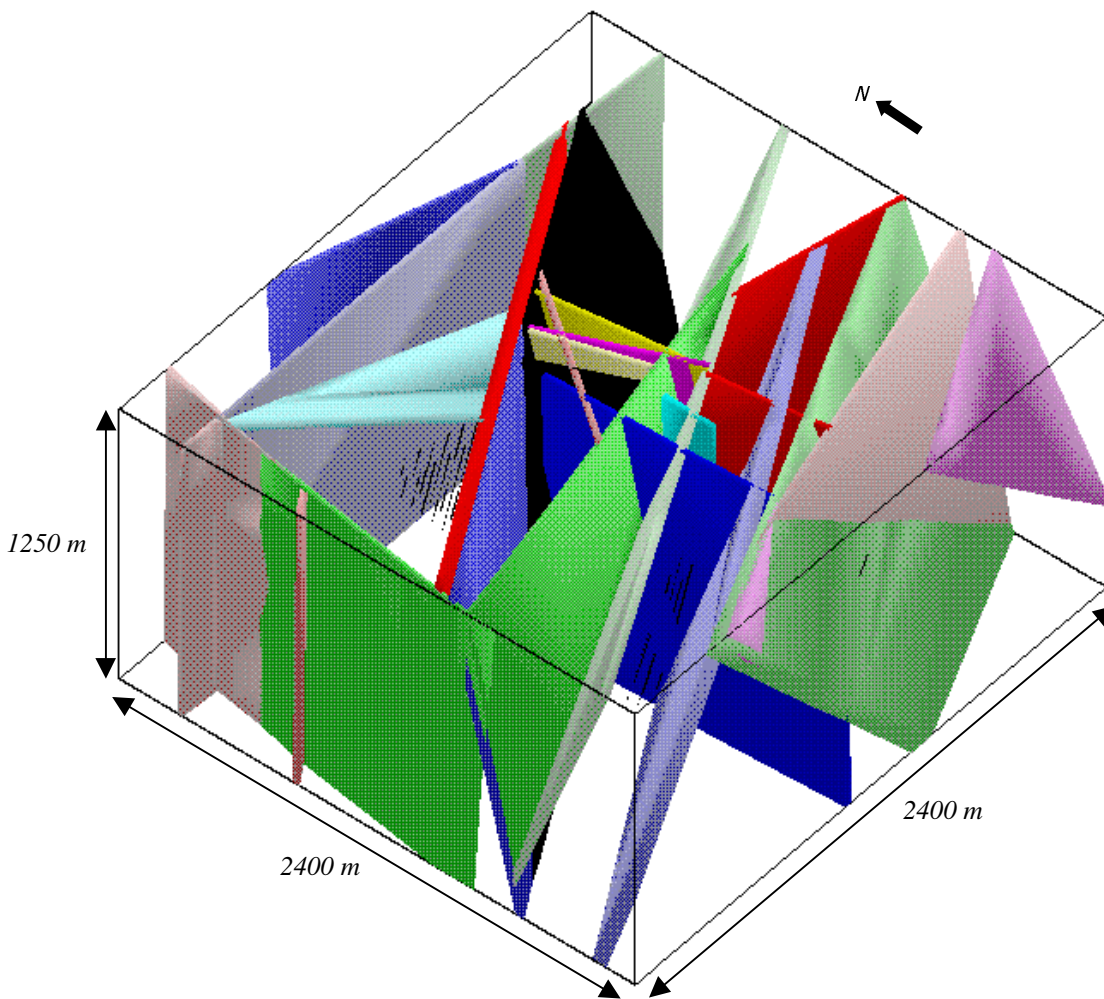
*Figure 3.5-5. HYDRASTAR representation of Aberg conductive fracture zones (SCD).
(Isometric view from southwest and slightly above).*

The Base Case geostatistical model represents the rock domains and conductive fracture zones deterministically, extending throughout the entire depth of the model (Figures 3.5-2 and 3.5-3, respectively) . This deterministic representation is used even though the occurrence and extent of the SCD and SRD are uncertain and additional, undetected structures are possible (Rhén et al., 1997). An alternative HYDRASTAR option is available that includes large-scale structures stochastically via conditional geostatistical simulation (i.e., conditioning the fields using the measured hydraulic conductivity data). This latter approach tends to create structures whose size is limited by the data density of the range of the variogram. For the Aberg site, the inferred range is relatively short and the data is widely spaced, so that this conditional simulation approach generally will not create fields with conductive zones as extensive as those suggested by Rhén et al. (1997). Consequently, the Base Case geostatistical model uses a deterministic SCD and evaluates the associated uncertainty with a variant case for conditional simulation (Variant 4). This uncertainty does suggest an enhancement of the current version of HYDRASTAR to include a geostatistical simulation method that addresses large-scale structures stochastically (e.g., Indicator Categorical simulation).
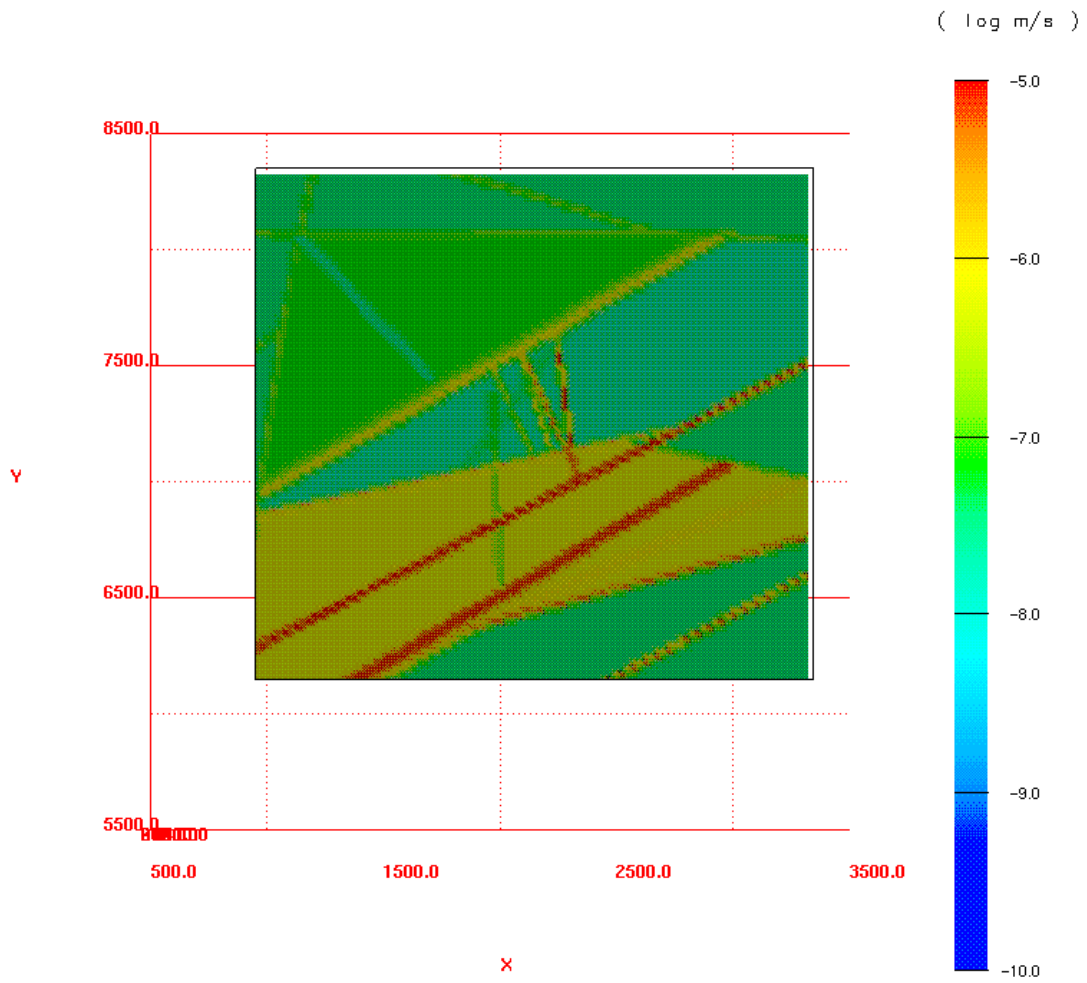
Figure 3.5-6. Log₁₀ of hydraulic conductivity on the upper model surface in Aberg. Variant 5 (deterministic representation of hydraulic conductivity, Äspö local coordinate system, scale in metres).
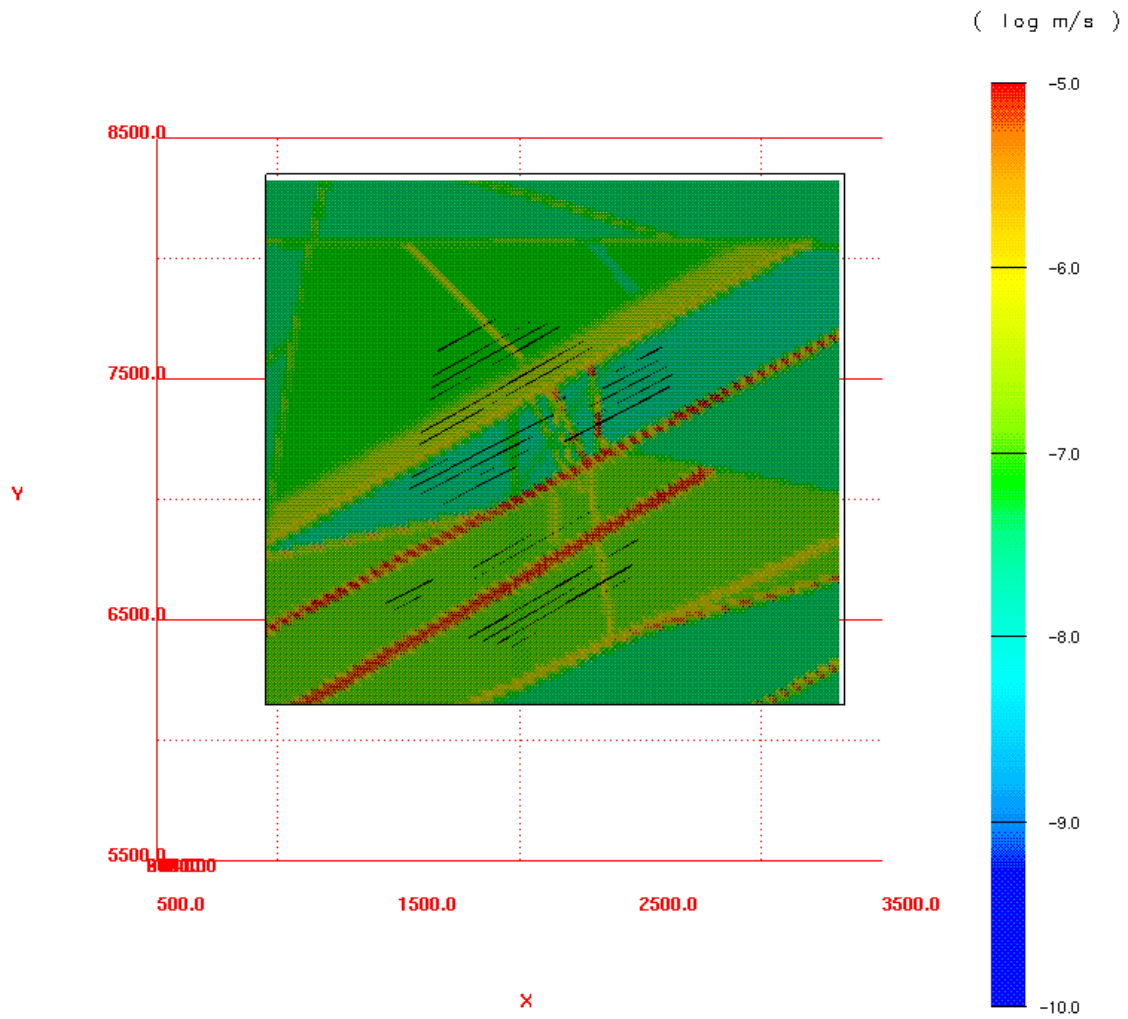
Figure 3.5-7. Log$_{10}$ of hydraulic conductivity in Aberg Variant 5 (deterministic representation of hydraulic conductivity) on a plane cutting through the upper repository level (Äspö local coordinate system, scale in metres).
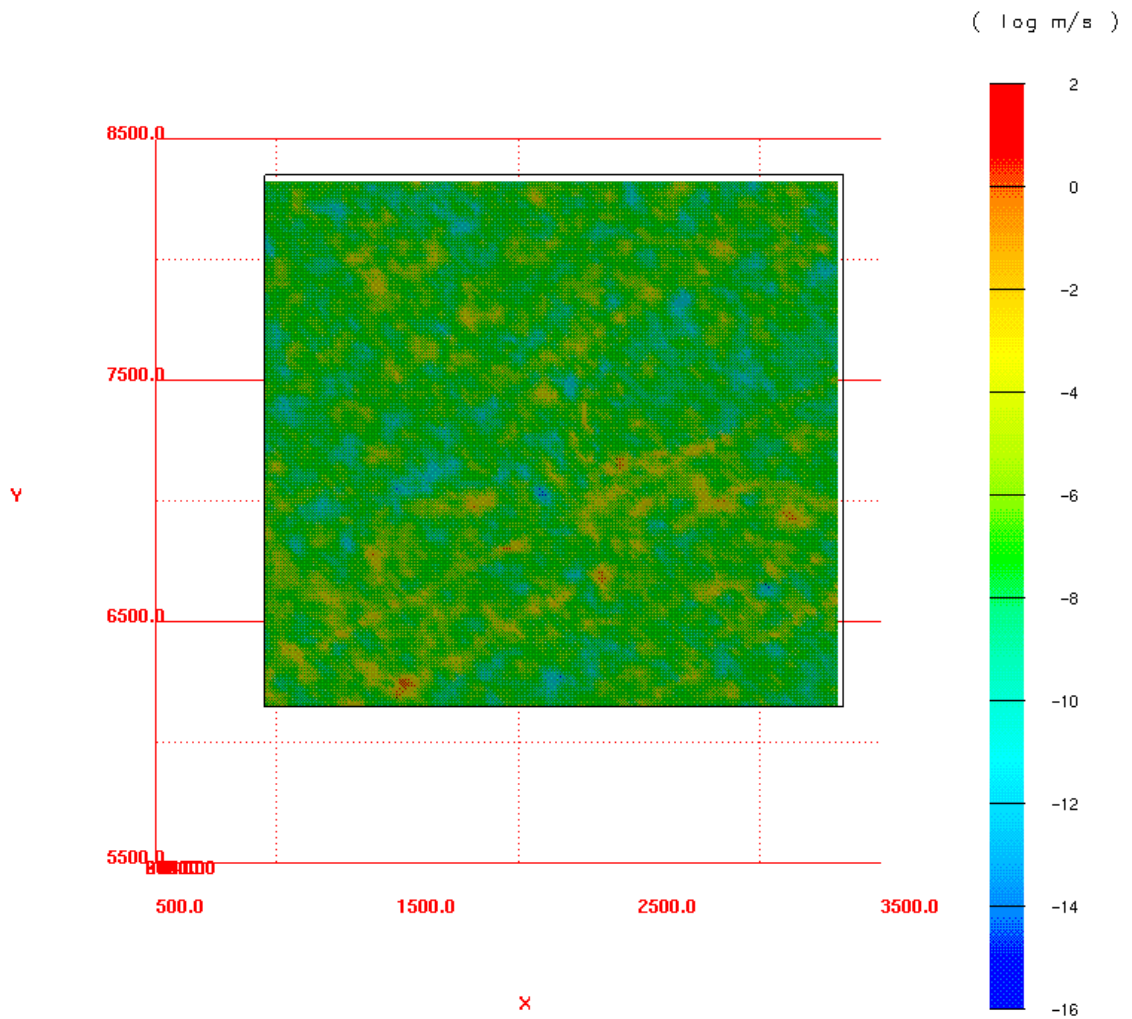
a)
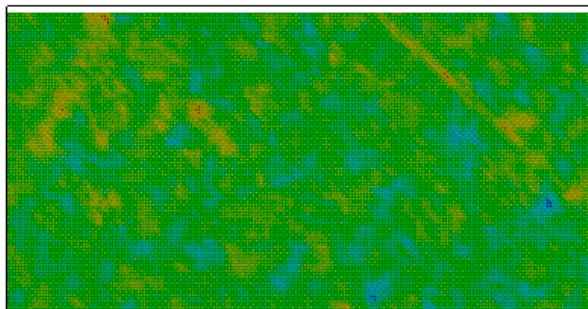
b)

Figure 3.5-8. One realisation of log$_{10}$ of hydraulic conductivity for the Aberg Base Case in a) plan view at z = 0 masl and b) on the southern model surface. (Äspö local coordinate system, scale in metres).

3.5.4   Other Parameters

The remaining HYDRASTAR input parameters are hydraulic parameters required for the advective transport calculations and performance measures. One of these is the flow (or kinematic) porosity, ε_f, which is generally acknowledged to be an uncertain parameter. Based on the site-specific data of Rhén et al. (1997), this study uses a flow porosity of $\varepsilon_f = 1 \times 10^{-4}$, uniform over the entire domain. It should be noted that the travel times reported in this study are directly proportional to this assumed flow porosity.

Another uncertain parameter is a_r, the flow-wetted surface area per rock volume. Similar to the flow porosity, the flow-wetted surface is assumed to be uniform over the entire model. As part of studies in support of SR 97, Andersson and Stigsson (1999) analysed the conductive fracture frequency at Äspö and recommended a flow-wetted surface of $a_r = 1.0 \text{ m}^{-1}$. This parameter is not used directly as model input for HYDRASTAR, but it is used in calculating the F-ratio, defined as:

$$ F = \frac{d_w\, a_r}{q_w} = \frac{t_w\, a_r}{\varepsilon_f} $$

Where:

d_w = travel distance for a particle [metres]

q_w = Darcy velocity = $v \cdot \varepsilon_f$ [metres/year]

a_r = specific surface per rock volume for a travel path [m^{-1}]

ε_f = flow (kinematic) porosity [.]

The F-ratio [years / m] is a ratio of resisting to driving forces for transport, which has been used to compare model results in performance assessments (SKI, 1997). Although the F-ratio is calculated for all cases, it is a simple multiple of the travel time and is therefore plotted only for the Base Case. SR 97 uses the F-ratio to compare the geosphere performance for the three hypothetical repositories, where the flow-wetted surface varies from site to site.

4   Base Case

This section of the report presents the Base Case simulation and analysis. The Base Case represents the expected site conditions as described in the Section 3.0, and it is the reference case for comparison to all other cases. The premodelling study of Gylling et al. (1998) examined the extent of the domain and suggested a volume likely to contain all exit locations. Boundaries for this domain are specified head (Dirichlet) boundaries on all sides of the model domain, taken from the steady-state head values of a deterministic, freshwater simulation of the regional model. The details of the regional simulation and boundary condition transfer are given in Appendix B. The hydraulic conductivity field is created via unconditional simulation (i.e., no direct use of measured hydraulic conductivities), prescribing the mean of $\log_{10}K$ for each rock unit (SRD and SCD).

100 realisations of the hydraulic conductivity field, each with 120 starting locations, are used to estimate the distributions of travel time and canister fluxes. All statistics are calculated with respect to the common logarithm transform ($\log_{10}$) of the travel times, canister fluxes, and F-ratios to facilitate summary and display.

4.1   Monte Carlo Stability

A practical consideration in Monte Carlo simulation studies is that statistics of interest for the model results be stable with respect to the number of realisations. That is, the number of realisations is adequate for reliable estimates of the variability of the results. This study monitored the stability of the estimators of the median travel time and median canister fluxes to stable with respect to the number of realisations. Figures 4.1-1 and 4.1-2 present the medians of the logarithm of travel time and the logarithm of canister flux, respectively, versus the number of realisations. The plots indicate these statistics are approximately constant after 30 realisations, with less than 3 % deviation from the median travel time or median canister flux for additional realisations. This suggests that for the purposes of this study, a total number of 100 realisations are adequate for estimating the medians of the performance measures.

The stability of the sample median should not be taken to imply that higher moments such as the sample variance are also stable. Estimators of higher moments and the extreme quantiles of distributions are usually much less efficient than the median or the mean (Larsen and Marx, 1986). In general, estimating these moments with a similar degree of accuracy requires many more realisations than are needed for stable estimators of the median (Hammersley and Handscomb, 1975). Consequently, the higher-order statistics may not have stabilised and should be used cautiously.
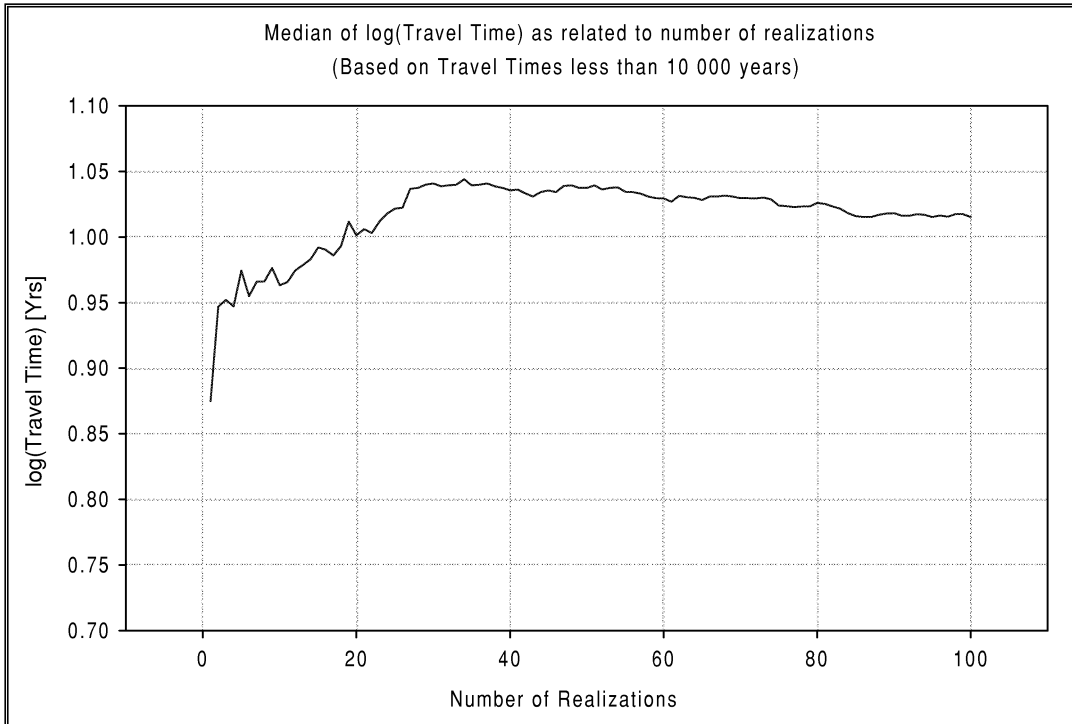
Figure 4.1-1. Monte Carlo stability in the Aberg Base Case. Median travel time versus number of realisations. Results for a flow porosity of $\varepsilon_f = 1x10^{-4}$ and travel times less than 10,000 years.
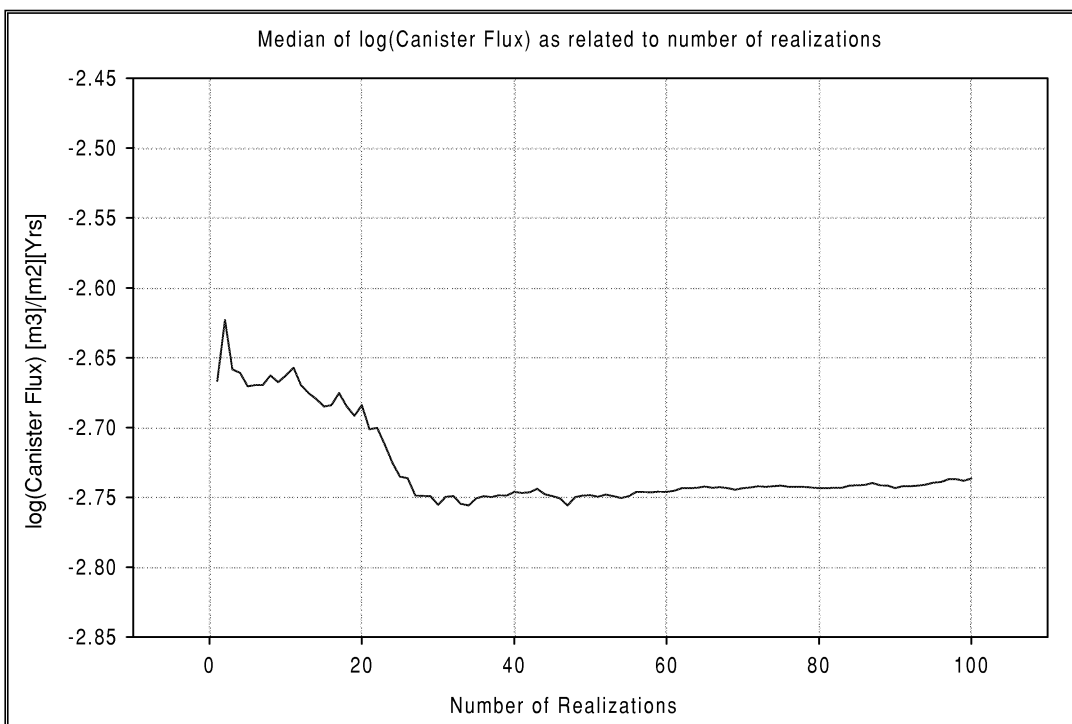
Figure 4.1-2. Monte Carlo stability in the Aberg Base Case. Median canister flux versus number of realisations.

4.2 Boundary Flux Consistency

Stochastic continuum theory suggests that, under certain conditions, there exists an effective hydraulic conductivity, K_e, that satisfies:

$$\langle \bar{q} \rangle = -K_e \nabla \langle \bar{h} \rangle$$

Where:

$\langle \bar{q} \rangle$ = the expected flux over the domain

$\nabla \langle \bar{h} \rangle$ = the expected gradient.

K_e is useful for nested models in that it can be used to estimate the expected value of the flux in a smaller domain (Dagan, 1986; Rubin and Gómez-Hernández, 1990). This suggests that a regional model with a homogeneous hydraulic conductivity of K_e could be used to determine the expected boundary fluxes of a site-scale model subdomain. If the rescaling of the geometric mean hydraulic conductivity is correct, the boundary flux of the regional model should be consistent with the average boundary flux of the site-scale stochastic continuum model. That is, the site-scale stochastic continuum model should conserve mass in an average sense with respect to the regional model fluxes.

Walker et al. (1997b) suggested that the upscaling of block scale hydraulic conductivity could be calibrated using the above relationship, adjusting the block scale mean until the average boundary fluxes of the ensemble matched the regional scale fluxes. However, there are several drawbacks to that approach. For example, the existence of K_e requires that the domain be stationary (statistically homogeneous), a condition that may be violated by the fracture zones interrupting the Aberg host rocks. Although the individual rock blocks (such as the SRDs) may be stationary, K_e also requires that the domain be extensive and under uniform flow conditions. In addition, although the regional models may conserve mass balance over the entire domain, they do so in an average sense. Consequently, the regional model may not conserve mass for the small subdomain corresponding to the site scale model of interest. This study reports and compares the boundary fluxes, but does not adjust the mean block hydraulic conductivity.

The regional model of Svensson (1997a) used a single stochastic realisation of heterogeneous hydraulic conductivities, with density-dependent flow effects of saline groundwater. For base case of this study, the Svensson regional model was rerun using homogeneous hydraulic conductivity of K_e and nonsaline conditions to determine the expected boundary heads and fluxes for the Base Case of the site scale model. Appendix B summarises the details of this regional simulation and its results. Variant 1 addresses the consequences of using other regional models and boundary transfer algorithms, in Section 5.1 of this report. Lovius (1998) describes the computation of boundary fluxes for a HYDRASTAR model domain, yielding the average flux over each boundary.
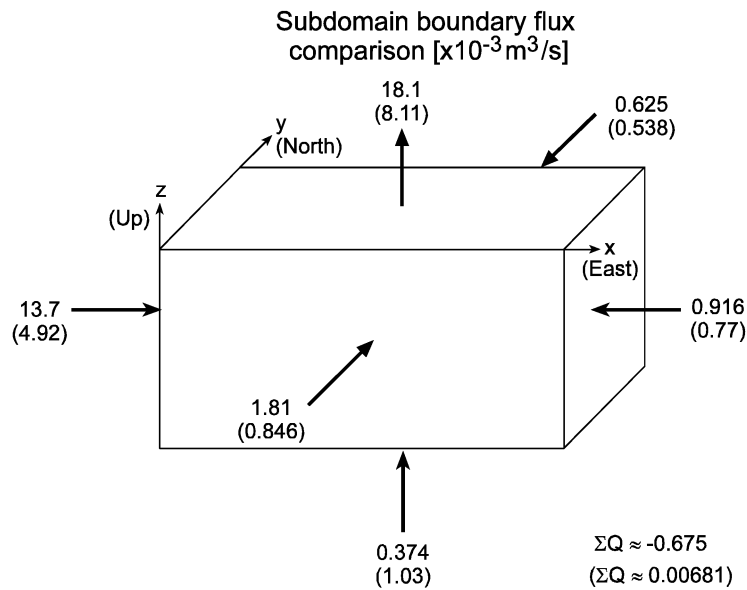
Figure 4.2-1. *Consistency of Aberg Base Case boundary fluxes, regional versus site-scale models. In parentheses are the site-scale fluxes calculated as the arithmetic mean of 5 realisations. Arrows show the regional flux direction.*

Figure 4.2-1 and Table 4-1 present the boundary fluxes for the Base Case model in comparison to the regional model (Appendix B). As shown in Figure 4.2-1, both models indicate that the majority of the inflow to the domain comes from the west, and the majority of the outflow is directed out the upper surface of the model to the Baltic Sea. This is consistent with the regional pattern of recharge and discharge. Table 4-1 summarises the boundary fluxes as the net flux over each face of the subdomain. The average of 5 realisations of the site model suggested that the site model tends to underestimate the regional boundary fluxes by a factor of approximately 1/2. It may be possible to adjust the mean of $\log_{10}$ hydraulic conductivities in an attempt to match the boundary fluxes, but this study has not attempted to do so.

Table 4-1. **Boundary flux consistency for Aberg Base Case, regional model versus site-scale model.**

Site Model Surface	Net Flux Through Site Model Surfaces (m^3/s x 10^{-3})	
	Regional Model (Appendix B)	Site-Scale Model (5 realisations)
West	13.7 (in)	4.92 (in)
East	0.916 (in)	0.77 (in)
South	1.81 (in)	0.846 (in)
North	0.625 (in)	0.538 (in)
Bottom	0.374 (in)	1.03 (in)
Top	18.1 (out)	8.11 (out)
Total Inflow	17.4	8.10
Total Outflow	18.1	8.11
Mass balance (In-Out)	-0.675	-0.00681

4.3   Ensemble Results

4.3.1   Travel Time and F-ratio

In each realisation, HYDRASTAR calculates the travel times for a particle to be advected from each starting position (release position) to the model surface. The resulting stream tubes are used later in one-dimensional transport calculations in the PA model chain. Although the advective travel time is a common statistic for comparing variant simulations, it is important to note that HYDRASTAR allows only a homogenous flow porosity to be specified for the entire domain. Consequently, the travel time in any stream tube is directly proportional to this homogeneous flow porosity. This study simply uses the flow porosity of $\varepsilon_f = 1 \times 10^{-4}$, and leaves further analysis of the flow porosity to the transport modelling studies associated with SR 97.

Figure 4.3-1 presents the frequency histogram of the common logarithm of travel time for 100 realisations. Each of these realisations has 120 starting positions as representative canister locations. A few outliers are seen at the upper tail of the histogram, corresponding to travel times of 10,000 years. These 0.4833 % are stream tubes that are intercepted by the side boundaries and fail to exit the upper surface of the model (Figure 4.4-1). In this circumstance, HYDRASTAR sets the travel times for these stream tubes to the default maximum travel time of 10,000 years.

The use of the default travel time does have noticeable effects on the performance measure statistics, as shown in Table 4-2 for the Base Case. To evaluate this effect, this study calculates the statistics both with and without the travel times greater than 10,000 years. The means and variances of the travel time and F-ratio change slightly if stream tubes with the default travel time of 10,000 years are deleted. In contrast, the canister flux statistics are virtually unaffected by this censoring, as are the medians of travel time and F-ratio. For the remainder of this study, the performance measure statistics are calculated both with and without the travel times greater than 10,000 years. For the sake of brevity, the discussions will emphasise the medians of all measures and the statistics of travel time and F-ratio for travel times less than 10,000 years. The canister flux will be summarised with statistics computed for the full set of stream tubes (no deletions). The variances and medians of the performance measures are emphasised in bold in the summary tables (e.g., Table 4-2). The effects of this censoring on subsequent performance assessment calculations are beyond the scope of this study.

Table 4-2 summarises the ensemble results, presenting the statistics for the 100 Monte Carlo realisations of the 120 starting positions for travel time, as well as canister fluxes and F-ratio. With the intercepted stream tubes deleted, the median of the travel time is 10 years, with an interquartile range from 3.4 years to 37 years.
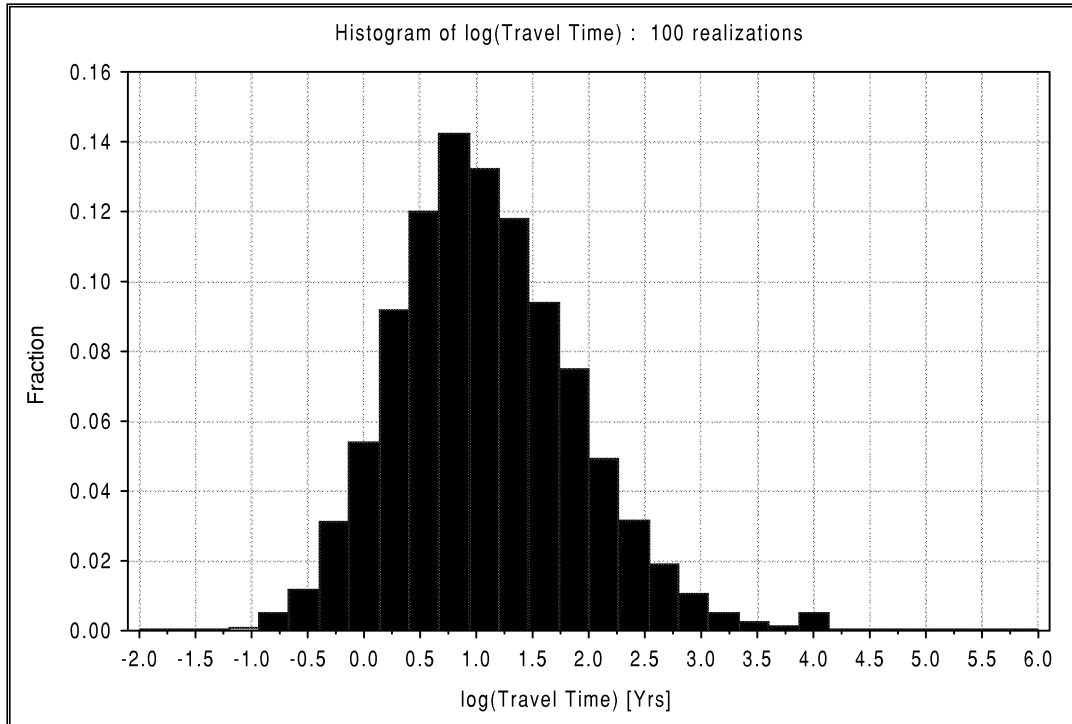
Figure 4.3-1. Relative frequency histogram of log$_{10}$ travel time for the Aberg Base Case. Results for 100 realisations of 120 starting positions and a flow porosity of $\varepsilon_f = 1x10^{-4}$.

Table 4-2. Summary statistics for Aberg Base Case. Results for 100 realisations of 120 starting positions, a flow porosity of $\varepsilon_f = 1x10^{-4}$ and flow-wetted surface $a_r = 1.0$ m^2/m^3. Statistics in bold are discussed in text.

	All values			**Travel Times > 10,000 years deleted**		
	Log$_{10}$ t$_w$	**Log$_{10}$ q$_c$**	**Log$_{10}$ F-ratio**	**Log$_{10}$ t$_w$**	**Log$_{10}$ q$_c$**	**Log$_{10}$ F-ratio**
Mean	1.083	-2.799	5.083	1.069	-2.796	5.069
Median	1.021	**-2.736**	5.021	**1.015**	-2.734	**5.015**
Variance	0.637	**0.935**	0.637	**0.599**	0.931	**0.599**
5th percentile	-0.125	-4.479	3.875	-0.125	-4.475	3.875
25th percentile	0.534	-3.430	4.534	0.533	-3.427	4.533
75th percentile	1.574	-2.114	5.574	1.563	-2.113	5.563
95th percentile	2.468	-1.298	6.468	2.431	-1.298	6.431

Figure 4.3-2 shows the frequency histogram of the common logarithm of F-ratio for 100 realisations for travel times less than 10,000 years. This histogram is essentially identical to the histogram of log$_{10}$ travel times (Figure 4.3-1) because the F-ratio is a simple multiple of the travel time (see Section 3.5.4). This report presents the F-ratio for

all variants, but in the interest of brevity will present the histogram of F-ratio only for the Base Case.

Figure 4.3-3 presents a box plot of the simulated travel times by realisation, which show a wide range of variability. Figure 4.3-4 presents the number of realisations with travel times less than 1 year and 10,000 years, by stream tube number. Because each stream tube number corresponds to a particular starting position, this plot also suggests that some positions tend to have shorter travel times (See Figures 3-5a and b). For example, starting positions 13 through 19, 41 through 50, 74 through 81, and 99 through 120 lie in rock blocks SRD2 and SRD4. These blocks have mean $\log_{10}$ hydraulic conductivities that are higher then the remaining host rocks. Consequently, stream tubes with starting positions in SRD2 and SRD4 have reduced travel times. Individual starting positions are discussed in greater detail in Section 4.5, and the results by repository level are discussed in Section 4.6.
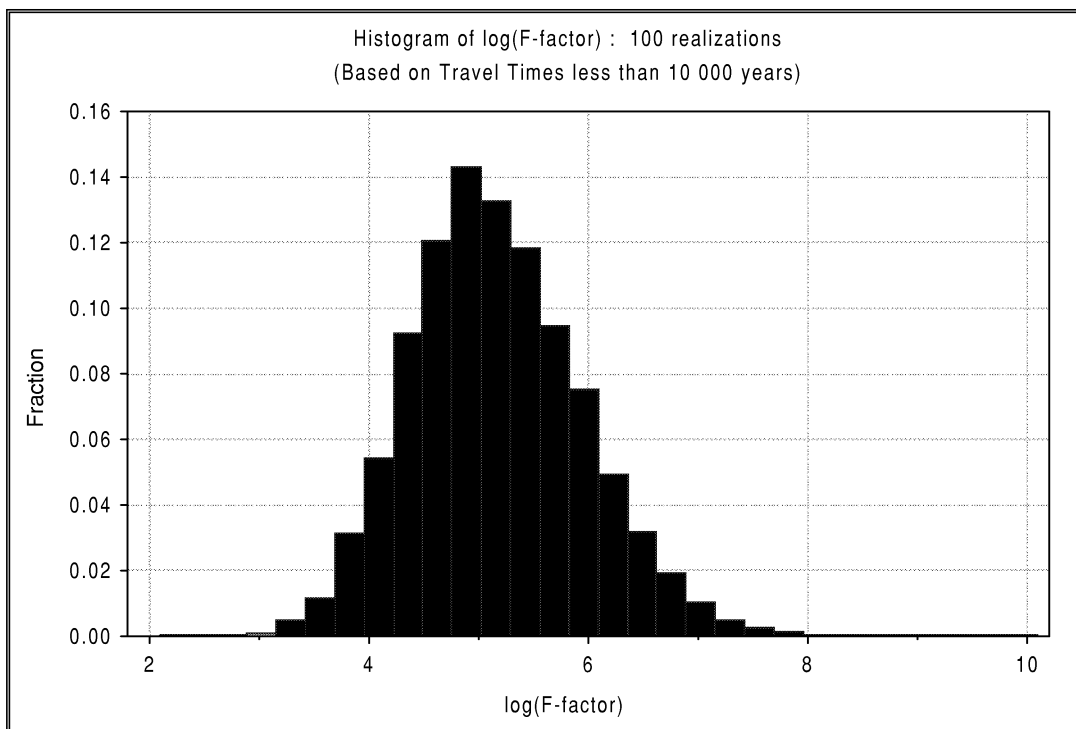
Figure 4.3-2. Relative frequency histogram of $\log_{10}$ F-ratio for the Aberg Base Case. Results for 100 realisations of 120 starting positions, a flow porosity of ε_f = 1×10^{-4} and $a_r = 1.0$ m^{-1}.
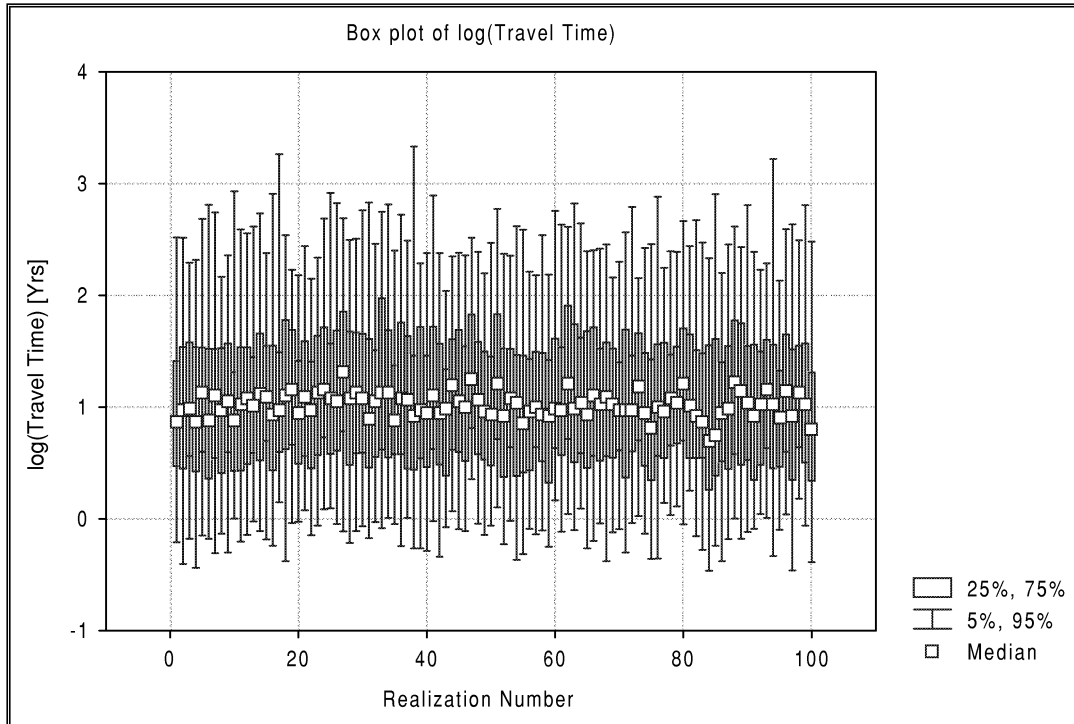
Figure 4.3-3. *Travel times by realisation for the Aberg Base Case. Results for flow porosity of* $\varepsilon_f = 1x10^{-4}$.
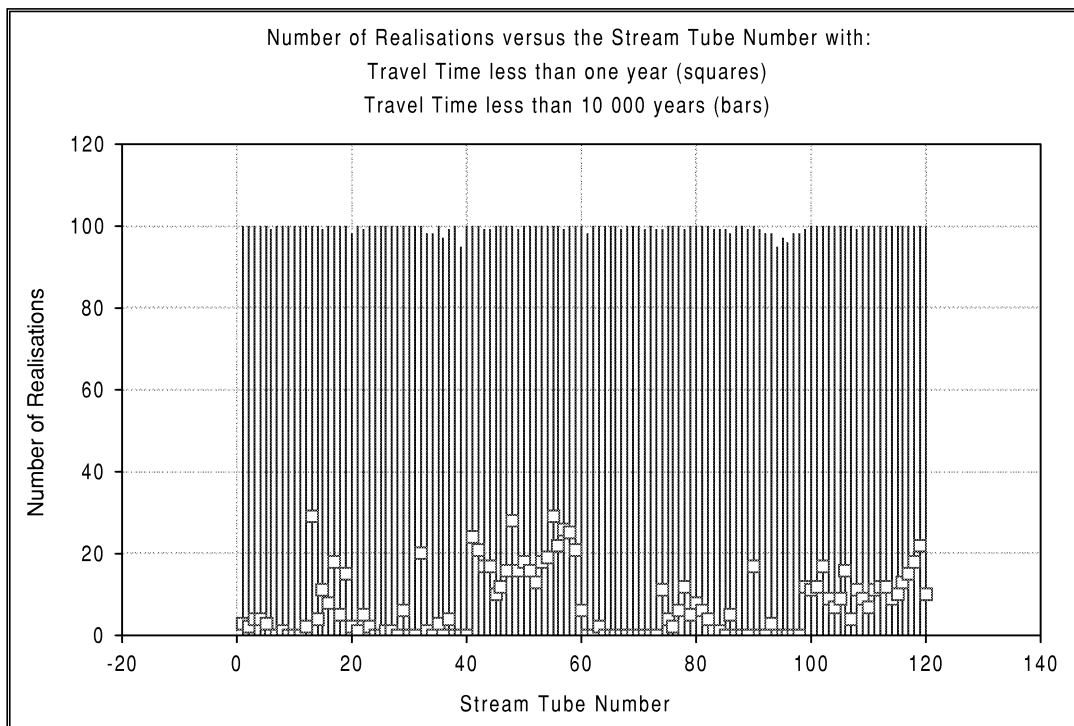
Figure 4.3-4. *Number of realisations with travel times less than 1 year (squares) and 10,000 years (lines), by stream tube number for the Aberg Base Case. Results for flow porosity of* $\varepsilon_f = 1x10^{-4}$.

4.3.2 Canister Flux

HYDRASTAR calculated the canister fluxes (Darcy groundwater velocity) at each of the 120 stream tube starting positions. Table 4-2 summarises the results for the canister flux, which indicate a median canister flux of 1.9×10^{-3} m/year and an interquartile range from 3.7×10^{-4} m/year to 7.8×10^{-3} m/year. Figure 4.3-5 presents the frequency histogram for the $\log_{10}$ canister flux for 100 realisations, each with 120 starting positions. Similar to the histogram of $\log_{10}$ travel time, this histogram is also slightly skewed, but in opposite direction. Figure 4.3-6 confirms that the logarithm of travel time is inversely correlated to the logarithm of canister flux. This might not be true for models that use a spatially variable porosity, rather than a homogeneous porosity as is used in HYDRASTAR. Figure 4.3-7 presents a box plot of canister fluxes by realisation, which indicates a variability of over 3 orders of magnitude.
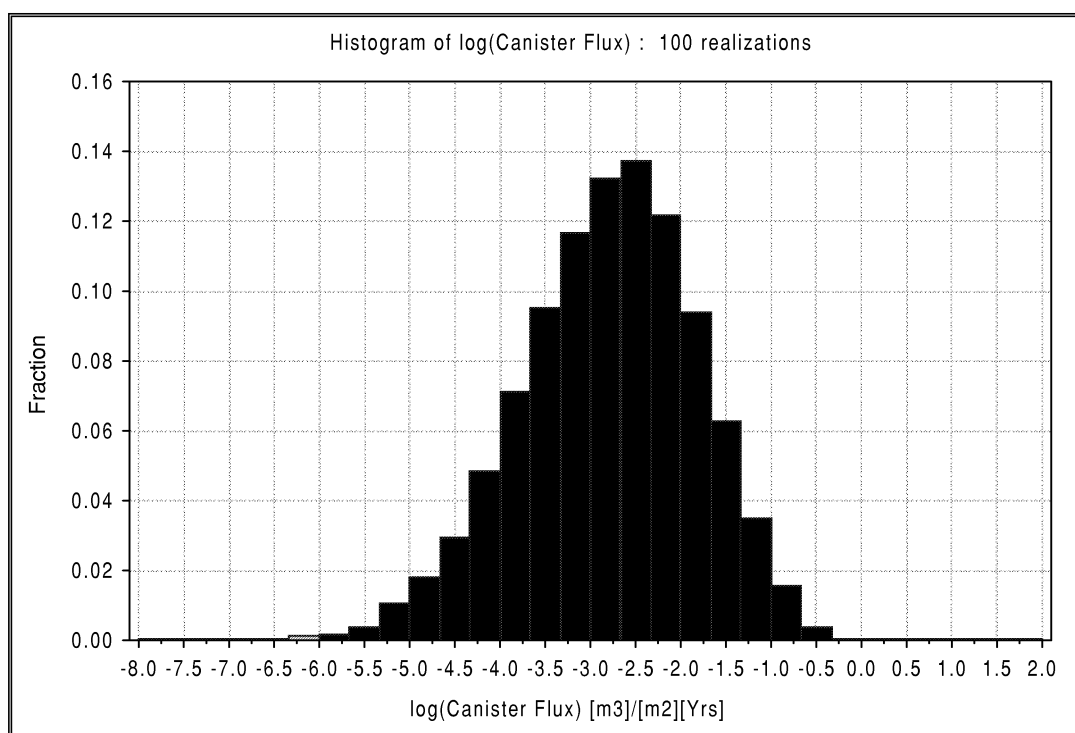
Figure 4.3-5. Relative frequency histogram of $\log_{10}$ canister flux for the Aberg Base Case. Results for 100 realisations, each with 120 starting positions.
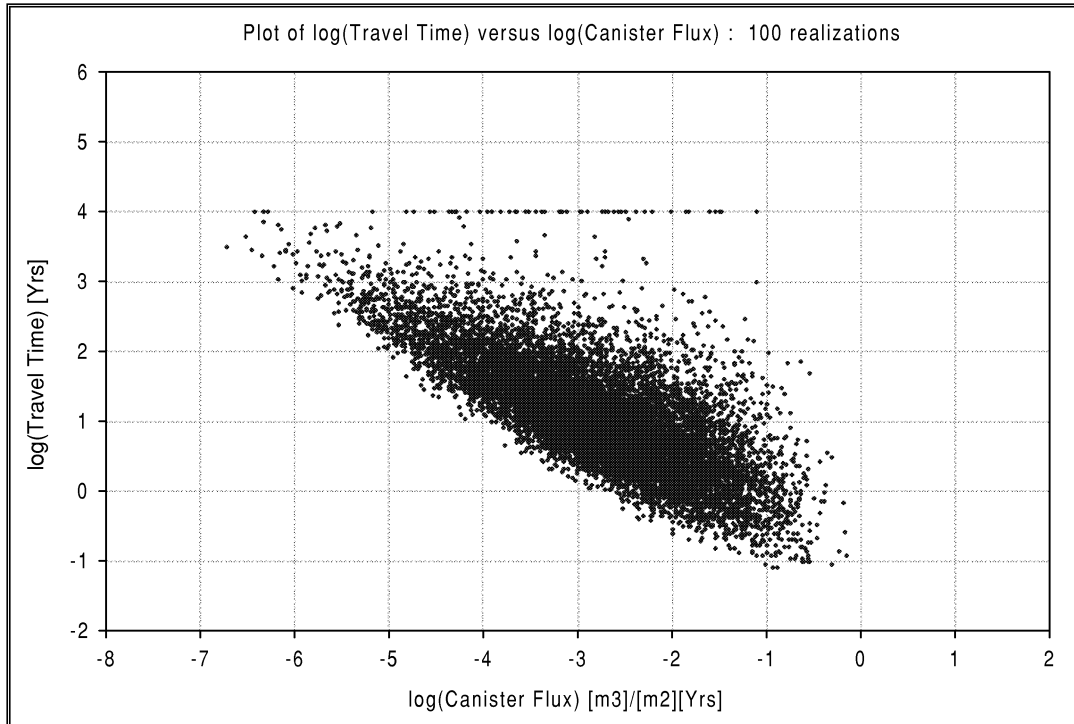
Figure 4.3-6. Log₁₀ travel time versus log₁₀ canister flux for the Aberg Base Case.
Results for 100 realisations of 120 starting positions and a flow porosity
of $\varepsilon_f = 1x10^{-4}$.
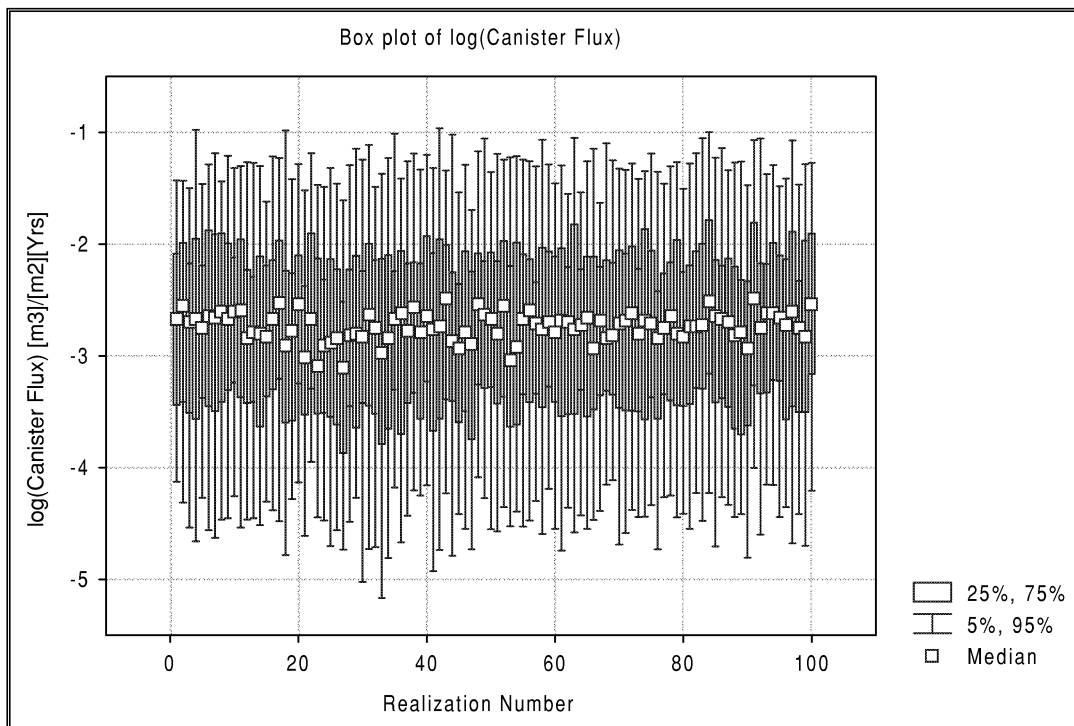
Figure 4.3-7. Box plot of log₁₀ canister flux by realisation number for the Aberg Base
Case. Results for 120 starting positions.

4.3.3   Exit Locations

HYDRASTAR calculates the exit locations for each of the particles as the last point of the travel path. Figure 4.3-8 presents a map of the exit locations on the model surface (-25 masl). As discussed earlier in this section, the flow paths are predominantly upward, reflecting the pattern of regional upward groundwater flow. The flow paths are also directed southward to exit locations in the shallow waterways just south of Äspö Island, reflecting the pattern of precipitation recharge on the island, discharging to the surrounding Baltic Sea. The exceptions to this pattern are the flow paths from the starting positions in the northeastern areas of the repository, which are influenced by the recharge under Mjälen.
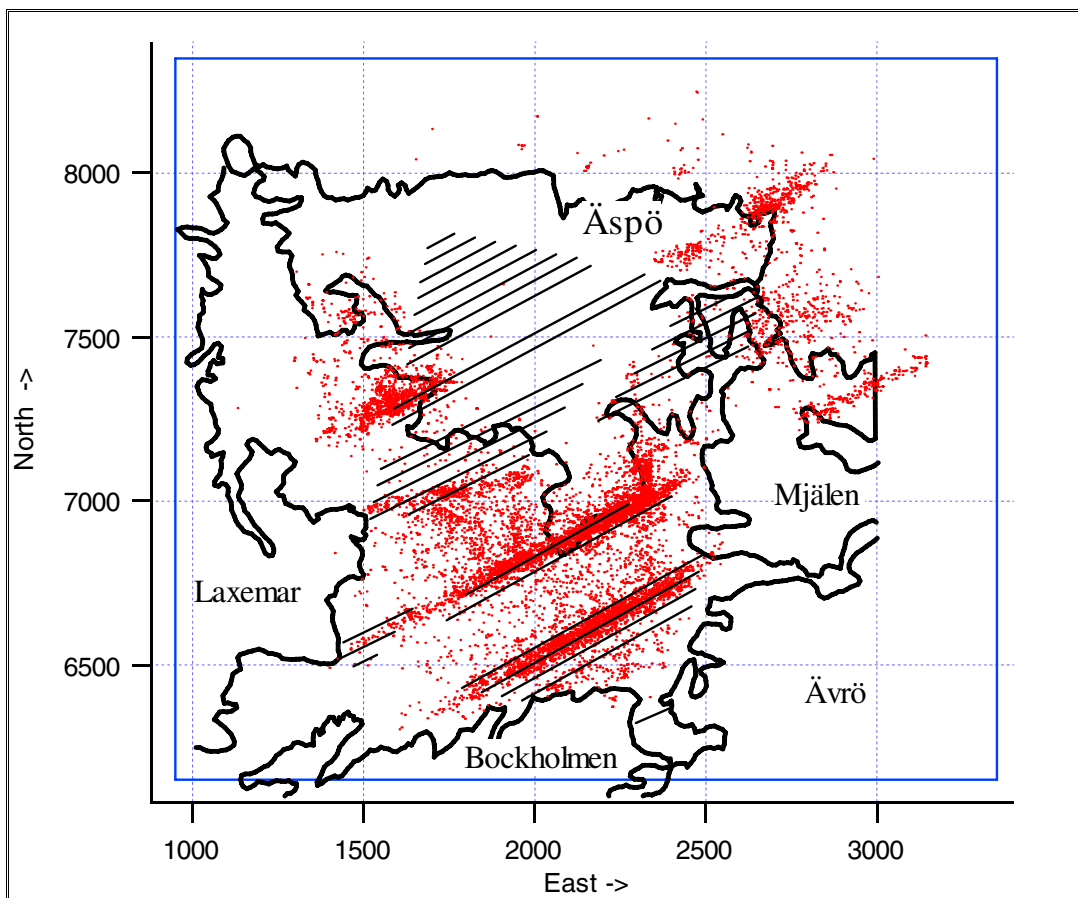
Figure 4.3-8.   Exit locations for the Aberg Base Case. Repository tunnels at –500 masl are shown as projected up to the model surface. Results for 100 realisations of 120 starting positions. (Äspö local coordinate system, scale in metres).

4.3.4   Validity of Results

An approximate calculation of the travel time from SRD 1 was performed as a check on the validity of the model (Appendix C.3). These computations used Darcy's law, the estimated gradient, a simple flow path, and the mean hydraulic conductivities to

estimate the advective travel time. The results showed that the travel times should be on the order of 10 years, roughly in agreement with the median of the model results.

In a previous study of the Äspö site, Svensson (1997b, cited in Rhén et al., 1997) determined the advective travel times from –450 masl to ground surface. Using a nonuniform flow porosity with an average of $\varepsilon_f = 4 \times 10^{-3}$, Svensson found that 15% of the particles would have reached the surface after 100 years. Although Svensson's model used a spatially variable flow porosity, the results can be roughly rescaled to a flow porosity of $\varepsilon_f = 1 \times 10^{-4}$ by dividing the travel times by 40 (i.e., 15% of the stream tubes would have arrived at ground surface after 2.5 years). This suggests that the travel times of this study are roughly comparable to those of Svensson (1997b).

It is also useful to compare the observed heads from boreholes at Äspö model simulated heads. Rhén and Forsmark (1993) provide a suitable set of observations to use for this comparison, the preconstruction undisturbed freshwater heads, estimated as a long term average of the transient heads in open boreholes and packed-off sections at the site. Figure 4.3-9 presents the Base Case simulated versus observed heads at locations corresponding to representative borehole sections at the site. These sections are:

- HAS02 (MA27) is north of EW-1, above 100 m;
- KAS03 (MA32) is north of EW-1, below 100 m;
- HAS13 (MA137) is south of EW-1, above 100 m;
- KAS06 (MA63) is south of EW-1, below 100 m; and
- KAS06 (MA65) is south of EW-1, in zone EW-3.

Because this is a Monte Carlo study of heterogeneous fields, each realisation will not exactly match the observed data. Based on a simple analysis of the errors (Appendix C.4), the maximum error of observed versus model simulated heads should be approximately 2.0 m. The heads of five realisations presented in Figure 4.3-9 are generally within this error, suggesting that the model-simulated heads agree with the observed heads.
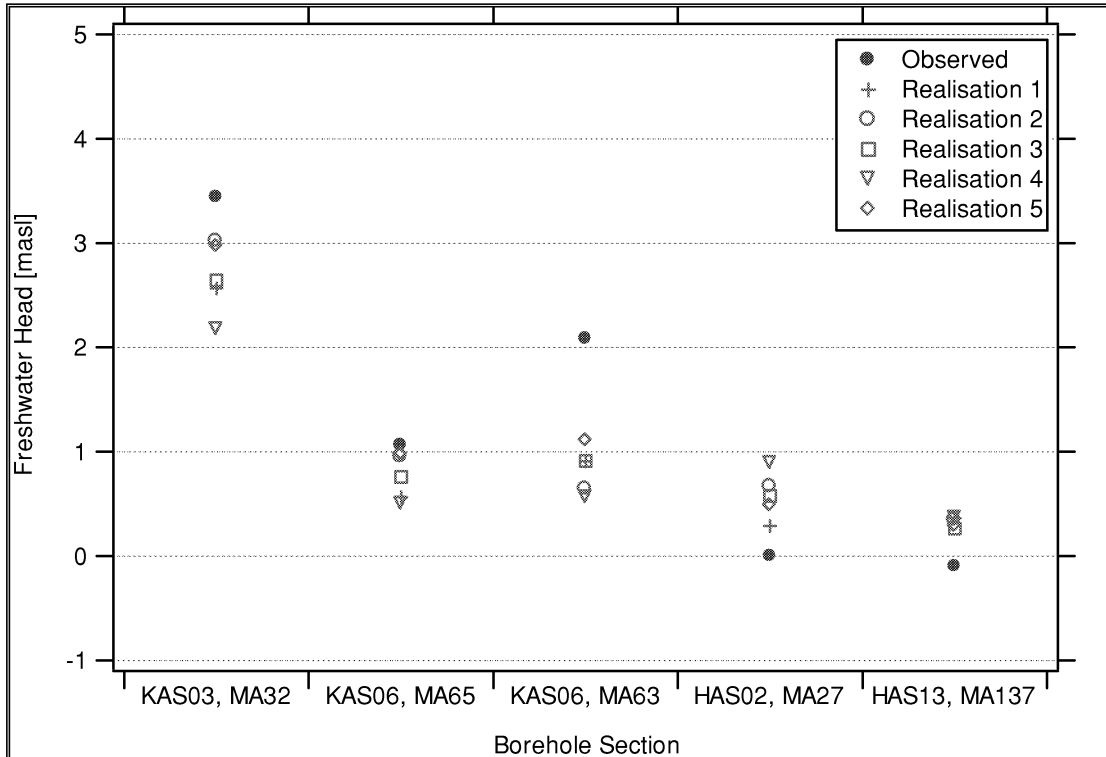
Figure 4.3-9. Observed and simulated freshwater heads for five realisations of the Aberg Base Case.

4.4   Individual Realisations

There are several strategies that could be used to select several realisations that are in some sense representative of the ensemble. For example, we could select a realisation whose travel time or canister flux is close to the median of the ensemble of the realisations. However, the probability of each realisation in a Monte Carlo set is equal by definition, so that no single realisation can be said to be representative of the ensemble. To illustrate the variability within and between realisations, this study examines three random realisations to get a sense of the ensemble behaviour. (Note that these are actually the first three realisations, whose sequence is randomised by the random number generation).

Figure 4.4-1 presents the stream tubes for realisation number one in plan and elevation views. The stream tubes reflect the overall upward flow pattern at the site, as a result of the regional discharge. The precipitation recharge on the land surface diverts the stream tubes around the islands to discharge areas under the Baltic. As discussed in the previous sections, this flow pattern is a consequence of the regional flow pattern and the effect of the island hydrology. The exit locations of the ensemble are discussed in Section 4.1.5. Figure 4.4-2 presents the stream tubes for realisations 1 through 3, showing the variability of stream tubes and exit locations between realisations. For the first three realisations, Figure 4.4-3 presents the histograms of travel time, canister flux and F-ratio, and Table 4-3 presents the summary statistics. Note that, although the stream tubes and exit locations can vary widely between realisations, the median travel

times and median canister fluxes are rather stable. This is further illustrated in Figures 4.4-4 and 4.4-5, which present plots of travel time and canister flux by starting position number for these three realisations. These plots also show that in any given realisation, the results for a particular starting position can vary widely. Section 4.5 discusses the results for individual starting positions of interest in greater detail.
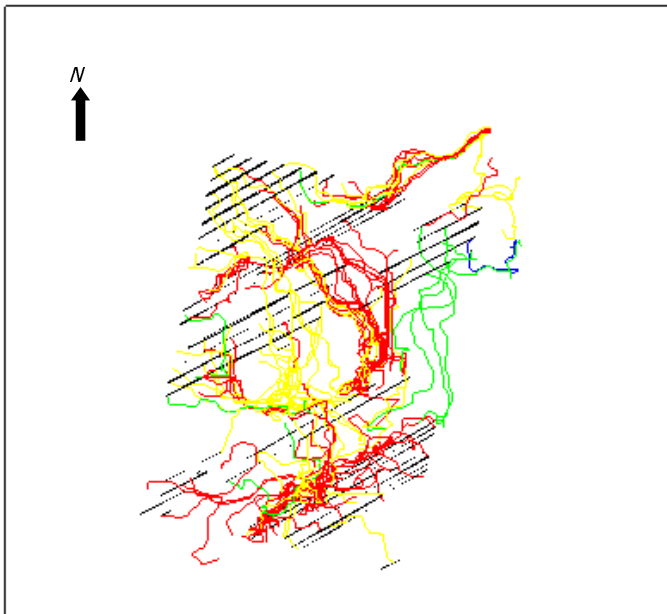
a) Plan view
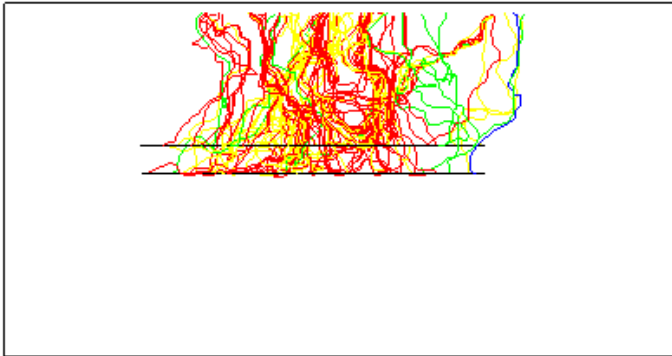
b) Elevation view, from South
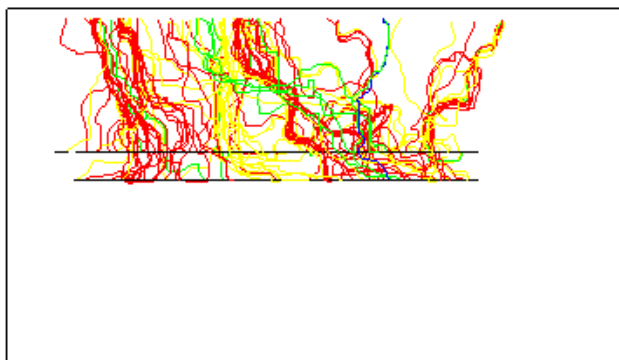
tw = Ground water travel time (years)

tw < 10
10 < tw < 100
100 < tw 1000
1000 < tw < 10000
tw > 10000

Approx. Scale

0   1000 m

c) Elevation view, from East
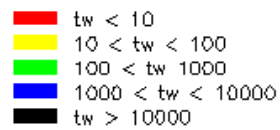
Figure 4.4-1. Stream tubes for Aberg Base Case realisation number 1. The y-positive axis of a) points in the direction of Äspö local North. Results for 120 starting positions and a flow porosity of $\varepsilon_f = 1x10^{-4}$.
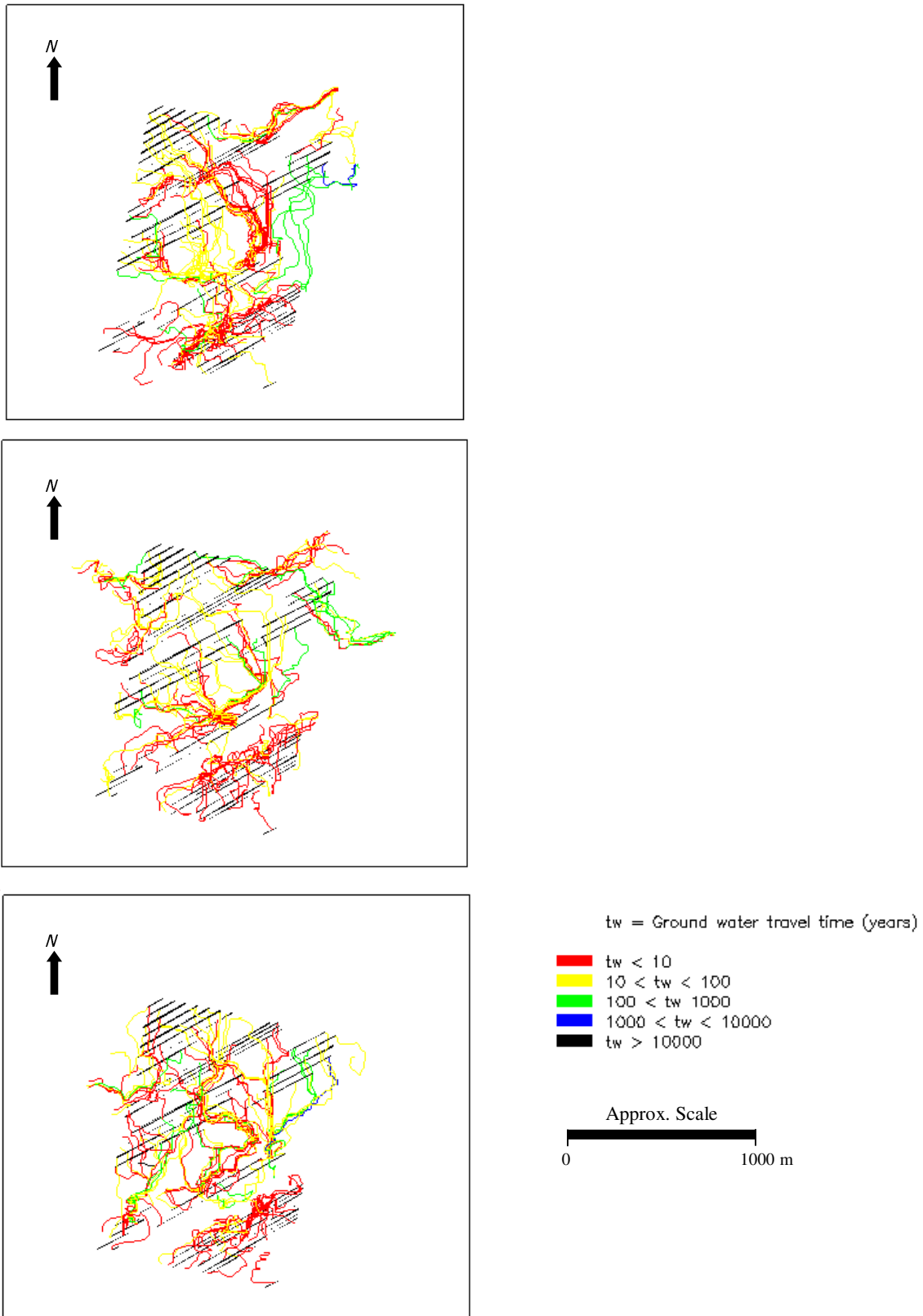
Figure 4.4-2. Stream tubes for 3 realisations of the Aberg Base Case. Plan view with the y-positive axis pointing in the direction of Äspö local North. Results for 120 starting positions and a flow porosity of $\varepsilon_f = 1x10^{-4}$.
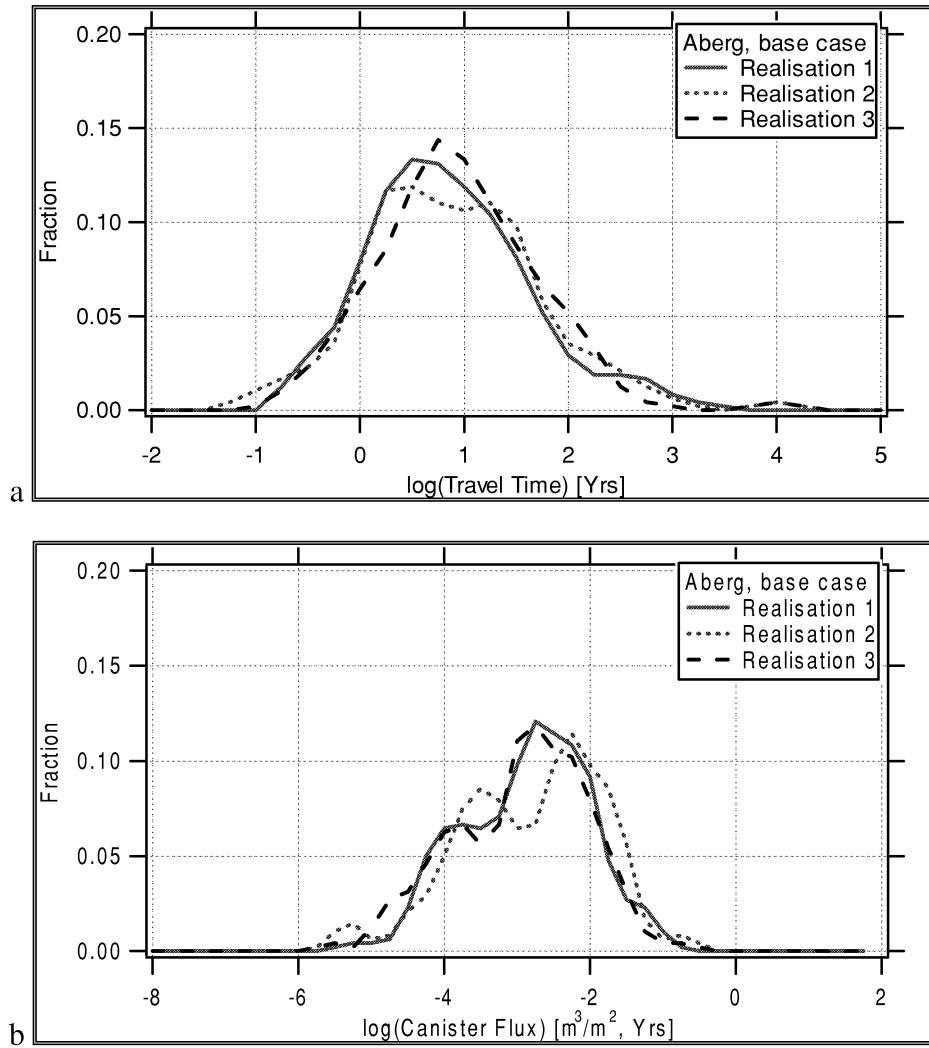
Figure 4.4-3. Realisations 1, 2 and 3 of the Aberg Base Case, statistics taken over all starting positions. Floating histograms of a) log10 travel time, b) log$_{10}$ canister flux. Results for a flow porosity of $\varepsilon_f = 1x10^{-4}$.

Table 4-3. Summary statistics for three realisations of Aberg Base Case. Results for 120 starting positions, a flow porosity of $\varepsilon_f = 1\times10^{-4}$ and flow-wetted surface $a_r = 1.0$ m^2/m^3. Statistics in bold are discussed in text.

	Realisation 1	Realisation 2	Realisation 3
Log$_{10}$ Travel Time for times < 10,000 years (years)			
Mean	0.992	1.000	1.034
Median	**0.875**	**0.966**	**0.975**
Variance	**0.578**	**0.636**	**0.501**
5th percentile	-0.172	-0.399	-0.164
25th percentile	0.477	0.450	0.565
75th percentile	1.410	1.525	1.511
95th percentile	2.454	2.466	2.230
Log$_{10}$ Canister Flux for all times (m/year)			
Mean	-2.745	-2.699	-2.842
Median	**-2.667**	**-2.558**	**-2.702**
Variance	**0.735**	**0.949**	**0.818**
5th percentile	-4.127	-4.279	-4.506
25th percentile	-3.438	-3.405	-3.507
75th percentile	-2.095	-1.999	-2.175
95th percentile	-1.467	-1.467	-1.528
Log$_{10}$ F-ratio for times < 10,000 years (year/m)			
Mean	4.992	5.000	5.034
Median	**4.875**	**4.966**	**4.975**
Variance	**0.578**	**0.636**	**0.501**
5th percentile	3.828	3.601	3.836
25th percentile	4.477	4.450	4.565
75th percentile	5.410	5.525	5.511
95th percentile	6.454	6.466	6.230
Percent of Stream tubes Failing to Exit	0	0.833	0.833
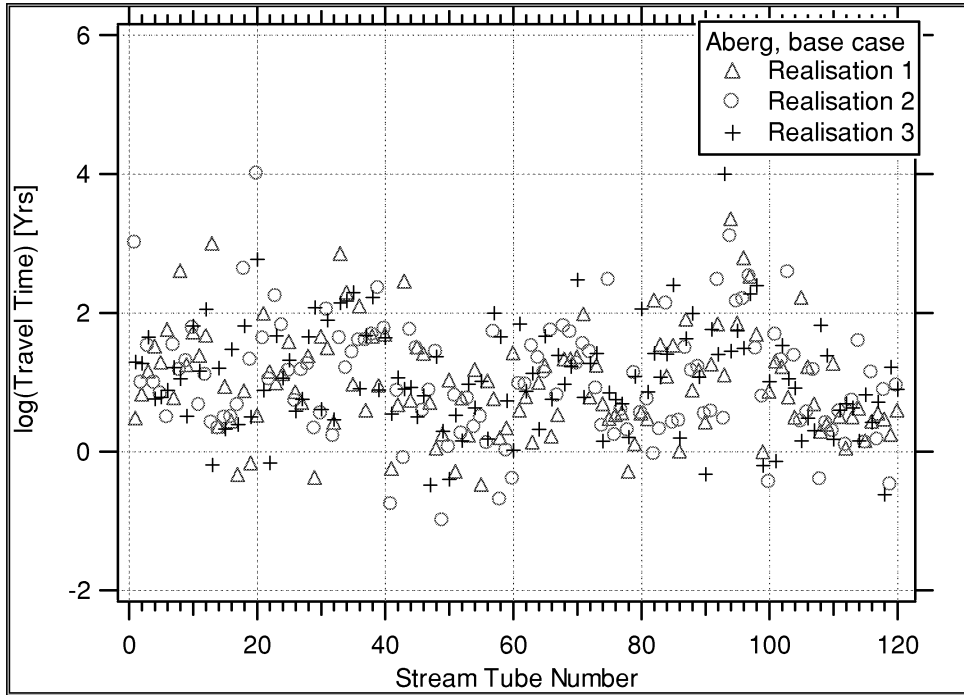
Figure 4.4-4. Log$_{10}$ travel time by stream tube number for 3 realisations of the Aberg Base Case. Results for a flow porosity of $\varepsilon_f = 1x10^{-4}$.
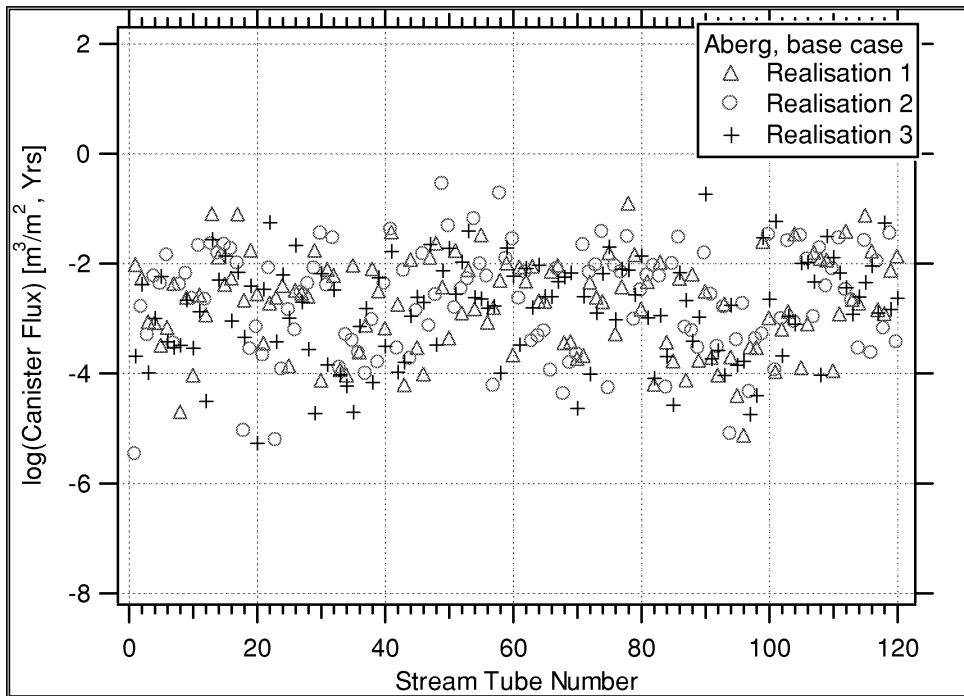
Figure 4.4-5. Log$_{10}$ canister flux by stream tube number for 3 realisations of the Aberg Base Case.

4.5   Individual Starting Positions

This study examines three individual stream tube starting positions to illustrate the performance of specific repository areas:

- Position 28, in the upper repository level that lies in rock unit SRD3 (rock block with relatively low conductivity, in the central part of the repository) with moderate travel times;

- Position 32, in the upper repository level that lies in rock unit SRD3. This position lies in NNW-2, a fracture zone whose occurrence is thought to be possible but is not well-defined (Munier et al, 1997; Rhén et al., 1997); and

- Position 51, in the upper repository level that lies in rock unit SRD4 (rock block with relatively high conductivity, in the southern part of the repository) with relatively short travel times.

Table 4-4 presents the summary statistics for the three starting positions listed above, compiled over all 100 realisations of the Base Case. As expected, the canister flux of starting position 32 is the highest of the three as a result of being within fracture zone NNW-2. Similarly, the canister fluxes of starting positions 51 and 28 are higher and lower, respectively, than the median canister flux of the entire ensemble (Table 4-4). The histograms of Figures 4.5-1 and 4.5-2 illustrate the relative performance of these starting positions, and also show that the differences are less dramatic for the travel times than the canister fluxes. Figure 4.5-3 is a plot of $\log_{10}$ travel time versus realisation number for these three starting positions, which shows that the travel time for any given starting position can vary by 3 orders of magnitude between realisations.

Table 4-4. Summary statistics for three starting positions in the Aberg Base Case. Results for 100 realisations, a flow porosity of $\varepsilon_f = 1\text{x}10^{-4}$ and flow-wetted surface $a_r = 1.0 \text{ m}^2/\text{m}^3$. Statistics in bold are discussed in text.

	Starting Position Number		
Log_{10} Travel Time for times < 10,000 years (years)	28	32	51
Mean	1.487	0.497	0.656
Median	**1.478**	**0.420**	**0.554**
Variance	**0.384**	**0.349**	**0.497**
5th percentile	0.459	-0.369	-0.435
25th percentile	1.078	0.125	0.190
75th percentile	1.869	0.886	1.132
95th percentile	2.555	1.498	1.883
Log_{10} Canister Flux for all times (m/year)			
Mean	-3.111	-1.863	-2.428
Median	**-3.061**	**-1.725**	**-2.352**
Variance	**0.727**	**0.516**	**0.824**
5th percentile	-4.519	-3.218	-3.988
25th percentile	-3.742	-2.211	-3.006
75th percentile	-2.480	-1.376	-1.731
95th percentile	-1.949	-0.844	-0.996
Log_{10} F-ratio for times < 10,000 years (year/m)			
Mean	5.487	4.497	4.656
Median	**5.478**	**4.420**	**4.554**
Variance	**0.384**	**0.349**	**0.497**
5th percentile	4.459	3.631	3.565
25th percentile	5.078	4.125	4.190
75th percentile	5.869	4.886	5.132
95th percentile	6.555	5.498	5.883
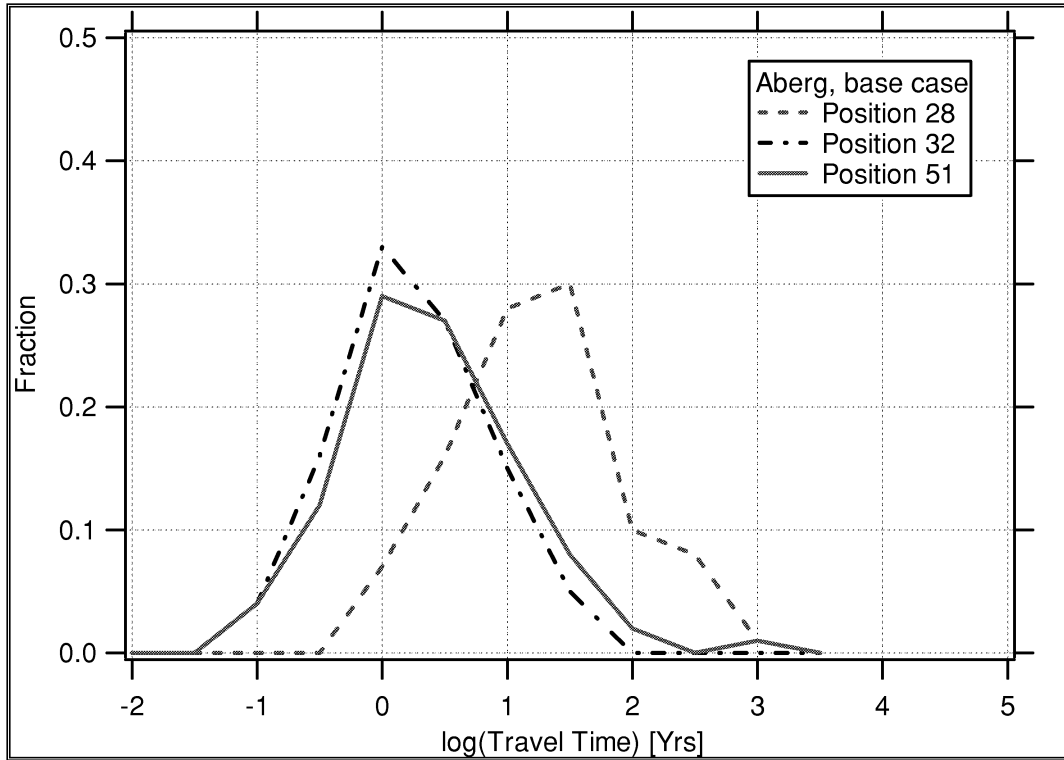
Figure 4.5-1. *Floating histogram of log$_{10}$ travel time for three starting positions in the Aberg Base Case. Results are for 100 realisations and a flow porosity of $\varepsilon_f = 1x10^{-4}$.*
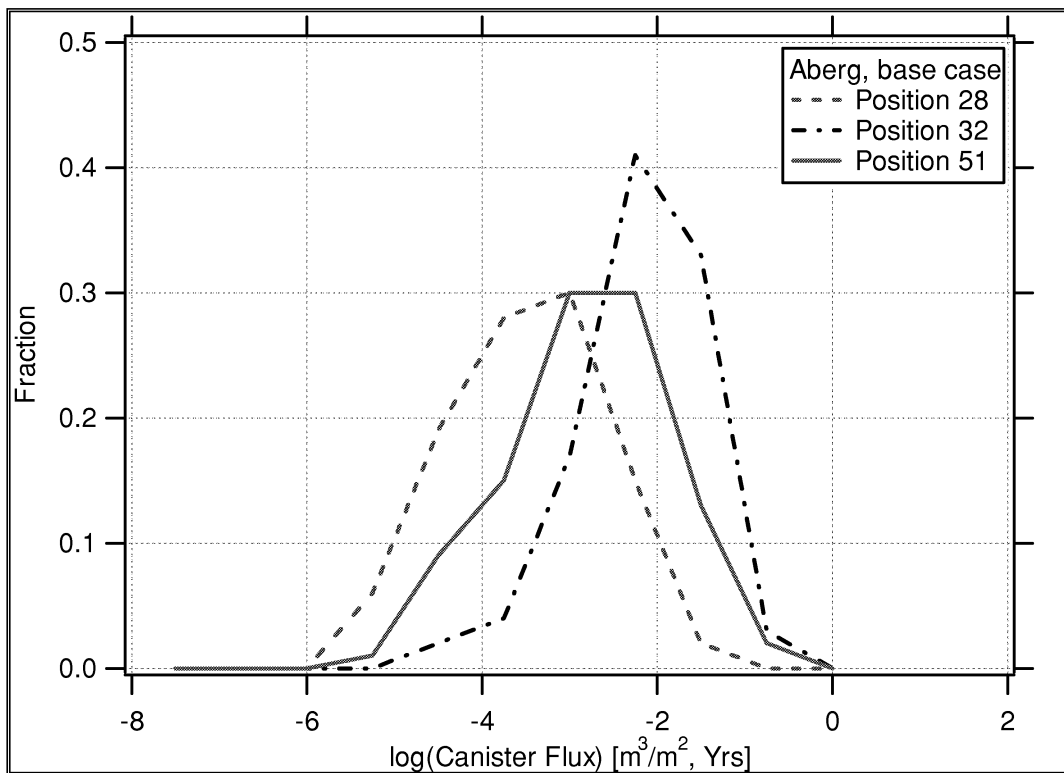
Figure 4.5-2. *Floating histogram of log$_{10}$ canister flux for three starting positions in the Aberg Base Case. Results for 100 realisations.*
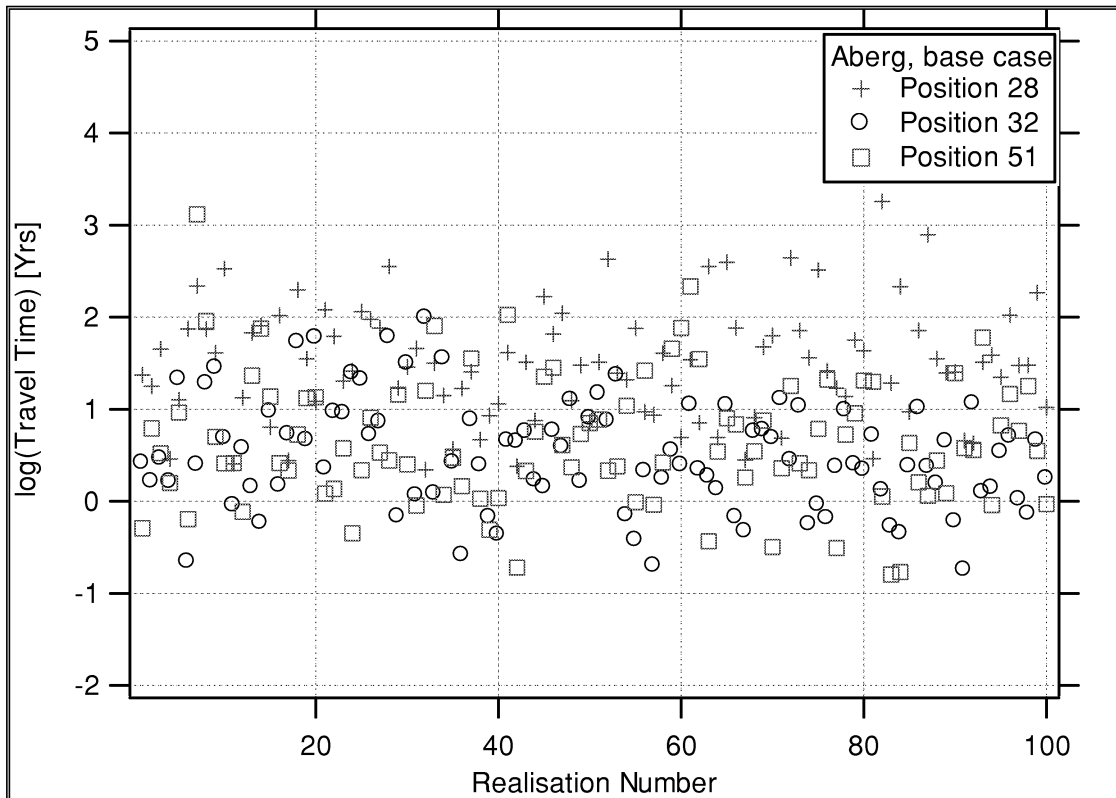
Figure 4.5-3. Log₁₀ travel time versus realisation number for three starting positions in the Aberg Base Case. Results for 100 realisations of 120 starting positions, a flow porosity of $\varepsilon_f = 1x10^{-4}$.

As was discussed in Section 4.1, it is important to examine the Monte Carlo stability of the estimators of the statistics of interest. Figure 4.5-4 presents the accumulated median of $\log_{10}$ travel time versus the number of realisations for each of the starting positions discussed above. The median $\log_{10}$ travel time for an individual starting position apparently requires more realisations to stabilise than the ensemble of starting positions, and may not have stabilised at all for position 32 (located within NNW-2). This suggests that evaluating the performance of individual positions may require more realisations than does the performance of the entire repository. Figure 4.5-5 presents the stream tubes for each of theses starting positions, showing that the exit locations can vary by as much as a kilometre.
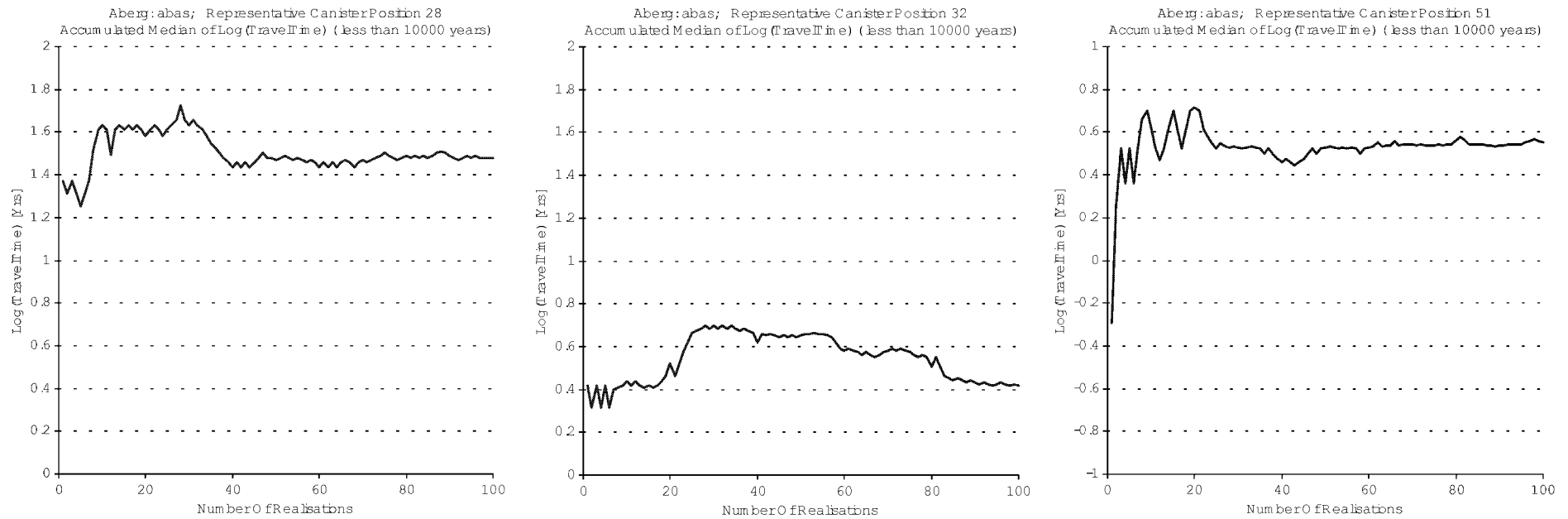
Figure 4.5-4. Monte Carlo stability at starting positions 28, 32 and 51 in the Aberg Base Case. Median log travel time versus number of realisations. Results for a flow porosity of $\varepsilon_f = 1x10^{-4}$.

a) Position 28

b) Position 32

c) Position 51

tw = Ground water travel time (years)

tw < 10
10 < tw < 100
100 < tw 1000
1000 < tw < 10000
tw > 10000

Approx. Scale

0   1000 m
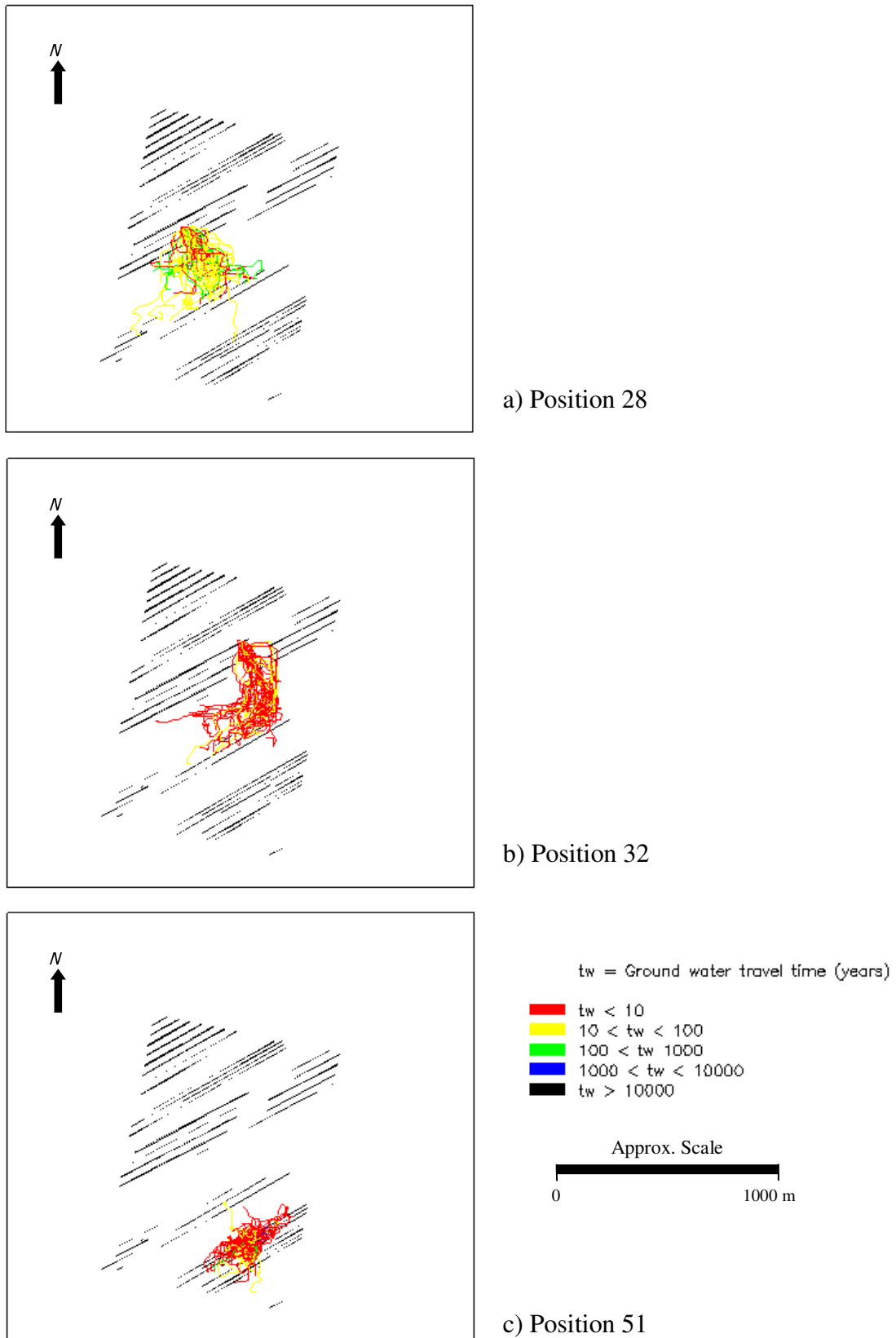
Figure 4.5-5. Stream tubes for Aberg Base Case, a) starting position 28, b) starting position 32, and c) starting position 51. Plan view with the y-positive axis pointing in the direction of Äspö local North. Results for a flow porosity of $\varepsilon_f = 1x10^{-4}$.

4.6 Repository Level

As discussed in Section 3.4, the Aberg repository design is divided into two levels of tunnels, an upper level at –500 masl and a lower level at –600 masl. This study represents the waste canisters by scattering 120 stream tube starting positions uniformly over both levels of the hypothetical repository. This section of the report examines the ensemble results of the Base Case to see if any differences can be observed in the performance of the repository by level.

Figures 4.6-1 and 4.6-2 present histograms for the Base Case, sorted by repository level, of the $\log_{10}$ travel time and $\log_{10}$ canister flux, respectively. The summary statistics for each level are presented in Table 4-5. Although the distributions of travel time and canister flux are very similar, the canister fluxes of the lower repository level are lower and the travel times are slightly greater than that of the upper level. The canister fluxes are lower because of the reduced hydraulic conductivity in the model domain below –600 masl (Section 3.5.3). The travel times of the lower level are longer as a consequence of both the reduced canister flux and the additional 100 m travel distance.
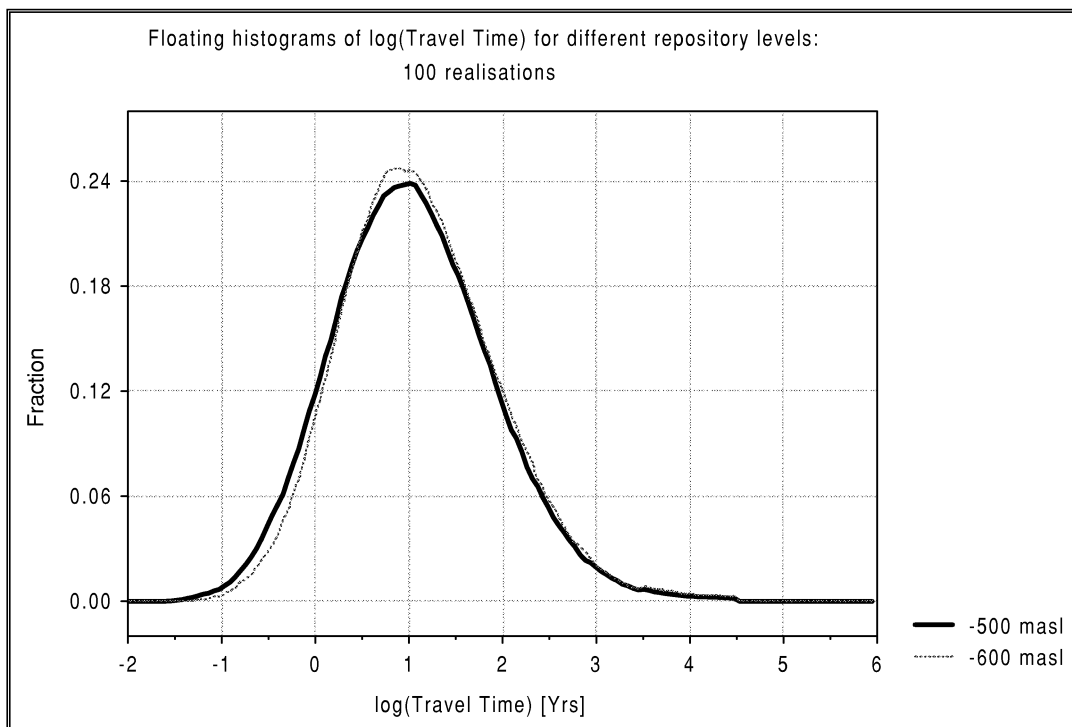
Figure 4.6-1. Floating histogram of $\log_{10}$ travel time by repository level for the Aberg Base Case. Results for 100 realisations of 120 starting positions and a flow porosity of $\varepsilon_f = 1x10^{-4}$.
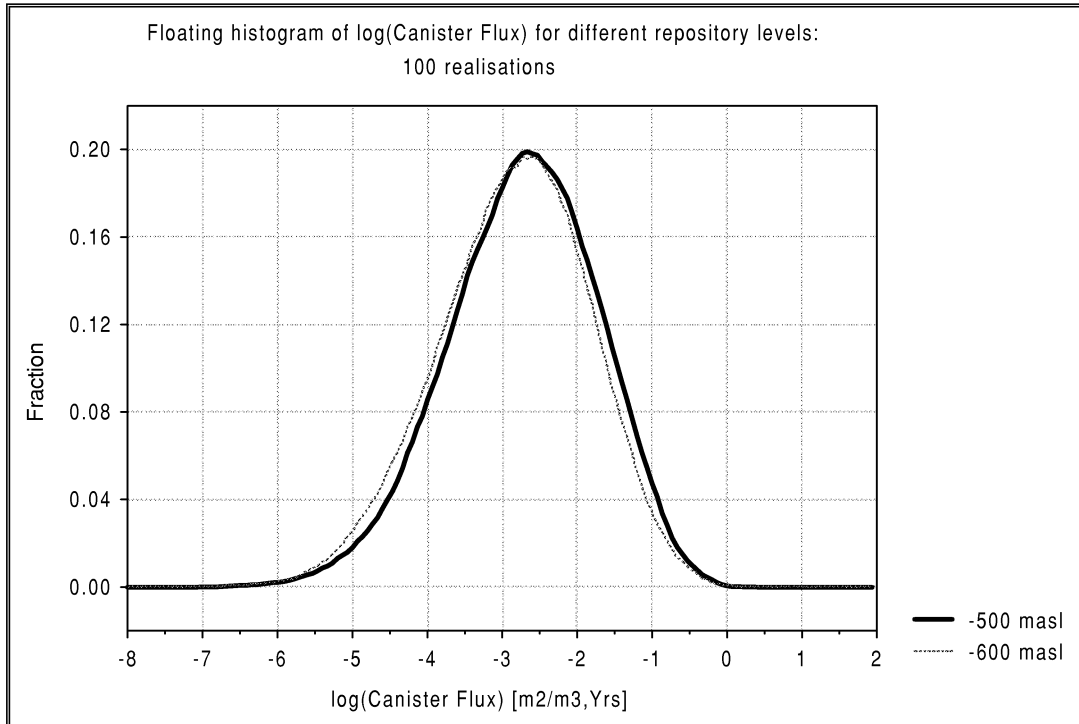
Figure 4.6-2. Floating histogram of log₁₀ canister flux by level for the Aberg Base Case.

Table 4-5. Summary statistics by repository level for the Aberg Base Case. Results for 100 realisations of 120 starting positions, a flow porosity of $\varepsilon_f = 1 \times 10^{-4}$ and flow-wetted surface $a_r = 1.0$ m^2/m^3. Statistics in bold are discussed in text.

	Repository Level	
Log$_{10}$ Travel Time for times < 10,000 years (years)	**-500 masl**	**-600 masl**
Mean	1.035	1.103
Median	**0.989**	**1.039**
Variance	**0.619**	**0.576**
5th percentile	-0.187	-0.051
25th percentile	0.489	0.569
75th percentile	1.536	1.592
95th percentile	2.383	2.451
Log$_{10}$ Canister Flux for all times (m/year)		
Mean	-2.736	-2.862
Median	**-2.676**	**-2.794**
Variance	**0.918**	**0.944**
5th percentile	-4.393	-4.568
25th percentile	-3.356	-3.494
75th percentile	-2.058	-2.174
95th percentile	-1.267	-1.357
Log$_{10}$ F-ratio for times < 10,000 years (year/m)		
Mean	5.035	5.103
Median	**4.989**	**5.039**
Variance	**0.619**	**0.576**
5th percentile	3.813	3.949
25th percentile	4.489	4.569
75th percentile	5.536	5.592
95th percentile	6.383	6.451

5   Variant Cases

Table 5-1 summarises the Base Case (the reference case for comparison) and the 5 variant cases evaluated for this study. Each variant corresponds to a possible interpretation of site hydrogeology, and is evaluated to address the acknowledged uncertainties. These are summarised as:

- Base Case (presented in Section 4.0, this represents the expected site conditions);

- Variant 1: Boundary condition variants;

- Variant 2: Upscaling of hydraulic conductivities;

- Variant 3: Anisotropic variogram of hydraulic conductivities;

- Variant 4: Conditional simulation of hydraulic conductivities; and

- Variant 5: Deterministic simulation.

The base case is discussed thoroughly in Section 4. The motivation and reasoning for each case is provided in the introduction of the sections corresponding to each case.

Table 5-1. Summary of Base Case and Variant Cases analysed in Aberg site-scale modelling study.

Case	Boundary conditions	Cell size	Hydraulic conductivity field				Conditioning on K	Remarks
	Obtained from		Scaling rule	Geostatistical model	Hydraulic units	EDZ/Backfill	on heads	
Base	TR 97-09, special case deliv_971129	25 m	Walker et al	Exponential isotropic Variance 2.7 Practical range 97 m	CD: SCD1 (Walker) RD: SRD1-5 (Walker)	No/10^{-10} m/s	No	BC for base case similar to SKB TR 97-09 (Appendix B)
Variant #1 Boundary Conditions 1.1; 1.2; 1.3; 1.4	TR 97-09 and some variants of the Base Case (5)	25 m						BC study for single realisation.
Variant #2 Upscaling		50 m		Variance=2.24				
Variant #3 Anisotropic variogram		25 m		Anisotropic variogram model (practical range ratio of) Variant 3.1=1:2:1 Variant 3.2=1:10:1	CD: Exclusion of NNW zones			Base Case BC
Variant #4 4.1 unconditional, 4.2 conditional		25 m		Variance = 3.14 Practical range = 122 m	No fracture zones included explicitly.			Pure stochastic continuum model. Geostatistical analysis using all data.
Variant #5 Deterministic		25 m	100 m Scale	Variance=0				Deterministic case

5.1   Boundary Conditions

As was noted in Section 3.0, this study uses a nested modelling approach, with a regional model providing the site-scale boundary conditions. The regional model of Svensson (1997a) originally included the salinity dependence in the simulations, but that regional model cannot be used directly to provide boundary heads to HYDRASTAR, which is unable to simulate salinity. Svensson (1997a) also used a single realisation of the hydraulic conductivity field as the reference (base) case. Although this results in flow fields that have an intuitively attractive heterogeneity, the boundary heads would change if a different realisation of hydraulic conductivities were used. For the purposes of this model, therefore, the regional model of Svensson (1997a) was rerun for the Base Case using a deterministic hydraulic conductivity field and freshwater conditions (Appendix B). However, there are several possible methods for calculating and transferring boundaries between the regional and site-scale models, including:

1.1 Use a regional model with a deterministic, effective hydraulic conductivity and freshwater conditions (i.e., a single realisation of the Base Case, as discussed in Section 4.1).

1.2 Use a regional model with a single stochastic realisation of hydraulic conductivity and the observed salinity. Convert the resulting boundary pressures and salinities to environmental freshwater heads.

1.3 Use a regional model with a single stochastic realisation of hydraulic conductivity and freshwater conditions.

1.4 Avoid the regional model entirely and use the observed watertable/sea level and hydrostatic conditions directly in the site scale model as simplified boundary conditions.

The purpose of these variants is to determine the sensitivity of the site-scale model results to other approaches to transferring boundary conditions. Each variant uses the same hydraulic conductivity realisation for the site-scale model, resetting the boundary heads as necessary. The effect of these boundary conditions are evaluated by comparing the travel time, canister flux and F-ratio.

5.1.1   Deterministic Regional Model, Freshwater

This variant case begins with a single realisation of the Base Case to be used for comparison to all the boundary condition variants. That is, the first realisation uses boundary conditions derived from the Svensson (1997a) regional model rerun with a deterministic hydraulic conductivity field. The effective hydraulic conductivity, K_e, is assigned to the regional-scale RD and CD as suggested in Walker et al. (1997b). Unlike the Svensson (1997a) model, this regional model uses freshwater conditions to calculate the boundary heads. The resulting hydraulic heads are transferred to the site-scale model via linear interpolation (Appendix B).

Figure 5.1-1 shows the exit locations for all starting positions in the single realisation of the site-scale model.
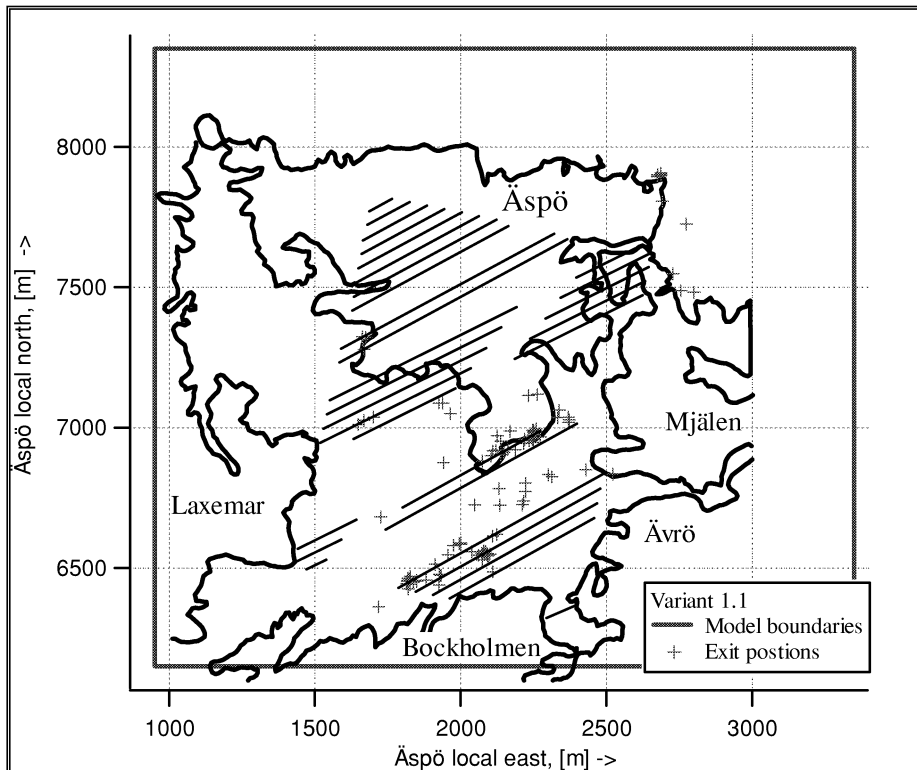
Figure 5.1-1. Exit locations for Aberg Variant 1.1 (deterministic, freshwater regional model). Results for a single realisation of the Base Case and 120 starting positions. (Äspö local coordinate system, scale in metres).

5.1.2   Stochastic Regional Model, Salinity Dependent

This case uses the Base Case of the Svensson (1997a) regional model to calculate the boundary heads for the site-scale model. That regional model used a single realisation of a stochastic hydraulic conductivity field under salinity dependent conditions to calculate the boundary heads. The resulting hydraulic heads transferred to the site-scale model as depth-integrated environmental heads and linear interpolation (Appendix B).

Figure 5.1-2 shows the exit locations for all starting positions in the single realisation of the site-scale model.
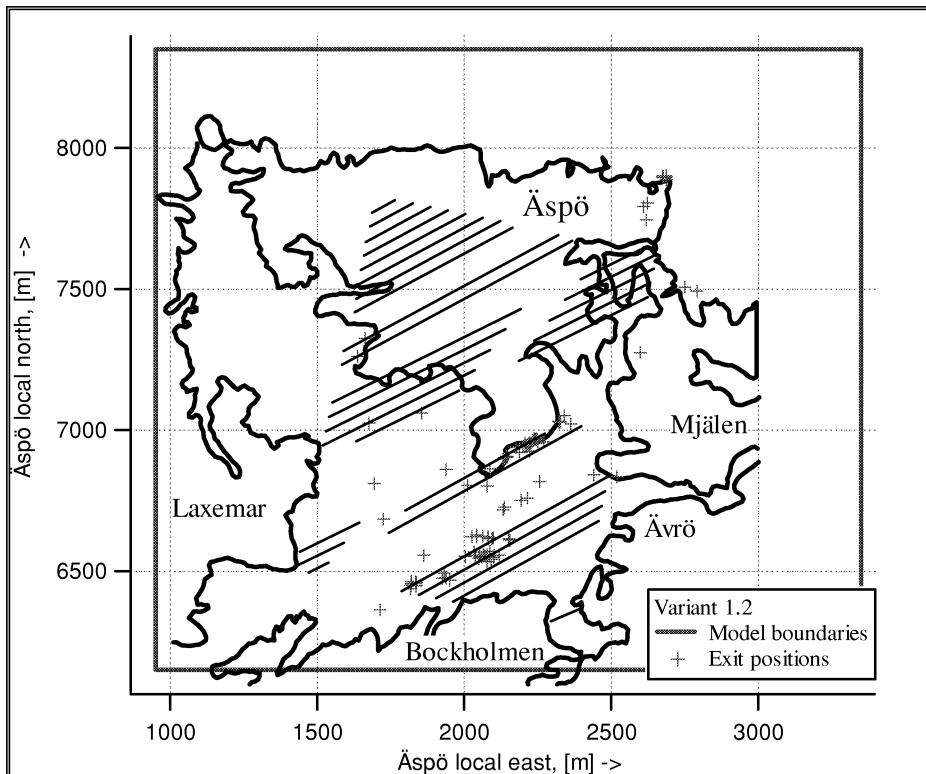
Figure 5.1-2. Exit locations for Aberg Variant 1.2 (stochastic, salinity dependent regional model). Results for a single realisation of the Base Case and 120 starting positions. (Äspö local coordinate system, scale in metres).

5.1.3 Stochastic Regional Model, Freshwater

This case uses the Svensson (1997a) regional model under freshwater conditions to calculate the boundary heads for the site-scale model. That regional model was a single realisation of a stochastic hydraulic conductivity field, similar to that the boundary conditions used by Widén and Walker (1998). The resulting hydraulic heads transferred to the site-scale model via linear interpolation (Appendix B).

Figure 5.1-3 shows the exit locations for all starting positions in the single realisation of the site-scale model.
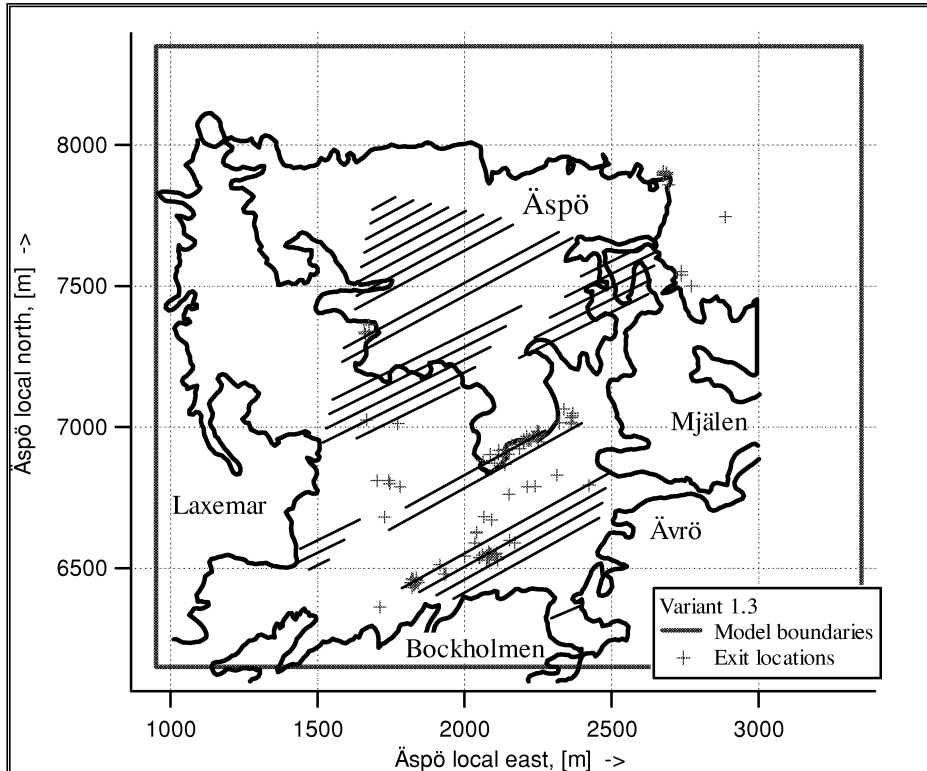
Figure 5.1-3. Exit locations for Aberg Variant 1.3 (stochastic, freshwater regional model). Results for a single realisation of the Base Case and 120 starting positions. (Äspö local coordinate system, scale in metres).

5.1.4 Simplified Boundaries

This variant examines the possibility of avoiding the nested modelling approach, and attempts to set boundary conditions using only the observed topography and simplified boundaries at depth. The upper constant head boundary is taken from the Äspö site digital terrain model and the empirical relationship of surface elevation to groundwater table elevation. Two variants are tested for the lateral and bottom boundary conditions, the first being to use no flow boundary conditions on the vertical and bottom sides, called variant 1.4b. Figure 5.1-4 presents the resulting exit locations for these boundary conditions for realisation number 1. In this case, the exit locations are widely dispersed over the model surface, and 5 of the stream tubes (4%) failed to exit the upper surface of the model.
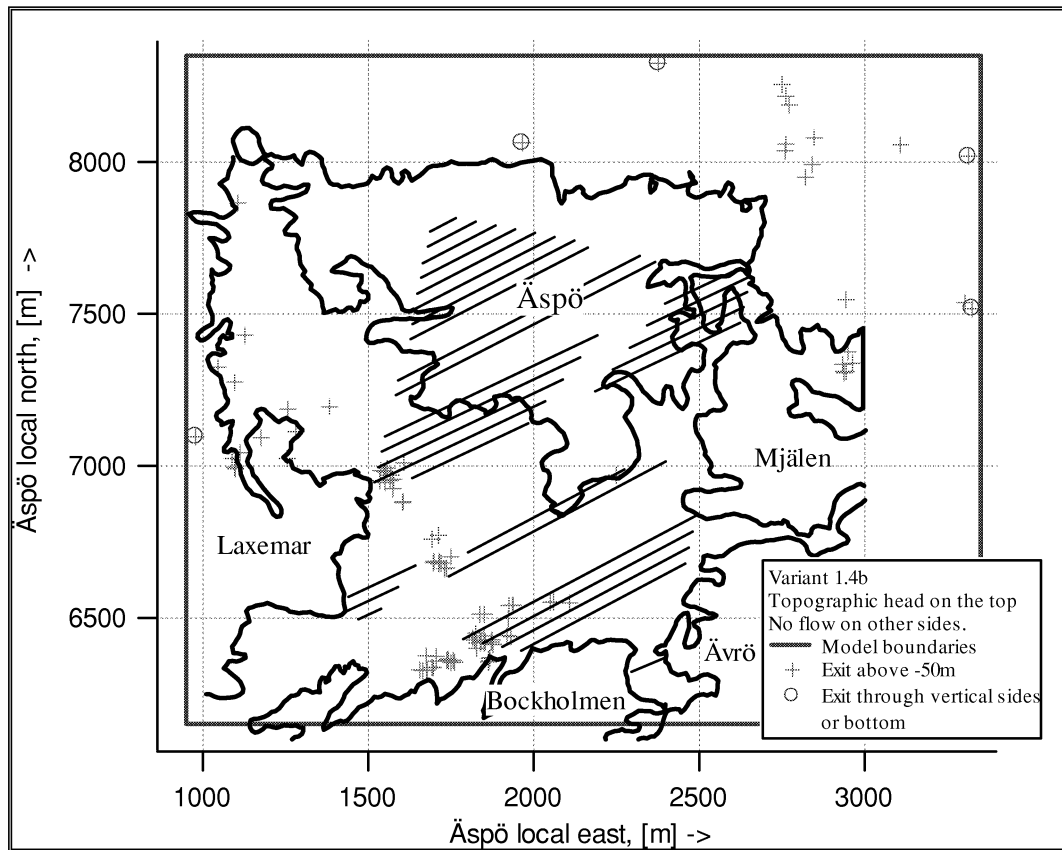
Figure 5.1-4. Exit locations for Aberg Variant 1.4b (simplified boundary conditions with no flow conditions on the vertical sides and bottom). Results for a single realisation of the Base Case and 120 starting positions. (Äspö local coordinate system, scale in metres).

Variant 1.4c attempts to set boundary conditions using the observed topography on the model's upper surface, hydrostatic head on the lateral surfaces, and no flow on the bottom surface. Figure 5.1-5 presents the resulting exit locations for these boundary conditions for realisation number 1. The exit locations are widely dispersed over the model surface, and 30 stream tubes (25%) failed to exit the upper surface of the model.
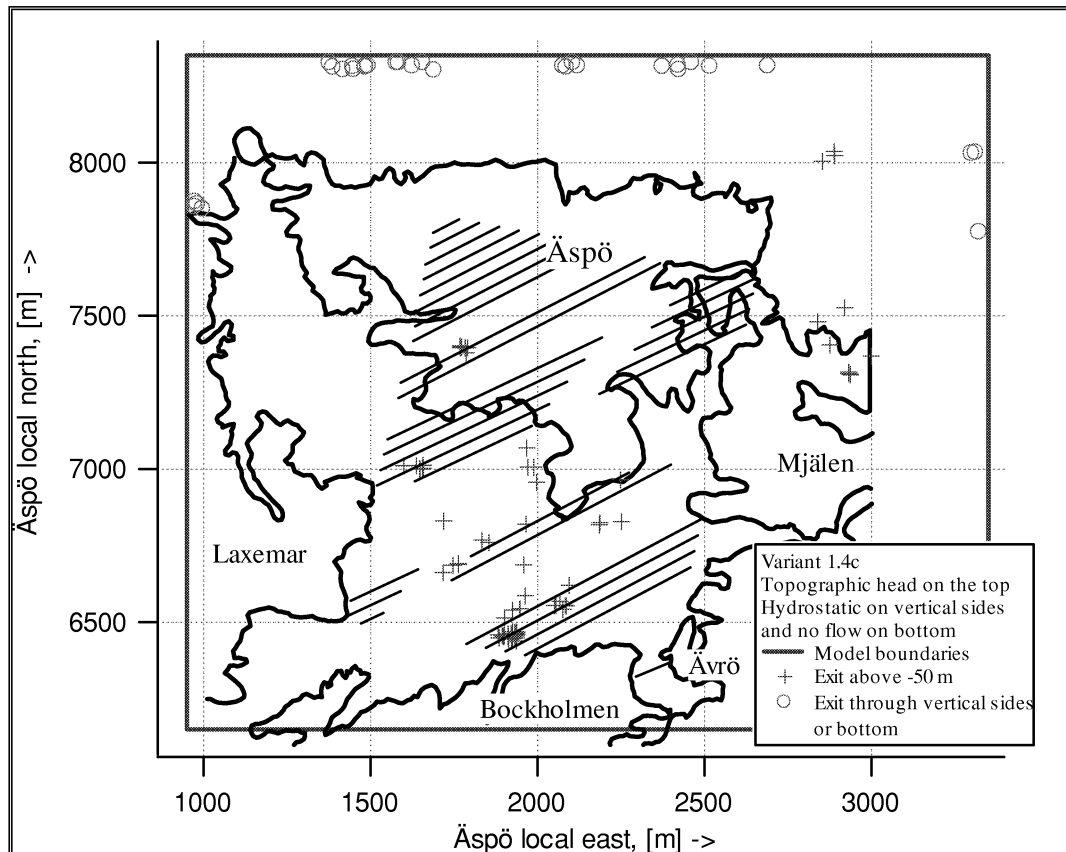
Figure 5.1-5. Exit locations for Aberg Variant 1.4c (simplified boundary conditions with hydrostatic head on the vertical sides and no flow conditions on bottom). Results for a single realisation of the Base Case and 120 starting positions. (Äspö local coordinate system, scale in metres).

5.1.5 Comparison

Figures 5.1-6 and 5.1-7 present the hydraulic head distributions on the southern surface of the model. The head distributions for variants 1.1, 1.2 and 1.3 are relatively similar, where variant 1.4c is strikingly different. These differences and similarities are reflected in the performance measure statistics for the 120 start positions for each method of assigning boundary conditions (Table 5.1-1). Comparing the results, note that all three variants for transferring heads from the regional model give rather similar results (i.e. variants 1.1, 1.2 and 1.3 have similar travel time, canister flux and F-ratios). Variant 1.4 (simplified boundary conditions based on topography) gives rather different results in comparison to the first variants. Likewise, Table 5.1-2 indicates that these similarities and differences are seen in the boundary fluxes as well. The comparative plots of $\log_{10}$ travel time and $\log_{10}$ canister flux histograms (Figures 5.1-8 and 5.1-9) show that both the travel times and canister fluxes are quite different for the simplified boundary conditions (variants 1.4b and 1.4c). This suggests that the regional flow pattern imparted by the nested modelling does have important effects.
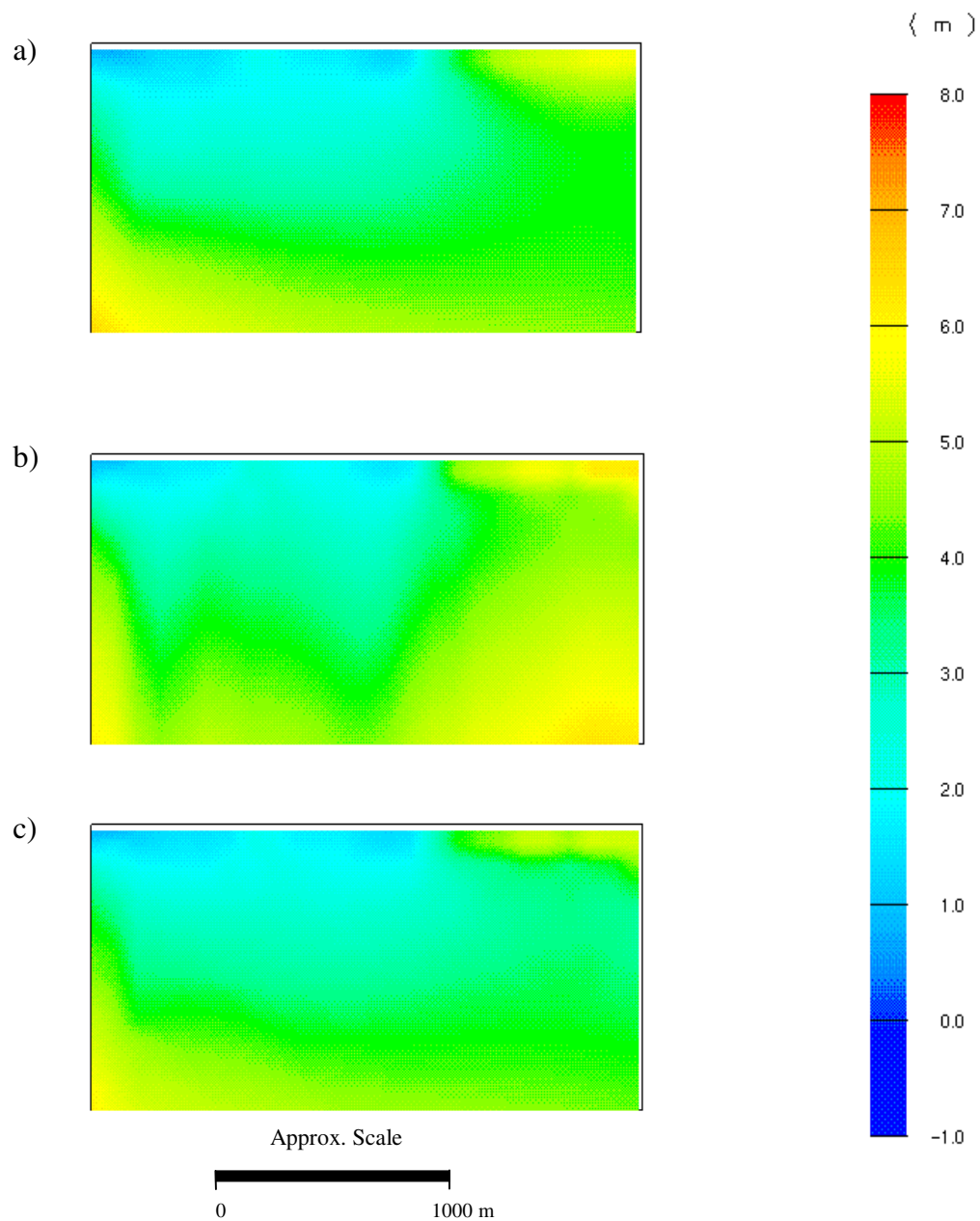
Figure 5.1-6. Head boundary conditions for Aberg Variant 1, on the southern model surface for a) Variant 1.1, b) Variant 1.2, and c) Variant1.3 (freshwater hydraulic head in metres).

This variant does have its limitations, however, since only constant head (Dirichlet) boundaries are investigated. A useful extension of this variant would be to investigate the effects of changing to constant flux (Neuman) or third-type boundaries. Unlike constant head boundaries, constant flux and third-type boundaries do not restrict the head variability on the boundaries and therefore would allow greater head variance in the domain. Such alternative boundary conditions are beyond the current capabilities of HYDRASTAR, however.
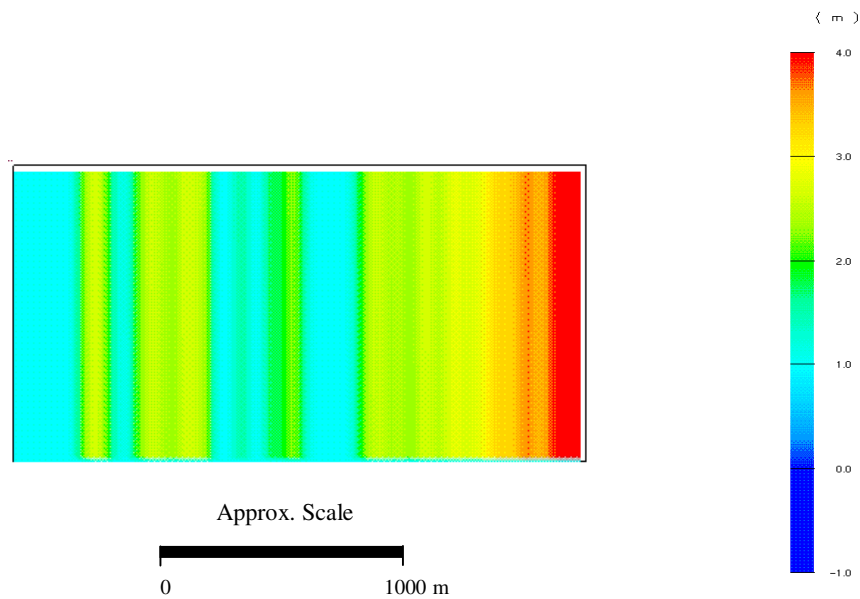
Figure 5.1-7. Head boundary conditions for Aberg Variant 1.4c, on the southern model surface. (Variant 1.4b used no flow condition on all vertical sides). (Freshwater hydraulic head in metres).

Table 5.1-1. Comparison of median performance measures within Aberg Variant 1. Results for a single realisation of 120 starting positions, a flow porosity of $\varepsilon_f = 1 \times 10^{-4}$ and flow-wetted surface $a_r = 1.0$ m^2/m^3.

	Median $\log_{10} t_w$ for times < 10,000 years (variance)	Median $\log_{10} q_c$ for all times (variance)	Median $\log_{10}$ F-ratio for times < 10,000 years (variance)	Percent of stream tubes failing to exit
Base Case	1.015 (0.599)	-2.736 (0.935)	5.015 (0.599)	0.5
Variant 1.1	0.875 (0.578)	-2.667 (0.735)	4.875 (0.578)	0
Variant 1.2	0.947 (0.513)	-2.667 (0.733)	4.947 (0.513)	0.9
Variant 1.3	0.912 (0.523)	-2.659 (0.747)	4.912 (0.523)	0
Variant 1.4b	1.951 (0.517)	-3.374 (0.872)	5.951 (0.517)	4.2
Variant 1.4c	1.485 (0.580)	-3.316 (0.8059	5.485 (0.580)	25

Table 5.1-2. Boundary flux comparison within Aberg Variant 1.

Model Surface	Net flux through subdomain (m^{-3}/s x 10^{-3})				
	Case 1.1	Case 1.2	Case 1.3	Case 1.4b	Case 1.4c
West	6.81 (in)	6.81 (in)	6.15 (in)	0	1.90 (in)
East	1.16 (in)	0.0703 (out)	0.453 (in)	0	0.152 (in)
South	0.349 (in)	0.190 (in)	0.564 (in)	0	0.738 (in)
North	0.363 (in)	0.474 (in)	0.372 (in)	0	0.141 (out)
Bottom	0.826 (in)	0.243 (in)	0.744 (in)	0	0
Top	9.50 (out)	7.65 (out)	8.32 (out)	$1.45 \cdot 10^{-5}$ (in)	2.650 (out)
Total inflow	9.508	7.7217	8.283	$1.45 \cdot 10^{-5}$	2.7890
Total outflow	9.500	7.7154	8.320	0	2.7907
Mass balance (In-Out)	0.008	0.0063	-0.037	$1.45 \cdot 10^{-5}$	-0.0017
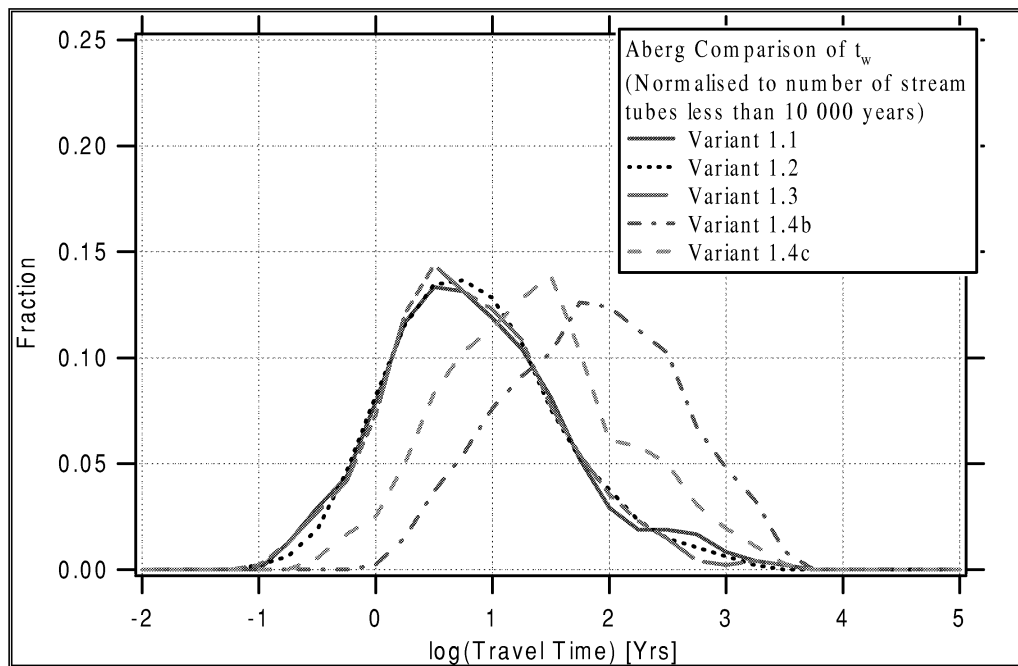
Figure 5.1-8. Floating histograms of log_{10} travel time for Aberg Variant 1, normalised to the number of stream tubes less than 10,000 years. Results for a single realisation of 120 starting positions and a flow porosity of $\varepsilon_f = 1x10^{-4}$.
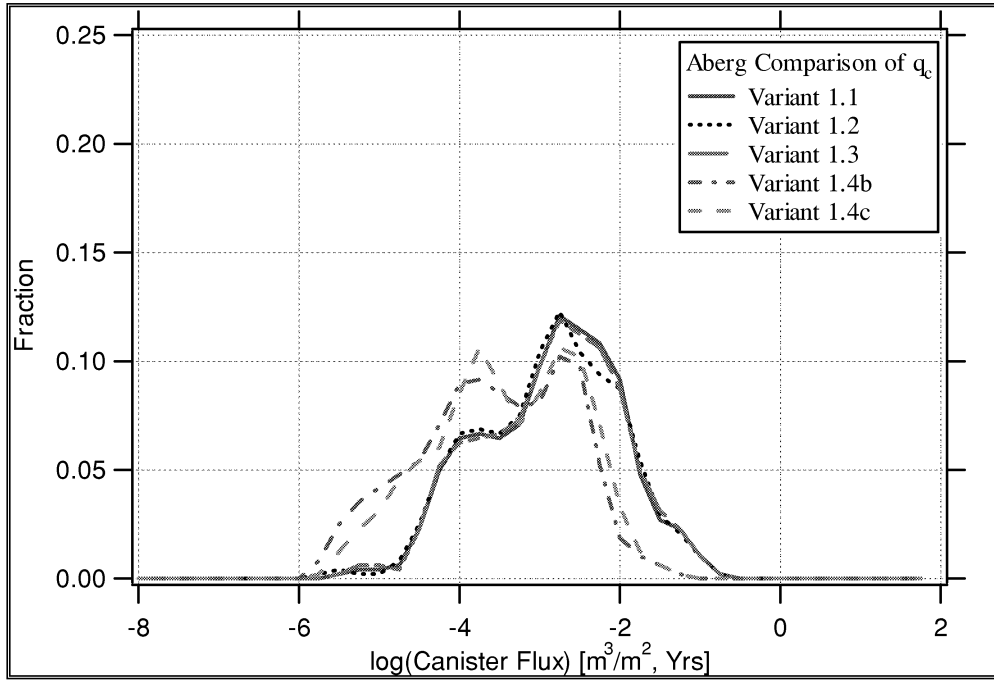
Figure 5.1-9. Floating histograms of log_{10} canister flux for Aberg Variant 1.

5.2 Upscaling

Hydraulic conductivity is thought to be scale dependent, but current research debates the correct method for scaling field measurements for use in continuum modelling. The Base Case uses the observed Äspö scale dependence to determine the geometric mean of hydraulic conductivity for the finite difference blocks, and the Moye's formula regularisation to determine the variogram. The resulting parameters are used to simulate hydraulic conductivity fields at the 25 m grid scale (Walker et al., 1997b). It is important to evaluate the uncertainty of this upscaling method on the model results.

This variant examines the affect of changing the model calculation scale to a 50 m regular grid with commensurate rescaling of the parameters for simulating the hydraulic conductivity field. Appendix C.2.2 summarises the geostatistical inference of a 50 m scale model for hydraulic conductivity. The SKB code INFERENS was used to infer a regularised variogram model for the 50 m scale, based on the 3 m packer tests in the rock mass domain. Results of this analysis indicated the following variogram model for the 50 m grid scale (Figure 5.2-1):

- Exponential model, isotropic,

- Practical range of 111 m, and

- Zero nugget, $\log_{10}$ K variance 2.24.

The SRD and SCD are treated as step changes in the geometric mean of block conductivities (0 order trends in K_b), with values provided in Table 5.2-1.
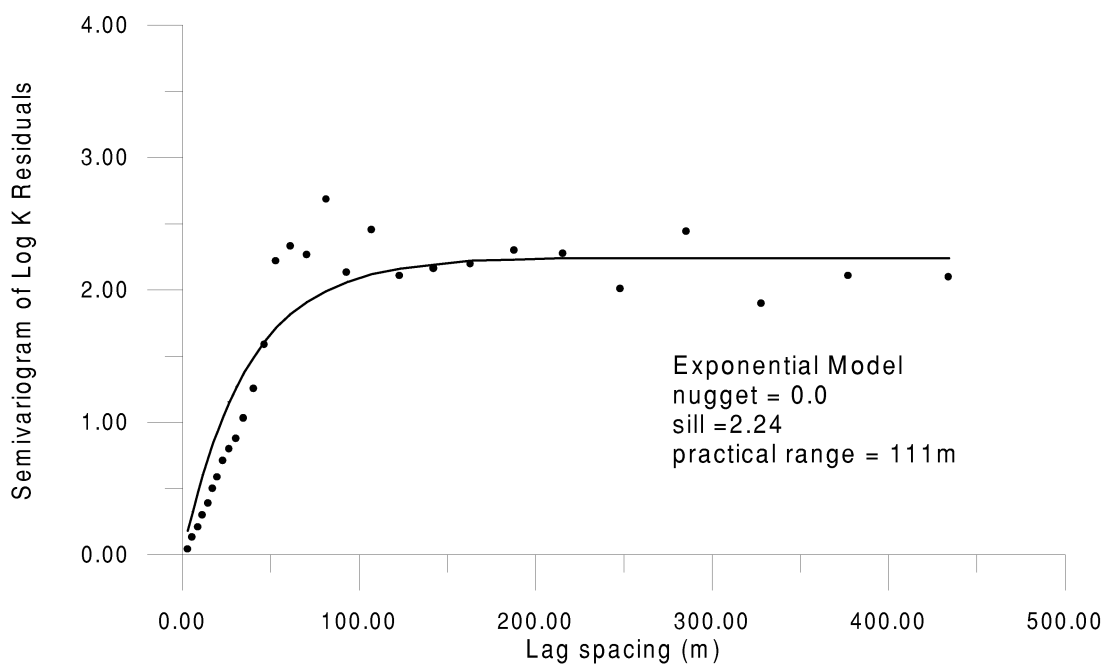
Figure 5.2-1. Semivariogram of Aberg $\log_{10}$ hydraulic conductivity for rock domain. 3 m data in rock domain, regularised to 50 m and fitted via INFERENS.

Table 5.2-1. **Upscaled Parameters for Base Case, Variant 2 and Variant 5.**
Measured parameters shown for comparison. Below z = -600 masl, the
hydraulic conductivities change by a factor of 1/10.

Parameter	Measured	Base Case 25 m Scale	Variant 2 50 m Scale	Variant 5 Deterministic
Variogram model				
Total variance	2.84	2.72	2.24	0
Practical range	112	97	111	-
Mean Log$_{10}$K				
SRD 1	-8.7	-8.0	-7.8	-7.6
SRD 2	-7.8	-7.1	-6.9	-6.6
SRD 3	-9.5	-8.8	-8.5	-8.3
SRD 4	-7.6*	-7.5	-7.3	-7.1
SRD 5	-8.3	-7.6	-7.4	-7.1
other	-9.3	-8.5	-8.3	-8.1
EW-1N	-7.3	-7.8	-7.5	-7.3
EW-1S	-6.1	-6.6	-6.4	-6.1
EW-3	-5.8	-6.3	-6.0	-5.8
EW-7	-5.2	-5.7	-5.4	-5.2
NE-1	-5.0	-5.5	-5.2	-5.0
NE-2	-7.1	-7.6	-7.3	-7.1
NE-3	-5.2	-5.7	-5.5	-5.2
NE-4	-6.1	-6.6	-6.4	-6.1
NNW-1	-6.3	-6.7	-6.5	-6.3
NNW-2	-5.6	-6.0	-5.8	-5.6
NNW-4	-4.8	-5.3	-5.1	-4.8
NNW-5	-7.0	-7.5	-7.2	-7.0
NNW-7	-6.6	-7.1	-6.9	-6.6
NNW-8	-6.3	-6.8	-6.5	-6.3
NW-1	-7.8	-8.3	-8.0	-7.8

* Inferred from calibration at 20 m scale, Svensson (1997a).

Tables 5.2-2 and 5.2-3 summarise the consequences of changing the grid resolution and rescaling the conductivities. In comparison to the Base Case, the median travel time is reduced from 10 to 5.8 years and the median canister flux is increased from 1.9×10^{-3} to 4.0×10^{-3} m/yr. The variances of both of these performance measures are reduced by approximately 30% (Table 5.2-4). The distributions of both travel time and canister flux for this variant are significantly different from the comparable distributions of the Base Case (Appendix A.2). The boundary fluxes are slightly increased with respect to the Base Case, but five realisations may be insufficient for the mean fluxes to have stabilised.

Table 5.2-2. Summary statistics for Aberg Variant 2. Results for 100 realisations of 120 starting positions, a flow porosity of $\varepsilon_f = 1 \times 10^{-4}$ and flow-wetted surface $a_r = 1 \times 10^{-4}$ and flow-wetted surface $a_r = 1.0$ m^2/m^3. Statistics in bold are discussed in text.

| | All Values | | | Travel Times>10,000 years deleted | | |
	$\text{Log}_{10}\, t_w$	$\text{Log}_{10}\, q_c$	Log_{10}F-ratio	$\text{Log}_{10} t_w$	$\text{Log}_{10} q_c$	Log_{10} F-ratio
Mean	0.825	-2.449	4.825	0.814	-2.448	4.814
Median	0.770	**-2.400**	4.770	**0.766**	-2.398	**4.766**
Variance	0.456	**0.560**	0.456	**0.426**	0.559	**0.426**
5th percentile	-0.187	-3.767	3.813	-0.187	-3.766	3.813
25th percentile	0.354	-2.933	4.354	0.352	-2.931	4.352
75th percentile	1.247	-1.912	5.247	1.242	-1.912	5.242
95th percentile	1.964	-1.311	5.964	1.940	-1.310	5.940

Table 5.2-3. Boundary flux consistency for Aberg Base Case, Variant 2 and regional models.

Net Flux Through Site Model Surfaces (m^3/s x 10^{-3})			
Model Surface	Regional	Base Case 25 m Scale	Variant 2 50 m Scale
West	13.7 (in)	4.92 (in)	6.66 (in)
East	0.916 (in)	0.77 (in)	0.730 (in)
South	1.81 (in)	0.846 (in)	0.489 (out)
North	0.625 (in)	0.538 (in)	0.340 (in)
Bottom	0.374 (in)	1.03 (in)	1.11 (in)
Top	18.1 (out)	8.11 (out)	8.34 (out)
Total Inflow	17.425	8.1137	8.834
Total Outflow	18.1	8.11	8.825
Mass balance (In – Out)	-0.675	-0.0037	0.009

Table 5.2-4. Comparison of median performance measures of Aberg Variant 2 and Base Case. Results for 100 realisations of 120 starting positions, a flow porosity of $\varepsilon_f = 1 \times 10^{-4}$ and flow-wetted surface $a_r = 1.0$ m^2/m^3.

	Median $\log_{10} t_w$ for times < 10,000 years (variance)	Median $\log_{10} q_c$ for all times (variance)	Median $\log_{10}$ F-ratio for times < 10,000 years (variance)
Base Case	1.015 (0.599)	-2.736 (0.935)	5.015 (0.599)
Variant 2	0.766 (0.426)	-2.400 (0.560)	4.766 (0.426)

While the relative agreement of the boundary fluxes from the 25 to 50 m scales suggests that the upscaling method is adequate, the disagreement of the median travel times and canister fluxes suggests that the method is not effective. Indelman and Dagan (1993) suggested that upscaling should be tied to the grid shape, size and density with respect the integral scale of correlation. McKenna and Rautman (1996) studied various upscaling algorithms and confirmed that the behaviour of upscaling approaches could be quite complex, depending on the grid density relative to the integral scale of correlation. Given differences between the site-scale boundary fluxes, it is unsurprising that the median travel times also differ for the 25 and 50 m scales. The increase in boundary flux and decrease in travel time suggest that the upscaling algorithm may excessively increase the effective conductivity of the domain.

The reduced variance of both the travel times and canister fluxes is appropriate, given the reduced input variance for the $\log_{10}$ hydraulic conductivities. Figure 5.2-2 presents the exit locations for this variant, whose general pattern is very similar to that of the Base Case. The locations appear to be slightly more dispersed than in the Base Case, which is attributed to the coarser grid of this variant.
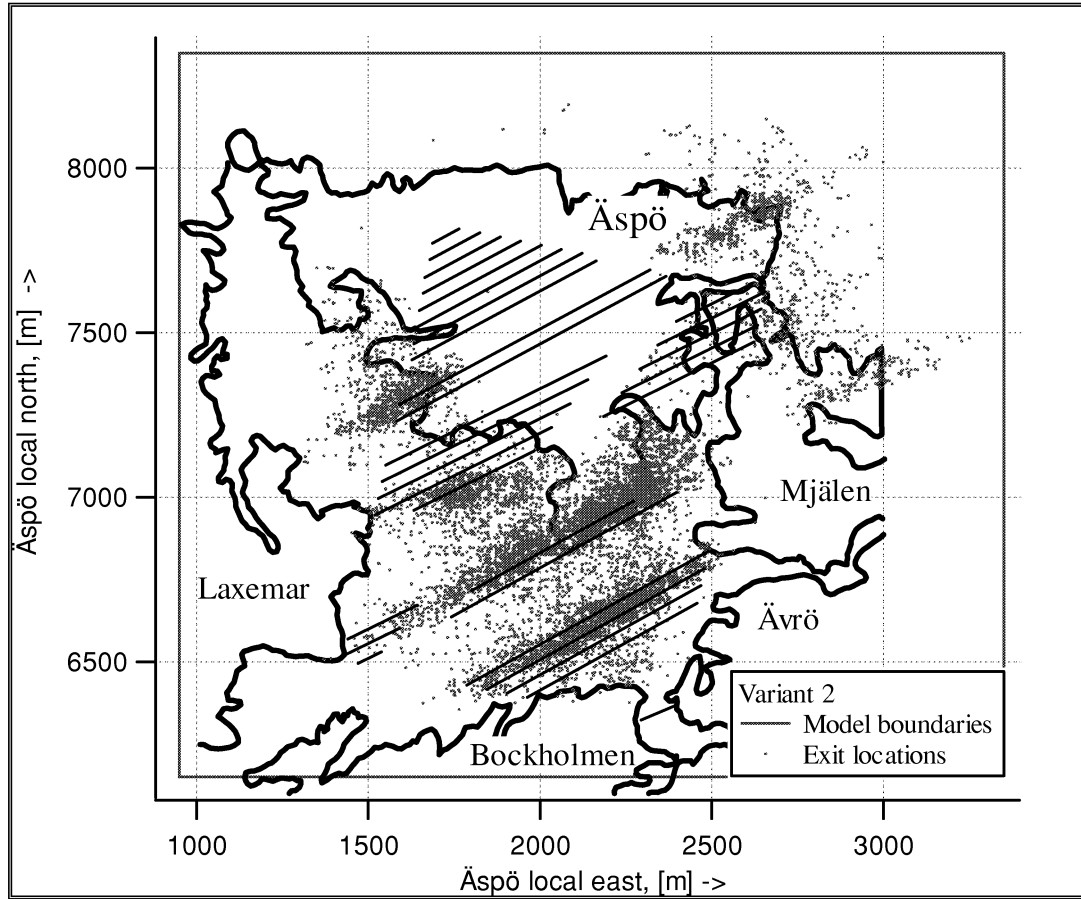
Figure 5.2-2. Exit locations for Aberg Variant 2 (upscaling to 50 m). Results for 100 realisations of 120 starting positions. (Äspö local coordinate system, scale in metres).

5.3 Anisotropic Variogram

Site investigations at Äspö and at various other locations in Sweden suggest that the host rocks may exhibit hydraulic anisotropy, with a preferred direction aligned with the principal axes of rock stress (Ericsson and Ronge, 1986; Rhén et al., 1997). Although the current version of HYDRASTAR (1.7.2) does not allow for block-scale anisotropy, the hydraulic anisotropic of a stochastic continuum model is related to the scale dependence of hydraulic conductivity. For example, Gutjahr, et al. (1978) found that a large-scale anisotropic hydraulic conductivity evolves from isotropic (scalar) point values of hydraulic conductivities with an anisotropic spatial variogram. That is, the anisotropic variogram of isotropic point hydraulic conductivities creates a large-scale anisotropic effective hydraulic conductivity. The problem of anisotropy is also tied to the complex problem of upscaling and the determination of block conductivities (Renard and de Marsily, 1997).

This variant uses stochastic anisotropy to examine the effects of hydraulic anisotropy on the model predictions. Bergman and Walker (1998) briefly examined this approach via numerical experiments using HYDRASTAR. They found that the analytical solutions of Gelhar and Axness (1983) could estimate the stochastic anisotropy ratio needed to produce a desired anisotropic effective hydraulic conductivity for low variances (less than $\sigma^2_{\log K} = 0.19$). For higher variances, Bergman and Walker (1998) found that the analytical solutions might not be useful in estimating the necessary stochastic anisotropy ratio. They found that increasing the variance would allow using a relatively low stochastic anisotropy ratio to produce much larger effective anisotropy ratios. Bergman and Walker (1998) also suggested that typical HYDRASTAR model grids used in SR 97 might not be sufficiently dense with respect to the integral scale to produce the desired anisotropic effective conductivity.

Applying the analytical solutions of Gelhar and Axness (1983) to field data, Neuman and Depner (1988) determined a stochastically anisotropic variogram model for a given anisotropic effective hydraulic conductivity. Appendix C.1 summarises the application of the Neuman and Depner (1988) approach to the Äspö data and the large-scale anisotropy suggested for Äspö by Rhén, et al. (1997). The Neuman and Depner approach indicated the anisotropy ratio of 1.5:2:1 in the Vertical:NW:NE directions. However, the relative coarseness of the model grid would not be able to adequately produce the indicated shortened range in the NE, forcing this study to simplify this ratio to 1:2:1. If the vertical range is preserved, the practical ranges of correlation are Vertical:NW:NE = 97 m:194 m:97 m. This simplified stochastic anisotropy should be expected to produce fields with a one-dimensional anisotropy, with a major axis toward the NW. Variant 3.1 evaluates this 1:2:1 ratio with 50 realisations, and Variant 3.2 examines the uncertainty of this approach by repeating the simulations with a ratio of 1:10:1.

Figure 5.3-1 presents the conductivity field at the upper repository level for Variant 3.1, which uses a variogram anisotropy of 1:2:1. The overall effect is to create rough ellipsoids of conductivity, with the long axes parallel to the major axis of anisotropy

(northwest-southeast; see Figure 5.3-1a). A vertical cross-section through the field (Figure 5.3-1b) reveals that there is no comparable continuity in the vertical direction, as might be expected with subvertical fracturing. This confirms that the simplified anisotropy ratio creates a one-dimensional anisotropy, whose effects are discussed further below.
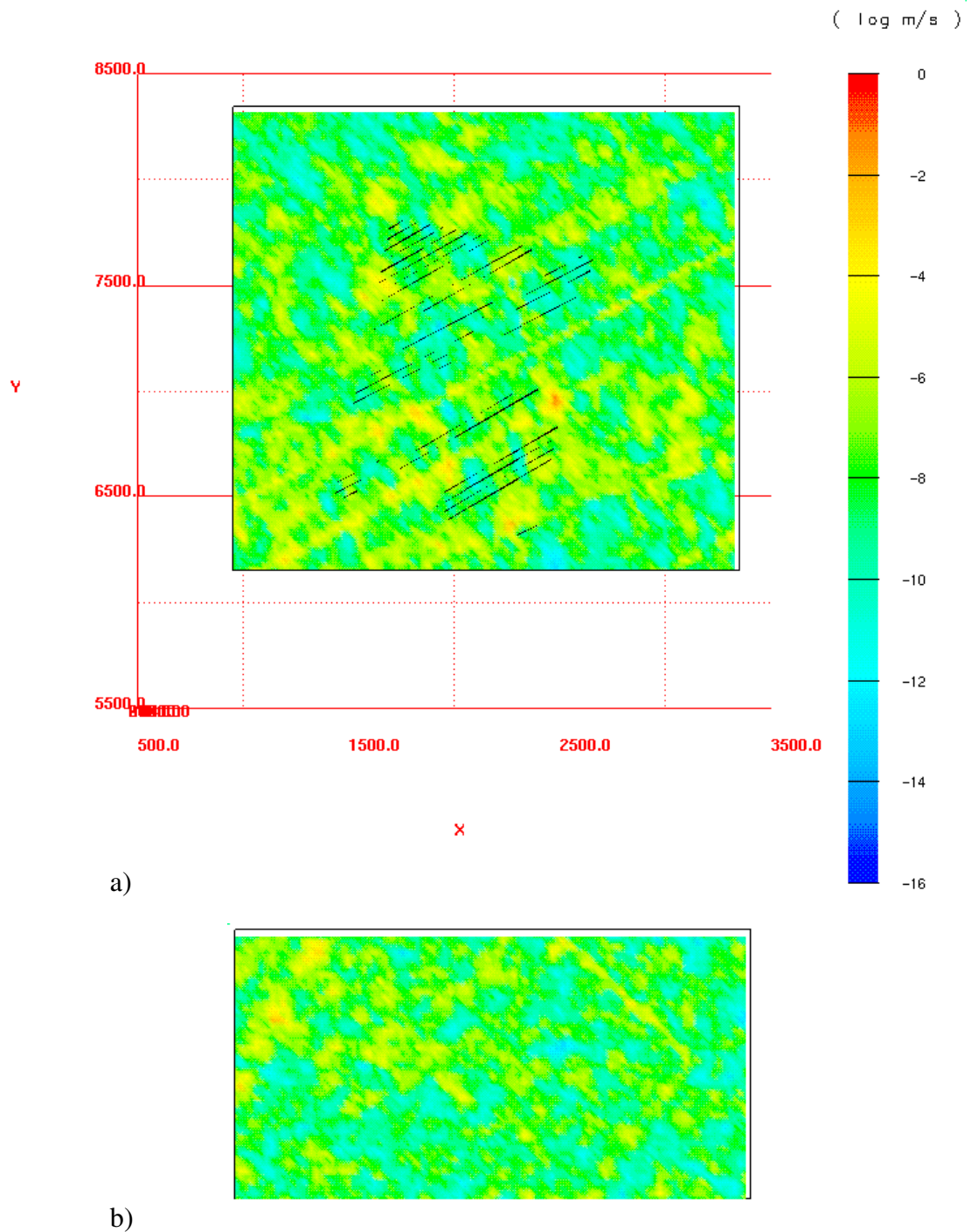
a)

b)

Figure 5.3-1. Log$_{10}$ hydraulic conductivity for one realisation of Aberg Variant 3.1 (anisotropic variogram), on a) upper model surface and b) on southern model surface. (Äspö local coordinate system, scale in metres).

Although the exit locations (Figure 5.3-2) are similar to those of the Base Case, Figure 5.3-3 shows that the flow pattern is changed, with stream tubes reorganised parallel to the major axis of anisotropy. Table 5.3-1 indicates that, in comparison to the Base Case, the median travel time is only slightly increased from 10 to 12 years and the median canister flux is only slightly decreased from 1.9×10^{-3} to 1.6×10^{-3} m/yr. The shapes of both the travel time and canister flux distributions for this variant are significantly different from those of the Base Case (Appendix A.2). Although the change in flow pattern is consistent with the findings of Svensson (1997a), the similarity of median travel times between this variant and the Base Case is not consistent with Svensson (1997a). Possible causes for this inconsistency are discussed below.

Table 5.3-1. Summary statistics for Aberg Variant 3.1. Results for 50 realisations of 120 starting positions, a flow porosity of $\varepsilon_f = 1 \times 10^{-4}$ and flow-wetted surface $a_r = 1.0$ m^2/m^3. Statistics in bold are discussed in text.

	All values			Travel Times > 10,000 years deleted		
	Log_{10} t_w	Log_{10} q_c	Log_{10} F-ratio	Log_{10} t_w	Log_{10} q_c	Log_{10} F-ratio
Mean	1.156	-2.859	5.156	1.140	-2.855	5.140
Median	1.099	**-2.803**	5.099	**1.091**	-2.801	**5.091**
Variance	0.720	**1.034**	0.720	**0.677**	1.023	**0.677**
5th percentile	-0.161	-4.635	3.839	-0.161	-4.623	3.839
25th percentile	0.568	-3.524	4.568	0.565	-3.518	4.565
75th percentile	1.694	-2.129	5.694	1.681	-2.129	5.681
95th percentile	2.638	-1.309	6.638	2.581	-1.310	6.581
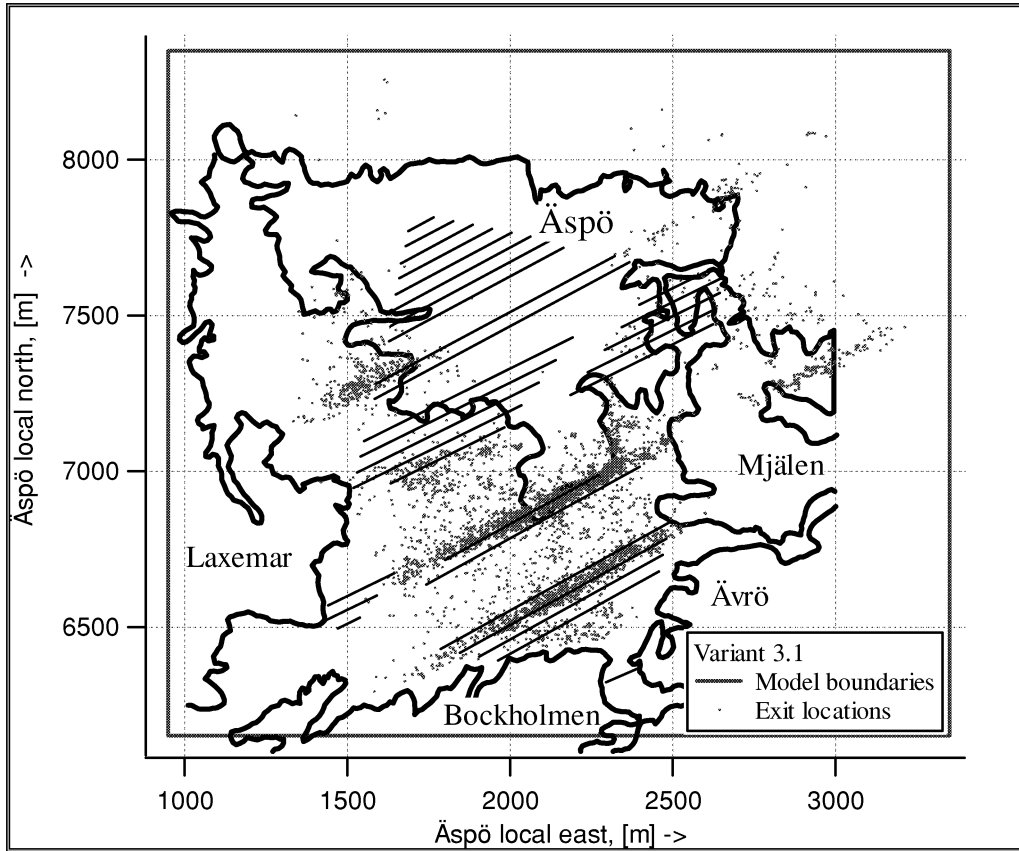
Figure 5.3-2. Exit locations for Aberg Variant 3.1 (anisotropic variogram). Results for 50 realisations of 120 starting positions. (Äspö local coordinate system, scale in metres).

a) Plan view

b) Elevation view, from South

c) Elevation view, from East

tw = Ground water travel time (years)

tw < 10
10 < tw < 100
100 < tw 1000
1000 < tw < 10000
tw > 10000

Approx. Scale

0   1000 m
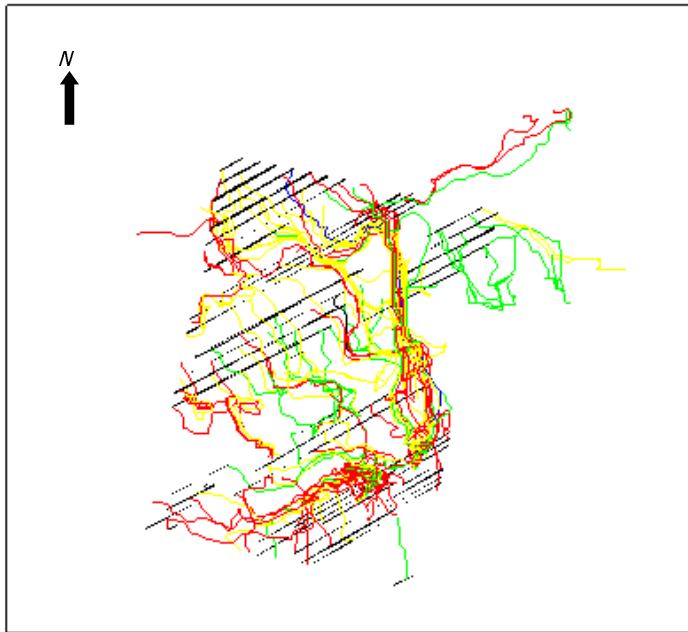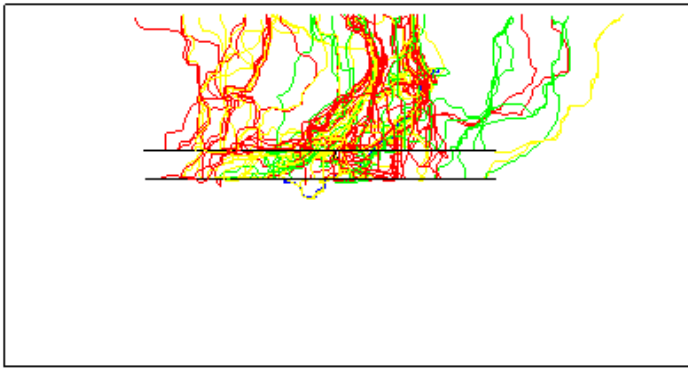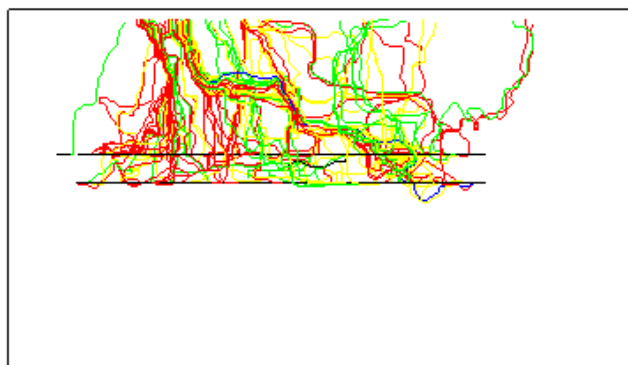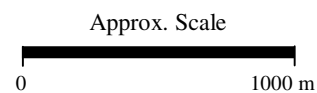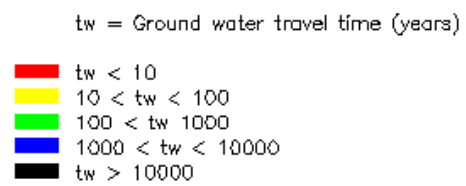
Figure 5.3-3. Stream tubes for realisation number 1 of Aberg Variant 3.1 (anisotropic variogram). The y-positive axis of a) points in the direction of Äspö local North. Results for 120 starting positions and a flow porosity of $\varepsilon_f = 1x10^{-4}$.

Figure 5.3-4 presents the $\log_{10}$ hydraulic conductivity field for Variant 3.2, with a variogram anisotropy of 1:10:1. Relative to the $\log_{10}$ hydraulic conductivity field of Variant 3.1, the ellipsoidal features are more prominent and much longer, but likewise show little vertical continuity. Figure 5.3-5 shows that the exit locations are shifted to the southeast, and the stream tubes of Figure 5.3-6 are now strongly oriented along the northwest-southeast axis.

Table 5.3-2 indicates that, in comparison to the Base Case, the median travel time is slightly increased from 10 to 11 years and the median canister flux is slightly decreased from 1.9×10^{-3} to 1.8×10^{-3} m/yr. The variances of both of these performance measures are reduced by 30% relative to the Base Case, and the shape of the distributions for this variant is significantly different from those of the Base Case (Appendix A.2).

Table 5.3-3 summarises the results of the two anisotropy ratios considered in this variant and compares them to the Base Case. The median travel times and median canister fluxes are nearly the same for both anisotropy ratios and also very similar to the median travel time and median canister flux of the Base Case. As noted above, the similarity of these isotropic and anisotropic cases is not consistent with the findings of Svensson (1997a), which suggested that travel times would be strongly affected by anisotropy. This inconsistency can be partly attributed to the use of a simplified stochastic anisotropy ratio in these variants, which creates fields with a single direction of continuity (northwest-southeast). As discussed above and in Appendix C.3, this simplification is forced by the coarseness of the model grid, resulting in fields that have an effective conductivity that is anisotropic in one-dimension with the major axis perpendicular to the upward gradient. Such an approach is very different from the 3-dimensional block-scale hydraulic anisotropy used by Svensson (1997a), whose increased vertical conductivity is aligned with the upward gradient.

For both anisotropy ratios considered in this variant the only apparent difference relative to the Base Case is an increase in the variance of the performance measures and a reorganisation of the stream tubes. This is attributed to the interception of stream tubes by the large scale structures represented by the ellipsoids of hydraulic conductivity.
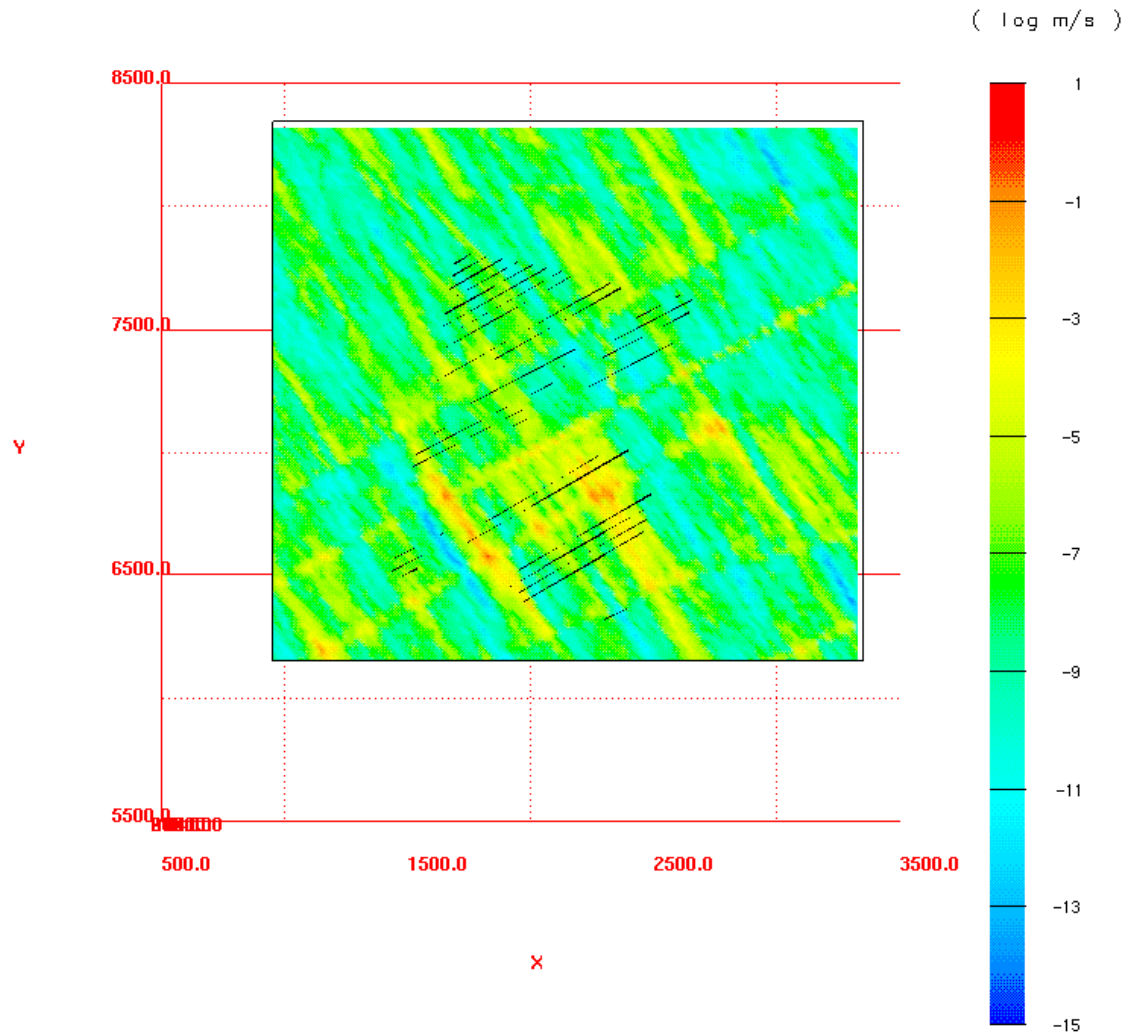
a)
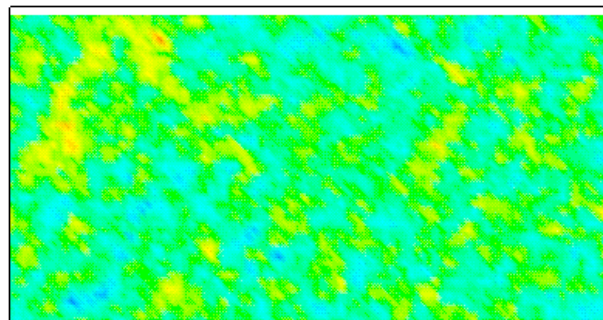
b)

Figure 5.3-4. Log$_{10}$ hydraulic conductivity for one realisation of Aberg Variant 3.2 (anisotropic variogram), on a) upper model surface and b) on southern model surface. (Äspö local coordinate system, scale in metres).

Table 5.3-2. **Summary statistics for Aberg Variant 3.2. Results for 50 realisations of 120 starting positions, a flow porosity of $\varepsilon_f = 1x10^{-4}$ and flow-wetted surface $a_r = 1.0$ m^2/m^3. Statistics in bold are discussed in text.**

| | All values | | | Travel Times > 10,000 years deleted | | |
	Log_{10} t_w	Log_{10} q_c	Log_{10} F-ratio	Log_{10} t_w	Log_{10} q_c	Log_{10}F-ratio
Mean	1.111	-2.770	5.111	1.086	-2.768	5.086
Median	1.043	**-2.733**	5.043	**1.032**	-2.737	**5.032**
Variance	0.794	**1.171**	0.794	**0.728**	1.153	**0.728**
5th percentile	-0.229	-4.604	3.771	-0.234	-4.588	3.766
25th percentile	0.496	-3.484	4.496	0.490	-3.483	4.490
75th percentile	1.656	-2.016	5.656	1.635	-2.020	5.635
95th percentile	2.667	-1.072	6.667	2.582	-1.070	6.582
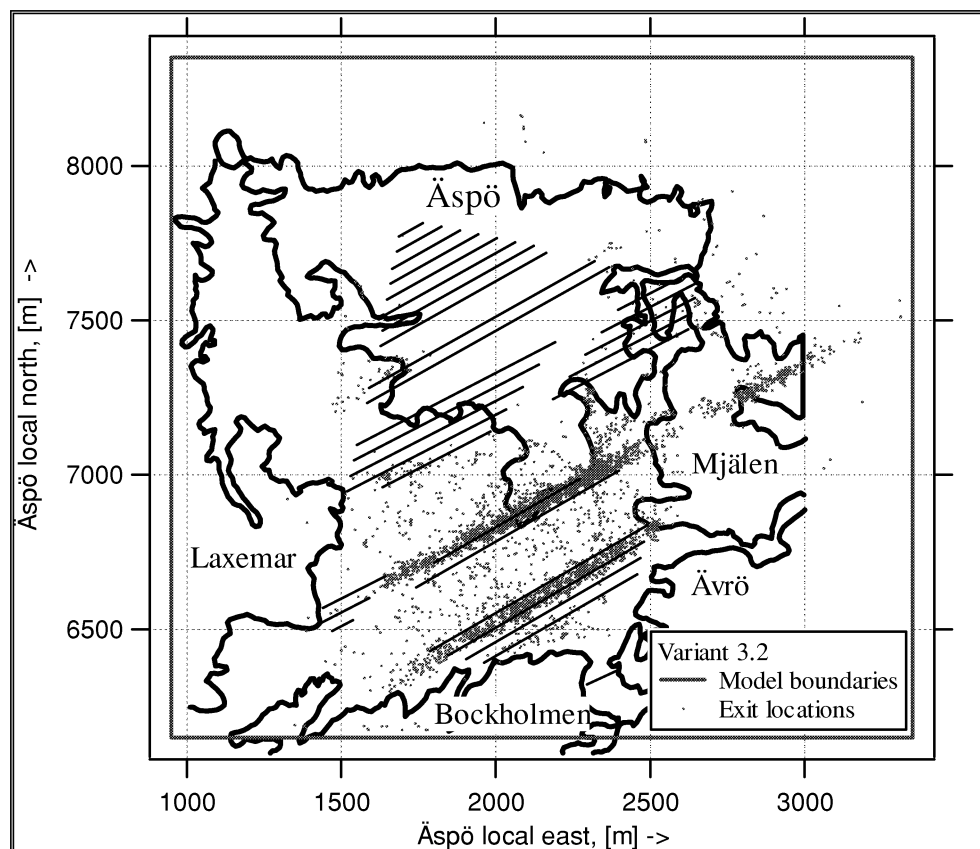
Figure 5.3-5. Exit locations for Aberg Variant 3.2 (anisotropic variogram). Results for 50 realisations of 120 starting positions. (Äspö local coordinate system, scale in metres).

a) Plan view

b) Elevation view, from South

c) Elevation view, from East

tw = Ground water travel time (years)

tw < 10
10 < tw < 100
100 < tw 1000
1000 < tw < 10000
tw > 10000

Approx. Scale

0   1000 m
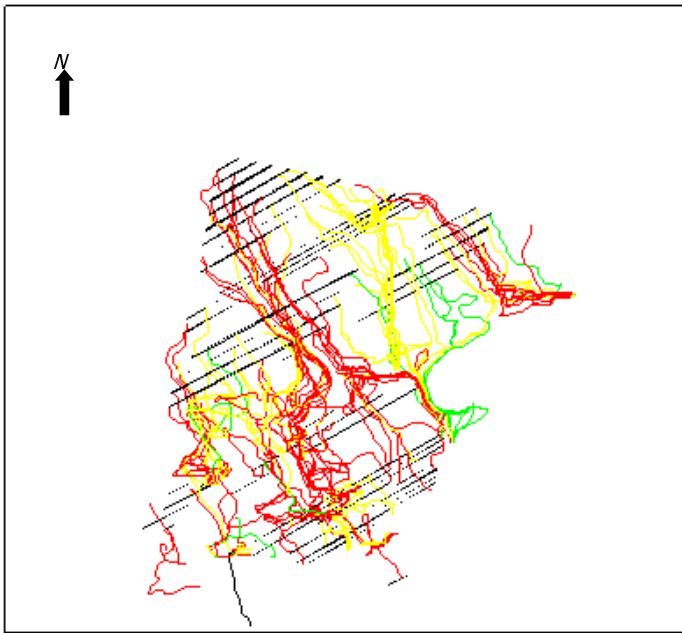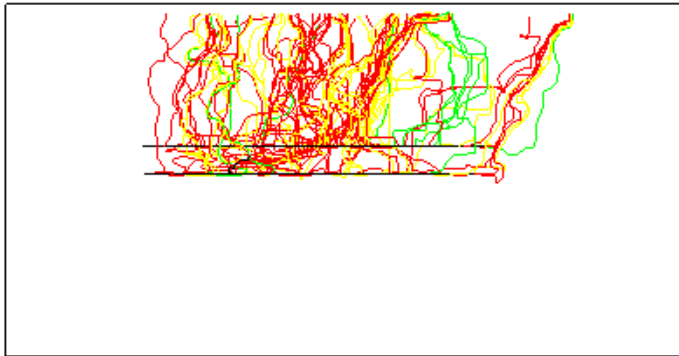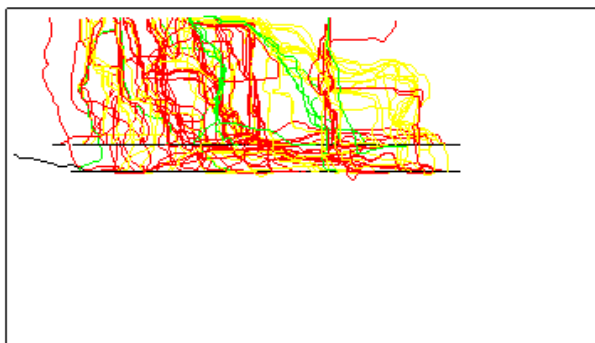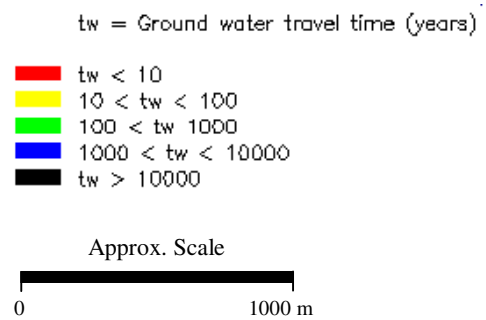
Figure 5.3-6. Stream tubes for realisation number 1 of Aberg Variant 3.2 (anisotropic variogram). The y-positive axis of a) points in the direction of Äspö local North. Results for 120 starting positions and a flow porosity of $\varepsilon_f = 1x10^{-4}$.

Table 5.3-3. Comparison of median performance measures Aberg Base Case and Variant 3. Results for 50 realisations of 120 starting positions, a flow porosity of $\varepsilon_f = 1 \times 10^{-4}$ and flow-wetted surface $a_r = 1.0 \ m^2/m^3$. Travel time statistics computed for t_w less than 10,000 years.

	Median $\log_{10} t_w$ (variance)	Median $\log_{10} q_c$ (variance)	Median $\log_{10}$ F-ratio (variance)	Percent of stream tubes failing to exit
Base Case	1.015 (0.599)	-2.736 (0.935)	5.015 (0.599)	0.4833
Variant 3.1	1.091 (0.677)	-2.803 (1.034)	5.091 (0.677)	0.5833
Variant 3.2	1.032 (0.728)	-2.733 (1.171)	5.032 (0.728)	0.8667

5.4 Conditional Simulation

The Base Case of this study (Section 4) uses unconditional geostatistical simulation to create the hydraulic conductivity fields, and includes fracture zones as deterministic zones of increased mean $\log_{10}$ hydraulic conductivity. This is not the only HYDRASTAR option for creating the hydraulic conductivity fields. For example, HYDRASTAR can also condition the fields on observed hydraulic conductivity measurements via conditional simulation, with ordinary kriging to imply fracture zones via kriging neighbourhoods. Conditional simulation was not used in the Base Case, however, because the relatively short correlation length implies that the main effect of conditioning is to control the mean of the kriging neighbourhood. HYDRASTAR also can condition the hydraulic conductivity fields by calibrating the fields to observed head values. This was not used for the Base Case because calibration demands an extreme level of computational effort.

Although conditioning on K measurements was not used for the Base Case, it is important to evaluate the effects of conditioning on model results. Two variants are considered:

- Variant 4.1: Unconditional simulation and

- Variant 4.2: Conditional simulation

Note that the above variants are without deterministic fracture zones. This is a consequence of a conflict between the defined zones, the conditioning data and kriging neighbourhoods. In principle, it is possible to define kriging neighbourhoods that corresponding to zones such that conditioning hydraulic conductivity measurements are assigned to the appropriate RD and CD domains. In practice, however, it is not possible to use such detailed kriging neighbourhoods in HYDRASTAR 1.7.2, and therefore this study does not examine the joint effect of deterministic zones and conditioning on hydraulic conductivity measurements.

These variants use a simplified geostatistical model, with a variogram fitted to all of the hydraulic conductivities of the 3 m packer test data within the site-scale model domain. The variants use no deterministic zones at all and use a single kriging neighbourhood to allow conditioning the simulated hydraulic conductivity fields to measured hydraulic conductivities. In addition, this variant uses the Moye's-based upscaling algorithm to determine the expectation and variogram of the upscaled hydraulic conductivities. (See Appendix C). This approach yields the following geostatistical model:

- A mean $\log_{10}$ hydraulic conductivity = -7.7 m/s,

- Isotropic exponential variogram model, total variance = 3.11, and

- Practical range of 122 m.

Both the variance and the $\log_{10}$ hydraulic conductivity are increased relative to the Base Case rock mass (SRD) parameters. These increases can be attributed to the inclusion of the CD data in the data used in the INFERENS variogram analysis.

5.4.1 Unconditional Simulation

This variant is simulated without fracture zones and without conditioning data. Its primary purpose is to establish the changes in the results that arise from removing the fracture zones. It is therefore useful in comparison to the Base Case and for the conditional simulation variants.

The $\log_{10}$ hydraulic conductivity field appears to be unstructured, as expected with the removal of the deterministic fracture zones (Figure 5.4-1). The exit locations are nearly random, controlled only by the recharge under the land surface (Figure 5.4-2). Likewise, the stream tubes travel randomly in the domain, and show no organisation along conductive features (Figure 5.4-3).
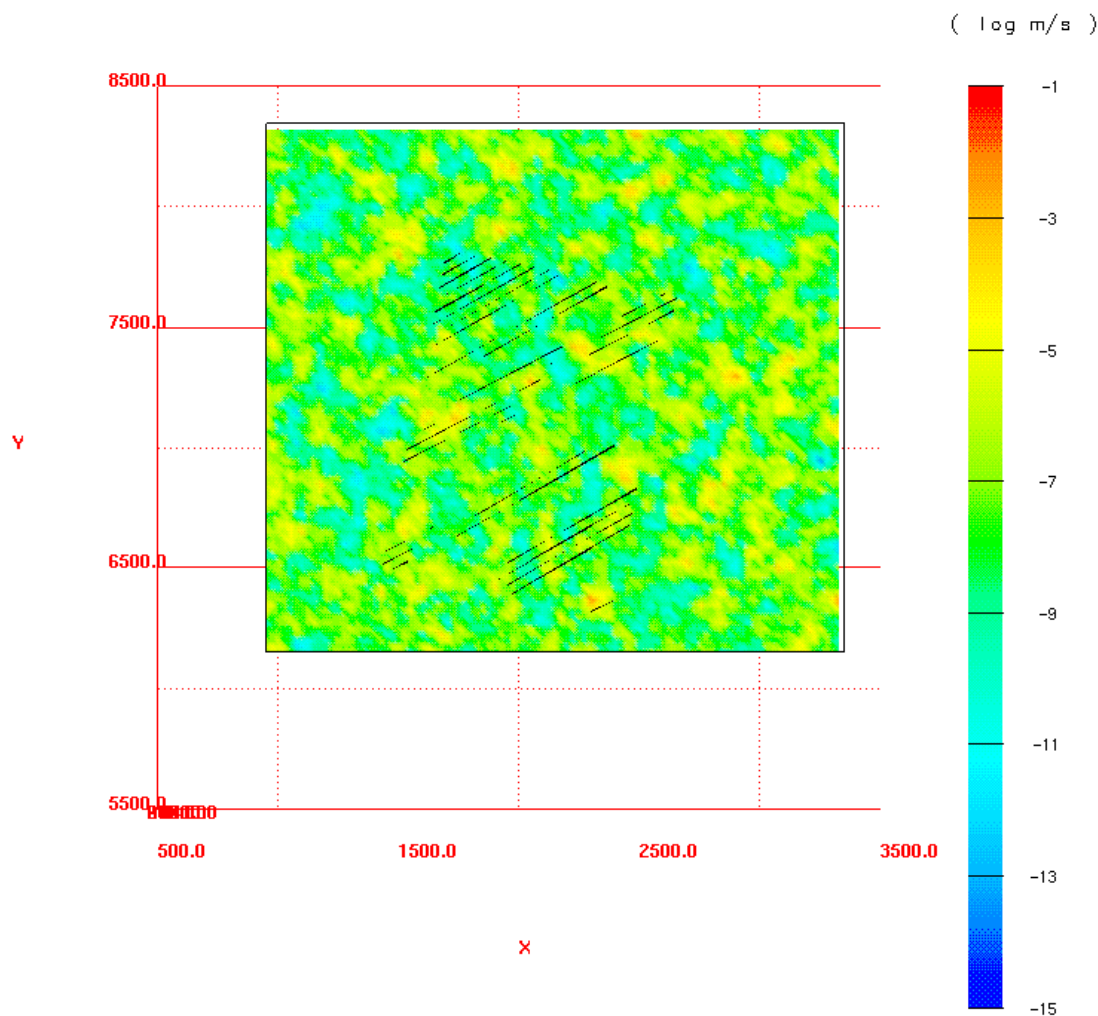
Figure 5.4-1. Log$_{10}$ hydraulic conductivity at repository level for Aberg Variant 4.1 (unconditional simulation). (Äspö local coordinate system, scale in metres).
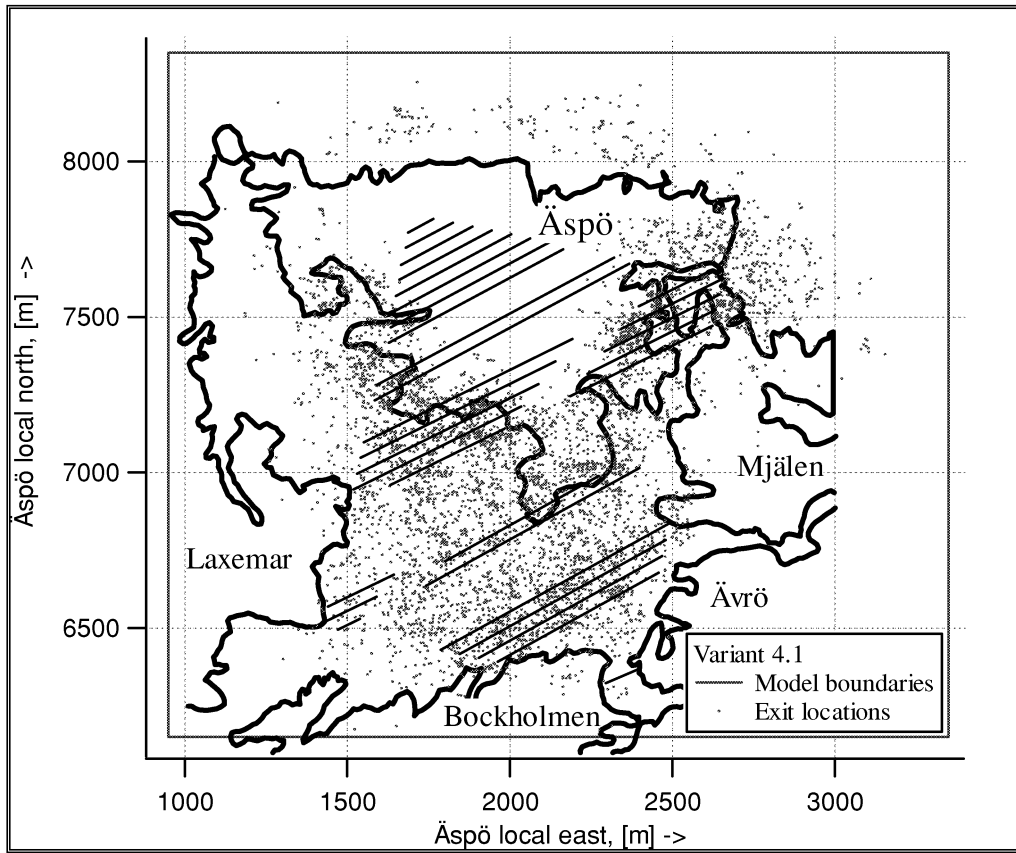
Figure 5.4-2. Exit locations for Aberg Variant 4.1 (unconditional simulation). Results for 50 realisations of 120 starting positions. (Äspö local coordinate system, scale in metres).

a) Plan view

b) Elevation view, from South

tw = Ground water travel time (years)

tw < 10
10 < tw < 100
100 < tw 1000
1000 < tw < 10000
tw > 10000

Approx. Scale

0   1000 m
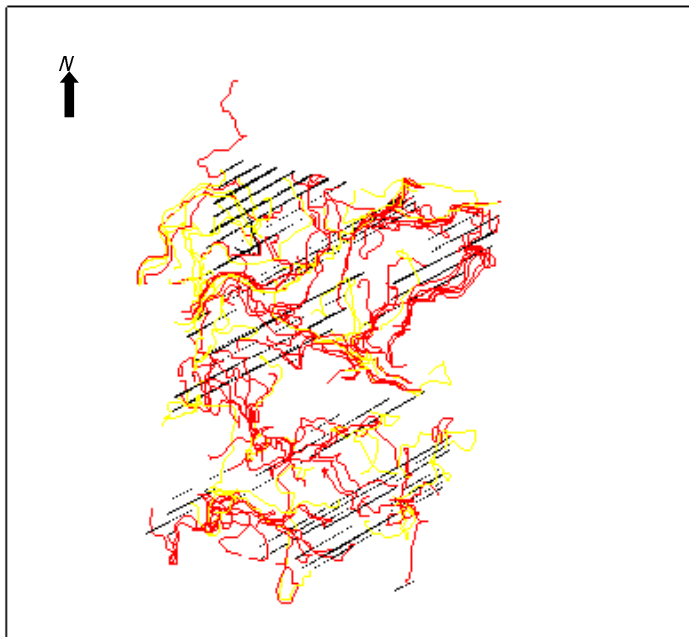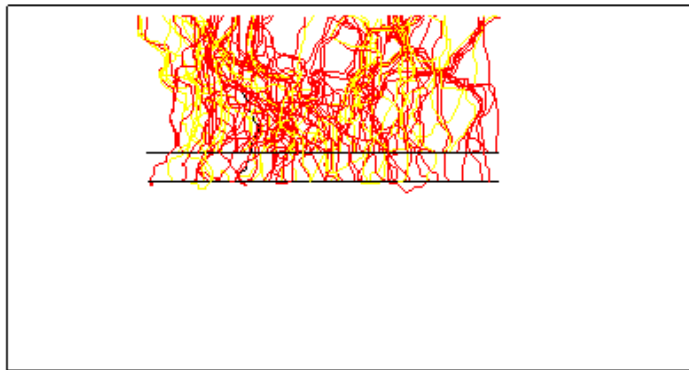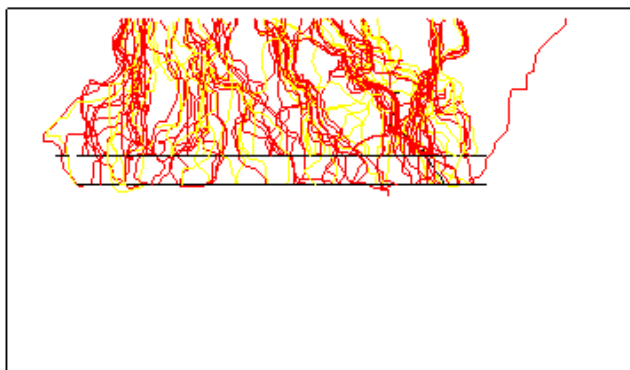
c) Elevation view, from East
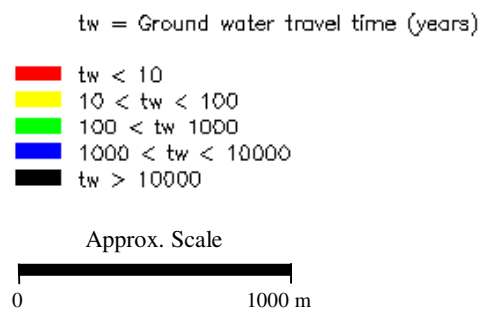
Figure 5.4-3. Stream tubes for realisation number 1 of Aberg Variant 4.1 (unconditional simulation). The y-positive axis of a) points in the direction of Äspö local North. Results for 120 starting positions and a flow porosity of $\varepsilon_f = 1x10^{-4}$.

The performance measure statistics for this variant are given in Table 5.4-1. Comparing this variant versus Base Case (Section 4.3), the median travel time is shortened from 10 to 4.1 years, and its variance is reduced from 0.599 to 0.465. The median canister flux is increased from 1.9×10^{-3} to 6.7×10^{-3} m/yr. Both the travel time and canister flux distributions for this variant are significantly different from those of the Base Case (Appendix A.2). As anticipated, the travel paths show no organisation around linear patterns associated with fracture zones. One might anticipate that removing the deterministic zones might delete the fast paths. However, recall that K_g and the variance of $\log_{10} K$ have increased relative to the Base Case. As is discussed briefly in Section 5.3, the increases of both the mean and variance of $\log_{10} K$ tend to increase the effective conductivity of the domain (Gutjahr et al., 1978), resulting in reduced travel times. Also note that the travel time variance is reduced even though the input variance of $\log_{10} K$ has been increased (from 2.7 to 3.1). This travel time variance increase is attributed to removing the fracture zones (SCD), such that only a single domain is encountered by any given stream tube.

Table 5.4-1 Summary statistics for Aberg Variant 4.1. Results for 50 realisations of 120 starting positions, a flow porosity of $\varepsilon_f = 1 \times 10^{-4}$ and flow-wetted surface $a_r = 1.0$ m^2/m^3. Statistics in bold are discussed in text.

	All values			Travel Times > 10,000 years deleted		
	Log_{10} t_w	Log_{10} q_c	Log_{10} F-ratio	Log_{10} t_w	Log_{10} q_c	Log_{10} F-ratio
Mean	0.673	-2.232	4.673	0.661	-2.233	4.661
Median	0.620	**-2.173**	4.620	**0.617**	-2.174	**4.617**
Variance	0.502	**0.891**	0.502	**0.465**	0.890	**0.465**
5th percentile	-0.387	-3.898	3.613	-0.387	-3.898	3.613
25th percentile	0.196	-2.847	4.196	0.196	-2.848	4.196
75th percentile	1.089	-1.564	5.089	1.080	-1.566	5.080
95th percentile	1.880	-0.810	5.880	1.842	-0.810	5.842

5.4.2 Conditional Simulation

As with Variant 4.1, this variant is simulated without fracture zones and a mean $\log_{10}$ hydraulic conductivity of –7.7, a variance of 3.11 and a practical range 122 m. In this variant, however, the 3 m-interpreted hydraulic conductivities are included as conditioning data in the simulated conductivity fields. The purpose of this variant is to establish the changes in the results that arise from including conditioning data. It should be compared to Variant 4.1, the unconditional simulation. Unlike the Base Case, which relies on interference test data for the conductivity of the deterministic fracture zones, this simulation uses only the 3 m packer test data.

The $\log_{10}$ hydraulic conductivity field appears to be identical to the unconditional case. Figure 5.4-4 presents the $\log_{10}$ hydraulic conductivities at the upper repository level, which shows that no large-scale structures have been created as a result of including

measurements in the fracture zones. This is attributed to the relatively short practical range of correlation of 122 m and the wide data spacing. Similar to the unconditional case in this variant, the exit locations are nearly random, controlled only by the recharge under the land surface (Figure 5.4-5). Likewise, the stream tubes travel randomly in the domain, and show no organisation along conductive features (Figure 5.4-6).

The performance measure statistics for this variant are given in Table 5.4-2. Comparing this variant versus the unconditional simulation (Section 5.4.1), the median travel times are slightly decreased to 3.2 years, and the variance is slightly increased to 0.512. The median canister flux is slightly increased to 8.2 x 10^{-3} m/year (Table 5.4-3). Both the travel time and canister flux distributions for this variant are significantly different from those of the Base Case (Appendix A.2). It is possible that these changes reflect the implicit inclusion of conductive structures. The stream tubes have a similar degree of disorganisation as those of Variant 4.1.

Table 5.4-2. Summary statistics for Aberg Variant 4.2. Results for 50 realisations of 120 starting positions, a flow porosity of $\varepsilon_f = 1 \times 10^{-4}$ and flow-wetted surface $a_r = 1.0$ m^2/m^3. Statistics in bold are discussed in text.

	All values			Travel Times > 10,000 years deleted		
	Log_{10} t_w	Log_{10} q_c	Log_{10} F-ratio	Log_{10} t_w	Log_{10} q_c	Log_{10} F-ratio
Mean	0.575	-2.136	4.575	0.551	-2.137	4.551
Median	0.508	**-2.087**	4.508	**0.502**	-2.088	**4.502**
Variance	0.590	**0.973**	0.590	**0.512**	0.969	**0.512**
5$^\text{th}$ percentile	-0.553	-3.827	3.447	-0.553	-3.825	3.447
25$^\text{th}$ percentile	0.064	-2.780	4.064	0.061	-2.780	4.061
75$^\text{th}$ percentile	1.027	-1.441	5.027	1.012	-1.444	5.012
95$^\text{th}$ percentile	1.834	-0.627	5.834	1.786	-0.627	5.786

Table 5.4-3. Comparison of Base Case and Variant 4. Results for a single realisation of 120 starting positions, a flow porosity of $\varepsilon_f = 1 \times 10^{-4}$ and flow-wetted surface $a_r = 1.0$ m^2/m^3.

	Median $\log_{10} t_w$ for times < 10,000 years (variance)	Median $\log_{10} q_c$ for all times (variance)	Median $\log_{10}$ F-ratio for times < 10,000 years (variance)
Base Case	1.015	-2.736	5.015
	(0.599)	(0.935)	(0.599)
Variant 4.1 Unconditional	0.617 (0.465)	-2.173 (0.891)	4.617 (0.465)
Variant 4.2 Conditional	0.502 (0.512)	-2.087 (0.973)	4.502 (0.512)
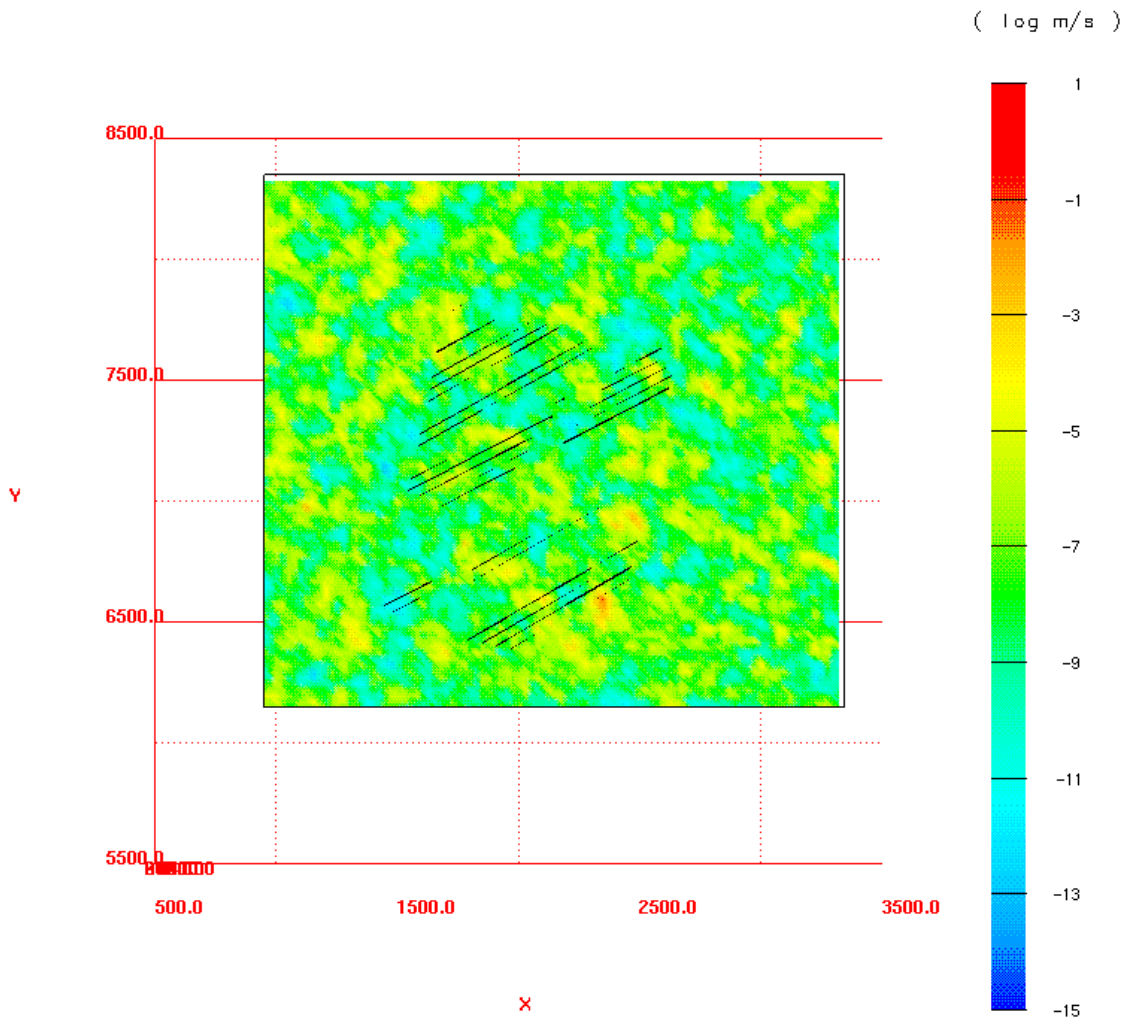
Figure 5.4-4. *Log$_{10}$ hydraulic conductivity for one realisation at repository level for Aberg Variant 4.2 (conditional simulation). (Äspö local coordinate system, scale in metres).*
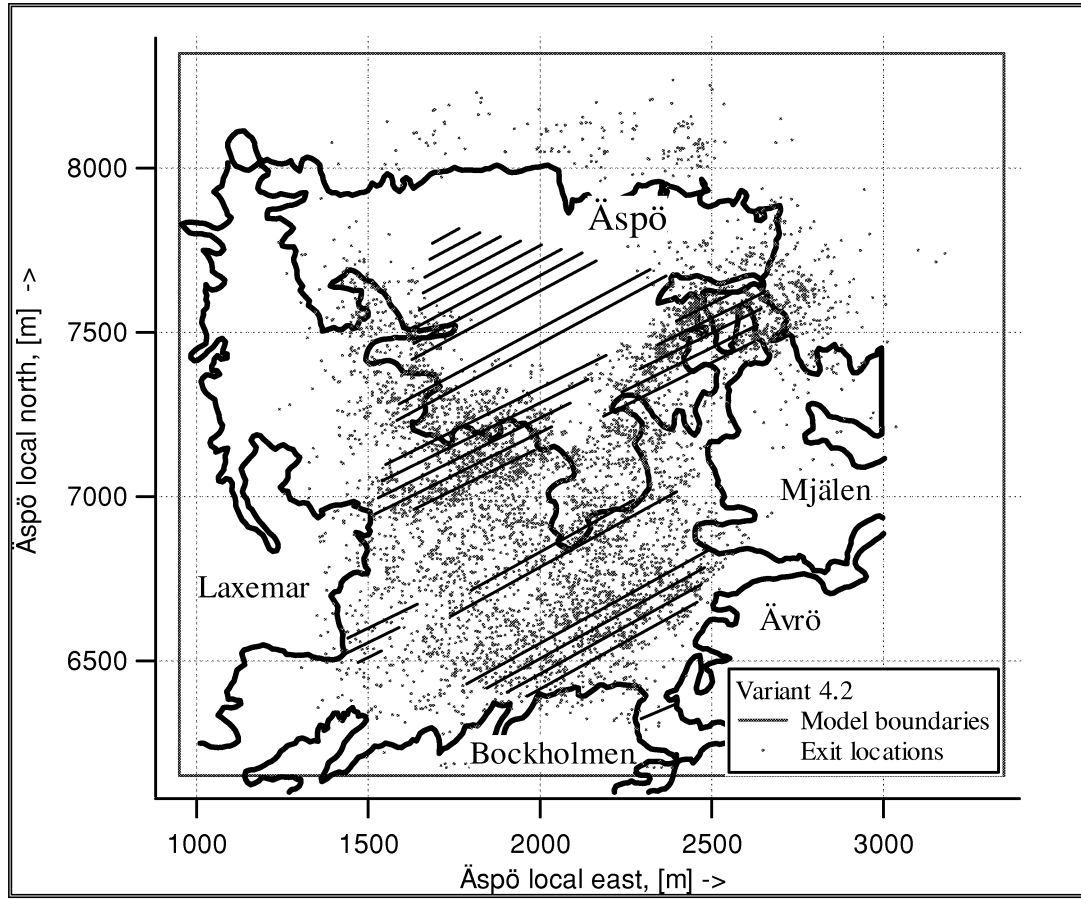
Figure 5.4-5. Exit locations for Aberg Variant 4.2 (conditional simulation). Results for 50 realisations of 120 starting positions. (Äspö local coordinate system, scale in metres).

a) Plan view

b) Elevation view, from South

c) Elevation view, from East

tw = Ground water travel time (years)

tw < 10
10 < tw < 100
100 < tw 1000
1000 < tw < 10000
tw > 10000

Approx. Scale

0   1000 m
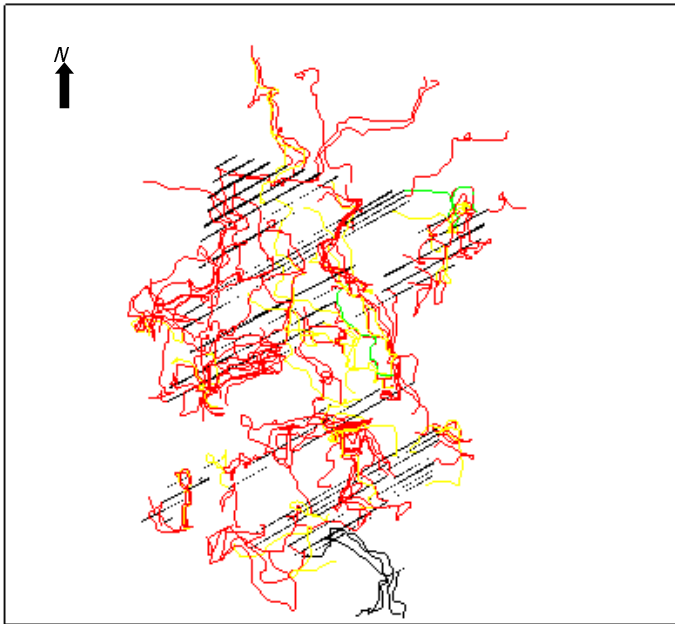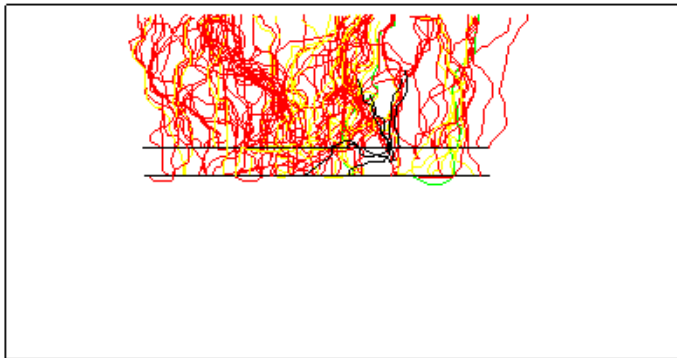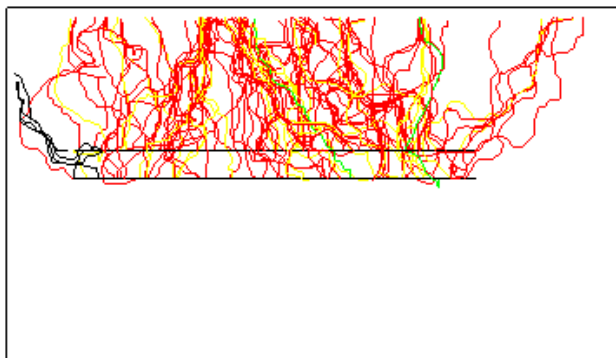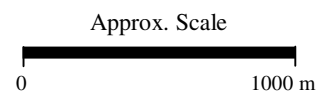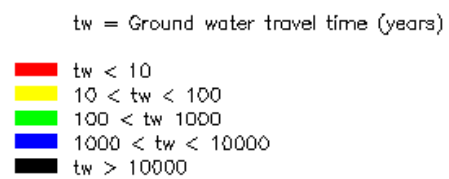
Figure 5.4-6. Stream tubes for realisation number 1 of Aberg Variant 4.2 (conditional simulation). The y-positive axis of a) points in the direction of Äspö local North. Results for 120 starting positions and a flow porosity of $\varepsilon_f = 1x10^{-4}$.

5.5　Deterministic Simulation

This variant is a simplified simulation of the site using a deterministic representation of the hydraulic conductivity field (i.e., the field has no random component and thus needs only one 'realisation'). The objectives of this simulation are to further evaluate the empirical upscaling and nested modelling, and to examine the effects of the large-scale heterogeneity (e.g., the fracture zones and rock blocks). As was discussed in Sections 4.2, 5.1 and Appendix C.2, choosing the appropriate hydraulic conductivities is complicated by the apparent scale dependence of hydraulic conductivity. We might choose to use exactly the same hydraulic conductivities as the regional model of Svensson (1997a; see also Appendix B), but the site scale model includes rock blocks and fracture zones that have no corresponding regional structures. As a compromise, this study uses the empirical upscaling rule (Appendix C.2) to determine the effective conductivity, K_e, for each rock unit. If the nested modelling and upscaling are consistent, the boundary fluxes should be approximately the same for the regional model, the Base Case and this deterministic variant. The parameters for this case were previously presented in Table 5.2-1, and represent as the effective conductivities of each unit. Note that for this variant, there is no block-scale variability (zero variance).

Table 5.5-1 summarises the results of this deterministic simulation in terms of the travel time, canister flux and F-ratio, averaged over all the starting positions. In comparison to the Base Case, the median travel time is increased from 10 to 12 years, and the median canister flux is increased from 1.9×10^{-3} to 2.1×10^{-3} m/yr (Table 5.5-2). The variances of both of these measures are dramatically reduced, as expected for a deterministic field.

Table 5.5-1. Summary statistics for Aberg Variant 5. Results for120 starting positions, a flow porosity of $\varepsilon_f = 1 \times 10^{-4}$ and upper flow-wetted surface a_r $= 1.0$ m^2/m^3. No stream tubes fail to exit the model surface in this variant. Statistics in bold are discussed in text.

| | **All values** | | |
	$Log_{10}\ t_w$	**$Log_{10}\ q_c$**	**Log_{10} F-ratio**
Mean	1.049	-2.708	5.049
Median	**1.074**	**-2.672**	**5.074**
Variance	**0.273**	**0.192**	**0.273**
5th percentile	0.260	-3.417	4.260
25th percentile	0.584	-3.028	4.584
75th percentile	1.386	-2.354	5.386
95th percentile	2.048	-2.094	6.048

Table 5.5-2. Comparison of median performance measures within Aberg Base Case, Variant 2 and Variant 5. Results for a single realisation of 120 starting positions, a flow porosity of $\varepsilon_f = 1x10^{-4}$ and flow-wetted surface $a_r = 1.0 \ m^2/m^3$.

	Median $\log_{10} t_w$ for times < 10,000 years (variance)	Median $\log_{10} q_c$ for all times (variance)	Median $\log_{10}$ F-ratio for times < 10,000 years (variance)
Base Case	1.015	-2.736	5.015
	(0.599)	(0.935)	(0.599)
Variant 2	0.766	-2.400	4.766
	(0.426)	(0.560)	(0.426)
Variant 5	1.074	-2.672	5.074
	(0.273)	(0.192)	(0.273)

Table 5.5-3 summarises the boundary fluxes; note that this deterministic variant under predicts the Base Case boundary fluxes by approximately a factor of ½ to 1/3. This variant also under predicts the boundary fluxes of the regional model by 1/6, which may be due to the mismatch of the regional and site-scale conductors and rock domains. Figures 5.5-1 and 5.5-2 present the exit locations and stream tubes for this variant, which are little different from those of the Base Case. This indicates that the exit locations and the flow paths are strongly influenced by the deterministic fracture zones. As discussed in Section 3.5.3, the occurence and extent of these zones is uncertain, but this uncertainty cannot be rigorously evaluated using the geostatistical algorithms in the current version of HYDRASTAR.

Table 5.5-3 Boundary Flux Consistency for Aberg Base Case, Variant 2, Variant 5 and Regional Models.

Model Surface	Net Flux Through Subdomain (m^3/s x 10^{-3})			
	Regional	Base Case 25 m Scale	Variant 2 50 m Scale	Variant 5 Deterministic
West	13.7 (in)	4.92 (in)	6.66 (in)	2.00 (in)
East	0.916 (in)	0.77 (in)	0.730 (in)	0.234 (in)
South	1.81 (in)	0.846 (in)	0.489 (out)	0.477 (in)
North	0.625 (in)	0.538 (in)	0.340 (in)	0.0919 (in)
Bottom	0.374 (in)	1.03 (in)	1.11 (in)	0.677 (in)
Top	18.1 (out)	8.11 (out)	8.34 (out)	3.49 (out)
Total Inflow	17.4	8.11	8.83	3.48
Total Outflow	18.1	8.11	8.83	3.49
Mass balance (In – Out)	-0.675	-0.0037	0.009	-0.010
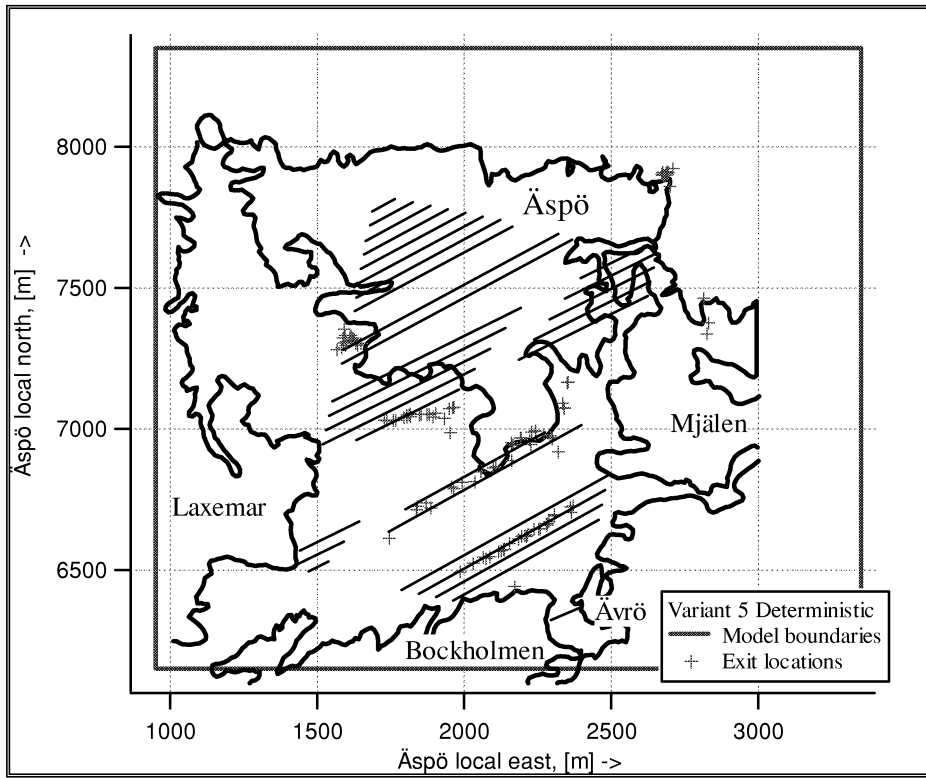
Figure 5.5-1. Exit locations for Aberg 5 (deterministic). Results for 120 starting positions. (Äspö local coordinate system, scale in metres).

a) Plan view

b) Elevation view, from South

c) Elevation view, from East

tw = Ground water travel time (years)

tw < 10
10 < tw < 100
100 < tw 1000
1000 < tw < 10000
tw > 10000

Approx. Scale

0   1000 m
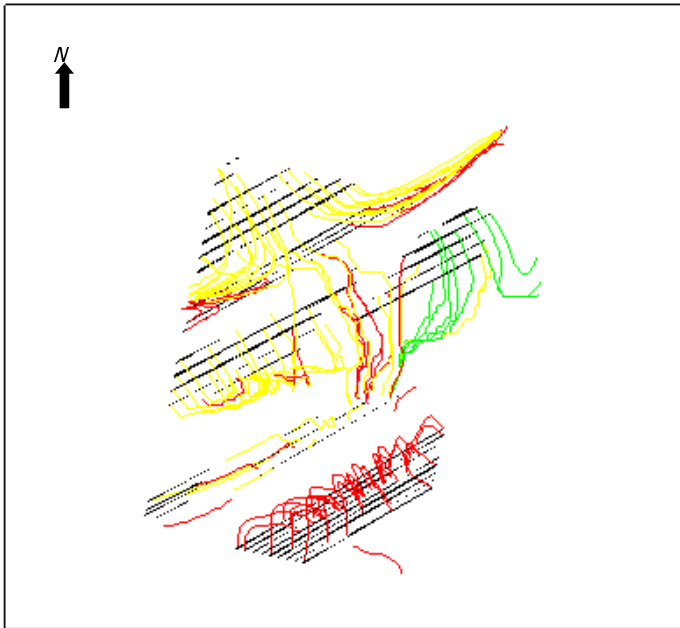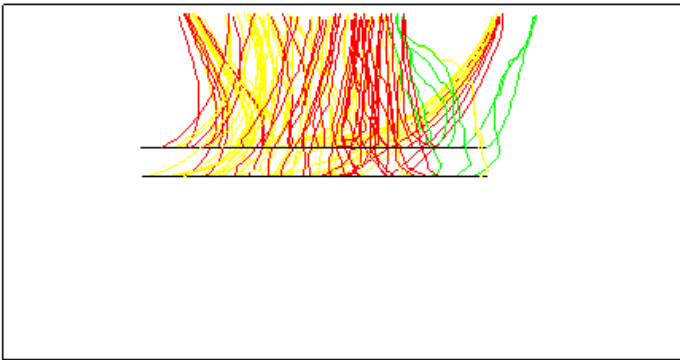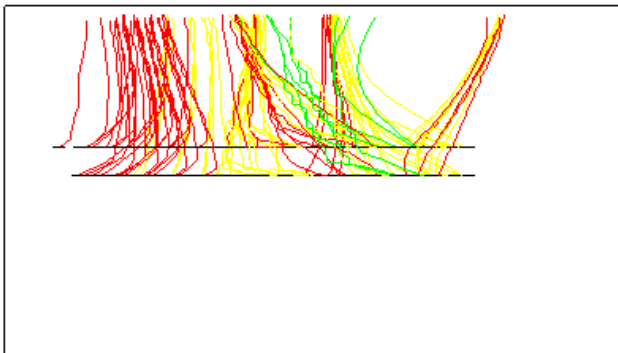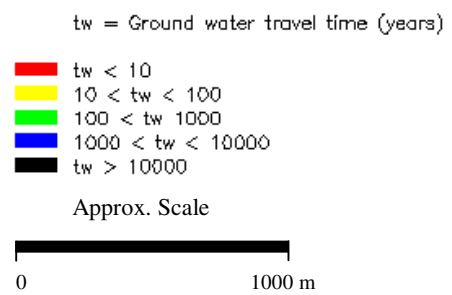
Figure 5.5-2. Stream tubes for realisation number 1 of Aberg Variant 5 (deterministic).
The y-positive axis of a) points in the direction of Äspö local North.
Results for 120 starting positions and a flow porosity of $\varepsilon_f = 1x10^{-4}$.

6 Discussion and Summary

The SKB SR 97 study is a comprehensive performance assessment illustrating the results for three hypothetical repositories in Sweden. This study addresses the hydrogeologic modelling of Aberg, one of the three SR 97 sites. The study uses HYDRASTAR, a stochastic continuum groundwater flow and transport modelling program developed by SKB. The application is relatively straightforward, with the majority of the model parameters and boundary conditions explicitly specified in Walker et al. (1997). This section of the report summarises the modelled cases and discusses the main results of the study in terms of statistics for travel time, F-ratio and canister flux. It also summarises the findings of the study with regard to model parameter uncertainty.

6.1 Input Data

Input data for the model is unmodified from that given by Walker et al. (1997b) except for the rescaling of hydraulic conductivities as suggested by Walker et al. (1997b). The SKB geostatistical analysis code INFERENS is used to infer a regularised variogram model based on the 3 m interpreted hydraulic conductivities taken from SICADA.

The boundary conditions for this model are constant head boundaries, derived from a deterministic, freshwater, regional scale model modified from that of Svensson (1997a). The overall flow pattern of the regional model is typical of coastal areas: topographically driven flow from the inland areas exiting to the coastal waters. The transfer of regional heads via constant head boundaries preserves this pattern in the site-scale model. Adjustment of the scaling of hydraulic conductivity to fine-tune the boundary flux mass balance is not pursued.

6.2 Base Case

The Base Case uses 100 realisations of the hydraulic conductivity field with 120 starting positions to evaluate the travel times, canister fluxes and F-ratios for the proposed repository. As discussed in Section 4.0, the median travel times and median canister fluxes of the Base Case appear to be stable with respect to the number of simulations and are reasonably consistent with the regional model fluxes. All statistics are calculated with respect to the common logarithm transforms of the travel times, canister fluxes, and F-ratios to facilitate summary and display.

For the Base Case, the boundary fluxes of the regional model and the site scale model appeared to be consistent with respect to orientation, but the site-scale model may tend to underpredict the regional fluxes by a factor of approximately 1/2 to 1/3. While this

broadly supports the validity of the nested modelling and the associated upscaling, the site scale boundary fluxes are calculated for a relatively small number of realisations.

The ensemble results taken over all realisations of all starting positions suggest the following statistics for the Base Case:

- Median travel time is 10 years, with an interquartile range from 3.4 years to 37 years.

- Median canister flux is 1.8×10^{-3} m/year, with an interquartile range from 3.7×10^{-4} m/year to 7.8×10^{-3} m/year.

- Median F-ratio is 1.0×10^{5} year/m, with an interquartile range from 3.4×10^{4} year/m to 3.7×10^{5} year/m.

The current version of HYDRASTAR is limited to homogeneous flow porosity over the entire domain. Consequently, the F-ratio is a simple multiple of the travel time, and the canister flux is inversely correlated to the travel time. The $\log_{10}$ travel time and $\log_{10}$ canister flux distributions are slightly skewed as a consequence of the relatively high hydraulic conductivity in the region south of Äspö. The model domain is only slightly restrictive, with 0.5% of the stream tubes failing to reach the model domain upper surface.

The flow paths and exit locations of the realisations are compatible with the overall pattern of flow at the site. The travel times are consistent with scoping calculations based on Darcy's law and the observed gradient. The results are also consistent with the site-scale model of Svensson (1997b) and on-site head observations.

Three individual realisations are examined briefly to illustrate the variability within and between realisations. Although the stream tubes and exit locations may shift dramatically from one realisation to the next, the medians of performance measures are relatively stable between realisations.

Three individual starting positions are examined over all 100 realisations to illustrate variability due to the differences in stream tube starting positions. As suspected, placing a canister in a host rock of relatively low hydraulic conductivity increases the median travel time. Several individual regions and starting positions were studied, revealing that some areas were less preferable with respect to travel time (e.g., rock blocks with relatively high measured conductivities, the upper repository level relative to the lower repository level).

6.3   Variant Cases

6.3.1   Boundary Conditions

This study uses a nested modelling approach, with a regional model providing the site-scale boundary conditions. This set of variants evaluates the uncertainties associated with calculating and transferring boundaries between the regional and site-scale models. Four methods for determining boundary conditions are compared using a single realisation of the hydraulic conductivity field for the site-scale model. The effect of these boundary conditions are evaluated by comparing the travel time, canister flux and F-ratio and boundary flux. The four methods for calculating and transferring boundaries between the regional and site-scale models include the following:

1.1   Use a regional model with a deterministic, effective hydraulic conductivity and freshwater conditions (i.e., a single realisation of the Base Case, as discussed in Section 4.1)

1.2   Use a regional model with a single stochastic realisation of hydraulic conductivity and the observed salinity. Convert the resulting boundary pressures and salinities to environmental freshwater heads.

1.3   Use a regional model with a single stochastic realisation of hydraulic conductivity and freshwater conditions.

1.4   Avoid the regional model entirely and use the observed water table/sea level and hydrostatic conditions directly in the site scale model as simplified boundary conditions.

Variants 1.1, 1.2 and 1.3 suggest that the model results were relatively insensitive to the approach to calculating and transferring the heads from a regional model. The three methods for transferring boundary conditions from the regional model give similar values for median travel time and canister fluxes. In contrast, the simplified boundary condition variants, Variants 1.4b and 1.4c, suggested that the results were very sensitive to the regional flow patterns created by the use of nested modelling. A possible extension of this variant would be to investigate the effects of using constant flux (Neuman) or third-type boundaries that would allow greater head variance in the domain. Such boundary conditions are beyond the current capabilities of HYDRASTAR, however.

6.3.2   Upscaling

Hydraulic conductivity is thought to be a scale dependent parameter, but current research debates the correct method for scaling field measurements of hydraulic conductivity for use in continuum modelling. The Base Case uses the upscaling approach proposed by Walker et al. (1997b) to determine the mean and variogram of log hydraulic conductivity at the 25 m grid scale. This upscaling variant examines the

self-consistency of the upscaling approach by changing the model calculation scale to a 50 m regular grid. This new grid scale requires a commensurate rescaling of the simulation parameters for the hydraulic conductivity field.

The simulations indicate that changing the model grid scale from 25 to 50 m reduces the variance while increasing the range of the variogram and increasing the mean of $\log_{10}$ hydraulic conductivity. Monte Carlo simulations with this coarser grid yield travel times, canister fluxes and boundary fluxes that weakly agree with the Base Case. Although the method appears to be approximately self-consistent with respect to the median performance measures at various grid scales, the reduced travel times, the increased canister fluxes and increased boundary fluxes collectively suggest that the upscaling method may increase the effective hydraulic conductivity of the domain. The coarser grid also reduces the variability of the performance measures, as is expected with the decrease in the input variance of $\log_{10}$ hydraulic conductivity.

6.3.3   Anisotropic Variogram

Site investigations at Äspö and at various other locations in Sweden suggest that the host rocks may exhibit hydraulic anisotropy, which the current version of HYDRASTAR (1.7.2) cannot directly incorporate. This variant addresses the possible hydraulic anisotropy of the host rocks using an anisotropic variogram of hydraulic conductivities to create a large-scale anisotropic effective hydraulic conductivity. The overall effect is to create rough ellipsoids of conductivity, with the long axes parallel to the suggested major axis of anisotropy (northwest-southeast).

Two cases are evaluated, the first using a variogram anistropy ratio of 1:2:1 in the Vertical:NW:NE directions. Consistent with the findings of Svensson (1997a), the flow pattern is changed, with stream tubes reorganised parallel to the major axis of anisotropy. The second case uses a variogram anistropy ratio of 1:10:1, resulting in stream tubes that are strongly oriented in the NW-SE direction. However, both variants indicate that the median performance measures are only slightly different from the Base Case. This may be a consequence of the coarseness of the model grid, which forces a simplification of the anistropy ratio. This results in hydraulic conductivity fields with limited vertical correlation. Therefore, the preferential flow paths only exist in the NW-SE direction. For both cases, the only apparent difference is an increase in the variance of the performance measures and a reorganisation of the stream tubes.

6.3.4   Conditional Simulation

The Base Case of this study (Section 4) uses unconditional geostatistical simulation to create the hydraulic conductivity fields, and includes fracture zones as deterministic zones of increased mean $\log_{10}$ hydraulic conductivity. An alternative approach is to condition the fields on observed hydraulic conductivity measurements via conditional simulation, and to include fracture zones implicitly with ordinary kriging. No deterministic fracture zones can be included rigorously in HYDRASTAR conditional simulations because it is not possible in practice to include such detailed kriging neighbourhoods in HYDRASTAR 1.7.2. Two variants are considered. The first is

unconditional simulation without deterministic fracture zones, which evaluates the effect of removing the conductive features from the Base Case. The second is conditional simulation without fracture zones, to evaluate the effects of conditioning the simulations on the observed hydraulic conductivities.

These variants use a simplified geostatistical model, with a variogram fitted to all of the hydraulic conductivities of the 3 m packer test data within the site-scale model domain. Both the variance and the $\log_{10}$ hydraulic conductivity are increased relative to the Base Case rock mass (SRD) parameters. These increases can be attributed to the inclusion of the CD data in the data used in the INFERENS variogram analysis.

The unconditional simulation without fracture zones has a median travel time half an order of magnitude lower than the Base Case, and the travel paths show no organisation around fracture zones. The change in median travel time is a result of removing the deterministic fracture zones, pooling all the data and determining a new geostatistical model. Removing the fracture zones (SCD) also appears to reduce the variance of travel time, since only a single domain is encountered by any given stream tube. Including the conditioning data yields slightly shorter travel times than the unconditional case. This may be the effect of the conditioning data creating relatively conductive regions where the packer tests results reflect the occurrence of a fracture zone. However, the large scale of the fracture zones (as in the Base Case) is not captured by conditional ssimulation because large amounts of measurement data are required to completely describe the fracture zone geometry. With the limited amount of data and short correlation length, the continuity of the fracture zone cannot be reproduced.

6.3.5   Deterministic Simulation

This variant is a simplified simulation of the site using a deterministic representation of the hydraulic conductivity field (i.e., the field has no random component and thus needs only one 'realisation'). This variant uses the empirical upscaling rule (Appendix C.2) to determine the effective conductivity, K_e, for each rock unit. If the nested modelling and upscaling are consistent, the boundary fluxes should be approximately the same for the regional model, the Base Case and this deterministic variant.

The median travel time and median canister flux are slightly higher than that of the Base Case, while the variances of both of these measures are dramatically reduced, as expected for a deterministic field. However, this variant under predicts both the Base Case boundary fluxes and the boundary fluxes of the regional model. Taken with Variant 2 (upscaling), this variant suggests that the upscaling approach is generally self-consistent but could be investigated further.

6.3.6   Comparison

Table 6.1 presents a summary of the medians and variances of the performance measures for the Base Case (in bold) and for Variants 2 through 5. Variant 1 was not included because only a single realisation was considered, and the mean and variance of the performance measures cannot be compared to the ensemble values from the other

variants. However, note that Variant 1 indicated that alternative methods for transferring boundary conditions had little impact on the performance measures. Variant 4.2, using conditional simulation, yields the shortest median travel time and greatest median canister flux. The anisotropic variogram case, Variant 3.1, yields the longest median travel time and lowest median canister flux.

Figures 6-1 and 6-2 present floating histograms of the $\log_{10}$ travel time and $\log_{10}$ canister flux, respectively, for the Base Case, and Variant Cases 2, 3.1, 4.2, and 5. Note that the variabilities of the performance measures are quite high for the Base Case, and that the variability between the variants is comparatively low. For example, the Base Case has an interquartile range from 3.4 years to 37 years, while the range of median travel times for the variants is from 3.2 years (Variant 4.2) to 12 years (Variant 3.1). Thus the variability of the Base Case due to parameter variability is greater than the variability of the cases studied to address uncertainty. Within the limitations of the variant cases studied, this suggests that Base Case has adequately characterised the Aberg hypothetical performance.

Table 6.1. Summary of Aberg flow modelling results.

Performance Measure		Base Case	Variant 2 Upscaling to 50 m	Variant 3.1 Anisotropic Variogram	Variant 4.2 Conditional Simulation	Variant 5 Deterministic
Log_{10} Travel time (years)	Median	1.015	0.766	1.091	0.502	1.074
	Variance	0.599	0.426	0.677	0.512	0.273
Log_{10} Canister Flux (m/y)	Median	-2.736	-2.400	-2.803	-2.087	-2.672
	Variance	0.935	0.560	1.034	0.973	0.192
F-ratio (y/m)	Median	5.015	4.766	5.091	4.502	5.074
	Variance	0.599	0.426	0.677	0.512	0.273
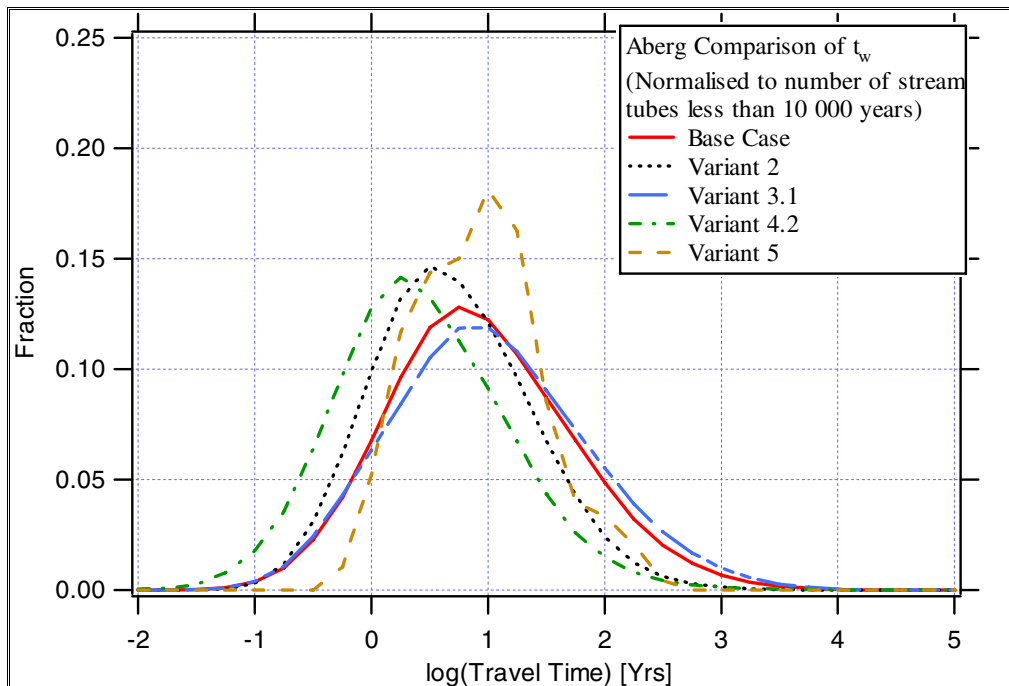
Figure 6-1. Floating histograms of log$_{10}$ travel time for Base Case, Variants 2, 3.1, 4.2 and 5, each normalised to the number of stream tubes with travel times less than 10,000 years. Results for 120 starting positions and a flow porosity of $\varepsilon_f = 1x10^{-4}$.
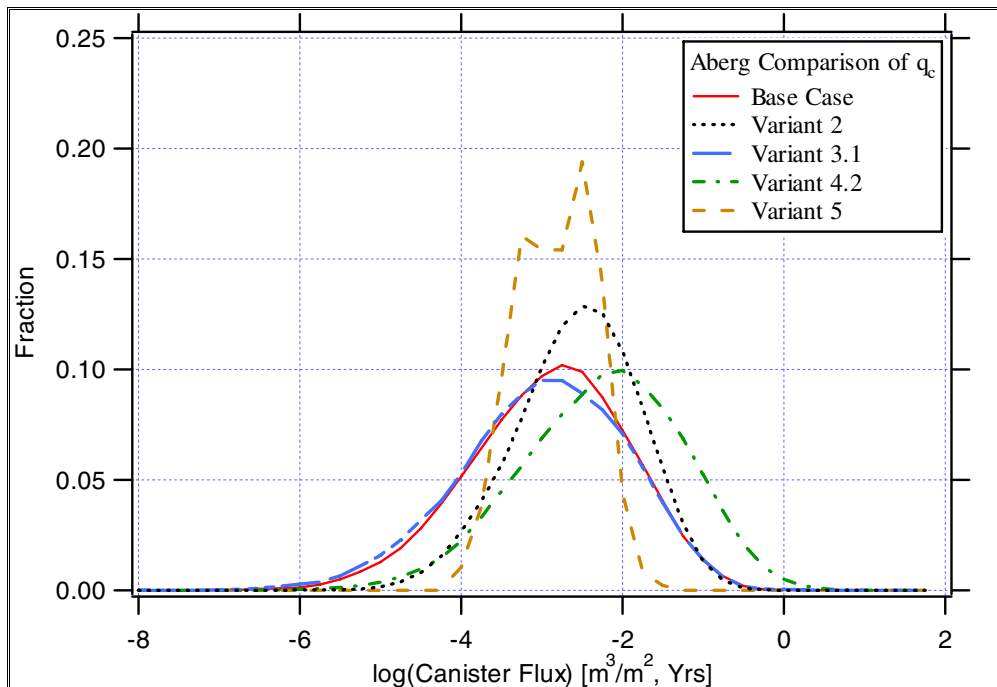
Figure 6-2. Floating histograms of log$_{10}$ canister flux for the Base Case, Variants 2, 3.1, 4.2 and 5, each normalised to the total number of stream tubes.

6.4   Possible Model Refinements

In several respects, the modelling could be improved within the current features of HYDRASTAR. These include the use of a denser grid to improve the representation of both the fracture zones and the variogram of hydraulic conductivity. This improved representation would allow a more rigorous examination of possible hydraulic anisotropy. The number of realisations may have to be increased to improve the stability of performance measures if the performance of individual starting positions is of interest.

Other model refinements are possible but are outside of the current features of HYDRASTAR. These include the development and use of alternative upscaling methods that would be more widely applicable and self-consistent. Nonparametric geostatistical simulation might allow a more realistic representation of the observed distribution of hydraulic conductivities. A stochastic representation of conductive features would allow a more rigorous evaluation of the fracture zone uncertainties. And finally, a variant case to investigate the effects of using constant flux (Neuman) or third-type boundaries is suggested to examine changes to the head variance within the domain.

6.5   Summary of Findings

The Base Case results suggest that the expected performance measures of the Aberg hypothetical repository are as follows:

- The median travel time is 10 years, with an interquartile range from 3.4 years to 37 years.

- The median canister flux is 1.8×10^{-3} m/year, with an interquartile range from 3.7×10^{4} m/year to 7.8×10^{-3} m/year.

- The median F-ratio is 1.0×10^{5} year/m, with an interquartile range from 3.4×10^{4} year/m to 3.7×10^{5} year/m.

The Base Case model is supported by the scoping calculations, previous modelling studies, and on-site observations. The variant cases suggest that the median travel time ranges from 3.2 to 12 years, the median canister flux ranges from 1.5 to 8.2×10^{-3} m/year, and the median F ratio ranges from 0.32 to 1.2×10^{5} year/m. The variability of the Base Case due to parameter variability is greater than the variability of the cases studied to address uncertainty. Within the limitations of the variant cases studied, this suggests that Base Case has adequately characterised the Aberg hypothetical performance.

Other notable findings of this study can be summarised as follows:

- The canister flux appears to be inversely correlated to the travel time.

- The flow paths and exit locations are compatible with the pattern of flow at the site, and appear to be dominated by the deterministic fracture zones.

- The performance measures are relatively insensitive to alternative methods of incorporating the regional boundary conditions, but are very sensitive to the regional flow patterns.

- The upscaling method used in this study appears to be approximately self-consistent with regard to the medians of the performance measures.

- The performance measures are relatively insensitive to the anisotropic variogram, but this effect may be limited by the model grid density.

- The conditional and unconditional variants that rely on Moye's formula upscaling and a pooled data set of both rock mass and fracture zone data results in the shortest travel times and greatest canister fluxes.

Acknowledgements

References

Anderson M.P., and Woessner W.W., 1992. Applied groundwater modeling. Simulation of flow and advective transport. Academic Press.

Andersson J., and Stigsson M., 1999. Integration of data and uncertainties for the base and initial canister defect scenario analyses of SR 97. Swedish Nuclear Fuel and Waste Management Co., SKB Technical Report in preparation, 1999.

Bergman B., and Walker D., 1998. The relationship between stochastic anisotropy and hydraulic anisotropy: Numerical experiments using HYDRASTAR 1.7.2. Swedish Nuclear Fuel and Water Management Co., SKB Progress Report U-98-12, Stockholm, Sweden.

Boghammar A., and Marsic N., 1997. Using Stastistica when evaluating results from Hydrastar 1.5+. Swedish Nuclear Fuel and Waste Management Co., SKB Progress Report U-97-18, Stockholm, Sweden.

Dagan G., 1986. Statistical theory of groundwater flow and transport: pore to laboratory, laboratory to formation, and formation to regional scale. Water Resources Research, 22(9), p 120S-134S.

de Marsily G., Lavedan C., Boucher M., and Fasanino G., 1984. Interpretation of Interference Tests in a Well Field Using Geostatistical Techniques to Fit the Permeability Distribution in a Reservoir Model, in Geostatistics for Natural Resources Characterisation. Second NATO Advanced Study Institute, GEOSTAT 1983, Tahoe City, California. Edited by G. Verly, M. David, A.G. Journel, and A. Marachal, p 831-849, D. Reidel, Hingham, Mass, USA.

Ericsson L.O., and Ronge B., 1986. Correlation between tectonic lineaments and permeability values of crystalline bedrock in the guide area. Swedish Nuclear Fuel and Waste Management Co., SKB Technical Report 86-19, Stockholm, Sweden.

Follin S., 1992. Numerical calculations on heterogeneity of groundwater flow. Swedish Nuclear Fuel Management Co., SKB Technical Report 92-14, Stockholm, Sweden.

Geier J., 1993. Verification of the geostatistical inference code INFERENS, Version 1.1, and demonstration using data from Finnsjön. Swedish Nuclear Fuel Management Co., SKB Technical Report TR 93-09, Stockholm, Sweden.

Gelhar, L.W., 1993. Stochastic Subsurface Hydrology. Prentice Hall, Englewood Cliffs, New Jersey

Gelhar L.W., 1986. Stochastic Subsurface Hydrology from Theory to Applications, Water Resources Research, 22(9), p 135S-145S.

Gelhar L.W., and Axness C.L., 1983. Three-Dimensional Stochastic Analysis of Macrodispersion in Aquifers, Water Resources Research, 19(1), p 161-180.

Gutjahr A.L., Gelhar L.W., Baker A.A, and MacMillan J.R., 1978. Stochastic Analysis of Spatial Variability in Subsurface Flows 2. Evaluation and Application, Water Resources Research, 14(5), p 953-959.

Gylling B., Lindgren M. and Widén H., 1998. Preparatory hydrogeological calculations for Aberg, Beberg and Ceberg – A pre-study for SR 97 calculations. Swedish Nuclear Fuel Management Co., SKB working report, in preparation, Stockholm, Sweden.

Hammersley, J.M., and Handscomb, D.C., 1975. Monte Carlo Methods, Methuen, London.

Hodgkinson D.P., and Barker J., 1985. Specification of a Test Problem for HYDROCOIN Level 1 Case1: Transient Flow from a Borehole in a Fractured Permeable Medium, Report AERE R-11574, UK Atomic Energy Authority, Harwell Laboratories, UK.

Hufschmied P., 1986. Estimation of three –dimensional statistically anisotropic hydraulic conductivity field by means of single well pumping tests combined with flowmeter measurements. Hydrogéologie 2, p 163-174.

Hultman S., 1997. Visualisation of HYDRASTAR Simulation Data in the AVS 5 System. Swedish Nuclear Fuel Management Co., SKB U-97-01, Stockholm, Sweden.

Indelman P., and Dagan G., 1993. Upscaling of permeability of anisotropic heterogeneous formations 1. The general framework. Water Resources Research, 29(4), p 917-923.

Journel A.G., and Huijbregts Ch J., 1978. Mining Geostatistics, Academic Press.

La Pointe P.R., 1994. Evaluation of stationary and non-stationary geostatistical models for inferring hydraulic conductivity values at Äspö. Swedish Nuclear Fuel Management Co., SKB Technical Report TR 94-22, Stockholm, Sweden.

Leake S.A., Lawson P.W., Lilly M.R, and Claar D.V., 1998. Assignment of boundary conditions in embedded groundwater flow models, Ground Water 36(4), p 621-625.

Larsen R.J., and Marx M.L., 1986. An Introduction to Mathematical Statistics and its Applications, Prentice-Hall, London.

Lovius L., 1998. Calculation of flux through boundaries in HYDRASTAR. Swedish Nuclear Fuel Management Co., SKB Progress Report PR U-98-08, Stockholm, Sweden.

Lovius L., and Eriksson L., 1993. Verification of HYDRASTAR version 1.4. Swedish Nuclear Fuel Management Co., SKB Working Report AR 93-46, Stockholm, Sweden.

Lovius L., and Eriksson L., 1994. Development of a Transient Version of HYDRASTAR. Swedish Nuclear Fuel Management Co., SKB Working report AR 94-12, Stockholm, Sweden.

Lusczynski N.J., 1961. Head and flow of ground water of variable density. Journal of Geophysical Research, 66(12), p 4247-4256.

Marsic N., 1998. Using STATISTICA and MATLAB when evaluating results from HYDRASTAR 1.5+, Swedish Nuclear Fuel and Waste Management Co., SKB Progress Report in press, Stockholm, Sweden.

McKenna S.A., and Rautman C.A., 1996. Scaling of material properties for Yucca Mountain: Literature review and numerical experiments on saturated hydraulic conductivity, Sandia Report SAND95-2338.

Morris S.T., and Cliffe K.A., 1994. Verification of HYDRASTAR: Analysis of hydraulic conductivity fields and dispersion. Swedish Nuclear Fuel Management Co., SKB Technical Report TR 94-21, Stockholm, Sweden.

Munier R., Sandstedt H., and Niland L., 1997. Förslag till principiella utformningar av förvar enligt KBS-3 för Aberg, Beberg and Ceberg. Swedish Nuclear Fuel Management Co., SKB Report R 97-09, Stockholm, Sweden.

Neuman S., 1988. A proposed conceptual framework and methodology for investigating flow and transport in Swedish crystalline rocks. Swedish Nuclear Fuel Management Co., SKB AR 88-37, Stockholm, Sweden.

Neuman S., and Depner J., 1988. Use of Variable-Scale Pressure Test Data To Estimate The Log_{10} Hydraulic Conductivity Covariance and Dispersivity of Fractured Granites Near Oracle, Arizona, Journal of Hydrology, 102, p 475-501.

Neuman S., and Jacobson E., 1984. Analysis of nonintrinsic spatial variability by residual kriging with application to regional groundwater levels. Mathematical Geology, 16(5), p 499-521.

Niemi A., 1995. Modelling of Äspö hydraulic conductivity data at different scales by means of 3-dimensional Monte Carlo simulations. Swedish Nuclear Fuel Management Co., SKB International Corporate Report ICR 95-08, Stockholm, Sweden.

Norman S., 1991. Verification of HYDRASTAR - A code for stochastic continuum simulation of groundwater flow. Swedish Nuclear Fuel Management Co., SKB Technical Report TR 91-27, Stockholm, Sweden.

Norman S., 1992a. HYDRASTAR - A code for stochastic simulation of groundwater flow. Swedish Nuclear Fuel Management Co., SKB Technical Report TR 92-12, Stockholm, Sweden.

Norman S., 1992b. Statistical inference and comparison of stochastic models for the hydraulic conductivity at the Finnsjön-site. Swedish Nuclear Fuel Management Co., SKB Technical Report TR 92-08, Stockholm, Sweden.

OECD, 1983. The International HYDROCOIN Project: Groundwater hydrology modelling strategies for performance assessment of nuclear waste disposal. Level: Code verification.

Renard Ph., de Marsily G., 1997. Calculating equivalent permeability: a review, Advance in Water Resources, 20(5-6), p 253-278.

Rhén I., and Forsmark T., 1993. Äspö Hard Rock Laboratory. Information for numerical modeling. Undisturbed piezometric levels and uncertainty of piezometric levels. Swedish Nuclear Fuel Management Co., SKB Technical Note 25-92-63G, Stockholm, Sweden.

Rhén I., Gustafson G., Stanfors R., and Wikberg P., 1997. Äspö Hard Rock Laboratory – Geoscientific Evaluation 1997/5. Models based on site characterisation 1986-1995. Swedish Nuclear Fuel Management Co., SKB Technical Report TR 97-06, Stockholm, Sweden.

Rubin Y., and Gómez-Hernández J.J., 1990. A stochastic approach to the problem of upscaling of conductivity in disordered media: Theory and unconditional numerical simulations. Water Resources Research, 26(4), p 691-701.

SKB, 1992. SKB 91: Final disposal of spent nuclear fuel. Importance of bedrock for safety. Swedish Nuclear Fuel Management Co., SKB Technical Report TR 92-20, Stockholm, Sweden.

SKB, 1996a. SR-95: Template for safety reports with descriptive example. Swedish Nuclear Fuel Management Co., SKB Technical Report TR 96-05, Stockholm, Sweden.

SKB, 1996b. User's Guide to HYDRASTAR 1.5. Swedish Nuclear Fuel Management Co., SKB Progress Report PR U-96-15, Stockholm, Sweden.

SKI, 1997. Report 97:5 Ski Site-94 Deep Repository Performance Assessment Project. Swedish Nuclear Fuel Management Co., Stockholm, Sweden.

Svensson U., 1997a. A regional analysis of groundwater flow and salinity distribution in the Äspö area. Swedish Nuclear Fuel Management Co., SKB Technical Report TR 97-09. Stockholm, Sweden.

Svensson U., 1997b. A site scale analysis of groundwater flow and salinity distribution in the Äspö area. Swedish Nuclear Fuel Management Co., SKB Technical Report TR 97-17, Stockholm, Sweden.

Walker D., and Bergman B., 1998. Verification of HYDRASTAR v.1.5 Inverse Modelling. Swedish Nuclear Fuel Management Co. Technical Report in preparation. Stockholm, Sweden.

Walker D., and Lovius L., Eriksson L., 1997a. Verification of HYDRASTAR 1.7: Nugget effect in geostatistical simulations. Swedish Nuclear Fuel Management Co., SKB Progress Report, U-97-22, Stockholm, Sweden.

Walker D., Rhén I., and Gurban I., 1997b. Summary of Hydrogeologic Conditions at Aberg, Beberg and Ceberg. Swedish Nuclear Fuel Management Co., SKB Technical Report 97-23. Stockholm, Sweden.

Ward D., Buss D., Mercer J., and Hughes S., 1987. Evaluation of a groundwater corrective action at the Chem-Dyne hazardous waste site using a telescopic mesh refinement modeling approach, Water Resour. Res., 23(4), p 603-617.

Widén H., and Walker D., 1998. SR 97 Alternative Modelling Project: Stochastic Continuum modelling of Aberg. Swedish Nuclear Fuel Management Co., SKB Progress Report in preparation, Stockholm, Sweden.

Wikberg P., Gustafson G., Rhén I., and Stanfors R. 1991. Äspö Hard Rock Laboratory. Evaluation and conceptual modelling based on the pre-investigations 1986-1990. Swedish Nuclear Management Co., SKB Technical Report TR 91-22, Stockholm, Sweden.

Winberg A., 1989. Analysis of Spatial Variability of Hydraulic Conductivity Data in the SKB Database GEOTAB, Swedish Nuclear Fuel Management Co., SKI Technical Report TR 89:12, Stockholm, Sweden.

Winberg A., 1994. Geostatistical analysis of transmissivity data from fracture zones at Äspö, Swedish Nuclear Fuel Management Co., SKB Progress Report PR 25-94-17, Stockholm, Sweden.

APPENDIX A. Definition of Statistical Measures

A.1 Floating Histograms

This study generally uses binned histograms to display the frequency distributions of the performance measures. The bin width of such histograms is determined by the default algorithms of Statistica. Although the bin width is somewhat subjective, binned histograms do provide a relatively unprocessed image of the data. However, binned histograms are not well-suited to graphical comparisons (e.g. overlaying multiple binned histograms is confusing to the eye).

An alternative method of constructing a frequency distribution histogram is to use a floating histogram. Floating histograms are single curved line representations of the frequency of the data. Although floating histograms are smoothed representations of the data, they are more legible when superimposed for the comparison of multiple histograms.

Statistica (Appendix F) calculates smoothed histograms using a moving window as a filter passing over the ordered sequence of the data. For each data value centred in the window, the frequency is calculated as the fraction of the data falling within the window. The width of the window in Statistica is set to $\pm \frac{1}{2}$ an order of magnitude around the data value in the centre of the window.

A.2 Statistical Significance of the Comparison of Distributions

Section 5 makes a number of comparisons of variant cases versus the Base Case or versus other variants, concluding that the 'distributions are significantly different'. This statement of significance is quantitatively supported by a statistical comparison of the distributions, testing the null hypothesis:

H_0: the distributions are the same

The significance of this test, or p-value, is the probability of rejecting H_0 when it is in fact true (a so-called Type I error). Thus, a small p-value indicates that we can safely reject the hypothesis that the distributions are the same (Larsen and Marx, 1986). Because the distributions to be compared in this study are skewed, they are not suited to test statistics that assume normally (Gaussian) distributed data. This study therefore uses nonparametric (distribution-free) test statistics to compute the p-value of the above test. The Kolmogorov-Smirnov test (K-S) is a nonparametric test used to compare distributional shapes (i.e., skewness, variability, and location), as documented in the

Statistica manual. The p-value of a K-S test of H_0 is computed for the various combinations of the Base and variant cases (Tables A-1, A-2, A-3, and A-4).

Note: When computing the p-value for the comparisons of log_{10} travel time distributions, times greater than the default maximum travel time of 10,000 years are deleted from the distributions prior to the comparison. The resulting K-S p-value therefore ignores the flow paths failing to exit the upper surface of the model.

Table A-1 Test for Similarity of Travel Time Distributions (Kolmogorov-Smirnov 2-sample).

Case	Base Case	Variant 2	Variant 3.1	Variant 3.2	Variant 4.1	Variant 4.2
Base Case	-	Reject (p<0.001)	Reject (p<0.001)	Reject (p<0.001)	Reject (p<0.001)	Reject (p<0.001)
Variant 2	Reject (p<0.001)	-	Reject (p<0.001)	Reject (p<0.001)	Reject (p<0.001)	Reject (p<0.001)
Variant 3.1	Reject (p<0.001)	Reject (p<0.001)	-	Reject (p<0.001)	Reject (p<0.001)	Reject (p<0.001)
Variant 3.2	Reject (p<0.001)	Reject (p<0.001)	Reject (p<0.001)	-	Reject (p<0.001)	Reject (p<0.001)
Variant 4.1	Reject (p<0.001)	Reject (p<0.001)	Reject (p<0.001)	Reject (p<0.001)	-	Reject (p<0.001)
Variant 4.2	Reject (p<0.001)	Reject (p<0.001)	Reject (p<0.001)	Reject (p<0.001)	Reject (p<0.001)	-

Table A-2 Test for Similarity of Canister Flux Distributions (Kolmogorov-Smirnov 2-sample).

Case	Base Case	Variant 2	Variant 3.1	Variant 3.2	Variant 4.1	Variant 4.2
Base Case	-	Reject (p<0.001)	Reject (p<0.025)	Reject (p<0.001)	Reject (p<0.001)	Reject (p<0.001)
Variant 2	Reject (p<0.001)	-	Reject (p<0.001)	Reject (p<0.001)	Reject (p<0.001)	Reject (p<0.001)
Variant 3.1	Reject (p<0.025)	Reject (p<0.001)	-	Reject (p<0.001)	Reject (p<0.001)	Reject (p<0.001)
Variant 3.2	Reject (p<0.001)	Reject (p<0.001)	Reject (p<0.001)	-	Reject (p<0.001)	Reject (p<0.001)
Variant 4.1	Reject (p<0.001)	Reject (p<0.001)	Reject (p<0.001)	Reject (p<0.001)	-	Reject (p<0.001)
Variant 4.2	Reject (p<0.001)	Reject (p<0.001)	Reject (p<0.001)	Reject (p<0.001)	Reject (p<0.001)	-

Table A-3 Test for Similarity of Travel Time Distributions in Variant 1 (Kolmogorov-Smirnov 2-sample test, for a single realisation).

Case	Variant 1.1	Variant 1.2	Variant 1.3	Variant 1.4a	Variant 1.4b	Variant 1.4c
Variant 1.1	-	Accept (p>0.1)	Accept (p>0.1)	Reject (p<0.001)	Reject (p<0.001)	Reject (p<0.001)
Variant 1.2	Accept (p>0.1)	-	Accept (p>0.1)	Reject (p<0.001)	Reject (p<0.001)	Reject (p<0.001)
Variant 1.3	Accept (p>0.1)	Accept (p>0.1)	-	Reject (p<0.001)	Reject (p<0.001)	Reject (p<0.001)
Variant 1.4a	Reject (p<0.001)	Reject (p<0.001)	Reject (p<0.001)	-	Reject (p<0.005)	Reject (p<0.001)
Variant 1.4b	Reject (p<0.001)	Reject (p<0.001)	Reject (p<0.001)	Reject (p<0.005)	-	Accept (p>0.1)
Variant 1.4c	Reject (p<0.001)	Reject (p<0.001)	Reject (p<0.001)	Reject (p<0.001)	Accept (p>0.1)	-

Table A-4 Test for Similarity of Canister Flux Distributions (Kolmogorov-Smirnov 2-sample test, for a single realisation).

Case	Variant 1.1	Variant 1.2	Variant 1.3	Variant 1.4a	Variant 1.4b	Variant 1.4c
Variant 1.1	-	Accept (p>0.1)	Accept (p>0.1)	Reject (p<0.001)	Reject (p<0.001)	Reject (p<0.005)
Variant 1.2	Accept (p>0.1)	-	Accept (p>0.1)	Reject (p<0.001)	Reject (p<0.001)	Reject (p<0.005)
Variant 1.3	Accept (p>0.1)	Accept (p>0.1)	-	Reject (p<0.001)	Reject (p<0.001)	Reject (p<0.001)
Variant 1.4a	Reject (p<0.001)	Reject (p<0.001)	Reject (p<0.001)	-	Accept (p>0.1)	Accept (p>0.1)
Variant 1.4b	Reject (p<0.001)	Reject (p<0.001)	Reject (p<0.001)	Accept (p>0.1)	-	Accept (p>0.1)
Variant 1.4c	Reject (p<0.005)	Reject (p<0.005)	Reject (p<0.001)	Accept (p>0.1)	Accept (p>0.1)	-

APPENDIX B. Supplemental Regional Simulations

B.1 Approach

This application of HYDRASTAR employs a nested modelling strategy, with the site-scale model taking its boundary conditions from a regional model of much greater extent. Because the area is adjacent to the brackish Baltic Sea, it is possible that saltwater intrusion of Baltic sea water may create density dependent effect. However, HYDRASTAR cannot incorporate these effects directly, and must adapt the regional model heads to freshwater equivalent conditions. Similarly, regional models of hydraulic conductivity are uncertain; some authors have suggested stochastic models on the regional scale, whereas others have suggested deterministic (Walker et al, 1997b).

This section of the report describes the regional boundary conditions and the methods used to transfer these conditions to the site-scale HYDRASTAR model. For the purpose of this modelling study, Urban Svensson of CFE was contracted to perform supplementary simulations using the Aberg regional model described in Svensson (1997a). The resulting pressures, salinities and fluxes were delivered on a 100 m grid for variants 1.1, 1.2 and 1.3, and then interpolated to the site scale model grid as described below. Variant 1.4 addressed the feasibility of using simplified boundary conditions. The variants to study the influence of the boundary conditions are as follows:

1.1   Deterministic, effective hydraulic conductivity and freshwater conditions (i.e., the Base Case discussed in Sections 4.1 and 4.2).

1.2   Regional model with a single stochastic realisation of hydraulic conductivity and the observed salinity. The resulting boundary pressures and salinities are converted to environmental freshwater heads.

1.3   Regional model with a single stochastic realisation of hydraulic conductivity and freshwater conditions.

1.4   Simplified boundary conditions obtained from estimated watertable using topography data and sea level.

B.2 Transferring Boundary Conditions from PHOENICS to HYDRASTAR

The PHOENICS regional boundary condition values for each case were delivered in two files, one for the top surface and one for the other sides of the model. The files contain coordinates and the corresponding fluid pressures in PA. The values are given for a 100 m grid and need to be transferred to the 25 m block size used in the site scale model. The pressures at the vertical sides and the bottom are given in one file, and the pressures at the top are given in another. These data are processed for HYDRASTAR input as follows:

1. The files (e.g. Press and Pz0) are concatenated to one file.

2. The file is sorted for x, y, z letting the corresponding pressure value follow using e.g. Excel

3. The sorted file is processed using a MATLAB script, which:

    - reads the concatenated pressure file and a file with the local model coordinates,

    - interpolates the values to 25 m for each face, using 2D linear interpolation,

    - visualises the interpolated values, and

    - writes it to a file named hypac.out, in HYDRASTAR format.

4. The file is transferred to the SKB Convex for use.

The 2D interpolation of head values is the same approach used by similar nested modelling studies (Ward et al., 1987; Leake et al., 1998).

B.3 Environmental Head

For Variant 1.2, the regional model includes the effects of salinity. This necessitates an additional step to transfer boundary heads to the site-scale model, since HYDRASTAR does not address salinity dependence. One method for converting from saline water head to freshwater head is to calculate the environmental head (or density adjusted head). The environmental head (Lusczynski, 1961) is calculated as:

$$H_e = \frac{P - \int_{z_0}^{z} (\rho - \rho_0) g \, dz}{\rho_0 g}$$

where P is the pressure, ρ is the density of saline water, ρ_0 is the density of fresh water, z is the vertical distance to the reference datum z_0, and g is the acceleration of gravity.

B.4 Simplified Boundary Conditions

Boundary conditions for Variant 1.4 were derived from topographic data (data delivery from Ragnar Ström, SKB). The files, SITE20_4.DAT (elevation data in XYZ format – 20 m spacing), SITE20_4.GRD (elevation data in SURFER grid format – 20 m spacing) and ASPOKUST.BNA (coastline), were received May 4, 1998. The topographic data were converted into head boundary conditions for the top of the model domain by interpolation of elevation data to 25 m grid, estimation of water table and conversion into HYDRASTAR format i.e. in PA. The interpolated topography is shown in Figure B.1. Mean sea level was used for area covered by the Baltic sea.

The estimation of the water table, W.T., was calculated by:

$$W.T. = 0.333Z - 0.39 \ (m)$$

constrained by W.T. greater or equal to zero.
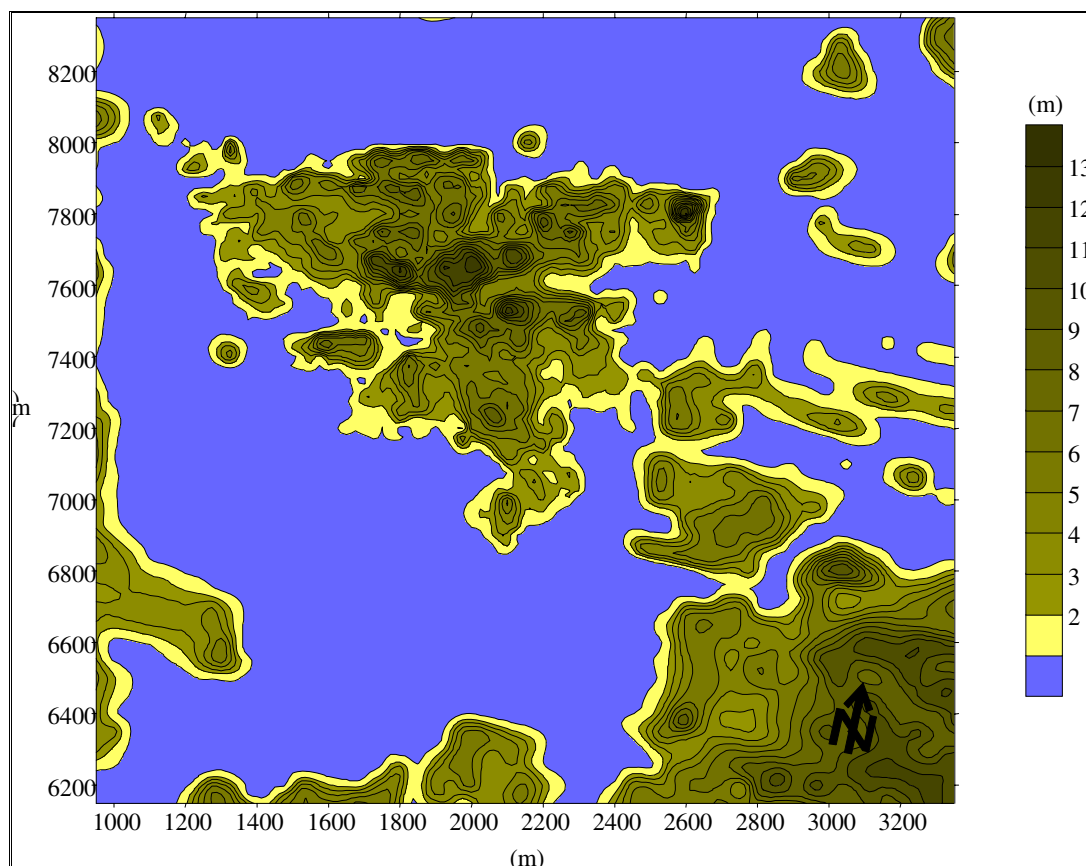
Figure B.1. The topography and sea level at the modelling region.

Three approaches were tested for the lateral and bottom boundary conditions. Variant 1.4a uses topographic head on the top, depth dependent head on the vertical sides and hydrostatic head on the bottom. The resulting gradient ignores vertical gradients along

the model sides, allowing many stream tubes to exit the model's lateral boundaries, as shown in the pattern of exit locations shown in Figure B.2. This is thought to be an unrealistic representation, and is not pursued further.

In Variant 1.4b, no-flow boundary conditions were used on all sides except the top, where the same topographic boundary conditions is used as in Variant 1.4a. In Variant 1.4c, hydrostatic head was used on the vertical sides and no-flow condition on the bottom (Figure B.3). Approach 1.4b results in all of the stream tubes arriving at the model's upper surface. Approach 1.4c gives statistics more like the Base Case.
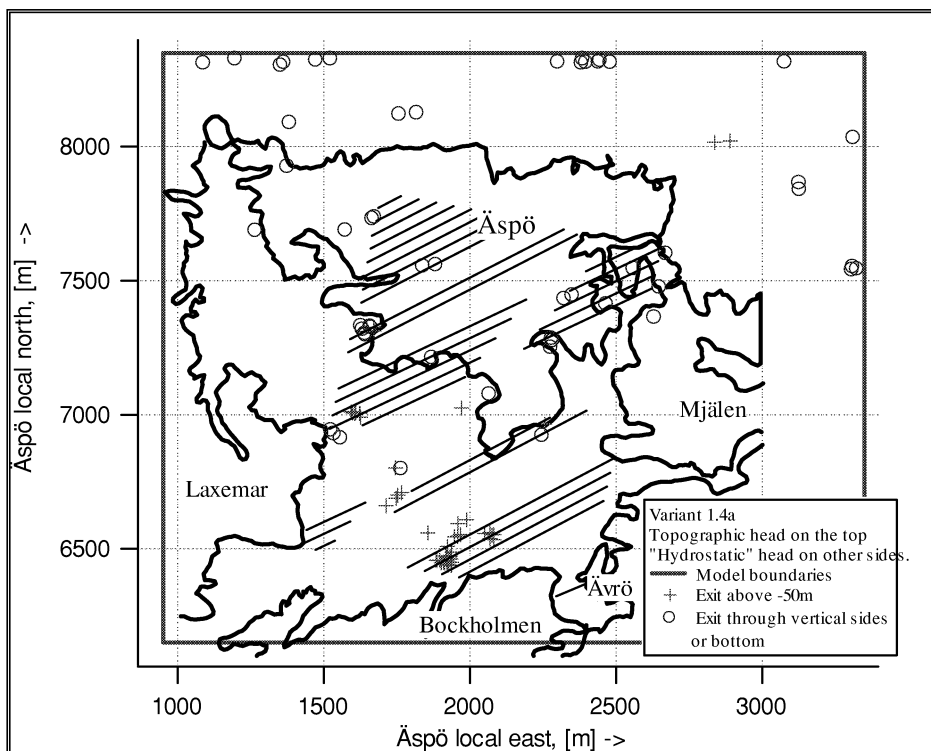
Figure B.2. Exit locations in Variant 1.4a. Boundary conditions on the surface based on the topography and hydrostatic head on the vertical sides and bottom.
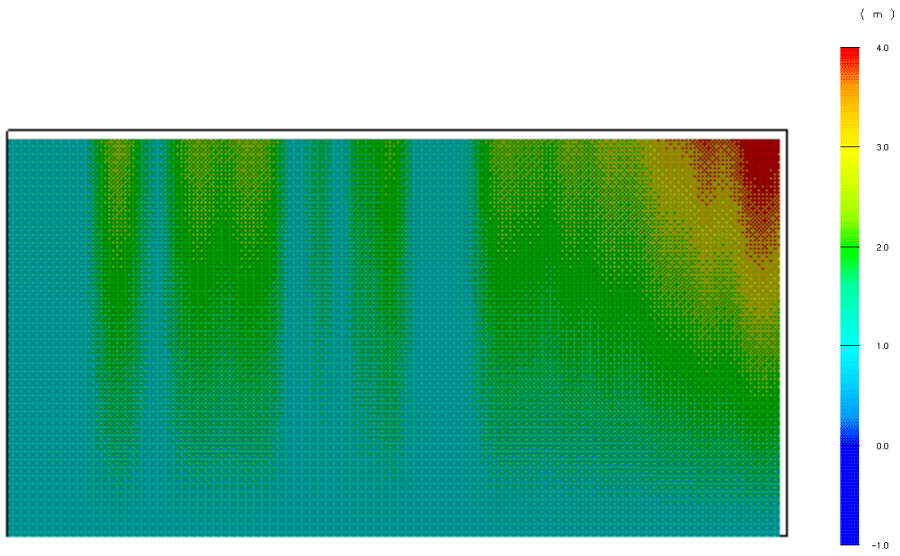
Figure B.3. Boundary conditions on the southern side forVariant 1.4c.

APPENDIX C. Supplemental Calculations

C.1 Inference of Anisotropic Variogram

HYDRASTAR requires a stochastic description of hydraulic conductivity at the model grid scale, including the expected value of hydraulic conductivity and its spatial variogram. This is complicated by the suggestion of Rhén et al. (1997) that the host rocks at Äspö exhibit hydraulic anisotropy – a feature that HYDRASTAR cannot directly include in its simulations. In addition, the upscaling method in HYDRASTAR and INFERENS is heuristic even for scalars, and was not developed to account for hydraulic anisotropy. However, for the purposes of SR 97, this study evaluates the effects of hydraulic anisotropy on the performance assessment.

Gutjahr et al. (1978) found that a large-scale hydraulic anisotropy can evolve from isotropic (scalar) point values of hydraulic conductivities with an anisotropic spatial variogram. That is, the anisotropic variogram of isotropic point hydraulic conductivities creates a large-scale anisotropic effective hydraulic conductivity. The following Sections describe an attempt to exploit this relationship and infer an anisotropy variogram for the Äspö site, following an approach similar to that of Neuman and Depner (1988).

C.1.1 Theory

Gutjahr et al. (1978) used a first-order, perturbation approach to determine that the three-dimensional statistically anisotropic effective conductivity can be expressed as:

$$K_{ii} = K_g \left[1 + \sigma^2_{\ln K} \left(\frac{1}{2} - g_{ii} \right) \right]$$

(C.1)

$i = 1, 2, 3$ (no sum on i)

Where:

$$g_{ii} = \int\int\int_{-\infty}^{\infty} \frac{k_i k_j}{k^2} \frac{\lambda_1 \lambda_2 \lambda_3 dk_2 dk_3}{\pi^2 (1+u^2)^2}$$

$$u^2 = \lambda_1^2 k_1^2 + \lambda_2^2 k_2^2 + \lambda_3^2 k_3^2$$

K_{ii} = the components of the anisotropic effective conductivity, K_e

$\mathrm{Ln}K$ = natural logarithm of the point values of hydraulic conductivity (isotropic).

K_g = the geometric mean of K

λ_i = the integral scale of the variogram of ln$K$ in direction i

k_i = the spectrum of ln$K$ in direction i.

Also note that Gelhar and Axness (1983) suggested that equation C.1 could be extrapolated to larger values of σ_{lnK} using:

$$K_{ii} = K_g \exp\left[\sigma^2_{\ln K}\left(\frac{1}{2} - g_{ii}\right)\right] \qquad (C.2)$$

This solution suggests that, although ln$K$ is hydraulically isotropic, the anisotropic variogram of ln$K$ creates an effective hydraulic conductivity that is hydraulically anisotropic. Further, it suggests that the components of an anisotropic effective hydraulic conductivity, K_e, can be estimated from the mean and anisotropic variogram of ln$K$.

At many sites, boreholes are subvertical and the horizontal spacing is such that only the vertical component of the variogram can be estimated using traditional geostatistical methods (Winberg, 1989; La Pointe 1994). In this situation, Hufschmied (1986) and Neuman and Depner (1988) suggested that, if one knew K_{ii} from interference tests and the vertical variogram and K_g from packer tests, it would be possible to estimate λ_i, the remaining components of the anisotropic variogram of LnK. Neuman and Depner began by rearranging equation C.2 to

$$g_{ii} = \frac{1}{2} + \left(\ln K_{ii} - K_g\right)\sigma^{-2}_{\ln K} \qquad (C.3)$$

If, for example, we could estimate K^*_{ii} via interference tests, and estimate K_g^* and σ^{2*}_{lnK} via packer tests, we could therefore estimate g^*_{ii} via the above. However, g_{ii}^* also should be approximately equal to:

$$\hat{g}_{ii} = F_{ii}\sigma^{-2}_{\ln K} \qquad (C.4)$$

Where F_{ii} found as a function of $\hat{\lambda}_i$ via numerical integration. Neuman and Depner force this by requiring $\hat{g}_{11} \equiv 1 - \hat{g}_{22} - \hat{g}_{33}$ and then minimising $\left(\hat{g}_{22} - g^*_{22}\right)^2 + \left(\hat{g}_{33} - g^*_{33}\right)^2$ by repeated guesses of $\hat{\lambda}_i$.

C.1.2 Algorithm

In summary, the algorithm for estimating the components of the variogram is:

1. Estimate K^*_{ii} from cross-hole interference tests, K^*_g from packer tests, and σ^{2*}_{lnK} from packer tests, then calculate estimate g_{ii}^* by substituting into equation C.3. Note that we also constrain $\Sigma g^*_{ij} = 1$ and force $g_{11} = 1 - g_{22} - g_{33}$.

2. Use the plots of g_{ii} versus $\lambda_1/\lambda_2, \lambda_1/\lambda_3$ from Gelhar and Axness (1983, figures 4a and b) to estimate $\hat{\lambda}_i$ by successive guesses. Note that we solve for λ_2 and λ_1 using λ_3 = vertical range determined from the observed point variogram estimates.

3. Apply the ratios $\lambda_1/\lambda_2, \lambda_1/\lambda_3$ to the upscaled isotropic variogram, previously determined via application of INFERENS (Walker et al., 1997).

The algorithm described above differs from that proposed by Neuman and Depner (1988) in several respects. The components of K_{ii} are taken from Rhén's analysis of multidirectional probehole tests, rather than a large scale, multidirectional test for anisotropy. Additionally, values for the numerical integration in (1) are taken from plots provided in Gelhar and Axness (1983, plots 4a and 4b), and thus the minimisation Ω is found only approximately.

There are several reasonable concerns regarding the applicability of this algorithm to this problem. These include that the components K_{ii} are grossly estimated from probehole data, and that the integral scale λ is weakly defined by field data. Follin (1992) suggests that the solutions of Gutjahr et al (1978) may not be valid for fractured media since they assume that the point hydraulic conductivity is isotropic. The HYDRASTAR upscaling algorithm is heuristic, and does not specifically address anisotropy. We might speculate, for example, that the block conductivities should include both hydraulic and stochastic anisotropy, since the block scale lies between the two extremes of point and infinite scale (Indelman and Dagan, 1993).

C.1.3 Application

Programs from GSLIB are used to analyse the 3 m data in the rock domain (i.e., deterministic fracture zones excluded) within the tunnel spiral (SRD3) to estimate the directional variograms. The median indicator variograms are used as robust-resistant estimators to augment the traditional variogram (Figures C.1, C.2 and C.3). The vertical direction is reasonably well defined with a practical range of around 80 m (correlation integral scale of 13 m). The other directions have virtually no pairs until 100 m separation, and are erratic beyond that distance (Figures C.4, C.5, and C.6).

Rhén et al. (1997) suggested an anisotropy of 100:1:10 for NW:NE:vertical hydraulic conductivity, which Svensson (1997a) applied using

$$10*S : S/10 : S$$

where S = the hydraulic conductivity in SRD3 (at the appropriate scale).

The algorithm described in Section C.1.2 was used to infer variograms in the NW and NE directions, given the vertical variogram and Rhén's estimate. The results suggest that, at the 3 m scale, a suitable anisotropic variogram would be:

C_0 (nugget) = 8.3, C1 (sill) = 7.2,

Practical Ranges: NW = 120 m, NE = 60 m, Vertical = 80 m

Note that, because the nugget is 50% of the total variance, the correlation integral scales are approximately 20, 10, and 15 m. This suggests that the zero nugget, isotropic exponential model fitted by INFERENS be converted to an anisotropic model using the anisotropy ratio 2:1:1.5 (for NW:NE:Vertical practical ranges). Preserving the vertical range, this yields practical ranges of approximately 129:65:97 m.

Note that the finite difference grid spacing is 25 m, and that this is larger than the shortest integral scale determined above (i.e., 65 m/3 < 25 m). Thus we should anticipate that the model grid is too coarse to implement this ratio (Bergman and Walker, 1998). This study consequently simplifies the ratio to 2:1:1, and uses 10:1:1 to assess the uncertainty. It is reasonable to expect that this will result in a one-dimensional large-scale effective anisotropy with the major axis in the NW direction.
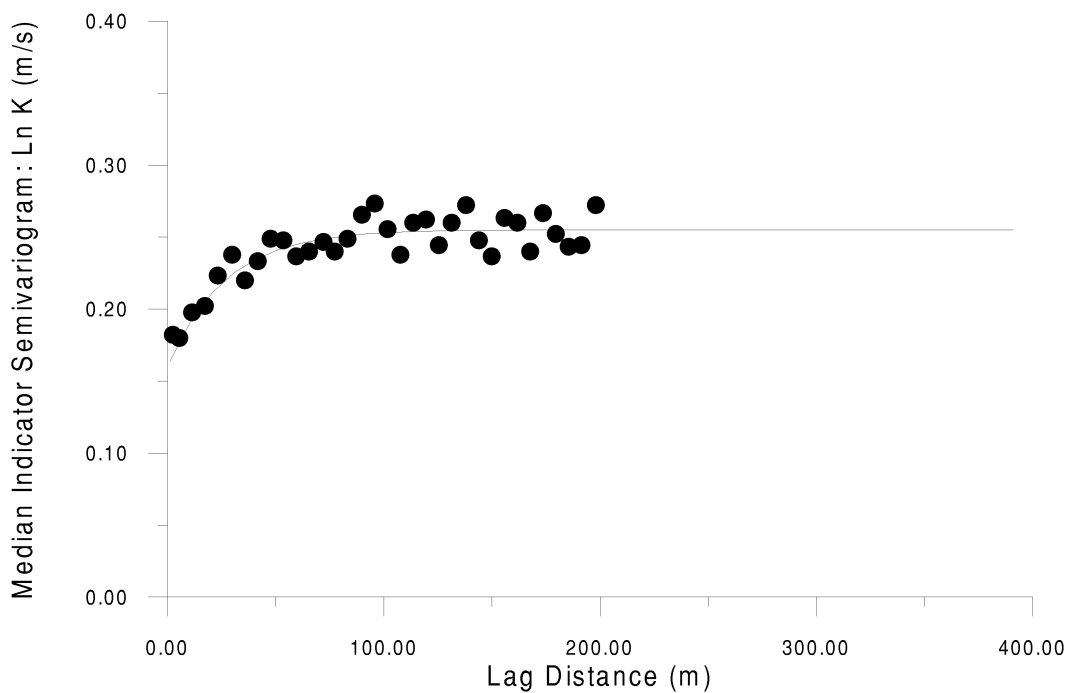
Figure C.1 Median Indicator variogram, vertical direction. 3 m Äspö data in rock domain.
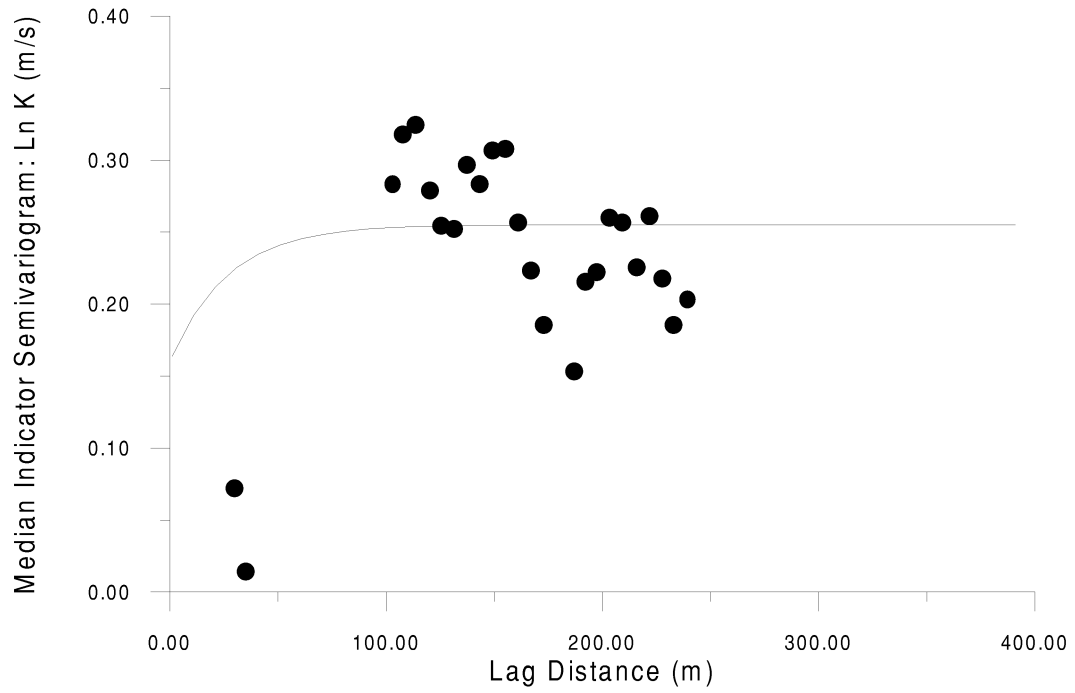
Figure C.2 Median Indicator variogram, Northwest direction. 3 m Äspö data in rock domain.
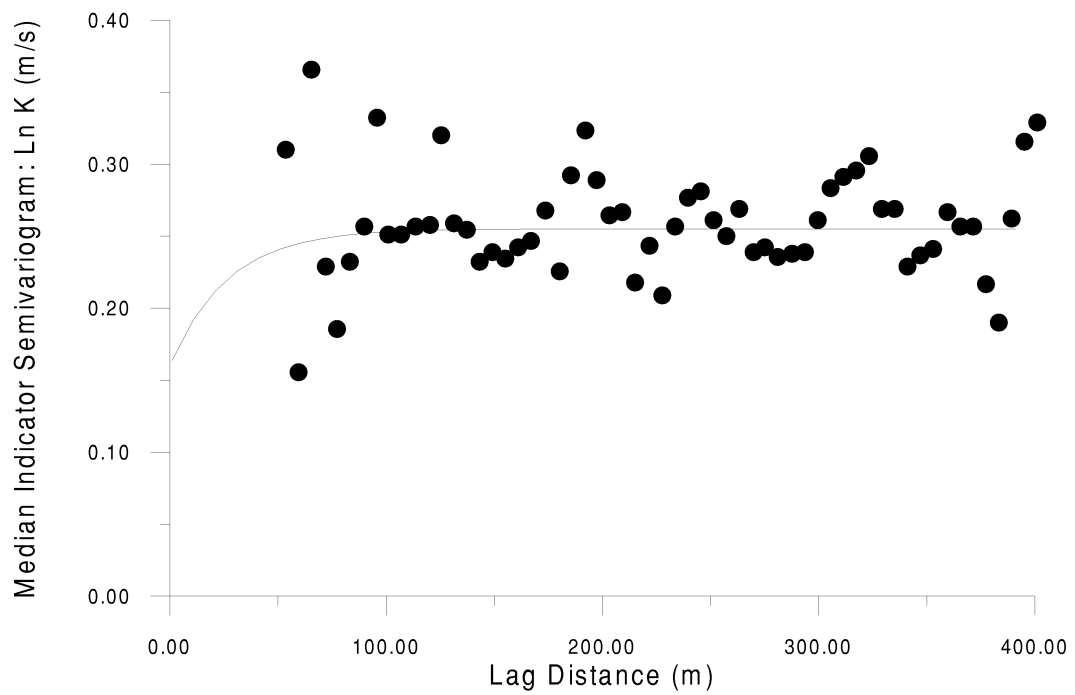
Figure C.3 Median Indicator variogram, Northeast direction. 3 m Äspö data in rock domain.
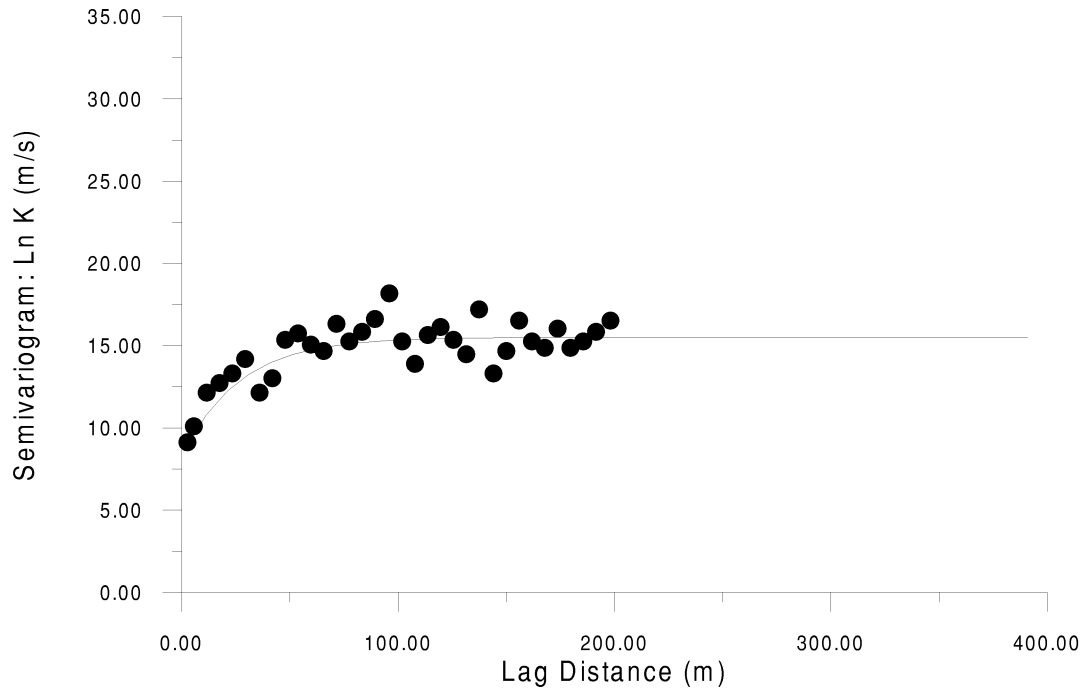
Figure C.4 Variogram, Vertical direction. 3 m Äspö data in rock domain.
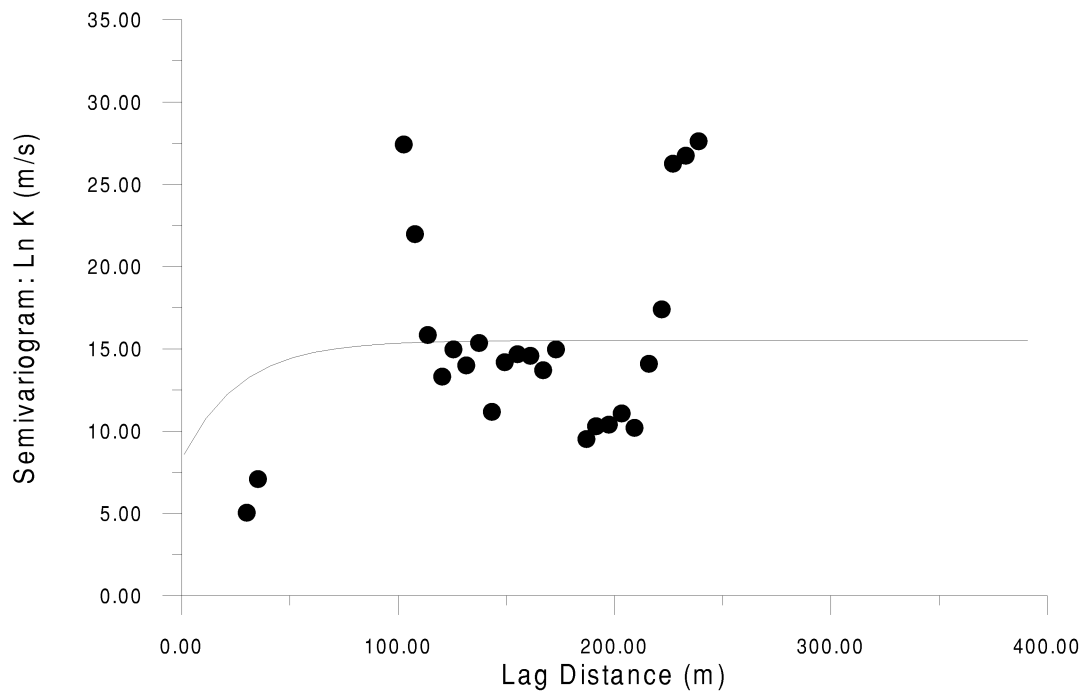
Figure C.5 Variogram, Northwest direction. 3 m Äspö data in rock domain.
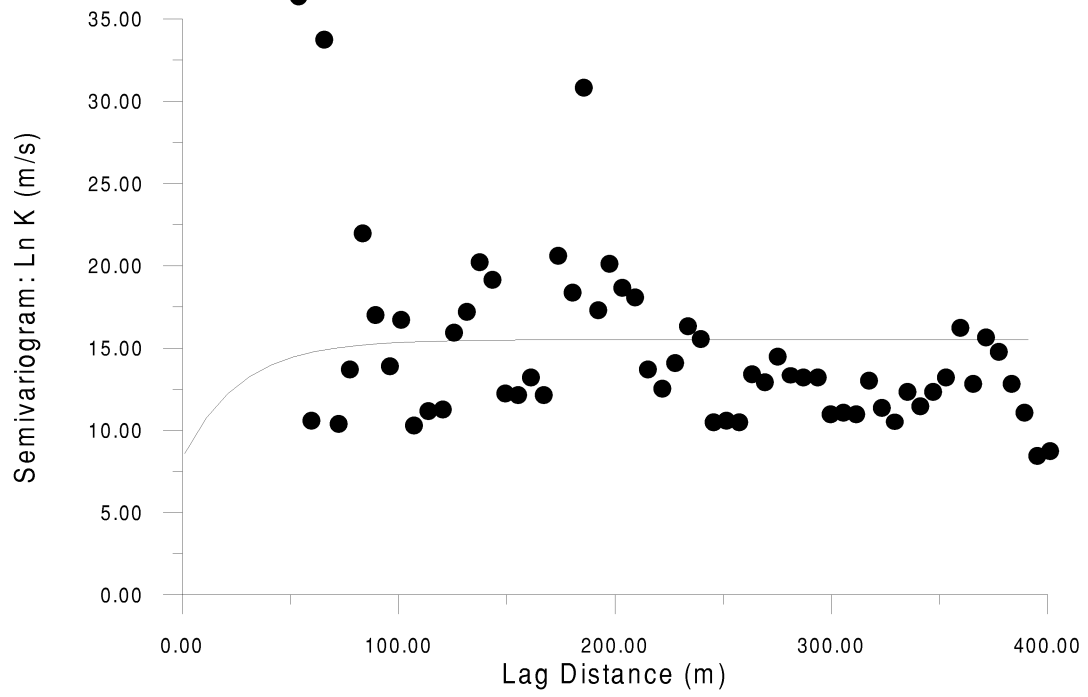
Figure C.6 Variogram, Northeast direction. 3 m Äspö data in rock domain.

C.2 Upscaling of Hydraulic Conductivity Model

C.2.1 Approach

The injection and pumping tests performed in the cored boreholes and tunnel probeholes are the principal source of hydraulic conductivity data. These tests were interpreted and the measurements reported for various depths, rock types, etc. as described by Rhén et al. (1997). The interpreted hydraulic conductivities for the 3 m packer tests were taken directly from the SKB SICADA database and analysed with the SKB geostatistical inference code INFERENS.

The scale of these measurements (as inferred from the packer length) is much different from the proposed model grid scale. As discussed in Walker et al. (1997b), hydraulic conductivity is a scale-dependent parameter, which requires that the measured hydraulic conductivities be upscaled to the finite difference grid scale of the model. Thus, HYDRASTAR requires that the geometric means of interpreted hydraulic conductivities found in SICADA must be rescaled. This study uses the scaling relationship provided in Rhén et al. (1997), which assumes that the geometric mean of hydraulic conductivity at the measurement scale, L_m, may be adjusted for scale using the regression equation:

$$Log_{10}K_{gu} = Log_{10}K_{gm} + 0.782(Log_{10}L_u - Log_{10}L_m)$$

where:

K_g = geometric mean of hydraulic conductivity (m/s)

L = length scale (m), assumed equal to the packer interval.

The subscripts m and u refer to the measurement and upscaled values, respectively. Rhén et al. (1997) developed this empirical scaling relationship using the 3 m, 30 m, 100 m packer tests and full-length tests in the same cored boreholes.

C.2.2 Upscaling and Inference for 50 m Scale

This inference of spatial correlation models for Aberg site-scale hydraulic conductivity begins by dividing the domain into SRD1 through 5, the SCD. The elevation zones, SRD, and SCD are treated as step changes in the mean of log_{10} conductivities, and a single variogram model is inferred for the entire domain (i.e., the same variogram for SRD and SCD). As discussed in Walker et al. (1997b), the correct approach to the upscaling of hydraulic conductivities to the numerical grid block is not known. As an interim approach, this study uses the Äspö scaling relationships of Rhén et al. (1997) to determine the geometric mean of hydraulic conductivity in each SRD and depth zone (Appendix C.2.1). The effect of upscaling on the variogram is determined by applying the Moye's formula-based regularisation algorithm and fitting a variogram–trend model via iterative generalised least squares estimation (IGLSE; see Neuman and Jacobsen,

1984) to the regularised data. The SKB program INFERENS, which includes the Moye's formula-based regularisation, automates the IGLSE fitting algorithm. Program restrictions of HYDRASTAR and INFERENS limit the geostatistical model to one variogram model for both domains. Because the majority of the 3 m packer tests fall in the SRDs and this data yields a clearer variogram, the geostatistical model will be developed from the interpreted hydraulic conductivities in the SRDs.

Walker et al. (1997b) explores the data and fits a model for the 24 m scale. This study merely repeats the INFERENS fitting using a 50 m regularisation scale, and applies the Äspö scale relationships to determine the geometric mean (Kg) at the 50 m scale. The resulting experimental and model variograms are shown in Figure 5.2-1, and the upscaled Kg is presented in Table 5.2-1 . The effect of the upscaling is to decrease the total variance of the experimental variogram and to increase the practical range.

C.3 Scoping Calculation for Approximate Travel Times

The purpose of this section is to provide rough estimations of travel times to be used as check on the model results. It uses Darcy's law applied to a single travel path, with the hydraulic gradient roughly estimated from the observed watertable.

C.3.1 Approach

The approach is to apply Darcy's Law and use the hydraulic gradient (∇h) and hydraulic conductivity (K) from various reports. The apparent velocity (V_a) is found by:

Darcy's Law: $\qquad V_a = K\nabla h$ $\qquad\qquad\qquad$ (C.3.1)

The gradient is calculated by using the difference in watertable divided by the horizontal distances between the release and the exit locations.

Hydraulic gradient: $\qquad \nabla h = \dfrac{h_{exit} - h_{start}}{Distance}$ $\qquad\qquad$ (C.3.2)

The average particle velocity (V_{mean}) is given by dividing the apparent velocity (V_a) by the porosity ρ.

Average particle velocity: $\qquad V_{mean} = \dfrac{V_a}{\rho}$ $\qquad\qquad$ (C.3.3)

The porosity is given a fixed value of ρ=1e-4 for all calculations. The travel times for the average particle is then given by

Travel times: $\qquad\qquad travel\,time = \dfrac{Travel\,lenght}{V_{mean}}$ $\qquad$ (C.3.4)

C.3.2 Application

The gradient is difficult to estimate due to the complexity of the flow pattern. For this scoping calculation, we assumed that the hydraulic head at the starting position could be estimated as the water table elevation immediately above the starting position of interest. The head at the exit location was taken to be sea level. For Aberg the watertable is taken from Figure 2-15, SKB 97-23.

The horizontal distances were measure at the map provided in Figure 2-17, SKB 97-23 with the block location found in SKB R-97-09. The values for the hydraulic conductivity used are taken from Table 2-8 and table 2-9 in SKB 97-23.

Three paths are considered:

- Path one: Start point in middle of Block 1 at –600 masl following a straight line trough SRD 1 up to surface with exit point 310 m north of start point. This represents a "slow" pathway.

- Path two: Start point in south part of block 4 at –600 masl following fracture NE-1a up to surface 270 m south of start point. This represents a "fast" pathway.

- Path three: Start point in middle part of block 1 at –500 masl south trough rock mass in 150 m to EW-1N, then within EW-1N east 400 m up to surface. This represents an "expected" pathway.

Path 1			
Hydraulic Gradient		0,01612903	
Rock mass	Travel length	$Log10\ K_3$	$Log10\ K_{24}$
SRD 1	675	-8.74	-8.03
Travel Times	K_3	K_{24}	
SRD 1	72.9 yr	14.2 yr	

Path 2			
Hydraulic Gradient		0,0037037	
Fracture	Travel length	$Log10\ K_{100}$	$Log10\ K_{24}$
NE-1	657	-5	-5.48
Travel Times	K_{100}	K_{24}	
NE-1	0.0563 yr	0.170 yr	

Path3			
Hydraulic Gradient	SRD 1		0.02
		EW-1N	0.005
Fracture		Travel length	Log10 K_{24}
SRD 1		190	-8.03
EW-1N		500	-7.79
Total		690	
Travel Times		K_{24}	
SRD 1		3.22787716	
EW-1N		19.5520992	
Total		22.8 yr	

C.4 Error Analysis of Observed versus Model Simulated Heads

According to Anderson & Woessner (1992, p229), the acceptable level of head error (calibration target) for groundwater model is the sum of several independent errors, expressed as:

$$\sigma_T = \sigma_m + \sigma_i + \sigma_h + \sigma_t \qquad (C.4.1)$$

where :

σ_T = the maximum acceptable total error of simulated vs. observed heads

σ_m = measurement error

σ_i = interpolation error

σ_h = Scale-up error arising from heterogeneity

σ_t = error arising from unmodelled transient effects

Rhén and Forsmark (1993) analyzed the Äspö piezometric data and reported that, for head measurements of 10 m or less, the total estimated measurement error in packed sections was $\sigma_m \leq 0.15$ m and $\sigma_m \leq 0.06$ m in open boreholes.

For this grid size, 25 m, the interpolation error would be the maximum difference in head (from the model simulated head at the node)that could be seen within a grid block. This would be the gradient times the maximum distance:

$$\sigma_i = J \cdot d_{max}. \qquad (C.4.2)$$

where

J = gradient, which at Äspö is approximately 0.02 m/m

d_{max} is the distance from the block centre to the farthest corner in the block

$$d_{max} = \left[(17.7)^2 + (12.5)^2\right]^{\frac{1}{2}} = 21.7m$$

so that

$$\sigma_i = (0.02)(21.7) = 0.433m$$

The error due to heterogeneity is difficult to quantify, since we should expect that each Monte Carlo realisation should be different from the next. Gelhar (1986) suggests that heterogeneity results in head variability that can be expressed as:

$$\sigma_h^2 = \frac{1}{3}J^2\sigma_{\ln K}^2\lambda^2 \qquad \text{in isotropic, 3-D fields} \qquad (C.4.3)$$

Where

λ = integral scale (isotropic), which at Äspö is approximately 32.3 m

$\sigma_{\log K}^2$ = 2.7, which is approximately $\sigma_{\ln K}^2$ = 14.0

so that

$$\sigma_h = \left\{\frac{(0.02)^2(14.0)(32.33)^2}{3}\right\}^{1/2} = 1.40m$$

This error is large because the variance $\sigma_{\ln K}^2$ is large. Although this expression for σ_h is thought to be valid only for $\sigma_{\ln K}^2 \leq 1.0$ (Bakr, et al., 1978), it has been shown to be valid for much larger variances. (Gelhar, 1993). Note that, strictly speaking, equation C.4.3 was derived considering the unmodelled heterogeneity of a domain when the model is represented by a uniform effective conductivity. We attempt to model this heterogeneity in each Monte Carlo realisation, and thus this variance assumed to address the Monte Carlo variability as well.

Transient effects are also difficult to quantity. Rhén and Forsmark (1993) provide the max and min measured heads during 1990 & 1991. If we assume that the data is normally distributed and the range corresponds to a 95% confidence interval, then

$$\sigma_{heads} = \frac{\text{max} - ave}{1.96}$$

so that the variance of the mean head is

$$\sigma_t = \sigma_{ave} = \frac{\sigma_{heads}}{\sqrt{n}}$$

The number of measurements, *n*, is not given in Rhén and Forsmark (1993), but should be on the order of 100. For the sections selected for examination, (max-ave) < 2.0 m, so that $\sigma_{heads} = O(1)$ so that $\sigma_t = 0(10^{-1})$ and thus negligible relative to the other errors

In summary, the calibration target given in equation 1 is:

$$\sigma_T = 0.15 + 0.433 + 1.4 + (0.1) = 2.0 \text{ m (in open boreholes)}$$

and

$$\sigma_T = 0.06 + 0.433 + 1.4 + (0.1) = 1.9 \text{ m (in packed sections)}$$

APPENDIX D. Summary of Input Parameters

Table D-1 Mechanisms and model parameters considered in this study when modelling groundwater flow at Aberg using HYDRASTAR.

Mechanism	HYDRASTAR model parameter		Source
	Symbol (unit)	Description	
Topographically driven flow	-	Fracture zone and rock domain geometries	Based on the interpreted geologic structural model for the site, TR 97-06, Table A2-6
	T (m^2/s)	Fracture zone transmissivities	Based on the interpreted geohydrological model for the site, TR 97-06, Tables A2-7 and A2-8. 100m interference tests rescaled as described in Section 3.0
	K (m/s)	Rock mass hydraulic conductivity	Based on the interpreted geohydrological model for the site (TR 97-06) and single-hole water injection tests on 3m scale. These tests are the basis for geostatistical analysis and are used directly in conditional simulation. Upscaling as described in Section 3.0. See Appendix C.
	S_s (m^{-1})	Specific storativity. Necessary for transient simulations.	Not used
	-	Top boundary condition	Constant head, as provided by Svensson. See Appendix B. Files: Pz0, Press
	-	Vertical/lower boundary conditions	Constant head, as provided by Svensson. See Appendix B. Files: Press
	–	BC Variant cases	1.2 TR 97-09 as environmental head, Files: Psz0, Ps 1.3 TR 97-09 as freshwater head, Files: Pz0, PressVert 1.4: see Appendix B of this report
	ε_f (-)	Flow porosity Necessary for travel time calculation, but is poorly known in general	From TR 97-06, uniform throughout model at $\varepsilon_f=1\times10^{-4}$
Thermally and/or salinity driven flow	ρ (kg/m^3)	Groundwater density	Constant density.
Repository	Tunnel Layout		Two level (-500 and –600 masl) layout H, (for hydraulic structural model) from R 97-09 Figures 6-18 and 6-19. File: h_koord.xls
	Starting Positions		120 starting positions spread uniformly over layout H of R 97-09
	EDZ / Backfill K (m/s)		No / 10^{-10} m/s, based on SKB AR D-96-011
Model Domain	-	Extent of model required to assess travel times	Premodelling study of Gylling et al., 1998.

APPENDIX E. Data Sources

This appendix documents the data transfers from SKB archives that has been used as input to the calculations. These data include coordinates for fracture zones, deposition tunnels, observed heads and boundary conditions. These were taken directly from SKB SICADA database, as documented in this section. The data is summarised by type in Appendix D.

E.1 For Coordinates and Previous Interpreted K Values

Date: 970324 18:02:21

Table(s): transient_inj_cd

Columns :transient_inj_cd.idcode, transient_inj_cd.start_date, transient_inj_cd.stop_date, transient_inj_cd.seclen,

transient_inj_cd.secup, transient_inj_cd.bc, transient_inj_cd.k_steady_state, transient_inj_cd.k_injection,

transient_inj_cd.k_fall_off, transient_inj_cd.k_jacob, transient_inj_cd.k_prel, transient_inj_cd.k, transient_inj_cd.skinfactor_i,

transient_inj_cd.skinfactor_t, transient_inj_cd.spec_cap, transient_inj_cd.goodness, transient_inj_cd.test_date,

transient_inj_cd.comment

New Columns: midpoint

Condition: Expr=secup+(seclow-secup)/2

Criteria: (transient_inj_cd.idcode ='KAS02' OR

transient_inj_cd.idcode ='KAS03' OR transient_inj_cd.idcode ='KAS04' OR

transient_inj_cd.idcode ='KAS05' OR transient_inj_cd.idcode ='KAS06' OR

transient_inj_cd.idcode ='KAS07' OR transient_inj_cd.idcode ='KAS08' OR

transient_inj_cd.idcode ='KLX01') AND transient_inj_cd.seclen =3

Result: 1300 rows written

Filename: trans_l.csv

Fileformat: CSV

Coordinate system: Local

Coordinate calculation column: midpoint

E.2 For Rock/Conductor Codes and Rhén K Values

Date   :970324 18:05:05

Tables :sic_dba.transient_inj_cd

Columns :transient_inj_cd.idcode, transient_inj_cd.start_date, transient_inj_cd.stop_date, transient_inj_cd.seclen,

transient_inj_cd.secup, transient_inj_cd.bc, transient_inj_cd.k_steady_state, transient_inj_cd.k_injection,

transient_inj_cd.k_fall_off, transient_inj_cd.k_jacob, transient_inj_cd.k_prel, transient_inj_cd.k, transient_inj_cd.skinfactor_i,

transient_inj_cd.skinfactor_t, transient_inj_cd.spec_cap, transient_inj_cd.goodness, transient_inj_cd.test_date,

transient_inj_cd.comment

New Columns: midpoint

Condition: Expr=secup+(seclow-secup)/2

Criteria: (transient_inj_cd.idcode ='KAS02' OR

transient_inj_cd.idcode ='KAS03' OR transient_inj_cd.idcode ='KAS04' OR

transient_inj_cd.idcode ='KAS05' OR transient_inj_cd.idcode ='KAS06' OR

transient_inj_cd.idcode ='KAS07' OR transient_inj_cd.idcode ='KAS08' OR

transient_inj_cd.idcode ='KLX01') AND transient_inj_cd.seclen =3

Result: 1300 rows written

Filename: trans_r.csv

Fileformat: CSV

Coordinate system: RT

Coordinate calculation column: midpoint

Output to: File

Date   :970606 15:31:46

Table(s) :sic_dba.zone_model96

Columns   :zone_model96.site, zone_model96.idcode,

      zone_model96.borehole, zone_model96.sub_secup,

      zone_model96.sub_seclow,

      zone_model96.zone_name, zone_model96.rocktype,

      zone_model96.k,

      zone_model96.k_source, zone_model96.q$_c$_ok,

Criteria :1=1

Result   : 1300 rows written to file.

Filename   : /home/skbee/rhen_k.csv

File format : csv

E.3 Structural Data

Coordinates for the fracture zones are based on the interpreted structural model given by Table A2-6 of Rhén et al., (1997). The hydraulic properties of the fracture zones and SRD's are from Walker et al. (1997b).

E.4 Repository Lay-out

The layout of the repository is the two-level layout H, taken from Figures 6-18 and 6-19 of Munier et al (1997). The layout is described by tunnel endpoint coordinates in Excel spreadsheets, received directly from Raymond Munier of Scandia Consult. The file h_ koord.xls contains tunnel coordinates for a layout based on hydraulic structures and the file kapkoord.xls contains canister positions. The latter file was used to check that all the positions fall into the designed tunnels.

File	Main contents here	Date received	Source
h_koord.xls	Tunnel coordinates	April 16 1998	R. Munier, SCC
kapkoord.xls	Canister positions	April 16 1998	(and R 97-09)

E.5 Boundary Conditions

Three sets of boundary conditions were obtained from Svensson (personal communication, 1998). The different sets correspond to the Base Case (deterministic regional realisation), Variant 1.2 (saline conditions as environmental head) and Variant 1.3 (single stochastic regional realisation). Variant 2 (increased block size) uses the same boundary conditions as the Base Case, but with less resolution in the interpolation. Variants 3, 4 and 5 use the same boundary conditions as the Base Case.

Case	Files	Main Contents	Date received	Source
Base	Press, Pz0	Pressure, coordinates	November 27 1997	Svensson, CFE
	Uvel, Vvel, Wvel	flux over the boundaries		
Variant 1.2	Ps, Psz0	Pressure, coordinates and salt concentration	March 23 1998	Svensson, CFE
	Uvel, Vvel, Wvel	flux over the boundaries		
Variant 1.3	PressVert, Pz0	Pressure, coordinates	March 25 1998	Svensson, CFE
	Uvel, Vvel, Wvel	flux over the boundaries		

E.6 Location of HYDRASTAR Input Files

Files are located within the following directories on the SKB Convex or on the SKB SUN machines. The path to the input files and result files on Convex starts with:

/slow/s92/tmp-hyd/aberg

or on the SUN machines (e.g. sultan):

/net/s92/export/home/tmp-hyd/aberg

In each directory, there is a file with a short description of the performed simulations in addition to the necessary files for HYDRASTAR and result files:

README.txt   Description of the problem

The necessary HYDRASTAR files and result files may be found at:

abas/   Base Case with unconditional stochastic simulations, HYDRABOOT

avar1.1/   Variant 1.1, Realisation 1 of the Base Case

avar1.2/   Variant 1.2, Stochastic single realisation, saline case

avar1.3/   Variant 1.3, Boundary conditions from stochastic regional realisation

avar1.4a/   Variant 1.4a, Simplified boundary conditions

avar 1.4b/   Variant 1.4b,Simplified boundary conditions

avar 1.4c/   Variant 1.4c, Simplified boundary conditions

avar2/   Variant 2, Coarse grid, stochastic, 100 realisations

avar3a/   Variant 3.1, Anisotropic variogram (2:1:1), stochastic

avar3b/   Variant 3.2, Anisotropic variogram (10:1:1), stochastic

avar4/   Variant 4.2, Conditional stochastic continuum

determ/   Variant 5, Deterministic calculations

avar6/   Variant 4.1, Unconditional stochastic contiuum

holes/   Borehole information

APPENDIX F. Additional Software Tools

INFERENS (Norman, 1992b; Geier, 1993). INFERENS is a FORTRAN program developed by SKB that incorporates the HYDRASTAR regularisation algorithm and Universal Kriging via iterative generalised least squares estimation (IGLSE). It is necessary in this study because each of the sites in SR 97 divides the model domain into a series of fracture zones, rock masses and depth zones that represent stepwise changes in the hydraulic conductivity. HYDRASTAR represents this complex hydraulic conductivity field as a multivariate lognormal regionalised variable with local trends in $\log_{10}$ hydraulic conductivity. A single variogram model is inferred for the entire domain (i.e., the same variogram for SRD, SCD, etc). Although not a restriction of HYDRASTAR itself, this study will consider the trends as constants within well-defined volumes in the domain (0 order trends in $\log_{10} K_b$). This complex model of trend and spatial correlation violates the assumptions of ordinary least squares estimation (i.e., fitting trends by simple least squares regression). This study instead uses the more versatile IGLSE for universal kriging suggested by Neuman and Jacobsen (1984). INFERENS is an SKB computer program for geostatistical inference that automates the IGLSE fitting and data exploration (Norman, 1992b). INFERENS is unique in that includes the same regularisation algorithm as HYDRASTAR to upscale the data and apply universal kriging. Thus the resulting model of trends and variogram are compatible with the conditioning data and the chosen grid scale.

A program limitation prohibited using the crossvalidation option in INFERENS for this study. Alternative methods that met QA standards were not readily available during this study; therefore, crossvalidation was omitted.

HYDRAVIS (Hultman, 1997) HYDRAVIS is a graphical post-processor for HYDRASTAR, permitting users to view the repository layout, deterministic zones, hydraulic conductivities, stream tubes, and hydraulic heads. HYDRAVIS is an Advanced Visual Systems (AVS) system 5 application module developed by Cap Gemeni under contract to SKB. HYDRAVIS scans the HYDRASTAR input <casename>.hyd file and the output files for the required information, which is then displayed in a GUI format for the user. The system runs under Sun/OS, and requires a compatible version of AVS to be available. (AVS is a commercial software package for scientific visualisation on Windows NT and UNIX platforms).

IGOR Pro (WaveMetrics) IGOR Pro is a commercial Mac and MS/Windows package used in this study to produce exit location plots and special plots; e.g., for studying single realisations and single starting positions. IGOR Pro is an interactive programmable environment for data analysis and plotting. It handles large data sets (more than 100,000 points) and it includes a wide range of capabilities for analysis and graphing.

MATLAB (MathWorks) MATLAB is a commercial software package for numerical computation, visualisation and programming. It supplies a large number of high-level mathematical operations that are convenient for data analysis and visualisation. In this study, several MATLAB programs are used to interpolate between the regional and site-

scale modelling domains and to post-process HYDRASTAR results. These programs include the following:

GENERAL SCRIPTS FOR PRE-PROCESSING TO THE STATISTICA PACKAGE:

Path: 2149ac\matlab

`layerabc.m` These files start up and run the GUI in **MATLAB**.

`layerfunc.m` Reads the input data files and generates *casename.nim*. The definitions of

layers and end point areas are also made here as well as the definition of the string variable '`HomeDir`'. This string must be adjusted to match the installation path of the **MATLAB** files.

`perfm.m` Calculates the performance measures for the entire data file as well as for separate canisters (defined here) and layers or end point areas (depending on which model domain is being studied).

`perfmout.m` Generates a text file called *casename_s.txt* containing performance measures for the entire data file and the chosen canisters.

`perfplot.m` Draws graphs of accumulated mean and median (including standard deviation) of $\log_{10}$ (TT) and log(CF) for each one of the three canisters selected and also scatter plots for the three canisters.

`a_out.m` Generates text files containing performance measures for the different layers of canisters in Aberg. They are given the names *AbergX.txt* where *X* is the number of the layer.

FOR INTERPOLATION AND VISUALISATION OF BOUNDARY CONDITIONS:

Path: 2149ac\aberg\bcplot

`Interpol2.m` Interpolates the values from the regional model to HYDRASTAR format.

`rand_a.m` Creates a figure containing the boundary conditions of Aberg visualised as six sides of an opened box.

`boxplot.m` Creates two figures containing the boundary conditions of Aberg visualised as boxes showed from different angles. This file is a subroutine used by `rand_a.m`.

`cntrl_1.m` Function used by `boxplot.m`.

`cntrl_2.m` Function used by `boxplot.m`.

Statistica (StatSoft) Statistica is commercial MS/Windows software package that performs general statistical analysis of data. One of its strengths is a macro scripting language that allows users to automate a series of sorting, analysis and plotting operations. Under contract to SKB, Kemakta has developed scripts that translate

HYDRASTAR output and compute summary statistics of the simulation results. The first script, statistica.pl, is a Perl script that scans and extracts the raw HYDRASTAR travel time and canister flux files and organises them into a format for Statistica input. A second Perl script, endpoints.pl, extracts the exit locations from the HYDRASTAR travel path files. A Statistica Basic program, Hydrast_.STB, is a Statistica Basic program that acts as a macro for the Statistica GUI. Optional outputs include tables of summary statistics, histograms, and box plots of canister fluxes, travel time and F-ratio. This study uses Statistica version 5.1 and the scripts documented in Boghammar and Marsic (1997). Marsic (1998) updated the script Hydrasta_.STB for use in this study. Additional statistical post-processing was provided by MATLAB.

TRAZON
This program is a modification of HYDRASTAR 1.7.2 that helps identify the canister locations versus the deterministic zones. It reads the HYDRASTAR input <casename>.hyd file and compares the stream tube starting position versus the ZONE and XALFA definitions. If the starting position falls within a defined ZONE or XALFA, a comment is written to the logfile. This feature is intended to be included as an option in future versions of HYDRASTAR.

APPENDIX G. Base Case HYDRASTAR Input File

```
#   AVS
#-------------------------------------
-------------------
#
#   NAME: abas.hyd
#   DESC: Base case  HYDRASTAR LOCAL
AESPOE MODEL
#   DATE: 980421
#   USER: BJORN GYLLING, KEMAKTA
#
#   VERSION: HS 1.7.1
#
#-------------------------------------
-------------------
#
SYSTEM SAVE_SCRATCH_FILES
SYSTEM IGNORE_ERRORS
#SYSTEM SKIP_USER_INTERFACE
#SYSTEM VERBOSE
#
#
BEGIN_BLOCK COVARIANCE
#   DETERMINISTIC   YES
#SPHERIVAL MODEL
#   VARIANCE        2.7
#   RANGE           97.
    VARIANCE        2.72
    RANGE           -32.33
BEGIN_DEF   ANISOTROPY
        KXX         1.0
        KXY         0.0
        KXZ         0.0
        KYY         1.0
        KYZ         0.0
        KZZ         1.0
    END_DEF
#   RELATIVE_TOL    1.0E-8
    RELATIVE_TOL    0.01
    NUM_ICOSAHEDRON 40
    NUM_LINES       0
    ORIGIN          0.0 0.0 0.0
    MUL_FACTOR      0.2
    TRUNCATION      999.
END_BLOCK
#
BEGIN_BLOCK GEOM
#
# 25 METER BLOCK SCALE
# PHOENICS BC
#
    AXISLENGTH      2400. 2200. 1250.
    NUMBER_OF_NODES  97 89  49
    BOUNDARY         NAMMU
#
#
 BEGIN_DEF USER_SYSTEM
    XY_ROTATE  0.
    ZY_ROTATE  0.
    TRANSLATE  950  6150 -1250
    SYSTEM RIGHT
 END_DEF
  BEGIN_DEF WORLD_SYSTEM
     XY_ROTATE   0.0
     ZY_ROTATE   0.0
     TRANSLATE 950  6150 -1250
  SYSTEM RIGHT
 END_DEF
END_BLOCK
#
#
```

```
BEGIN_BLOCK KRGE_NBH
  BEGIN_DEF SECONDARY
        NORMAL       0.  0. 1.
        WIDTH        3000.0
        OVERLAP      50.0
        MEASUREMENTS 16
  END_DEF
END_BLOCK
#
#
#
BEGIN_BLOCK KRIGE
   NUM_ITERATIONS  60
   RESIDUAL_TOL    0.01
   METHOD          NR
   RESTART
   PATH            /skbtmp/2149/aberg
END_BLOCK
#
#
#
BEGIN_BLOCK HYDROLOGY_EQ
   NUM_ITERATIONS  16000
   RESIDUAL_TOL    1.0E-08
   PRECOND         DIAGONAL
END_BLOCK
#
BEGIN_BLOCK TRANSPORT
   TRANSPORT_MODEL STREAM
   PLOT_TIMES      1
   BACK_INTERPOL   NOBACKINT
   INTERVALS       FIXED
   DELIMITERS
                   1.0
                   10.0
                   100.0
                   1000.0
   END_LIST
   LOGON
   TOLERANCE       0.2
   PRESENTATION    1.0
   CELL_SHIFTS     1024
   PLOTTING_MOMENTS 1.0E4
#  STREAM_TUBES    121
   STREAM_TUBES    120
   DIVISION        SPATIAL
   VIEW            ALL
END_BLOCK
#
BEGIN_BLOCK RESULT_ESTIMATION
   PERIOD          1
   SAVE_TRANSPORT  TRANSPORT
END_BLOCK
#
BEGIN_BLOCK PRESENTATION
   POST_PROCESSOR  AVS
   VIEW            ZDIR
   PRESENT         ALL
   NUM_REALIZATIONS
     1  2
   END_LIST
   INTERACTIVE     NO
   MODEL_NAME      FAA

   BEGIN_DEF PSLICE
       NORMAL       0. 0. -1.
       DISTANCE     105.
       WIDTH        70.
       C_THRESHOLD  0.
       V_THRESHOLD  0.
```

```
    END_DEF
END_BLOCK
BEGIN_BLOCK TRENDS
#
  REF_DEPTH   40.0
  ALFA        -8.56
  BETA         0.0
  STORATIVITY 1.0
#EW-1N
BEGIN_DEF PLANE
NAME P1
EQUATION   -0.488965   0.8716844  -
0.032849  -5636.181
TYPE UPPER
END_DEF


BEGIN_DEF PLANE
NAME U1
EQUATION   -0.488965   0.8716844  -
0.032849  -5651.181
TYPE UPPER
END_DEF


BEGIN_DEF PLANE
NAME L1
EQUATION   -0.488965   0.8716844  -
0.032849  -5621.181
TYPE UPPER
END_DEF
#EW-1S
BEGIN_DEF PLANE
NAME P2
EQUATION   -0.479232   0.8547282  -
0.199440  -5472.543
TYPE UPPER
END_DEF


BEGIN_DEF PLANE
NAME U2
EQUATION   -0.479232   0.8547282  -
0.199440  -5487.543
TYPE UPPER
END_DEF


BEGIN_DEF PLANE
NAME L2
EQUATION   -0.479232   0.8547282  -
0.199440  -5457.543
TYPE UPPER
END_DEF
#EW-3
BEGIN_DEF PLANE
NAME P3
EQUATION   -0.199396   0.9611595  -
0.190823  -6409.201
TYPE UPPER
END_DEF


BEGIN_DEF PLANE
NAME U3
EQUATION   -0.199396   0.9611595  -
0.190823  -6421.701
TYPE UPPER
END_DEF


BEGIN_DEF PLANE
NAME L3
EQUATION   -0.199396   0.9611595  -
0.190823  -6396.701
TYPE UPPER
END_DEF
#EW-7
BEGIN_DEF PLANE
NAME P4
```

```
EQUATION   -0.255724   0.9540446  -
0.156217  -5606.408
TYPE UPPER
END_DEF


BEGIN_DEF PLANE
NAME U4
EQUATION   -0.255724   0.9540446  -
0.156217  -5618.908
TYPE UPPER
END_DEF


BEGIN_DEF PLANE
NAME L4
EQUATION   -0.255724   0.9540446  -
0.156217  -5593.908
TYPE UPPER
END_DEF
#NE-1
BEGIN_DEF PLANE
NAME P5
EQUATION   -0.438044   0.8471511
0.3007530  -4905.346
TYPE UPPER
END_DEF


BEGIN_DEF PLANE
NAME U5
EQUATION   -0.438044   0.8471511
0.3007530  -4920.346
TYPE UPPER
END_DEF


BEGIN_DEF PLANE
NAME L5
EQUATION   -0.438044   0.8471511
0.3007530  -4890.346
TYPE UPPER
END_DEF
#NE-2
BEGIN_DEF PLANE
NAME P6
EQUATION   -0.788254   0.5727476  -
0.224978  -2588.858
TYPE UPPER
END_DEF


BEGIN_DEF PLANE
NAME U6
EQUATION   -0.788254   0.5727476  -
0.224978  -2601.358
TYPE UPPER
END_DEF


BEGIN_DEF PLANE
NAME L6
EQUATION   -0.788254   0.5727476  -
0.224978  -2576.358
TYPE UPPER
END_DEF
#NE-3
BEGIN_DEF PLANE
NAME P7
EQUATION   -0.481357   0.8336931
0.2706488  -4462.135
TYPE UPPER
END_DEF


BEGIN_DEF PLANE
NAME U7
EQUATION   -0.481357   0.8336931
0.2706488  -4487.135
TYPE UPPER
END_DEF
```

BEGIN_DEF PLANE
NAME L7
EQUATION   -0.481357   0.8336931
0.2706488 -4437.135
TYPE UPPER
END_DEF
#NE-4N
BEGIN_DEF PLANE
NAME P8
EQUATION   -0.385083   0.8646853   -
0.322537 -4794.608
TYPE UPPER
END_DEF

BEGIN_DEF PLANE
NAME U8
EQUATION   -0.385083   0.8646853   -
0.322537 -4814.608
TYPE UPPER
END_DEF

BEGIN_DEF PLANE
NAME L8
EQUATION   -0.385083   0.8646853   -
0.322537 -4774.608
TYPE UPPER
END_DEF
#NE-4S
BEGIN_DEF PLANE
NAME P9
EQUATION   -0.467000   0.8602138   -
0.204799 -4608.536
TYPE UPPER
END_DEF

BEGIN_DEF PLANE
NAME U9
EQUATION   -0.467000   0.8602138   -
0.204799 -4628.536
TYPE UPPER
END_DEF

BEGIN_DEF PLANE
NAME L9
EQUATION   -0.467000   0.8602138   -
0.204799 -4588.536
TYPE UPPER
END_DEF
#NW-1
BEGIN_DEF PLANE
NAME P10
EQUATION   0.3677331   0.3387457
0.8660391 -3132.454
TYPE UPPER
END_DEF

BEGIN_DEF PLANE
NAME U10
EQUATION   0.3677331   0.3387457
0.8660391 -3144.954
TYPE UPPER
END_DEF

BEGIN_DEF PLANE
NAME L10
EQUATION   0.3677331   0.3387457
0.8660391 -3119.954
TYPE UPPER
END_DEF
#NNW-1
BEGIN_DEF PLANE
NAME P11
EQUATION   0.9514486   0.3078076
0.0000000 -4312.293
TYPE UPPER

END_DEF

BEGIN_DEF PLANE
NAME U11
EQUATION   0.9514486   0.3078076
0.0000000 -4324.793
TYPE UPPER
END_DEF

BEGIN_DEF PLANE
NAME L11
EQUATION   0.9514486   0.3078076
0.0000000 -4299.793
TYPE UPPER
END_DEF
#NNW-2
BEGIN_DEF PLANE
NAME P12
EQUATION   0.9159572   0.4012761
0.0000000 -4958.393
TYPE UPPER
END_DEF

BEGIN_DEF PLANE
NAME U12
EQUATION   0.9159572   0.4012761
0.0000000 -4970.893
TYPE UPPER
END_DEF

BEGIN_DEF PLANE
NAME L12
EQUATION   0.9159572   0.4012761
0.0000000 -4945.893
TYPE UPPER
END_DEF
#NNW-3
BEGIN_DEF PLANE
NAME P13
EQUATION   0.9995033   -0.0315147
0.0000000 -1921.132
TYPE UPPER
END_DEF

BEGIN_DEF PLANE
NAME U13
EQUATION   0.9995033   -0.0315147
0.0000000 -1933.632
TYPE UPPER
END_DEF

BEGIN_DEF PLANE
NAME L13
EQUATION   0.9995033   -0.0315147
0.0000000 -1908.632
TYPE UPPER
END_DEF
#NNW-4
BEGIN_DEF PLANE
NAME P14
EQUATION   0.9882466   0.1255517
0.0872093 -3176.610
TYPE UPPER
END_DEF

BEGIN_DEF PLANE
NAME U14
EQUATION   0.9882466   0.1255517
0.0872093 -3189.110
TYPE UPPER
END_DEF

BEGIN_DEF PLANE
NAME L14

```
EQUATION   0.9882466   0.1255517
0.0872093  -3164.110
TYPE UPPER
END_DEF
#NNW-5
BEGIN_DEF PLANE
NAME P15
EQUATION   0.9987798   0.0493855
0.0000000  -2325.567
TYPE UPPER
END_DEF

BEGIN_DEF PLANE
NAME U15
EQUATION   0.9987798   0.0493855
0.0000000  -2338.067
TYPE UPPER
END_DEF

BEGIN_DEF PLANE
NAME L15
EQUATION   0.9987798   0.0493855
0.0000000  -2313.067
TYPE UPPER
END_DEF
#NNW-6
BEGIN_DEF PLANE
NAME P16
EQUATION   0.9900987   0.1403732
0.0000000  -3266.708
TYPE UPPER
END_DEF

BEGIN_DEF PLANE
NAME U16
EQUATION   0.9900987   0.1403732
0.0000000  -3279.208
TYPE UPPER
END_DEF

BEGIN_DEF PLANE
NAME L16
EQUATION   0.9900987   0.1403732
0.0000000  -3254.208
TYPE UPPER
END_DEF
#NNW-7
BEGIN_DEF PLANE
NAME P17
EQUATION   0.9039969   0.4186277
0.0868357  -4915.147
TYPE UPPER
END_DEF

BEGIN_DEF PLANE
NAME U17
EQUATION   0.9039969   0.4186277
0.0868357  -4927.647
TYPE UPPER
END_DEF

BEGIN_DEF PLANE
NAME L17
EQUATION   0.9039969   0.4186277
0.0868357  -4902.647
TYPE UPPER
END_DEF
#NNW-8
BEGIN_DEF PLANE
NAME P18
EQUATION   0.7071068   0.7071068
0.0000000  -6788.225
TYPE UPPER
END_DEF
```

```
BEGIN_DEF PLANE
NAME U18
EQUATION   0.7071068   0.7071068
0.0000000  -6800.725
TYPE UPPER
END_DEF

BEGIN_DEF PLANE
NAME L18
EQUATION   0.7071068   0.7071068
0.0000000  -6777.725
TYPE UPPER
END_DEF
#SFZ01
BEGIN_DEF PLANE
NAME P19
EQUATION   0.2026884   0.9792433
0.0000000  -12455.699
TYPE UPPER
END_DEF

BEGIN_DEF PLANE
NAME U19
EQUATION   0.2026884   0.9792433
0.0000000  -12468.199
TYPE UPPER
END_DEF

BEGIN_DEF PLANE
NAME L19
EQUATION   0.2026884   0.9792433
0.0000000  -12443.199
TYPE UPPER
END_DEF
#SFZ02
BEGIN_DEF PLANE
NAME P20
EQUATION   0.9672847  -0.2536935
0.0000000   4674.310
TYPE UPPER
END_DEF

BEGIN_DEF PLANE
NAME U20
EQUATION   0.9672847  -0.2536935
0.0000000   4661.810
TYPE UPPER
END_DEF

BEGIN_DEF PLANE
NAME L20
EQUATION   0.9672847  -0.2536935
0.0000000   4688.810
TYPE UPPER
END_DEF
#SFZ03a
BEGIN_DEF PLANE
NAME P21
EQUATION   0.2539498   0.9672174
0.0000000  -7445.653
TYPE UPPER
END_DEF

BEGIN_DEF PLANE
NAME U21
EQUATION   0.2539498   0.9672174
0.0000000  -7458.153
TYPE UPPER
END_DEF

BEGIN_DEF PLANE
NAME L21
EQUATION   0.2539498   0.9672174
0.0000000  -7433.153
TYPE UPPER
```

```
END_DEF
#SFZ03b
BEGIN_DEF PLANE
NAME P22
EQUATION   0.0455553   0.9989618
0.0000000  -8112.644
TYPE UPPER
END_DEF


BEGIN_DEF PLANE
NAME U22
EQUATION   0.0455553   0.9989618
0.0000000  -8125.144
TYPE UPPER
END_DEF


BEGIN_DEF PLANE
NAME L22
EQUATION   0.0455553   0.9989618
0.0000000  -8100.144
TYPE UPPER
END_DEF
#SFZ03c
BEGIN_DEF PLANE
NAME P23
EQUATION   -0.006410   0.9999794
0.0000000  -8062.655
TYPE UPPER
END_DEF


BEGIN_DEF PLANE
NAME U23
EQUATION   -0.006410   0.9999794
0.0000000  -8075.155
TYPE UPPER
END_DEF


BEGIN_DEF PLANE
NAME L23
EQUATION   -0.006410   0.9999794
0.0000000  -8050.155
TYPE UPPER
END_DEF
#SFZ03d
BEGIN_DEF PLANE
NAME P24
EQUATION   0.0581538   0.9983076
0.0000000  -8222.178
TYPE UPPER
END_DEF


BEGIN_DEF PLANE
NAME U24
EQUATION   0.0581538   0.9983076
0.0000000  -8234.678
TYPE UPPER
END_DEF


BEGIN_DEF PLANE
NAME L24
EQUATION   0.0581538   0.9983076
0.0000000  -8209.678
TYPE UPPER
END_DEF
#SFZ03e
BEGIN_DEF PLANE
NAME P25
EQUATION   0.0430223   0.9990741
0.0000000  -8172.187
TYPE UPPER
END_DEF


BEGIN_DEF PLANE
NAME U25
```

```
EQUATION   0.0430223   0.9990741
0.0000000  -8184.687
TYPE UPPER
END_DEF


BEGIN_DEF PLANE
NAME L25
EQUATION   0.0430223   0.9990741
0.0000000  -8159.687
TYPE UPPER
END_DEF
#SFZ03f
BEGIN_DEF PLANE
NAME P26
EQUATION   -0.027657   0.9996175
0.0000000  -7766.554
TYPE UPPER
END_DEF


BEGIN_DEF PLANE
NAME U26
EQUATION   -0.027657   0.9996175
0.0000000  -7779.054
TYPE UPPER
END_DEF


BEGIN_DEF PLANE
NAME L26
EQUATION   -0.027657   0.9996175
0.0000000  -7754.054
TYPE UPPER
END_DEF
#SFZ04
BEGIN_DEF PLANE
NAME P27
EQUATION   -0.548901   0.8358871
0.0000000  -5818.566
TYPE UPPER
END_DEF


BEGIN_DEF PLANE
NAME U27
EQUATION   -0.548901   0.8358871
0.0000000  -5831.066
TYPE UPPER
END_DEF


BEGIN_DEF PLANE
NAME L27
EQUATION   -0.548901   0.8358871
0.0000000  -5806.066
TYPE UPPER
END_DEF
#SFZ05a
BEGIN_DEF PLANE
NAME P28
EQUATION   -0.398723   0.8007621   -
0.446989  -4423.415
TYPE UPPER
END_DEF


BEGIN_DEF PLANE
NAME U28
EQUATION   -0.398723   0.8007621   -
0.446989  -4435.915
TYPE UPPER
END_DEF


BEGIN_DEF PLANE
NAME L28
EQUATION   -0.398723   0.8007621   -
0.446989  -4410.915
TYPE UPPER
END_DEF
#SFZ05b
```

BEGIN_DEF PLANE
NAME P29
EQUATION   -0.233401   0.8634220   -
0.447242   -4675.218
TYPE UPPER
END_DEF

BEGIN_DEF PLANE
NAME U29
EQUATION   -0.233401   0.8634220   -
0.447242   -4687.718
TYPE UPPER
END_DEF

BEGIN_DEF PLANE
NAME L29
EQUATION   -0.233401   0.8634220   -
0.447242   -4662.718
TYPE UPPER
END_DEF
#SFZ05c
BEGIN_DEF PLANE
NAME P30
EQUATION   -0.419466   0.7900307   -
0.447101   -3832.040
TYPE UPPER
END_DEF

BEGIN_DEF PLANE
NAME U30
EQUATION   -0.419466   0.7900307   -
0.447101   -3844.540
TYPE UPPER
END_DEF

BEGIN_DEF PLANE
NAME L30
EQUATION   -0.419466   0.7900307   -
0.447101   -3819.540
TYPE UPPER
END_DEF
#SFZ06a
BEGIN_DEF PLANE
NAME P31
EQUATION   -0.439634   0.8981770
0.0000000   -8231.319
TYPE UPPER
END_DEF

BEGIN_DEF PLANE
NAME U31
EQUATION   -0.439634   0.8981770
0.0000000   -8243.819
TYPE UPPER
END_DEF

BEGIN_DEF PLANE
NAME L31
EQUATION   -0.439634   0.8981770
0.0000000   -8218.819
TYPE UPPER
END_DEF
#SFZ06b
BEGIN_DEF PLANE
NAME P32
EQUATION   -0.131607   0.9913019
0.0000000   -9067.080
TYPE UPPER
END_DEF

BEGIN_DEF PLANE
NAME U32
EQUATION   -0.131607   0.9913019
0.0000000   -9079.580
TYPE UPPER

END_DEF

BEGIN_DEF PLANE
NAME L32
EQUATION   -0.131607   0.9913019
0.0000000   -9054.580
TYPE UPPER
END_DEF
#SFZ06c
BEGIN_DEF PLANE
NAME P33
EQUATION   -0.127971   0.9917778
0.0000000   -9079.886
TYPE UPPER
END_DEF

BEGIN_DEF PLANE
NAME U33
EQUATION   -0.127971   0.9917778
0.0000000   -9092.386
TYPE UPPER
END_DEF

BEGIN_DEF PLANE
NAME L33
EQUATION   -0.127971   0.9917778
0.0000000   -9067.386
TYPE UPPER
END_DEF
#SFZ07a
BEGIN_DEF PLANE
NAME P34
EQUATION   -0.663461   0.7482103
0.0000000   -4272.753
TYPE UPPER
END_DEF

BEGIN_DEF PLANE
NAME U34
EQUATION   -0.663461   0.7482103
0.0000000   -4285.253
TYPE UPPER
END_DEF

BEGIN_DEF PLANE
NAME L34
EQUATION   -0.663461   0.7482103
0.0000000   -4260.253
TYPE UPPER
END_DEF
#SFZ07b
BEGIN_DEF PLANE
NAME P35
EQUATION   -0.667030   0.7450302
0.0000000   -4257.660
TYPE UPPER
END_DEF

BEGIN_DEF PLANE
NAME U35
EQUATION   -0.667030   0.7450302
0.0000000   -4270.160
TYPE UPPER
END_DEF

BEGIN_DEF PLANE
NAME L35
EQUATION   -0.667030   0.7450302
0.0000000   -4245.160
TYPE UPPER
END_DEF
#SFZ10a
BEGIN_DEF PLANE
NAME P36

EQUATION   -0.988371   0.1520572
0.0000000   2447.360
TYPE UPPER
END_DEF

BEGIN_DEF PLANE
NAME U36
EQUATION   -0.988371   0.1520572
0.0000000   2434.860
TYPE UPPER
END_DEF

BEGIN_DEF PLANE
NAME L36
EQUATION   -0.988371   0.1520572
0.0000000   2459.860
TYPE UPPER
END_DEF
#SFZ10b
BEGIN_DEF PLANE
NAME P37
EQUATION   -0.965653   0.2598344
0.0000000   1498.702
TYPE UPPER
END_DEF

BEGIN_DEF PLANE
NAME U37
EQUATION   -0.965653   0.2598344
0.0000000   1486.202
TYPE UPPER
END_DEF

BEGIN_DEF PLANE
NAME L37
EQUATION   -0.965653   0.2598344
0.0000000   1511.202
TYPE UPPER
END_DEF
#SFZ11
BEGIN_DEF PLANE
NAME P38
EQUATION   0.1978365   0.9802350
0.0000000   -7540.771
TYPE UPPER
END_DEF

BEGIN_DEF PLANE
NAME U38
EQUATION   0.1978365   0.9802350
0.0000000   -7553.271
TYPE UPPER
END_DEF

BEGIN_DEF PLANE
NAME L38
EQUATION   0.1978365   0.9802350
0.0000000   -7528.271
TYPE UPPER
END_DEF
#SFZ13a
BEGIN_DEF PLANE
NAME P39
EQUATION   0.4472136   0.8944272
0.0000000   -8152.704
TYPE UPPER
END_DEF

BEGIN_DEF PLANE
NAME U39
EQUATION   0.4472136   0.8944272
0.0000000   -8165.204
TYPE UPPER
END_DEF

BEGIN_DEF PLANE
NAME L39
EQUATION   0.4472136   0.8944272
0.0000000   -8140.204
TYPE UPPER
END_DEF
#SFZ13b
BEGIN_DEF PLANE
NAME P40
EQUATION   0.2782189   0.9605177
0.0000000   -8506.609
TYPE UPPER
END_DEF

BEGIN_DEF PLANE
NAME U40
EQUATION   0.2782189   0.9605177
0.0000000   -8519.109
TYPE UPPER
END_DEF

BEGIN_DEF PLANE
NAME L40
EQUATION   0.2782189   0.9605177
0.0000000   -8494.109
TYPE UPPER
END_DEF
#SFZ14a
BEGIN_DEF PLANE
NAME P41
EQUATION   -0.990023   0.1409022
0.0000000   -23.416
TYPE UPPER
END_DEF

BEGIN_DEF PLANE
NAME U41
EQUATION   -0.990023   0.1409022
0.0000000   -35.916
TYPE UPPER
END_DEF

BEGIN_DEF PLANE
NAME L41
EQUATION   -0.990023   0.1409022
0.0000000   -10.916
TYPE UPPER
END_DEF
#SFZ14b
BEGIN_DEF PLANE
NAME P42
EQUATION   -0.978468   0.2063957
0.0000000   -550.847
TYPE UPPER
END_DEF

BEGIN_DEF PLANE
NAME U42
EQUATION   -0.978468   0.2063957
0.0000000   -563.347
TYPE UPPER
END_DEF

BEGIN_DEF PLANE
NAME L42
EQUATION   -0.978468   0.2063957
0.0000000   -538.347
TYPE UPPER
END_DEF
#SFZ15
BEGIN_DEF PLANE
NAME P43
EQUATION   -0.991411   0.1307767
0.0000000   1029.536
TYPE UPPER

END_DEF

BEGIN_DEF PLANE
NAME U43
EQUATION   -0.991411   0.1307767
0.0000000   1017.036
TYPE UPPER
END_DEF

BEGIN_DEF PLANE
NAME L43
EQUATION   -0.991411   0.1307767
0.0000000   1042.036
TYPE UPPER
END_DEF
#FixNNW5
BEGIN_DEF PLANE
NAME F1
EQUATION   0.0000000   -1.0000000
0.0000000   7394.100
TYPE UPPER
END_DEF
#FixNNW3N
BEGIN_DEF PLANE
NAME F2
EQUATION   0.0000000   -1.0000000
0.0000000   7025.400
TYPE UPPER
END_DEF
#FixNNW3S
BEGIN_DEF PLANE
NAME F3
EQUATION   0.0000000   -1.0000000
0.0000000   6812.900
TYPE UPPER
END_DEF
#Fix NNW-8
BEGIN_DEF PLANE
NAME A1
EQUATION   0.0000000   0.0000000
1.0000000   300.000
TYPE UPPER
END_DEF
#Fix NNW-8
BEGIN_DEF PLANE
NAME A2
EQUATION   0.0000000   0.0000000
1.0000000   700.000
TYPE UPPER
END_DEF
#Fix EW-5
BEGIN_DEF PLANE
NAME Q1
EQUATION   0.0000000   1.0000000
0.0000000   -7352.500
TYPE UPPER
END_DEF
#Fix EW-5
BEGIN_DEF PLANE
NAME Q2
EQUATION   -1.000000   0.0000000
0.0000000   2265.000
TYPE UPPER
END_DEF
#Fix EW-5
BEGIN_DEF PLANE
NAME Q3
EQUATION   0.0000000   1.0000000
0.0000000   -7277.500
TYPE UPPER
END_DEF
#Fix EW-5
BEGIN_DEF PLANE
NAME Q4

EQUATION   -1.000000   0.0000000
0.0000000   2115.000
TYPE UPPER
END_DEF
#Fix EW-5
BEGIN_DEF PLANE
NAME Q5
EQUATION   0.0000000   0.0000000   -
1.000000   -387.500
TYPE UPPER
END_DEF
#Fix EW-5
BEGIN_DEF PLANE
NAME Q6
EQUATION   0.0000000   0.0000000   -
1.000000   -312.500
TYPE UPPER
END_DEF
#Fix SFZ07a&b
BEGIN_DEF PLANE
NAME X07
EQUATION   0.7466274   0.6652425
0.0000000   -3157.360
TYPE UPPER
END_DEF
#Fix SFZ03b&c
BEGIN_DEF PLANE
NAME X03
EQUATION   0.9998083   -0.0195816
0.0000000   -961.758
TYPE UPPER
END_DEF
#Fix SFZ07c&d
BEGIN_DEF PLANE
NAME X04
EQUATION   0.9996650   -0.0258815
0.0000000   -2469.974
TYPE UPPER
END_DEF
#EW-1N
BEGIN_DEF ZONE
NAME Z1
ALFA -7.79
BETA 0.0
STORATIVITY 1.0
PLANE U1
P_TYPE UPPER
PLANE L1
P_TYPE LOWER
PLANE P23
P_TYPE UPPER
PLANE P41
P_TYPE UPPER
TEST_POINT   2002.87   7585.23 -109.13
END_DEF
#EW-1S
BEGIN_DEF ZONE
NAME Z44
ALFA -6.62
BETA 0.0
STORATIVITY 1.0
PLANE U2
P_TYPE UPPER
PLANE L2
P_TYPE LOWER
PLANE P23
P_TYPE UPPER
PLANE P36
P_TYPE LOWER
PLANE P35
P_TYPE UPPER
TEST_POINT   3124.00   7932.00 -905.00
END_DEF
#EW-1S
BEGIN_DEF ZONE

```
NAME Z45                                    P_TYPE LOWER
ALFA  -6.62                                 PLANE P23
BETA 0.0                                    P_TYPE UPPER
STORATIVITY 1.0                             PLANE P2
PLANE U2                                    P_TYPE UPPER
P_TYPE UPPER                                TEST_POINT   2542.00  7347.00 -682.00
PLANE L2                                    END_DEF
P_TYPE LOWER                                #NE-2
PLANE P35                                   BEGIN_DEF ZONE
P_TYPE LOWER                                NAME Z6
PLANE P41                                   ALFA  -8.27
P_TYPE UPPER                                BETA 0.0
TEST_POINT   1321.00  7008.00 -517.00       STORATIVITY 1.0
END_DEF                                     PLANE U6
#EW-3                                       P_TYPE UPPER
BEGIN_DEF ZONE                              PLANE L6
NAME Z3                                     P_TYPE LOWER
ALFA  -6.50                                 PLANE P2
BETA 0.0                                    P_TYPE UPPER
STORATIVITY 1.0                             PLANE P5
PLANE U3                                    P_TYPE LOWER
P_TYPE UPPER                                PLANE P3
PLANE L3                                    P_TYPE LOWER
P_TYPE LOWER                                TEST_POINT   2036.00  7276.40 -116.47
PLANE P5                                    END_DEF
P_TYPE LOWER                                #NE-3
PLANE P41                                   BEGIN_DEF ZONE
P_TYPE UPPER                                NAME Z7
TEST_POINT   2167.80  7082.03 -180.73       ALFA  -5.72
END_DEF                                     BETA 0.0
#EW-7                                       STORATIVITY 1.0
BEGIN_DEF ZONE                              PLANE U7
NAME Z4                                     P_TYPE UPPER
ALFA  -6.05                                 PLANE L7
BETA 0.0                                    P_TYPE LOWER
STORATIVITY 1.0                             PLANE P38
PLANE U4                                    P_TYPE UPPER
P_TYPE UPPER                                PLANE P35
PLANE L4                                    P_TYPE UPPER
P_TYPE LOWER                                PLANE P29
PLANE P8                                    P_TYPE LOWER
P_TYPE UPPER                                TEST_POINT   2107.18  6593.47  -75.68
PLANE P36                                   END_DEF
P_TYPE LOWER                                #NE-4N
TEST_POINT   2189.17  6450.60  -77.27       BEGIN_DEF ZONE
END_DEF                                     NAME Z8
#NE-1                                       ALFA  -6.61
BEGIN_DEF ZONE                              BETA 0.0
NAME Z47                                    STORATIVITY 1.0
ALFA  -5.48                                 PLANE U8
BETA 0.0                                    P_TYPE UPPER
STORATIVITY 1.0                             PLANE L8
PLANE U5                                    P_TYPE LOWER
P_TYPE UPPER                                PLANE P38
PLANE L5                                    P_TYPE UPPER
P_TYPE LOWER                                PLANE P36
PLANE P41                                   P_TYPE LOWER
P_TYPE LOWER                                PLANE P29
PLANE P35                                   P_TYPE LOWER
P_TYPE UPPER                                TEST_POINT   2171.57  6484.10  -74.83
TEST_POINT    640.00  6205.00 -234.00       END_DEF
END_DEF                                     #NE-4S
#NE-1                                       BEGIN_DEF ZONE
BEGIN_DEF ZONE                              NAME Z9
NAME Z48                                    ALFA  -6.61
ALFA  -5.48                                 BETA 0.0
BETA 0.0                                    STORATIVITY 1.0
STORATIVITY 1.0                             PLANE U9
PLANE U5                                    P_TYPE UPPER
P_TYPE UPPER                                PLANE L9
PLANE L5                                    P_TYPE LOWER
P_TYPE LOWER                                PLANE P8
PLANE P41                                   P_TYPE UPPER
P_TYPE UPPER                                PLANE P29
PLANE P36                                   P_TYPE LOWER
```

```
TEST_POINT   -109.00  5066.00 -975.00
END_DEF
#NW-1
BEGIN_DEF ZONE
NAME Z10
ALFA  -8.65
BETA 0.0
STORATIVITY 1.0
PLANE U10
P_TYPE UPPER
PLANE L10
P_TYPE LOWER
PLANE P1
P_TYPE LOWER
PLANE P23
P_TYPE UPPER
PLANE P41
P_TYPE UPPER
TEST_POINT   1549.20  7775.60  -82.20
END_DEF
#NNW-1
BEGIN_DEF ZONE
NAME Z11
ALFA  -6.84
BETA 0.0
STORATIVITY 1.0
PLANE U11
P_TYPE UPPER
PLANE L11
P_TYPE LOWER
PLANE P3
P_TYPE LOWER
PLANE P2
P_TYPE UPPER
TEST_POINT   2176.87  7280.90 -666.67
END_DEF
#NNW-2
BEGIN_DEF ZONE
NAME Z12
ALFA  -6.13
BETA 0.0
STORATIVITY 1.0
PLANE U12
P_TYPE UPPER
PLANE L12
P_TYPE LOWER
PLANE P5
P_TYPE LOWER
PLANE P2
P_TYPE UPPER
TEST_POINT   2245.00  7232.10 -666.67
END_DEF
#NNW-3
BEGIN_DEF ZONE
NAME Z13
ALFA  -6.79
BETA 0.0
STORATIVITY 1.0
PLANE U13
P_TYPE UPPER
PLANE L13
P_TYPE LOWER
PLANE F2
P_TYPE LOWER
PLANE F3
P_TYPE UPPER
TEST_POINT   2139.13  6883.73 -666.67
END_DEF
#NNW-4
BEGIN_DEF ZONE
NAME Z14
ALFA  -5.71
BETA 0.0
STORATIVITY 1.0
PLANE U14
```

```
P_TYPE UPPER
PLANE L14
P_TYPE LOWER
PLANE P5
P_TYPE LOWER
PLANE P2
P_TYPE UPPER
TEST_POINT   2300.83  7291.93 -145.57
END_DEF
#NNW-5
BEGIN_DEF ZONE
NAME Z15
ALFA  -7.58
BETA 0.0
STORATIVITY 1.0
PLANE U15
P_TYPE UPPER
PLANE L15
P_TYPE LOWER
PLANE P8
P_TYPE LOWER
PLANE F1
P_TYPE LOWER
TEST_POINT   2001.47  6612.10 -666.67
END_DEF
#NNW-6
BEGIN_DEF ZONE
NAME Z55
ALFA  -6.79
BETA 0.0
STORATIVITY 1.0
PLANE U16
P_TYPE UPPER
PLANE L16
P_TYPE LOWER
PLANE P8
P_TYPE LOWER
PLANE P4
P_TYPE UPPER
TEST_POINT   2410.00  6290.00 -1000.00
END_DEF
#NNW-6
BEGIN_DEF ZONE
NAME Z56
ALFA  -6.79
BETA 0.0
STORATIVITY 1.0
PLANE U16
P_TYPE UPPER
PLANE L16
P_TYPE LOWER
PLANE P5
P_TYPE UPPER
PLANE P2
P_TYPE UPPER
PLANE P4
P_TYPE LOWER
TEST_POINT   2348.70  6705.43 -666.67
END_DEF
#NNW-7
BEGIN_DEF ZONE
NAME Z17
ALFA  -7.20
BETA 0.0
STORATIVITY 1.0
PLANE U17
P_TYPE UPPER
PLANE L17
P_TYPE LOWER
PLANE P3
P_TYPE LOWER
PLANE P2
P_TYPE UPPER
TEST_POINT   2059.33  7306.90  -61.67
END_DEF
```

```
#NNW-8                                          BEGIN_DEF ZONE
BEGIN_DEF ZONE                                  NAME Z23
NAME Z18                                         ALFA  -7.41
ALFA  -6.88                                      BETA 0.0
BETA 0.0                                         STORATIVITY 1.0
STORATIVITY 1.0                                  PLANE U23
PLANE U18                                        P_TYPE UPPER
P_TYPE UPPER                                     PLANE L23
PLANE L18                                        P_TYPE LOWER
P_TYPE LOWER                                     PLANE X03
PLANE P1                                         P_TYPE LOWER
P_TYPE LOWER                                     PLANE X04
PLANE P23                                        P_TYPE UPPER
P_TYPE UPPER                                     TEST_POINT    1900.00   8075.00 -975.00
PLANE A1                                         END_DEF
P_TYPE UPPER                                     #SFZ03d
PLANE A2                                         BEGIN_DEF ZONE
P_TYPE LOWER                                     NAME Z24
TEST_POINT   1866.67   7733.33 -433.33           ALFA  -7.41
END_DEF                                          BETA 0.0
#SFZ01                                           STORATIVITY 1.0
#BEGIN_DEF ZONE                                  PLANE U24
#NAME Z19                                         P_TYPE UPPER
#ALFA  -7.41                                      PLANE L24
#BETA 0.0                                         P_TYPE LOWER
#STORATIVITY 1.0                                  PLANE X04
#PLANE U19                                        P_TYPE LOWER
#P_TYPE UPPER                                     PLANE P25
#PLANE L19                                        P_TYPE LOWER
#P_TYPE LOWER                                     TEST_POINT    3195.00   8050.00 -975.00
#TEST_POINT    4636.67 11760.00 -500.00          END_DEF
#END_DEF                                         #SFZ03e
#SFZ02                                           #BEGIN_DEF ZONE
BEGIN_DEF ZONE                                   #NAME Z25
NAME Z20                                         #ALFA  -7.41
ALFA  -5.88                                      #BETA 0.0
BETA 0.0                                         #STORATIVITY 1.0
STORATIVITY 1.0                                  #PLANE U25
PLANE U20                                        #P_TYPE UPPER
P_TYPE UPPER                                     #PLANE L25
PLANE L20                                        #P_TYPE LOWER
P_TYPE LOWER                                     #PLANE P24
TEST_POINT  -3125.00   6510.00 -500.00           #P_TYPE LOWER
END_DEF                                          #PLANE P26
#SFZ03a                                          #P_TYPE LOWER
#BEGIN_DEF ZONE                                  #TEST_POINT    5103.33   7960.00 -500.00
#NAME Z21                                         #END_DEF
#ALFA  -7.41                                      #SFZ03f
#BETA 0.0                                         #BEGIN_DEF ZONE
#STORATIVITY 1.0                                  #NAME Z26
#PLANE U21                                        #ALFA  -7.41
#P_TYPE UPPER                                     #BETA 0.0
#PLANE L21                                        #STORATIVITY 1.0
#P_TYPE LOWER                                     #PLANE U26
#PLANE P22                                        #P_TYPE UPPER
#P_TYPE LOWER                                     #PLANE L26
#TEST_POINT  -2680.00   8401.67 -500.00           #P_TYPE LOWER
#END_DEF                                          #PLANE P25
#SFZ03b                                           #P_TYPE LOWER
BEGIN_DEF ZONE                                   #TEST_POINT    7486.67   7976.67 -500.00
NAME Z22                                         #END_DEF
ALFA  -7.41                                      #SFZ04
BETA 0.0                                         BEGIN_DEF ZONE
STORATIVITY 1.0                                  NAME Z27
PLANE U22                                        ALFA  -7.41
P_TYPE UPPER                                     BETA 0.0
PLANE L22                                        STORATIVITY 1.0
P_TYPE LOWER                                     PLANE U27
PLANE P21                                        P_TYPE UPPER
P_TYPE LOWER                                     PLANE L27
PLANE X03                                        P_TYPE LOWER
P_TYPE UPPER                                     PLANE P41
TEST_POINT   -415.00   8140.00 -975.00           P_TYPE LOWER
END_DEF                                          TEST_POINT  -1016.67   6293.33 -500.00
#SFZ03c                                          END_DEF
```

```
#SFZ05a
BEGIN_DEF ZONE
NAME Z28
ALFA  -5.88
BETA 0.0
STORATIVITY 1.0
PLANE U28
P_TYPE UPPER
PLANE L28
P_TYPE LOWER
PLANE P20
P_TYPE LOWER
PLANE P29
P_TYPE UPPER
TEST_POINT  -1978.67  4259.67 -500.00
END_DEF
#SFZ05b
BEGIN_DEF ZONE
NAME Z29
ALFA  -5.88
BETA 0.0
STORATIVITY 1.0
PLANE U29
P_TYPE UPPER
PLANE L29
P_TYPE LOWER
PLANE P28
P_TYPE UPPER
PLANE P30
P_TYPE LOWER
TEST_POINT   1348.67  5520.33 -500.00
END_DEF
#SFZ05c
BEGIN_DEF ZONE
NAME Z30
ALFA  -5.88
BETA 0.0
STORATIVITY 1.0
PLANE U30
P_TYPE UPPER
PLANE L30
P_TYPE LOWER
PLANE P29
P_TYPE LOWER
PLANE P26
P_TYPE UPPER
TEST_POINT   4705.67  7066.00 -500.00
END_DEF
#SFZ06a
BEGIN_DEF ZONE
NAME Z31
ALFA  -7.41
BETA 0.0
STORATIVITY 1.0
PLANE U31
P_TYPE UPPER
PLANE L31
P_TYPE LOWER
PLANE P21
P_TYPE LOWER
PLANE P32
P_TYPE UPPER
TEST_POINT   -683.33  8830.00 -500.00
END_DEF
#SFZ06b
BEGIN_DEF ZONE
NAME Z32
ALFA  -7.41
BETA 0.0
STORATIVITY 1.0
PLANE U32
P_TYPE UPPER
PLANE L32
P_TYPE LOWER
PLANE P31
```

```
P_TYPE UPPER
PLANE P33
P_TYPE UPPER
TEST_POINT   1506.67  9346.67 -500.00
END_DEF
#SFZ06c
BEGIN_DEF ZONE
NAME Z33
ALFA  -7.41
BETA 0.0
STORATIVITY 1.0
PLANE U33
P_TYPE UPPER
PLANE L33
P_TYPE LOWER
PLANE P32
P_TYPE UPPER
TEST_POINT   6315.00  9970.00 -500.00
END_DEF
#SFZ07a
BEGIN_DEF ZONE
NAME Z34
ALFA  -7.41
BETA 0.0
STORATIVITY 1.0
PLANE U34
P_TYPE UPPER
PLANE L34
P_TYPE LOWER
PLANE X07
P_TYPE UPPER
TEST_POINT  -2025.00  3915.00 -975.00
END_DEF
#SFZ07b
BEGIN_DEF ZONE
NAME Z35
ALFA  -7.41
BETA 0.0
STORATIVITY 1.0
PLANE U35
P_TYPE UPPER
PLANE L35
P_TYPE LOWER
PLANE X07
P_TYPE LOWER
PLANE P41
P_TYPE UPPER
TEST_POINT    212.50  5905.00 -975.00
END_DEF
#SFZ10a
BEGIN_DEF ZONE
NAME Z36
ALFA  -5.88
BETA 0.0
STORATIVITY 1.0
PLANE U36
P_TYPE UPPER
PLANE L36
P_TYPE LOWER
PLANE P37
P_TYPE UPPER
TEST_POINT   3363.33  5766.67 -500.00
END_DEF
#SFZ10b
BEGIN_DEF ZONE
NAME Z37
ALFA  -5.88
BETA 0.0
STORATIVITY 1.0
PLANE U37
P_TYPE UPPER
PLANE L37
P_TYPE LOWER
PLANE P36
P_TYPE UPPER
```

```
TEST_POINT   4603.33 11340.00 -500.00          P_TYPE LOWER
END_DEF                                          PLANE P41
#SFZ11                                           P_TYPE UPPER
BEGIN_DEF ZONE                                   PLANE P39
NAME Z38                                         P_TYPE UPPER
ALFA  -7.41                                      TEST_POINT    1185.00  8286.67 -500.00
BETA 0.0                                         END_DEF
STORATIVITY 1.0                                  #SFZ15
PLANE U38                                        BEGIN_DEF ZONE
P_TYPE UPPER                                     NAME Z43
PLANE L38                                        ALFA  -5.88
P_TYPE LOWER                                     BETA 0.0
PLANE P5                                         STORATIVITY 1.0
P_TYPE UPPER                                     PLANE U43
PLANE P2                                         P_TYPE UPPER
P_TYPE UPPER                                     PLANE L43
TEST_POINT   5926.67  6496.67 -500.00           P_TYPE LOWER
END_DEF                                          PLANE P32
#SFZ13a                                          P_TYPE LOWER
BEGIN_DEF ZONE                                   TEST_POINT    2635.00 12103.33 -500.00
NAME Z39                                         END_DEF
ALFA  -7.41                                      #EW-5  SRD5
BETA 0.0                                         BEGIN_DEF ZONE
STORATIVITY 1.0                                  NAME Z46
PLANE U39                                        ALFA  -7.61
P_TYPE UPPER                                     BETA 0.0
PLANE L39                                        STORATIVITY 1.0
P_TYPE LOWER                                     PLANE Q1
PLANE P31                                        P_TYPE UPPER
P_TYPE UPPER                                     PLANE Q2
PLANE P40                                        P_TYPE LOWER
P_TYPE LOWER                                     PLANE Q3
TEST_POINT    803.33  8713.33 -500.00           P_TYPE LOWER
END_DEF                                          PLANE Q4
#SFZ13b                                          P_TYPE UPPER
BEGIN_DEF ZONE                                   PLANE Q5
NAME Z40                                         P_TYPE UPPER
ALFA  -7.41                                      PLANE Q6
BETA 0.0                                         P_TYPE LOWER
STORATIVITY 1.0                                  TEST_POINT   2190.00  7315.00 -350.00
PLANE U40                                        END_DEF
P_TYPE UPPER                                     #Fix SRD-zoner
PLANE L40                                        BEGIN_DEF PLANE
P_TYPE LOWER                                     NAME F04
PLANE P39                                        EQUATION   0.00000   0.00000  1.00000
P_TYPE LOWER                                     600.000
PLANE P23                                        TYPE UPPER
P_TYPE LOWER                                     END_DEF
TEST_POINT   2196.67  8220.00 -500.00           #SRD1
END_DEF                                          BEGIN_DEF ZONE
#SFZ14a                                          NAME Z57
BEGIN_DEF ZONE                                   ALFA -8.03
NAME Z41                                         BETA 0.0
ALFA  -7.41                                      STORATIVITY 1.0
BETA 0.0                                         PLANE P23
STORATIVITY 1.0                                  P_TYPE UPPER
PLANE U41                                        PLANE P1
P_TYPE UPPER                                     P_TYPE LOWER
PLANE L41                                        PLANE P41
P_TYPE LOWER                                     P_TYPE UPPER
PLANE P35                                        PLANE P42
P_TYPE LOWER                                     P_TYPE UPPER
PLANE P42                                        PLANE F04
P_TYPE UPPER                                     P_TYPE LOWER
TEST_POINT   1031.67  7415.00 -500.00           TEST_POINT 1600.00  7700.00 -300.00
END_DEF                                          END_DEF
#SFZ14b                                          #SRD1
BEGIN_DEF ZONE                                   BEGIN_DEF ZONE
NAME Z42                                         NAME Z58
ALFA  -7.41                                      ALFA -9.03
BETA 0.0                                         BETA 0.0
STORATIVITY 1.0                                  STORATIVITY 1.0
PLANE U42                                        PLANE P23
P_TYPE UPPER                                     P_TYPE UPPER
PLANE L42                                        PLANE P1
```

```
P_TYPE LOWER                                    PLANE P3
PLANE P41                                       P_TYPE LOWER
P_TYPE UPPER                                    PLANE F04
PLANE P42                                        P_TYPE UPPER
P_TYPE UPPER                                    #TEST_POINT 2400.00  7400.00  -700.0
PLANE F04                                        END_DEF
P_TYPE UPPER                                    #SRD4
TEST_POINT 1600.00  7700.00 -1000.00            BEGIN_DEF ZONE
END_DEF                                          NAME Z63
#SRD2                                            ALFA -7.54
BEGIN_DEF ZONE                                   BETA 0.0
NAME Z59                                         STORATIVITY 1.0
ALFA -7.11                                       PLANE P41
BETA 0.0                                         P_TYPE UPPER
STORATIVITY 1.0                                  PLANE P3
PLANE P1                                         P_TYPE UPPER
P_TYPE UPPER                                     PLANE P38
PLANE P23                                        P_TYPE UPPER
P_TYPE UPPER                                     PLANE P8
PLANE P2                                         P_TYPE LOWER
P_TYPE LOWER                                     PLANE P36
PLANE P41                                        P_TYPE LOWER
P_TYPE UPPER                                     PLANE F04
PLANE F04                                        P_TYPE LOWER
P_TYPE LOWER                                     #TEST_POINT 2000.00  6500.00  -500.0
TEST_POINT 1700.00  7400.00  -100.0             END_DEF
END_DEF                                          #SRD4
#SRD2                                            BEGIN_DEF ZONE
BEGIN_DEF ZONE                                   NAME Z64
NAME Z60                                         ALFA -8.54
ALFA -8.11                                       BETA 0.0
BETA 0.0                                         STORATIVITY 1.0
STORATIVITY 1.0                                  PLANE P41
PLANE P1                                         P_TYPE UPPER
P_TYPE UPPER                                     PLANE P3
PLANE P23                                        P_TYPE UPPER
P_TYPE UPPER                                     PLANE P38
PLANE P2                                         P_TYPE UPPER
P_TYPE LOWER                                     PLANE P8
PLANE P41                                        P_TYPE LOWER
P_TYPE UPPER                                     PLANE P36
PLANE F04                                        P_TYPE LOWER
P_TYPE UPPER                                     PLANE F04
#TEST_POINT 1900.00  7300.00 -1000.0            P_TYPE UPPER
END_DEF                                          #TEST_POINT 2000.00  6500.00  -700.0
#SRD3                                            END_DEF
BEGIN_DEF ZONE                                   #SRD4
NAME Z61                                         BEGIN_DEF ZONE
ALFA -8.76                                       NAME Z65
BETA 0.0                                         ALFA -7.54
STORATIVITY 1.0                                  BETA 0.0
PLANE P2                                         STORATIVITY 1.0
P_TYPE UPPER                                     PLANE P5
PLANE P5                                         P_TYPE UPPER
P_TYPE LOWER                                     PLANE P3
PLANE P24                                        P_TYPE LOWER
P_TYPE UPPER                                     PLANE P38
PLANE P3                                         P_TYPE UPPER
P_TYPE LOWER                                     PLANE F04
PLANE F04                                        P_TYPE LOWER
P_TYPE LOWER                                     #TEST_POINT 2400.00  7150.00  -500.0
#TEST_POINT 2400.00  7400.00  -500.0            END_DEF
END_DEF                                          #SRD4
#SRD3                                            BEGIN_DEF ZONE
BEGIN_DEF ZONE                                   NAME Z66
NAME Z62                                         ALFA -8.54
ALFA -9.76                                       BETA 0.0
BETA 0.0                                         STORATIVITY 1.0
STORATIVITY 1.0                                  PLANE P5
PLANE P2                                         P_TYPE UPPER
P_TYPE UPPER                                     PLANE P3
PLANE P5                                         P_TYPE LOWER
P_TYPE LOWER                                     PLANE P38
PLANE P24                                        P_TYPE UPPER
P_TYPE UPPER                                     PLANE F04
```

```
#P_TYPE UPPER
TEST_POINT 2400.00  7050.00  -700.0
END_DEF
#SRD4
BEGIN_DEF ZONE
NAME Z67
ALFA -7.54
BETA 0.0
STORATIVITY 1.0
PLANE P8
P_TYPE UPPER
PLANE P4
P_TYPE LOWER
PLANE P36
P_TYPE LOWER
PLANE P38
P_TYPE UPPER
PLANE F04
P_TYPE LOWER
#TEST_POINT 3172.00  6709.00  -500.0
END_DEF
#SRD4
BEGIN_DEF ZONE
NAME Z68
ALFA -8.54
BETA 0.0
STORATIVITY 1.0
PLANE P8
P_TYPE UPPER
PLANE P4
P_TYPE LOWER
PLANE P36
P_TYPE LOWER
PLANE P38
P_TYPE UPPER
PLANE F04
P_TYPE UPPER
#TEST_POINT 3244.00  6681.00  -700.0
END_DEF
END_BLOCK
```

Appendix H - Coordinate System Transformations

The simulations for Aberg are performed using coordinates in the Äspö local system. This means that all input data in form of e.g. stream tube starting positions and fracture zones are defined for that system. The model is set up in the Äspö local system with the origin for the model cube at (950, 6150, -1250). The HYDRASTAR modelling terms "user system" and "world system" are defined using that point in the Äspö local system. The HYDRASTAR "cube system" is not rotated in relation to the Äspö system. The used definitions of coordinate systems give output data for e.g. exit locations, which could be extracted from the lines_<real>.hyp files, in the Äspö local system.

The Äspö local coordinate system is rotated 11.655 degrees west according to Walker et al. (1997) with an off-set of 1,550,827 and 6,360,252 in east and north, in relation to RAK. The coordinate systems for Aberg are right-handed with X toward east and Y toward north. The Z-direction is given in meter above sea level (m.a.s.l). To transform the modelling coordinates to RAK, the following equations have been used:

$$X_{RAK} = X_{Off\text{-}set} + X_A * \cos\theta - Y_A * \sin\theta$$

$$Y_{RAK} = Y_{Off\text{-}set} + X_A * \sin\theta + Y_A * \cos\theta$$

where X_{RAK} and Y_{RAK} stand for east and north, respectively, X_A and Y_A are Aberg modelling coordinates, $X_{Off\text{-}set} = 1,550,827$, $Y_{Off\text{-}set} = 6,360,252$ and, $\theta = 11.655$ degrees.

A slightly different transformation is used for the repository layout prescribed by Munier et al. (1997). Adapting their transformation into the preceding form, the Munier et al. (1997) transform is:

$$X_{RAK38} = 1,551,210.173 + 0.978799 * (X_A - 1956.68) - 0.204822 * (Y_A - 7484.309)$$

$$Y_{RAK38} = 6,367,978.295 + 0.204822 * (X_A - 1956.68) + 0.978799 * (Y_A - 7484.309)$$

That is, Munier et al. (1997) use a rotation angle θ of 11.819 degrees and an off-set of 1,551,210 and 6,367,978 in east and north, respectively. Munier et al. (1997) also use a local off-set of 1957 and 7484 in the local Äspö system. The differences between the Munier et al. (1997) system and the system used in this study is less than 25m (in terms of RAK-system coordinates) when calculating exit location using both set of equations.

List of SKB reports

Annual Reports

1977-78
TR 121
KBS Technical Reports 1 – 120
Summaries
Stockholm, May 1979

1979
TR 79-28
The KBS Annual Report 1979
KBS Technical Reports 79-01 – 79-27
Summaries
Stockholm, March 1980

1980
TR 80-26
The KBS Annual Report 1980
KBS Technical Reports 80-01 – 80-25
Summaries
Stockholm, March 1981

1981
TR 81-17
The KBS Annual Report 1981
KBS Technical Reports 81-01 – 81-16
Summaries
Stockholm, April 1982

1982
TR 82-28
The KBS Annual Report 1982
KBS Technical Reports 82-01 – 82-27
Summaries
Stockholm, July 1983

1983
TR 83-77
The KBS Annual Report 1983
KBS Technical Reports 83-01 – 83-76
Summaries
Stockholm, June 1984

1984
TR 85-01
Annual Research and Development Report 1984
Including Summaries of Technical Reports Issued
during 1984. (Technical Reports 84-01 – 84-19)
Stockholm, June1985

1985
TR 85-20
Annual Research and Development Report 1985
Including Summaries of Technical Reports Issued
during 1985. (Technical Reports 85-01 – 85-19)
Stockholm, May 1986

1986
TR 86-31
SKB Annual Report 1986
Including Summaries of Technical Reports Issued
during 1986
Stockholm, May 1987

1987
TR 87-33
SKB Annual Report 1987
Including Summaries of Technical Reports Issued
during 1987
Stockholm, May 1988

1988
TR 88-32
SKB Annual Report 1988
Including Summaries of Technical Reports Issued
during 1988
Stockholm, May 1989

1989
TR 89-40
SKB Annual Report 1989
Including Summaries of Technical Reports Issued
during 1989
Stockholm, May 1990

1990
TR 90-46
SKB Annual Report 1990
Including Summaries of Technical Reports Issued
during 1990
Stockholm, May 1991

1991
TR 91-64
SKB Annual Report 1991
Including Summaries of Technical Reports Issued
during 1991
Stockholm, April 1992

1992
TR 92-46
SKB Annual Report 1992
Including Summaries of Technical Reports Issued
during 1992
Stockholm, May 1993

1993
TR 93-34
SKB Annual Report 1993
Including Summaries of Technical Reports Issued
during 1993
Stockholm, May 1994

1994
TR 94-33
SKB Annual Report 1994
Including Summaries of Technical Reports Issued
during 1994
Stockholm, May 1995

1995
TR 95-37
SKB Annual Report 1995
Including Summaries of Technical Reports Issued
during 1995
Stockholm, May 1996

1996
TR 96-25
SKB Annual Report 1996
Including Summaries of Technical Reports Issued
during 1996
Stockholm, May 1997

List of SKB Technical Reports 1998

TR 98-01
**Global thermo-mechanical effects
from a KBS-3 type repository.
Summary report**
Eva Hakami, Stig-Olof Olofsson, Hossein Hakami,
Jan Israelsson
Itasca Geomekanik AB, Stockholm, Sweden
April 1998

TR 98-02
**Parameters of importance to determine
during geoscientific site investigation**
Johan Andersson[1], Karl-Erik Almén[2],
Lars O Ericsson[3], Anders Fredriksson[4],
Fred Karlsson[3], Roy Stanfors[5], Anders Ström[3]
[1] QuantiSci AB
[2] KEA GEO-Konsult AB
[3] SKB
[4] ADG Grundteknik KB
[5] Roy Stanfors Consulting AB
June 1998

TR 98-03
**Summary of hydrochemical conditions
at Aberg, Beberg and Ceberg**
Marcus Laaksoharju, Iona Gurban,
Christina Skårman
Intera KB
May 1998

TR 98-04
**Maqarin Natural Analogue Study:
Phase III**
J A T Smellie (ed.)
Conterra AB
September 1998

TR 98-05
**The Very Deep Hole Concept –
Geoscientific appraisal of conditions
at great depth**
C Juhlin[1], T Wallroth[2], J Smellie[3], T Eliasson[4],
C Ljunggren[5], B Leijon[3], J Beswick[6]
[1] Christopher Juhlin Consulting
[2] Bergab Consulting Geologists
[3] Conterra AB
[4] Geological Survey of Sweden
[5] Vattenfall Hydropower AB
[6] EDECO Petroleum Services Ltd.
June 1998

TR 98-06
**Indications of uranium transport
around the reactor zone at Bagombe
(Oklo)**
I Gurban[1], M Laaksoharju[1], E Ledoux[2], B Made[2],
A L Salignac[2],
[1] Intera KB, Stockholm, Sweden
[2] Ecole des Mines, Paris, France
August 1998

TR 98-07
**PLAN 98 – Costs for management of
the radioactive waste from nuclear
power production**
Swedish Nuclear Fuel and Waste Management Co
June 1998

TR 98-08
**Design premises for canister for spent
nuclear fuel**
Lars Werme
Svensk Kärnbränslehantering AB
September 1998

TR 98-09
**Test manufacturing of copper canisters
with cast inserts
Assessment report**
Claes-Göran Andersson
Svensk Kärnbränslehantering AB
Augusti 1998

TR 98-10
Characterization and Evaluation of Sites for Deep Geological Disposal of Radioactive Waste in Fractured Rocks
Proceedings from The 3rd Äspö International Seminar, Oskarshamn, June 10–12, 1998-11-10
Svensk Kärnbränslehantering AB
September 1998

TR 98-11
Leaching of 90-year old concrete mortar in contact with stagnant water
Jan Trägårdh, Björn Lagerblad
Swedish Cement and Concrete Research Institute
July 1998

TR 98-12
Geological-structural models used in SR 97
Uncertainty analysis
Pauli Saksa, Jorma Nummela
FINTACT Ltd
October 1998

TR 98-13
Late Quaternary changes in climate
Karin Holmgren and Wibjörn Karlén
Department of Physical Geography
Stockholm University
December 1998

TR 98-14
Partitioning and transmutation (P&T) 1997
Åsa Enarsson, Anders Landgren, Jan-Olov Liljenzin, Mats Skålberg, Lena Spjuth
Department of Nuclear Chemistry, Chalmers University of Technology, Gothenburg
and
Waclaw Gudowski, Jan Wallenius
Department of Nuclear and Reactor Physics, Royal Institute of Technology, Stockholm
May 1998

TR 98-15
Studies of surface complexation of H^+, NpO_2^+, Co^{2+}, Th^{4+} onto TiO_2 and H^+, UO_2^{2+} onto alumina
Anna-Maria Jakobsson, Yngve Albinsson
Department of Nuclear Chemistry, Chalmers University of Technology, Sweden
and
Robert S Rundberg
Los Alamos National Laboratory, USA
November 1998

TR 98-16
Backfilling with mixtures of bentonite/ ballast materials or natural smectitic clay?
Roland Pusch
Geodevelopment AB
October 1998

TR 98-17
Groundwater degassing in fractured rock:
Modelling and data comparison
Jerker Jarsjö and Georgia Destouni
Water Resources Engineering
Royal Institute of Technology, Stockholm
November 1998

TR 98-18
The interaction of sorbing and non-sorbing tracers with different Äspö rock types
Sorption and diffusion experiments in the laboratory scale
Johan Byegård, Henrik Johansson, Mats Skålberg
Department of Nuclear Chemistry, Chalmers University of Technology, Gothenburg, Sweden
and
Eva-Lena Tullborg
Terralogica AB, Gråbo, Sweden
November 1998

TR 98-19
Äspö Hard Rock Laboratory
Annual Report 1997
Svensk Kärnbränslehantering AB
May 1998

TR 98-20
The biosphere at Aberg, Beberg and Ceberg
– a description based on literature concerning climate, physical geography, ecology, land use and environment
Tobias Lindborg, Regina Schüldt
NaturRådet
December 1998

TR 98-21
Crustal structure and regional tectonics of SE Sweden and the Baltic Sea
Alan Geoffrey Milnes
Department of Geology, University of Bergen, Norway
David G Gee and Carl-Erik Lund
Department of Earth Sciences, Uppsala University
November 1998

TR 98-22

Development of a kinetic model for the dissolution of the UO$_2$ spent nuclear fuel

Application of the model to the minor radionuclides

Jordi Bruno, Esther Cera, Lara Duro, Jordi Pon
QuantiSci SL, Barcelona, Spain
Joan de Pablo
Department Enginyeria Quimica, UPC, Barcelona, Spain
Trygve Eriksen
Department Nuclear Chemistry, KTH, Stockholm

May 1998